University of Southampton

Faculty of Engineering and Physical Sciences

School of Chemistry and Chemical Engineering

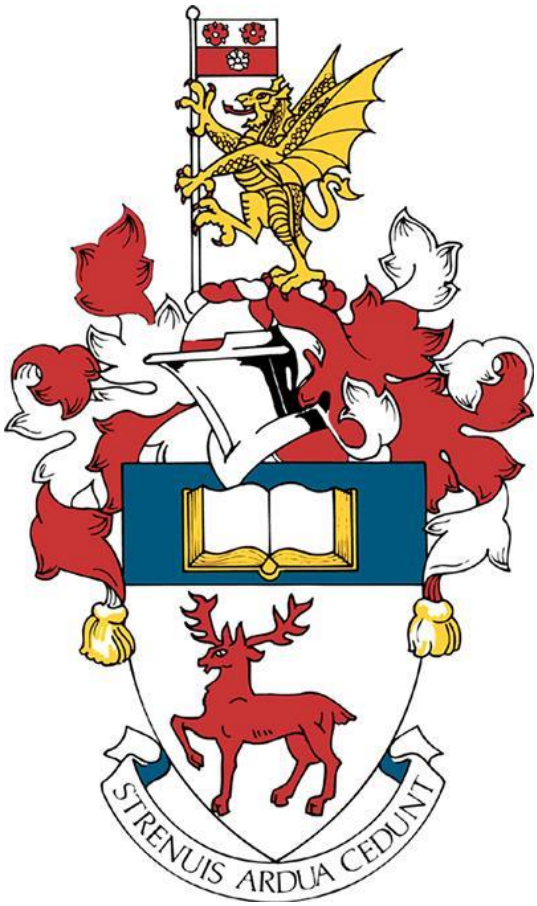

Modular DNA nanopore (NP) for targeted cell killing

Tina-Thien Ho

ORCID ID 0000-0002-0576-8428

Thesis for the degree Doctor of Philosophy

May 2025

Abstract

Faculty of Engineering and Physical Sciences

School of Chemistry and Chemical Engineering

Doctor of Philosophy

Modular DNA nanopore (NP) for targeted cell killing

by

Tina-Thien Ho

Cancer treatment strategies often rely on combination therapies that can be aggressive, time-consuming, and present severe side effects. To overcome these challenges, we have developed a modular therapeutic platform for targeted cell killing using self-assembling DNA nanopores (NPs). This study focuses on designing 6-helix bundle NP, featuring hydrophobic moieties that enable membrane insertion, leading to uncontrolled ion flow and ultimately to cell death. These NPs are conjugated site-specifically to rituximab, a CD20-targeting monoclonal antibody, using a dibromopyridazinedione-linker which rebridges interchain disulphides. This conjugation results in a precise 4:1 NP-to-antibody ratio, ensuring targeted delivery and cytotoxicity in B lymphocyte cells.

The NPs were synthesised in a one-step assembly process and verified using electromobility shift assays (EMSA). Successful conjugation was demonstrated through SDS-PAGE, and flow cytometry confirmed the preservation of the antibody's specificity to the CD20 receptor. Furthermore, the stability of the construct was verified in serum over a three-week period at 37°C. In co-culture with a malignant B-cell line (Ramos), the cholesterol-modified NPs exhibited a 20% increase in cell death compared to untreated controls after 48 hours.

This work describes the development of a stable and specific antibody-NP conjugate with defined antibody-drug ratios. The findings elucidate the potential of membrane-spanning NPs as a novel therapeutic platform for cancer treatment, with implications for future applications in various types of cancer.

Table of Contents

Table of Figures

Research Thesis: Declaration of Authorship

Print name: Tina-Thien Ho

Title of thesis: Modular DNA Nanopore for targeted cell killing

I declare that this thesis and the work presented in it are my own and has been generated by me as the result of my own original research.

I confirm that:

1. This work was done wholly or mainly while in candidature for a research degree at this University;
2. Where any part of this thesis has previously been submitted for a degree or any other qualification at this University or any other institution, this has been clearly stated;
3. Where I have consulted the published work of others, this is always clearly attributed;
4. Where I have quoted from the work of others, the source is always given. With the exception of such quotations, this thesis is entirely my own work;
5. I have acknowledged all main sources of help;
6. Where the thesis is based on work done by myself jointly with others, I have made clear exactly what was done by others and what I have contributed myself;
7. None of this work has been published before submission

Signature: ..... Date: 20/05/2025

Acknowledgements

Completing this PhD has been a challenging yet deeply rewarding journey, and I am immensely grateful to those who have supported me along the way.

First and foremost, I would like to express my gratitude to my supervisors, Dr. Eugen Stulz and Prof. Sean Lim, for your invaluable guidance, continuous support, and encouragement throughout this project. Your expertise and insights have helped me navigate the complexities of this research.

To Fritz—you have been my rock, my constant, my safe haven in this storm. Your unconditional love and support have been the foundation that kept me standing through the most difficult moments. You celebrated my wins with me, lifted me up when I stumbled, and reminded me of my strength when I felt I had none left. I could not have done this without you, and I am endlessly grateful to have you by my side.

I would also like to acknowledge my family, whose hard work and dedication have provided me with the opportunities that made this PhD possible. Their support has been fundamental to my academic and professional development, and I hope this accomplishment reflects the values they have instilled in me.

A special thank you goes to Anna and Lara for their incredible support in the lab, both technically and scientifically. From sharing resources and troubleshooting experiments to simply sitting together and making long days in the lab enjoyable, you made this experience infinitely better and I miss our days together more than I can say.

To Ysobel Baker—your support, wisdom, and generosity in and out of the lab meant the world to me. Whether it was scientific discussions, professional guidance, or just a good old chitchat, you were always there. Sharing a lab with you was an absolute privilege, and I will always be grateful for your kindness, advice, and, of course, your lab equipment!

Finally, to the Stulz, the Lim and the Baker group—thank you for your consistent support, insightful discussions, and for fostering an environment where I could grow as a scientist. Your expertise and feedback have been invaluable in shaping my research, and I am grateful for the time I spent working with you all.

Definitions and Abbreviations

A ..... Adenosine

AcOH ..... Acetic acid

ADC..... Antibody-drug conjugate

ADCC ..... Antibody dependent cellular cytotoxicity

AOC ..... Antibody-oligonucleotide conjugate

AO..... Acridine orange

APS ..... Ammonium persulfate

ASO..... Antisense oligonucleotide

BCN..... (1R, 8S, 9S)-Bicyclo[6.1.0]non-4-yn-9-yl

BCN-NHS ..... (1R, 8S, 9S)-Bicyclo[6.1.0]non-4-yn-9-ylmethyl N-succinimidyl carbonate

BCR ..... B-cell receptor

bsAb ..... Bispecific antibody

C ..... Cytosine

Cbl ..... Cobalamine

cEt..... S-constrained ethyl

$CHCl_3$ ..... Chloroform

CPG..... Controlled pore glass

CPP ..... Cell-penetrating peptide

DAPI..... 4’,6-diamidino-2-phenylindole

DBCO ..... Dibenzocyclooctyne

DC..... Dendritic cells

DCC..... N,N’-dicyclohexylcarbodiimide

DCM ..... Dichloromethane

DiBrPD ..... dibromopyridazinedione

DMF..... Dimethylformamide

DMT..... Dimethoxytrityl chloride

DMSO ..... Dimethyl sulfoxide

DNA ..... Desoxyribonucleic acid

EDC..... 1-Ethyl-3-(3-dimethylaminopropyl)carbodiimide

EGFR ..... Epidermal growth factor receptor

EtOAc..... Ethyl acetate

EtOH ..... Ethanol

FCS..... Fetal calf serum

FDA..... US Food and Drug Administration

FSHD ..... Facioscapulohumeral muscular dystrophy

G ..... Guanine

GC..... Germinal center

GP ..... L-glutamine & sodium pyruvate

HATU ..... Hexafluorophosphate azabenzotriazole tetramethyl uronium

His..... Histidine

HOBt..... Hydroxybenzotriazole

HPLC ..... High performance liquid chromatography

HU ..... Hydrophobic unit

IR spectroscopy..... Infrared spectroscopy

mAb..... Monoclonal antibody

MeCN ..... Acetonitrile

MES ..... (2-(N-morpholino)ethanesulfonic acid)

MHC ..... Major histocompatibility complexes

NaOH..... Sodium hydroxide

NHL..... Non-Hodgkin lymphoma

NHS..... N-Hydroxysuccinimide

NK..... Natural killer

NMR ..... Nuclear magnetic resonance

NP..... DNA Nanopore

NP1C18..... Modified DNA NP with 2 single alkyl chains

NP2c ..... Modified DNA NP with 2 cholesterol tags

NP3c ..... Modified DNA NP with 3 cholesterol tags

NP4c ..... Modified DNA NP with 4 cholesterol tags

NPk ..... Modified DNA NP with 2 double alkyl chains

NT ..... No treatment

OPOE ..... N-octyl- oligo-oxyethylene

PAGE ..... Poly acrylamide gel electrophoresis

PAMPs ..... Pathogen-associated molecular patterns

PBS ..... Phosphate buffered saline

PE ..... Petroleum ether

PEG ..... Polyethylene glycol unit

Pen/Strep ..... Penicillin/Streptomycin

PI ..... Propidium iodide

RNAse ..... Ribonuclease

ROS ..... Reactive oxygen species

RPMI ..... Roswell Park Memorial Institute

rtx ..... rituximab

scFv ..... Single chain variable fragment

SDS ..... Sodium dodecyl sulphate

siRNA ..... Small interfering RNA

SHM ..... Somatic hypermutation

SPAAC ..... Strain promoted azide alkyne cycloaddition

T ..... Thymidine

TB ..... Tris-borate

TBE ..... Tris-borate-EDTA

t-BuOH..... tert-butanol

TC ..... Transcobalamine

TEA ..... Triethylamine

TEAA ..... Triethylamine acetate

TEMED..... Tetramethylethylenediamine

THF ..... Tetrahydrofuran

TLC..... Thin layer chromatography

UTR..... Untranslated region

UV..... Ultraviolet

WGA ..... Wheat Germ Agglutinin

Chapter 1 Introduction

1.1 Cancer

Cancer is a major global health challenge that is accountable for an estimated 10 million deaths annually worldwide[1, 2] and has a significant economic burden of approximately $195 billion as of 2022[3, 4]. The estimated global economic impact of cancer is projected to rise to $25.2 trillion between 2020 and 2050, with tracheal, bronchus and lung cancers contributing the highest share (15.4%), followed by colon, rectum, breast, liver cancers, and leukaemia[5]. Cancer, characterised by the uncontrolled proliferation of malignant, clonal cells capable to invade surrounding healthy tissues, metastasize to distant organs and subsequent disruption of physiological processes[6]. Cancer is not a single disease; it is heterogeneous and consists of numerous types of diseases with distinct molecular, genetic, and cellular profiles; thus, presents considerable challenges in developing universally effective therapies. As such, an understanding of the specific mechanisms and behaviours of different cancer types is essential for advancing therapeutic strategies that are able to provide tailor-made and effective patient treatment.

1.1.1 B-cell lymphomas

Cancers of lymphatic tissue are referred to as lymphomas and are broadly classified into Hodgkin lymphoma (HL) and non-Hodgkin lymphoma (NHL). While HL is typically a more aggressive type, NHL are more common and represent most of the cases of lymphoma worldwide with approximately 85% being B-cell lymphomas. This high prevalence can be attributed to the development of B cells which become susceptible to acquire mutations

during the process of somatic hypermutation, an important step to create B lymphocytes with high-affinity antibody receptors expressed on their surface[7]. The 2016 World Health Organization classification of lymphoid neoplasm provides a framework for distinguishing these subtypes which is essential for accurate diagnosis and tailored therapeutic strategies (**Appendix 1**).

B-cell lymphomas represent a heterogenous group of malignancies with unique clinical behaviours. These range from slow-developing forms, such as follicular lymphoma, which can remain stable for years, to more aggressive subtypes like diffuse large B-cell lymphoma (DLBCL), which progresses over weeks or months[8]. The reason for the complexity of these malignancies lies in an array of molecular alterations that drive lymphomagenesis. For example, genetic mutations, such as those involving the anti-apoptotic *BCL2* gene, which promotes cell survival, and *MYC* which drives uncontrolled cell proliferation, play a critical role. Additionally, mutations in *EZH2*, an important epigenetic regulator, lead to aberrant histone methylation that inhibits the differentiation of germinal centre B cells out of their proliferative stage and thereby promotes lymphoma development.

To get a better insight on how these alterations arise, it is important to understand the normal B-cell developmental pathway. The development of B cells begins from haematopoietic stem cells in the bone marrow that undertake a high number of processes to eventually become naïve B cells that have not yet been exposed to an antigen and which migrate to secondary lymphoid organs like the spleen and the lymph nodes[2]. In these secondary lymphoid organs, the B cells mature through antigen exposure and differentiate into memory B cells or plasma cells in germinal centers (GC). In these GC, the B cells undergo rapid proliferation and experience isotype switching and somatic hypermutation (SHM), a process that involves point mutations on cytosine bases to enhance antigen exposure[9, 10]. Although this procedure is

essential for B-cell function, the high mutational rate makes them particularly susceptible for dysregulation and can result in a wide range of malignant mutations. Further insights and details on B cells and their role in lymphomas are found in section 1.2.2.

Beyond genetic mutations, epigenetic changes can also impact signalling pathways, such as NF-κB or PI3K/AKT, and further contribute to tumour progression and immune system evasion, enabling the lymphoma cells to avoid detection and destruction.

These molecular changes make both diagnosis and treatment more challenging. For example, the presence of overlapping genetic and cellular characteristics between subtypes can complicate accurate classification.

The conventional treatment approaches for B-cell lymphomas can be divided into three primary categories: chemotherapy, radiotherapy and monoclonal antibody-based treatments. Chemotherapy, which uses drugs to target rapidly dividing cells, is often used in combination therapy to target B cell malignancies; an example being CHOP which consists of cyclophosphamide (an alkylating agent that interferes with DNA replication), doxorubicin (a DNA-damaging anthracycline), vincristine (a mitotic inhibitor) and prednisone (a corticosteroid used to reduce inflammation and modulate the immune response)[11]. While chemotherapy as monotherapy or in combination therapies is effective in reducing tumor burden, it is inherently non-specific, affecting both malignant and healthy proliferative cells; for example, those in the bone marrow or the gastrointestinal tract are often depleted upon chemotherapy administration. This lack of specificity often leads to significant side effects, including immunosuppression, nausea, fatigue and increased susceptibility to infections which can limit the intensity or duration of treatments.

Radiotherapy, another common approach, uses high-energy radiation to destroy cancer cells. It is particularly effective in localised diseases[12, 13], such as early-stage follicular lymphoma,

but its efficacy decreases in more advanced or systemic cases. On the other hand, radiotherapy has the potential to cause unwanted damage to surrounding healthy tissues or cause chromosomal abnormalities[14], resulting in organ toxicity and long-term complications[15].

Immune checkpoint pathways normally regulate the immune system to prevent overactivation, but cancer cells can exploit these mechanisms to evade the immune attack. Immunotherapies, such as checkpoint inhibitors, aim to block these pathways and restore the immune system's ability to recognise and destroy cancerous cells (described further in section 1.2.4.3). Changes in these pathways, such as mutations or dysregulated protein expression like PD-L1, can affect the effectiveness of these therapies by either enhancing or diminishing the immune response to the tumour. In particular, upregulation of PD-L1 can lead to T-cell exhaustion, reducing cytotoxic T-cell activity and impairing the immune system's ability to eliminate malignant cells.

Monoclonal antibodies, such as rituximab (rtx), represent a more targeted approach. Rtx binds specifically to the CD20 protein on the B cell surface, marking them for destruction by the immune system. The detailed mechanism of action are outlined in section 1.2.4.3. In combination with chemotherapy (e.g. R-CHOP, which includes rituximab), monoclonal antibodies improve treatment outcomes by selective cancer cell killing. However, resistance mechanisms, such as the loss of CD20 expression on malignant cells, can lower their effectiveness over time.

Despite the progress with these therapies, there remains significant challenges. One of the major drawbacks of both chemotherapy and radiotherapy is their inability to distinguish between cancerous and healthy cells, leading to collateral damage and severe side effects. Additionally, many patients develop resistance, often driven by genetic mutations, such as

alterations in *TP53*[16, 17] or adaptive cellular mechanisms, like increased expression of pro-survival proteins (e.g. *BCL2*)[18]. This resistance reduces treatment efficacy and increases the likelihood of relapse, making sustained remission difficult to achieve. Understanding these complex biological features is needed for designing more effective and more targeted treatments that address the specific characteristics of each lymphoma subtype[19].

With the above challenges, innovative therapies with reduced off-target toxicity and consideration of resistance mechanism are required. Novel immunotherapies including chimeric antigen receptor CAR T-cell therapy, immune checkpoint inhibitors (e.g. pembrolizumab) and bispecific antibodies offer a new avenue for precision medicine in lymphoma treatment. These therapies are engineered to stimulate the patient's immune system to selectively kill cancer cells, overcoming the limitations of conventional approaches and leading to improved long-term patient outcomes.

1.2 Immune system in the context of cancer

The immune system is a complex network of cells and molecules designed to protect the body against pathogens and abnormal cells, maintaining homeostasis and health. It is composed of two components: the innate immune system, which provides immediate but non-specific responses by cells such as macrophages, neutrophils and natural killer (NK) cells and the adaptive immune system, which provides highly specific, long-lasting immunity through T lymphocytes and B lymphocytes[20]. In the context of cancer, this system plays a dual role: on one hand, it is able to recognise and eliminate emerging tumour cells; on the other hand, cancer cells are able to use immune pathways and develop mechanisms that suppress immune function and promote their survival.

1.2.1 T lymphocytes

T cells are a crucial component of the adaptive immune system and are divided into two cell types based on their surface markers and function: $CD4^+$ and $CD8^+$ cells. $CD4^+$ cells, among them T-helper cells, have the role of activating macrophages and granulocytes to kill cells and promote B-cell activation. Upon binding to the major histocompatibility complex (MHC) on antigen-presenting cells, cytokines are released that trigger the proliferation of CD4+ T-cells into three subtypes: T follicular helper cells (T_{FH}) that facilitate B-cell activation; regulatory T cells (T_{reg}) responsible for homeostasis and down-regulation of the immune response to prevent overreaction and lastly memory T cells (T_{mem}) which can be reactivated in case of reinfection with the same pathogen. In contrast, $CD8^+$ T cells, also known as cytotoxic T cells, recognise and kill virally infected as well as malignant cells through release of cytotoxic molecules such as perforin and granzyme[21].

1.2.2 B cells

B-cell development begins in the bone marrow, where haematopoietic stem cells differentiate into pro-B cells. During this stage, immunoglobulin heavy chain (IGHV) gene rearrangement occurs through V(D)J recombination, enabled by RAG1 and RAG2 enzymes. This leads to the formation of pre-B cells, which express the pre-B-cell receptor complex on their cell surface which drives proliferation and differentiation[22]. Small pre-B cells then undergo light chain rearrangement, resulting in fully functional B-cell receptors (BCR) on the cell surface and the expression of IgM and IgD, marking the transition to immature naïve B cells[23].

Immature B cells migrate to secondary lymphoid organs, such as the spleen and lymph nodes, where they undergo further maturation and antigen exposure. Activation occurs via T cell-independent or T cell-dependent pathways, with the latter involving interactions with T helper cells and cytokine signalling[24]. Also, plasma cells then form and the production of IgG and IgM antibodies commences. The interaction with T helper cells initiates the germinal centre reaction, where B cells undergo somatic hypermutation (SHM) within the dark zone, catalysed by activation-induced cytidine deaminase (AID), to enhance antigen affinity[25]. Successful clones transition to the selection zone, where their affinity is tested on follicular dendritic cells. High-affinity B cells undergo further proliferation and class switching, while non-functional cells are eliminated through apoptosis.

The final differentiation phase results in either antibody-secreting plasma cells or memory B cells, which provide long-term immunity. These cells are capable of recognising antigens in future encounters, resulting in faster and more effective immune responses. A subset of anergic B cells deviates from the classical maturation pathway and remains functionally inactive. Dysregulation in germinal centre processes, such as defective SHM or class switching, can lead to oncogenic mutations and malignant transformation, contributing to the pathogenesis of B-cell lymphomas[24, 25].

Interestingly, while B cells are primarily activated by MHC-antigen presentation, they also recognise antigens independent of MHC molecules. Once activated, they express MHC on their surface, which is detected by T_{FH} cells, completing a feedback loop that enhances B-cell activation[21]. The mechanism of B- and T-cell activation and proliferation is summarised in **Figure 1**.

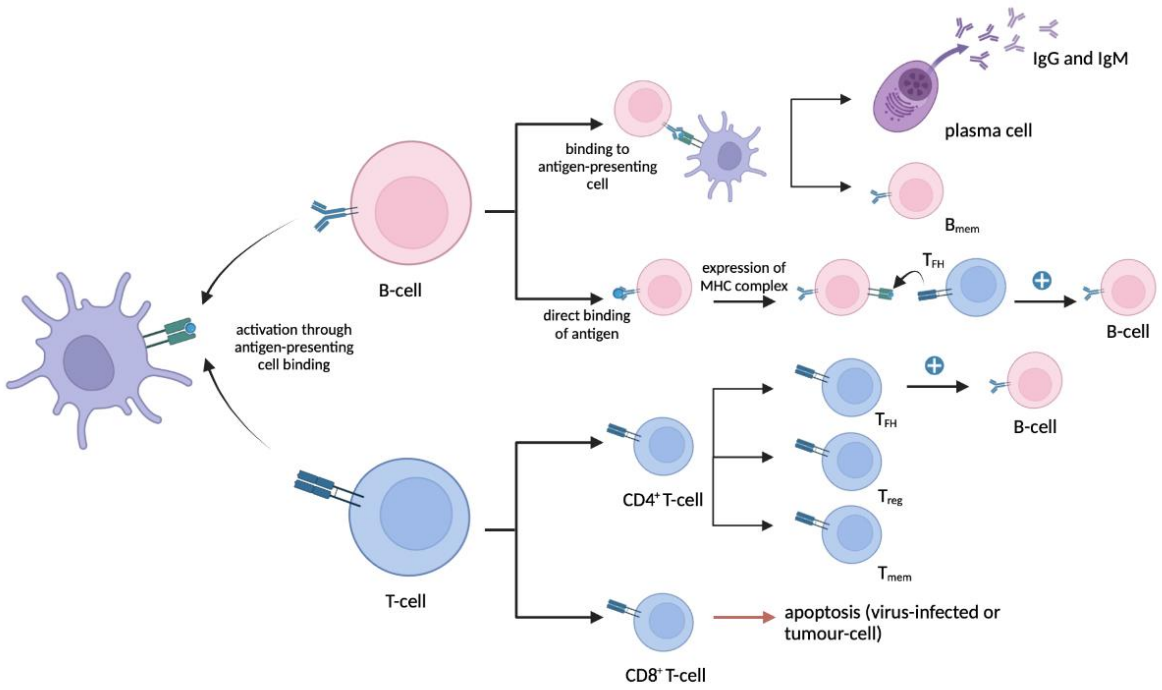

Figure 1 Mechanism of antigen detection and cell proliferation in B- and T-cell pathways. B cells are activated either through direct binding of antigens or via antigen-presenting cells (APCs). Once activated through APCs, B cells differentiate into plasma cells that secrete antibodies (IgG and IgM) or into memory B cells (B_{mem}) that provide long-term immune defence. T cells are activated by APCs to differentiate into various functional subsets. $CD4^+$ T cells differentiate into helper T cells (T_H), which enhance B cell activation, or regulatory T cells (T_{reg}), which modulate immune responses. $CD8^+$ T cells become cytotoxic T cells, which induce apoptosis in virus-infected or tumour cells. Memory T cells (T_{mem}) are also generated to enable faster responses to subsequent antigen exposures.
Arrows represent activation and differentiation pathways, "+" symbols indicate stimulatory interactions, and red arrows denote apoptosis induction by cytotoxic T cells. Created in Biorender.com

1.2.3 The concept of cancer immunoediting

The concept of cancer immunoediting describes the dynamic interaction between cancer cells and the immune system with a dual function in both controlling and promoting tumour

development. The process consists of three distinct stages: elimination, equilibrium and escape.

At the elimination phase, the immune cells such as NK cells, macrophages, and cytotoxic T cells identify and destroy evolving tumour cells. Mechanism involved in this phase include cytokine release, complement system activation and antigen presentation to initiate opsonisation, inflammation and destruction. Opsonisation facilitates immune recognition by tagging tumour cells with opsonins (e.g. antibodies or complement proteins) to induce the elimination by macrophages and neutrophils in a process known as phagocytosis. A few cancer cells may survive and reach the equilibrium phase, where they coexist with the immune system in a dormant state, often evading immune detection through genetic and epigenetic changes. In the escape phase, tumour cells acquire sufficient mutations and signalling pathways alterations that they become capable of immunosuppression and therefore proliferate uncontrollably. Besides leading to the development of tumours, this also creates a microenvironment to cause immune suppression, angiogenesis and metastasis.

1.2.4 Monoclonal antibodies as anti-cancer therapies

Monoclonal antibodies (mAbs) are a transformative class of cancer therapies with specific and targeted action against tumour cells. Derived from a single clone of B cells, mAbs are engineered to bind to a specific epitope on antigens and are therefore highly effective in selective cancer cell targeting without harming healthy tissue. They are used in a broad range of cancers, forming a cornerstone in the treatment of hematologic malignancies and solid tumours.

1.2.4.1 B-cell receptors and antibody structure

B cells have specific receptors on their surface that are embedded into cell membrane through a hydrophobic membrane-anchoring sequence at the C-terminus[26]. These receptors are characterised by their particular structure consisting two identical heavy chain and two identical light-chain immunoglobulin (Ig) polypeptides which are connected through four disulphide bridges[27]. Antibodies have the same structure as B-cell receptors, but with a hydrophilic sequence at the C-terminus instead of a hydrophobic one[26]. A schematic representation of the general Y-shaped structure is shown in **Figure 2** where a constant as well as a variable region can be defined. The variable region, approximately 110 amino acids long in each chain, is responsible for antigen recognition and binding with high specificity. The antigen-binding fragment (Fab) region contains the complementarity-determining regions (CDRs) that allows precise targeting of diverse pathogens such as bacteria, viruses and toxins. Upon binding to an antigen, the Fab region initiates immune responses by marking pathogens for destruction through mechanisms such as opsonisation and antibody-dependent cellular cytotoxicity (ADCC) further elucidated in section 1.2.4.3. The fragment crystallisable (Fc) region of an antibody, located at the base of the Y-shaped structure, interacts with several components of the immune system. Within the Fc region, the Fc gamma (Fcγ) portion specifically binds to Fcγ receptors expressed on immune cells such as macrophages, dendritic cells and NK cells. This interaction plays a significant role in initiating effector functions like phagocytosis, cytokine release and activation of the complement cascade. In addition, antigen recognition triggers the activation of the adaptive immune response, leading to the development of memory cells that provide long-term immunity against previously encountered pathogens.

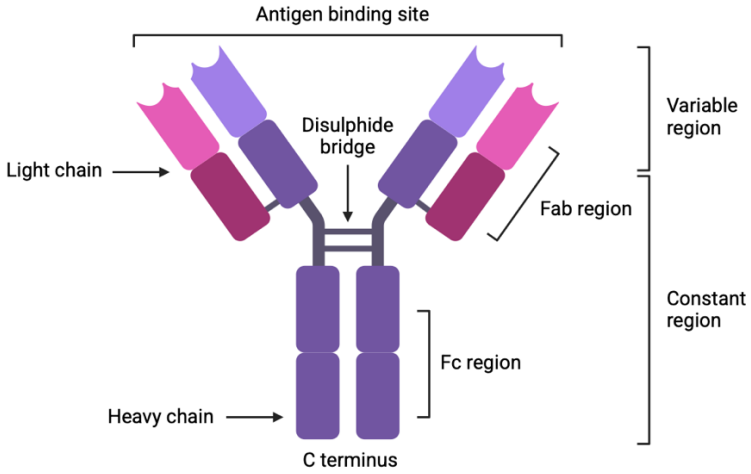

Figure 2 Schematic representation of the antibody's general structure. The figure illustrates the antibody's variable and constant regions, disulphide bridges and the heavy and light chains. The antigen-binding site is located at the variable regions, enabling specific binding with target antigens. Created in Biorender.com

In addition to their role in immunity, antibodies have demonstrated significant therapeutic potential beyond oncology. They are increasingly being used in the treatment of viral infections such as SARS-CoV-2[28], influenza[29] and HIV[30] where they help neutralise viral particles and prevent the spread of the infection. Antibodies are also employed in autoimmune diseases to modulate overactive immune responses and in bacterial infections where they neutralise toxins, such as those produced in diphtheria[31] and tetanus[32].

1.2.4.2 The development of monoclonal antibodies

In 1975, *Milstein* and *Köhler* were the first to describe the secretion of antibodies with predefined specificity[33] leading to the development of mAbs. Several years later, *Levy's* group at Stanford University produced anti-idiotypic patient-specific mAbs for the treatment of lymphoma, demonstrating the antitumour activity of these agents[34]. Anti-idiotypic antibodies are a type of mAbs that specifically recognise and bind to the unique immunoglobuline

variable region (idiotope). These observations at this time were revolutionary, but yet very limited due to the patient specificity.

mAbs are produced using hybridoma technology, which involves the fusion of antibody-producing B cells with myeloma cell lines to create hybridomas capable of both indefinite growth and the secretion of specific antibodies[35]. First to generate specific B cells directed against a desired antigen; this antigen is introduced into a mammal (e.g. mouse) provoking the activation of the immune cascade. Activated B cells from the spleen, which produce antibodies specific to the antigen, are fused with myeloma cells, forming hybridomas. This technology remains fundamental in antibody production, though newer methods have expanded on its principles such as phage display and transgenic animal models. Phage display involves the use of bacteriophages that are viruses that infect bacteria, to present antibody fragments on their surface. This has allowed researchers to screen large libraries of antibodies and select those with the highest binding affinity for a target antigen of interest. Transgenic animal models like genetically modified mice carrying human immunoglobulin genes, produce fully human antibodies when exposed to an antigen. This approach helps to overcome issues of immunogenicity that can arise with non-human antibodies used in therapeutic applications.

mAbs are differentiated according to their species of origin as illustrated in **Figure 3**. Murine antibodies are derived entirely from mouse proteins, making them 100% murine in origin. Chimeric antibodies, however, carry human constant regions fused with murine variable regions responsible for antigen recognition to improve compatibility with the human immune system. Humanised antibodies are predominantly human but with only the complementarity-determining regions originating from mice, which are essential for antigen binding. Fully human antibodies, produced in transgenic mice containing human immunoglobulin genes or

by display technologies like phage or yeast display, have no murine components, reducing the risk of immunogenicity and enhancing therapeutic efficacy in human patients.

Figure 3 Overview of monoclonal antibody variants, ranging from murine (entirely derived from mice), chimeric (mouse variable regions fused to human constant regions), humanised (mouse components reduced to antigen-binding regions, with the remainder human-derived), fully human (entirely human-origin antibodies) and hybridoma-derived antibodies (generated through fusion of B cells with myeloma cells for monoclonal antibody production). Created in Biorender.com.

1.2.4.3 Mechanism of action

mAbs act via several direct and immune-mediated mechanisms to target and kill cancer cells. The most widely explored mechanisms include:

- **ADCC:** mAbs bind through their Fc region to Fcγ receptors on immune effector cells, triggering the release of cytotoxic components such as perforin, which forms pores in the target cell membrane and granzyme, which enters through these pores to initiate cell death, ultimately leading to cell depletion[36, 37].
- **Complement-dependent cytotoxicity (CDC)**: upon binding to tumour cell surface antigens, mAbs initiate the complement cascade, leading to cancer cell lysis through the formation of the membrane attack complex (MAC), which punctures the tumour cell membrane[36, 38].
- **Immune checkpoint inhibition:** as mentioned in section 1.1.1, some tumour cells are able to evade the immune system by exploiting immune checkpoints (e.g. regulatory

proteins such as PD-1 and CTLA-4) that suppress the activity of immune cells like T cells. Immune checkpoint inhibitors block these inhibitory pathways and reactivate immune cells effectively which enables T cells to recognise and eliminate cancer cells, thus restoring the body's ability to initiate an antitumour response[36, 39].

- **Receptor signalling blocking:** by selectively targeting and binding to overexpressed tumour-specific receptors present on the surface of cancer cells, mAbs can effectively block critical signalling pathways that drive tumour growth and proliferation. Through this blockage essential processes like cell division and survival are inhibited, ultimately impeding cancer progression[40, 41].

1.2.4.4 CD20 Receptor and rituximab

CD20 is a non-glycosylated transmembrane phosphoprotein expressed exclusively on B cells from the pre-B cell stage to mature B cells, but it is absent on stem cells and plasma cells[42]. Its function has not yet been fully explored, but it is thought to play a role in B-cell development and calcium signalling[43]. Importantly, CD20 is not internalised upon antibody binding and has no known natural ligand, making it an attractive target for immunotherapy due to its high expression on B cells. Approved in 1997, rtx was the first anti-CD20 mAb and as of today is one of the standard therapy options for the treatment of NHL due to its specific affinity to CD20[44-46]. While there are few successes for the treatment of NHL with rituximab as monotherapy, patients are mainly treated in combination with chemo- or radiotherapy with accompanying adverse effects. Over the past 25 years, since its approval, many studies have demonstrated the efficacy of the drug as well as elucidated its tolerability[45]. Although monoclonal antibodies have revolutionised cancer treatment, they are faced with several challenges: resistance to treatment can develop through mutation and loss of the target

antigen and their limited efficacy as a monotherapy. New technologies, such as bispecific antibodies (bsAbs) and antibody-drug conjugates (ADCs), are expanding the scope of mAb therapies, offering greater specificity and potency. bsAbs are engineered hybrid molecules with two unique binding domains, each of which recognises a distinct target or enables high-affinity attachment of cargos. This dual targeting capability offers novel therapeutic strategies such as simultaneously engaging tumour cells and immune effector cells to enhance immune-mediated killing. A well-established example is blinatumomab[47, 48], which binds to CD19 on B cells and CD3 on T cells and induces targeted immune activation. Further details on antibody-drug conjugates (ADCs), including their mechanisms of action and therapeutic applications, are provided in section 1.4. mAbs have transformed cancer treatment by enabling the precise targeting of cancer cells, a breakthrough made possible by a deeper understanding of the molecular biology of cancer.

1.3 The central dogma of biology

The central dogma of biology describing the process by which DNA is transcribed into RNA and further translated into proteins[49], is fundamental to understanding how genetic mutations and epigenetic changes can contribute to cancer development and how targeted therapies can intervene at different stages. DNA replication allows genetic information to be faithfully passed to new cells during cell division, ensuring continuity of genetic material across generations. Transcription is the procedure in which a segment of DNA is transcribed into precursor messenger RNA (pre-mRNA) as a primary transcript by the enzyme RNA polymerase II. During RNA editing, the transcript is processed into mature messenger RNA (mRNA) by removing introns, the non-coding regions and leaving the coding regions, called exons, of the mRNA. This mRNA then exits the nucleus to be converted by ribosomes during

translation into the final protein, following the genetic code that relates the mRNA sequence to the specific amino acids[50].

Genetic mutations at any level of this pathway can lead to "faulty" cellular function that contributes to tumorgenesis by either the activation of oncogenes or the inactivation of tumor suppressor genes. For example, mutations in tumor suppressor genes such as *TP53* hinder the responsiveness of the cell to DNA damage, whereas overexpression of oncogenes like *MYC* directs uncontrolled cell division. These molecular alterations disrupt normal regulatory mechanisms and contribute to tumor progression by promoting proliferation, evasion of apoptosis and metastasis.

Targeting these mutations requires precise therapeutic strategies. For example, antisense oligonucleotides (ASOs) are able to bind to specific mRNA transcripts where they would exert different functions more specifically described in section 1.3.2.1, thereby preventing their translation into proteins. With these mechanism of action, ASOs offer a promising approach to cancer therapy by silencing oncogene expression. Similarly, gene-editing technologies such as CRISPR-Cas9 can correct these mutations directly at the DNA level and provide potential long-term solutions by modifying the genetic code itself.

As schematised in **Figure 4**, this fundamental pathway is the foundation for normal cellular function and further provides an insight into how genetic mutations can lead to cancer. By targeting these mutations, therapies can be designed to interfere at different levels of the central dogma, either by inhibiting aberrant RNA transcripts or correcting genetic alterations at the DNA level.

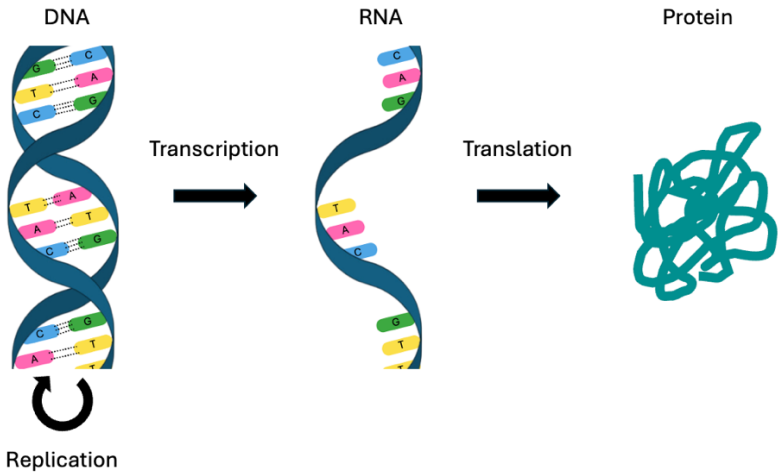

Figure 4 The central dogma of biology: DNA undergoes replication to maintain genetic integrity, transcription to produce RNA and translation to synthesise functional proteins.

1.3.1 Structure of nucleic acids

The Swiss chemist *Friedrich Miescher* was the first to precipitate and identify DNA out of leucocytes, which he first named "nuclein"[51]. Shortly after this discovery, *Albert Kossel* was able to isolate and determine the presence of four different heterocyclic bases which structurally can be divided into two classes, purines and pyrimidine nucleobases: adenine (A), guanine (G), cytosine (C) and thymine (T) as shown in **Figure 5**[52]. The nucleosides instead, bearing a ribose molecule, are named adenosine, guanosine, cytidine and thymidine respectively.

Nucleic acids can be classified into two types: 2'-deoxyribose nucleic acid (DNA) and ribonucleic acid (RNA). Both are composed of monomers, known as nucleotides, forming large polymeric molecules. Each nucleotide comprises a heterocyclic base, a pentose sugar and a phosphate group. If only the heterocyclic base is linked to the sugar molecule without the phosphate group, the molecule is named nucleoside. Although RNA is structurally similar to

DNA, there are significant differences: the heterocyclic base thymine is replaced by uracil (U) and the pentose sugar has an additional hydroxyl group attached on the 2'-position.

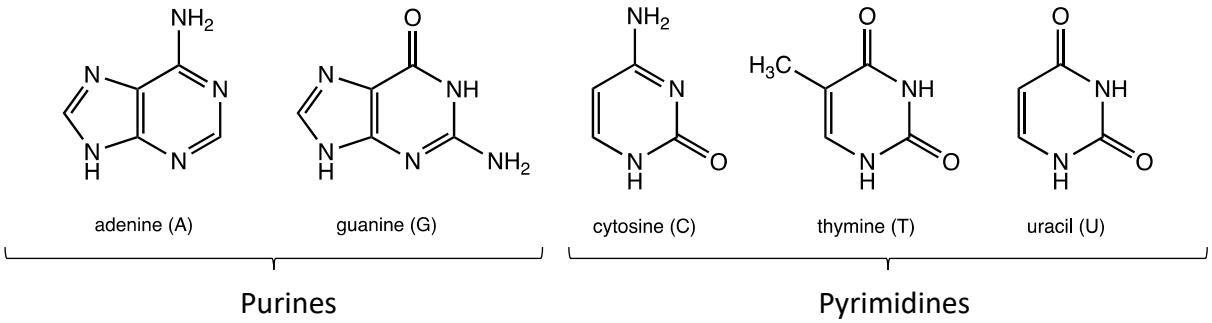

Figure 5 Purine bases: adenine and guanine, pyrimidine bases: cytosine, thymine and uracil

In 1919, Phoebus Levene revealed the sugar-phosphate backbone of the DNA molecule[51] that was followed by other subsequent discoveries in the field of molecular biology. For instance, *Torbjörn Caspersson* and *Jean Brachet* provided critical insights into the role of nucleic acids in cellular function, demonstrating their presence in both the nucleus and cytoplasm. The early work in the 1930s by *Rudolf Signer* also played a significant role, since he was able to isolate highly purified DNA which allowed for more detailed biochemical studies[53]. The groundbreaking discovery of the three-dimensional double helix structure of DNA was introduced by *Watson* and *Crick*[54] along with *Wilkins*[55] in 1953, based on crucial X-ray diffraction pictures from the group of *Rosalind Franklin*[56]. They found that only certain pairs of bases could be matched by hydrogen bonds: guanosine with cytidine and adenosine with thymidine, or uridine respectively (**Figure 6**).

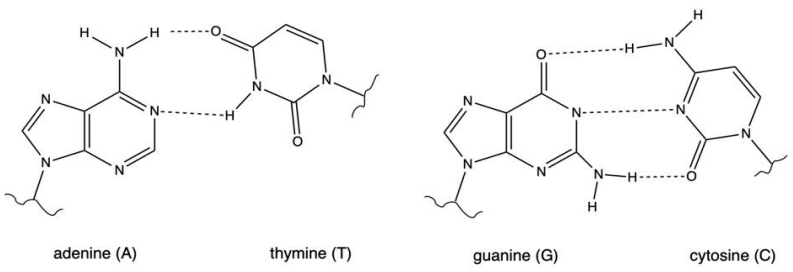

Figure 6 Hydrogen bonding between A-T and G-C base pairs

Most commonly, the B-DNA conformation of DNA is found. It is a structure made of two antiparallel strands forming a right-handed double helix with an outward facing negatively charged phosphate backbone. The strands are linked through the hydrogen bonds between the bases as pictured above[57]. In B-DNA, the distance between the bases was measured 3.4 Å and one helical turn counts about 10.5 base pairs.

Less common are the A-RNA and left-handed Z-DNA conformation that are also double-helical but with different spatial arrangements between the bases (**Figure 7**). Often RNA-RNA duplexes and RNA-DNA hybrids adopt the A-DNA conformation[58], but also DNA-DNA duplexes can transit from B to the A-form under specific conditions i.e. low relative humidity[56] or if the sequence is G/C-rich. In the latter, the sequence is also prone for the Z-DNA conversion.

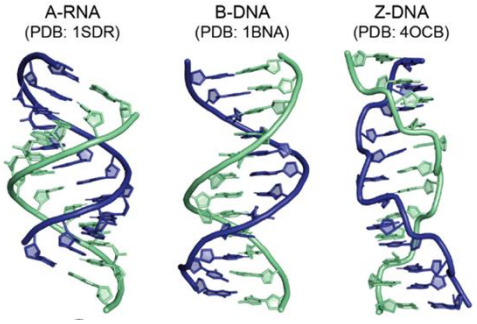

Figure 7 Secondary structure of the different DNA conformations based on single-crystal X-ray diffraction analysis with A-RNA, B-DNA, and Z-DNA representing the three major conformations of nucleic acids. A-RNA is a right-handed helix with a compact structure, B-DNA is the most common right-handed helix under physiological conditions, and Z-DNA adopts a left-handed helix with a zigzag backbone. Reproduced with permission of the rights holder[59].

1.3.2 Nucleic acids in the therapeutic context

Nucleic acids have recently gained significant attention with the emerging of mRNA vaccines during the COVID-19 pandemic. The Pfizer-BioNTech and Moderna vaccines demonstrated the immense potential of nucleic acid technology by delivering mRNA pieces into cells that

will be translated into the virus' spike protein. As outlined in sections 1.2.1 and 1.2.2, the immune system subsequently initiates an immune response to establish immunological memory[60]. Their success not only helped control the pandemic but also opened new avenues for mRNA-based therapies against cancer and other infectious diseases.

The rapid development, scalability and high efficacy of these vaccines highlighted the therapeutic potential of nucleic acids. Beyond vaccines, nucleic acid-based therapies have also expanded into numerous medical fields, offering precise treatments for genetic disorders, cancers, and viral infections. So far in 2024, there have been 20 FDA-approved nucleic acid-based drugs, including ASOs and small interfering RNA (siRNA) treatments[61]. Certain therapies are able to target genetic pathways directly, providing specificity and precision that traditional treatments often lack.

1.3.2.1 Antisense oligonucleotides

ASOs represent another powerful nucleic acid-based therapeutic tool with great promise in targeting and silencing harmful gene expression. Whereas mRNA vaccines mobilise the cellular mechanisms of the body to produce viral proteins and initiate an immune response, ASOs work by hybridising to specific mRNA sequences in order to prevent the synthesis of proteins that drive disease progression. This effect underlies different mechanism of action that are detailed in the following.

1. The most common mechanism involves the recruitment of ribonuclease (RNAse) H, an endonuclease that specifically cleaves the RNA strand of an RNA-DNA duplex. Once the ASO binds to its target mRNA through Watson-Crick base pairing, the enzyme recognises the RNA-DNA hybrid and cleaves the mRNA leading to its degradation and therefore causing a disruption in disease-causing protein synthesis[62, 63].

2. Additionally, ASOs can sterically block the splicing process or prevent ribosomes from binding to the mRNA and perform protein synthesis[64].
3. Translation may also be inhibited while the ASOs block the 5' untranslated region (UTR) or the start codon of a mRNA. This prevents ribosomes from initiating the translation process and therefore the production for the target protein.
4. In some cases, ASOs are designed to alter the splicing of pre-mRNA. Binding to splice sites or splicing enhancers, ASOs can either promote the inclusion or exclusion of specific exons in the final mRNA transcript, thereby restoring the production of a functional protein[65, 66].

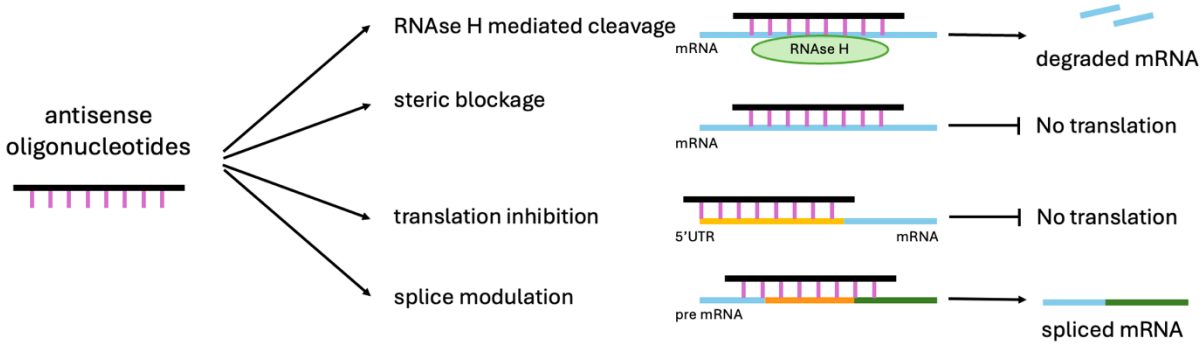

Figure 8 Overview of mechanism of action of ASOs. ASOs modulate gene expression through multiple pathways: RNase H-mediated cleavage leads to degradation of the target mRNA; steric blockage prevents translation; translation inhibition occurs by binding to the 5' UTR; and splice modulation alters pre-mRNA splicing to produce a functional mRNA variant.

With these diverse mechanisms, schematised in **Figure 8**, ASOs have become versatile tools within precision medicine. These allow very specific interventions for genetic disorders and cancers. Their ability to target mRNA makes them suitable for the treatment of diseases where faulty proteins are the root cause of the pathology, for example conditions like spinal muscular atrophy and cancers. As the field of nucleic acid-based therapies advances, several

new structures have been investigated and developed that extend DNA and RNA beyond the application as ASOs.

1.3.2.2 DNA origami as foundation for self-assembling DNA structures

It was not until the 1980s, that DNA was recognised to be manipulated in order to form any desired nanostructures through computer-assisted molecular designs based on the high affinity of Watson-Crick base pairing. *Nadrian Seeman*[67] laid the foundation for DNA nanotechnology and proposed a high variety of immobile nucleic acid junctions in which small DNA complexes hybridised through single stranded overhangs in order to form large crystalline structures with the first reported DNA nanostructure in 1991[68]. In 2006, *Rothemund* introduced the principle of „scaffolded DNA origami", where he exploited the high specificity of Watson-Crick base pairing to fold a long scaffold DNA strand using a high number of short staple strands allowing to create a big diversity of shapes and size[69]. To test his proposal, he used circular genomic DNA derived from the bacteriophage M13 (M13mp18) as the scaffold, which can be converted into linear DNA through the enzymatic digestion with BsrBI[69]. In fact, he first selected a desired shape and filled it with an even number of parallel double helices which are linked through crossovers indicating the position where a strand will switch the pairing to an adjacent helix. The scaffold strand is placed in such a way to include every double helix, then staple strands are positioned at the previously designated crossovers. His method could afford a high variety of shapes, shown in **Figure 9**, but also indicates an important factor that needs to be considered when creating shapes using DNA origami or also self-assembling DNA structures. As explained in the above section, each helical turn of the double helix in B-DNA conformation counts 10.5 base pairs, which must be considered when placing scaffold crossovers in order to fold the DNA sequence and therefore

when designing two or three-dimensional structures. Today, using computer software such as caDNAno, the manipulation and design of nanostructures has become much easier and symmetry matters could be taken into account[70]. With the introduction of DNA origami, new opportunities in different areas have emerged, for example structures for biomedical applications such as biosensing, genetics, drug delivery[71] or also in cancer therapy[72].

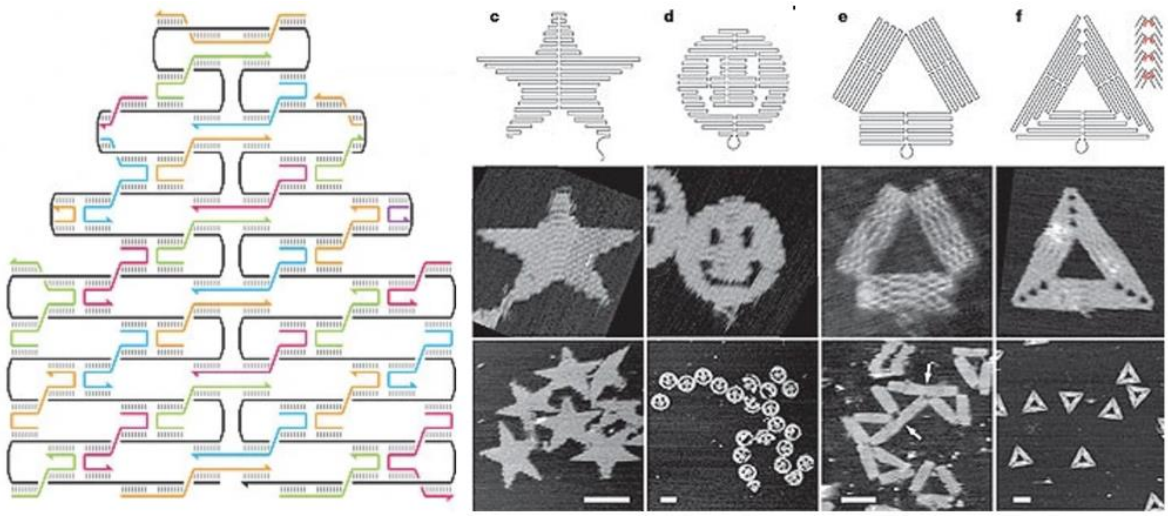

Figure 9 Left: simplified example of the DNA origami principle with a scaffold strand (black) folded through several short staple strands (coloured).
Right: *Rothemund*'s DNA origami shapes with AFM images.
Reproduced with permission of the rights holder[69].

1.3.2.3 DNA nanopores

Biological pores selectively allow ions, nutrients and genetic material to be transported across cell membranes to maintain cellular function. Membrane-spanning DNA nanopores (NPs) represent an innovative approach to create synthetic channels that mimic biological transmembrane pores. These structures are designed based on simple DNA self-assembly functionalised with hydrophobic modifications that allow them to integrate into lipid bilayers to form channels through which molecules can pass. It is based on the principle of DNA origami as previously described; however, these constructs are composed of only shorter DNA

strands of varied lengths which facilitates the design and enables more opportunities for customization e.g. the attachment of fluorophores or hydrophobic units (HU).

1.3.2.4 Membrane spanning DNA Nanopores

In 2012, *Langecker et al.* introduced self-assembled DNA-based nanostructures functionalised with hydrophobic modifications, designed to insert into lipid bilayers[73]. His system comprised 54 double-helical DNA domains with a transmembrane stem and 26 cholesterol units placed around it in order to anchor the structure in the membrane (**Figure 10**).

Figure 10 Schematic representation of a self-assembled DNA-based transmembrane channel structure proposed by *Langecker*. Double-helical DNA domains are depicted in white, cholesterol units in orange and the transmembrane stem are illustrated in red. Reproduced with permission of the rights holder[73].

Shortly after, *Burns et al.* reported a simpler and smaller system with six double-helical DNA domains interconnected by fourteen oligonucleotide strands. The nanostructures included a hydrophobic belt formed by ethyl-modified phosphorothioates that neutralised the negative charge of the phosphates and allowed for membrane embedding as shown in **Figure 11**[74]. They observed significant cytotoxicity in HeLa cells after co-culture, attributing this effect to the NP's disruption of membrane integrity, which compromised cell viability. Additionally, *Burns et al.* further demonstrated that through the alteration of the concentration of EP-modified NP, they could modulate cell death rates, thus showing a dose-dependent

cytotoxicity due to direct membrane interaction and cellular uptake. Later studies showed that similar NPs could be stabilised by substituting the ethyl modifications with other HUs, such as porphyrin[75] or cholesterol[73].

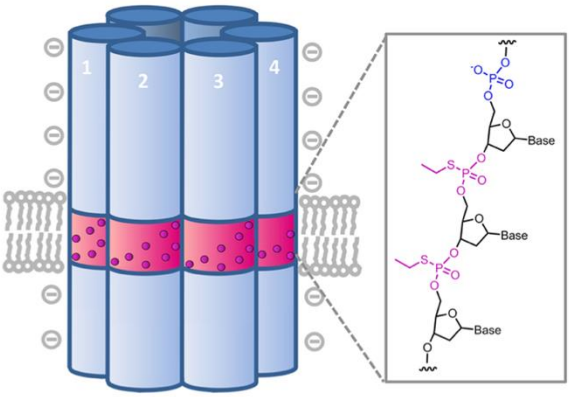

Figure 11 Schematic representation of the NP proposed by *Burns et al*. consisting of six duplexes which are interconnected. The pink area marks the ethyl-modified-phosphorothioates forming the hydrophobic belt. Reproduced with permission of the rights holder[74].

The promising cytotoxicity observed[76, 77] led our group to investigate the effect of two different sized NP constructs using various hydrophobic compounds such as cholesterol and palmitate looked into HEK293, B16-F10 and FM55-P cell lines[78]. The findings from *Lauren Entwistle* were very different depending on both the NP construct used but also on the cell lines treated. However, some findings aligned with the results found in the literature on HeLa cells when working with HEK293 cells. Several experiments were conducted to identify a suitable seeding concentration and treatment concentration. At low seeding density of 2000 cells per well, cell proliferation was affected negatively by the treatment with cholesterol-modified four-helix bundle DNA NPs (4HB-NPc) at a treatment concentration of 0.5 μM. Decreasing the concentration to 0.25 μM and/or increasing cell density to 5000 cells per well affected the outcome significantly, since no effect of the 4HB-NPc could be observed. Interestingly, the experiments performed with the six-helix bundle DNA NPs (6HB-NPc)

presented different findings. In this case, the treatment concentration of 6HB-NPc had to be increased to 1 μM to observe reduced cell viability, which unfortunately was statistically not significant. *Burns et al.* studied the effect of their proposed NP in HeLa cells at a concentration of 60 μg/ml which equals about 0.37 μM. They observed a decrease of cell viability already after 1 hour of incubation with their NP, lasting up to 72h[76]. *Li et al.* developed ethyl-phosphorothioate-modified NPs to improve membrane retention and enable precise transmembrane delivery of therapeutic molecules, such as doxorubicin achieving controlled, efficient release and cellular uptake, as demonstrated in fluorescence-based assays. This efficient delivery system underlines the therapeutic potential of NPs, which may be further elaborated for the transport of a broad range of drugs towards target cells with higher specificity and minimal off-target effects[79].

Expanding on these foundational studies, recent work has explored membrane-interacting DNA nanotubes for targeted cancer therapies[77]. *Kocabey et al.* investigated cholesterol-modified DNA nanotubes for their cytotoxic effects in cancer cells. These DNA nanotubes incorporated three cholesterol units to increase the hydrophobicity that allowed them to interact with cancer cell membranes as shown in **Figure 12**. When conjugated with cytochrome c, these nanotubes induced caspase-dependent apoptosis through the activation of intrinsic pathways, leading to programmed cell death without significant off-target effects.

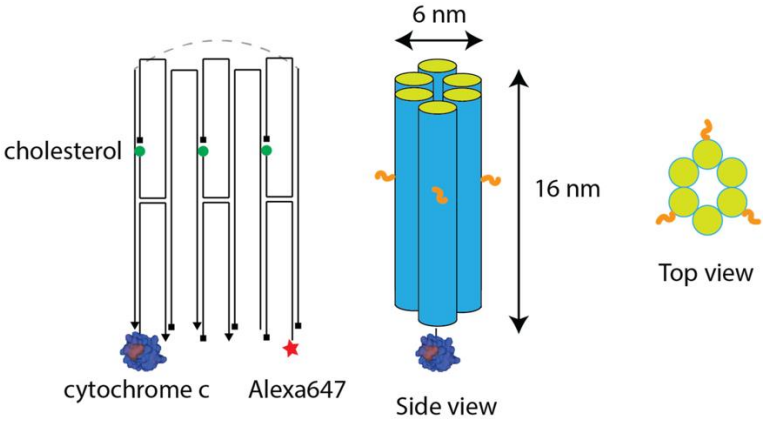

Figure 12 Schematic representation of the amphiphilic 6-helix DNA nanotubes in both 2D and 3D views. The nanotube structure consists of DNA strands, with 3' and 5' ends indicated by arrows and squares, respectively. Cholesterol moieties (green circles) are incorporated to allow membrane integration. The nanotube has a diameter of 6 nm and a length of 16 nm. Cytochrome c and Alexa Fluor 647 are conjugated to specific DNA strands at the 5' and 3' ends, respectively, to enable functional studies and visualisation. Reproduced with permission of the rights holder[77].

Using confocal microscopy, *Kocabey et al.* followed fluorescently labelled nanotubes confirming membrane interaction. Flow cytometry analyses validated these findings, showing consistent cellular uptake of nanotubes with significantly reduced cancer cell viability. These published findings demonstrate that the combination of structural stability, targeting specificity and cytotoxic effect of DNA nanostructures including NPs and nanotubes hold therapeutic potential by promoting controlled cell death in cancer cells while minimizing undesired off-target toxicity. By coupling NPs with specific targeting agents, such as antibodies or cell-specific peptides, researchers are exploring highly specific treatments for cancer with reduced side effects.

1.3.2.5 Specific cell recognition through conjugation with targeting moieties

Building on the innovative use of membrane-spanning NPs in cell targeting and cancer therapy, methods to enhance NP specificity by their conjugation with targeting moieties have recently been explored. These functional modifications allow NPs to bind selectively to unique cellular markers, increasing precision in drug delivery. For instance, *Guo et al.* successfully conjugated a Ramos cell aptamer and a cell-penetrating peptide (CPP) to a six-helix bundle NP, ensuring targeted binding to malignant B cells (Ramos), while the CPP facilitated cellular entry[80]. Other studies conducted in the *Stulz* group were focusing on the conjugation of the rtx to a small NP construct with four helix bundles, whereas the constructs could hardly be characterised and cell-binding assays could afford little information on relative binding affinities[81]. Bioconjugation to rtx was performed through strain promoted azide alkyne cycloaddition (SPAAC) targeting the N-terminus of lysine residues. The lysine residues were modified in an addition-elimination reaction with azido-pegylated-NHS ester to present azide groups. Through SPAAC, dibenzocyclooctyne (DBCO) modified oligonucleotides are reacted with the azide groups and therefore conjugated to the antibody. The disadvantage of this method includes the lack of control of the number of binding sites. It was unclear how many NPs were conjugated to rtx and to what extent the NPs influenced the binding of rtx to the CD20 receptor. These findings highlight the need for precise and controlled conjugation strategies which would provide a superior approach to afford a homogeneous construct with optimised therapeutic efficacy.

1.3.3 Solid phase oligonucleotide synthesis

The phosphoramidite method, today the established standard technique to synthesise oligonucleotides, was developed by *Marvin Caruthers* in the early 1980s[82, 83]. The synthesis

proceeds from the 3’-end to 5’-end and can be assigned to solid-phase synthesis. A full synthesis cycle shown in **Figure 13** must be completed in order to add a nucleoside to form a sequence. All the steps of the synthesis are described in detail hereinafter.

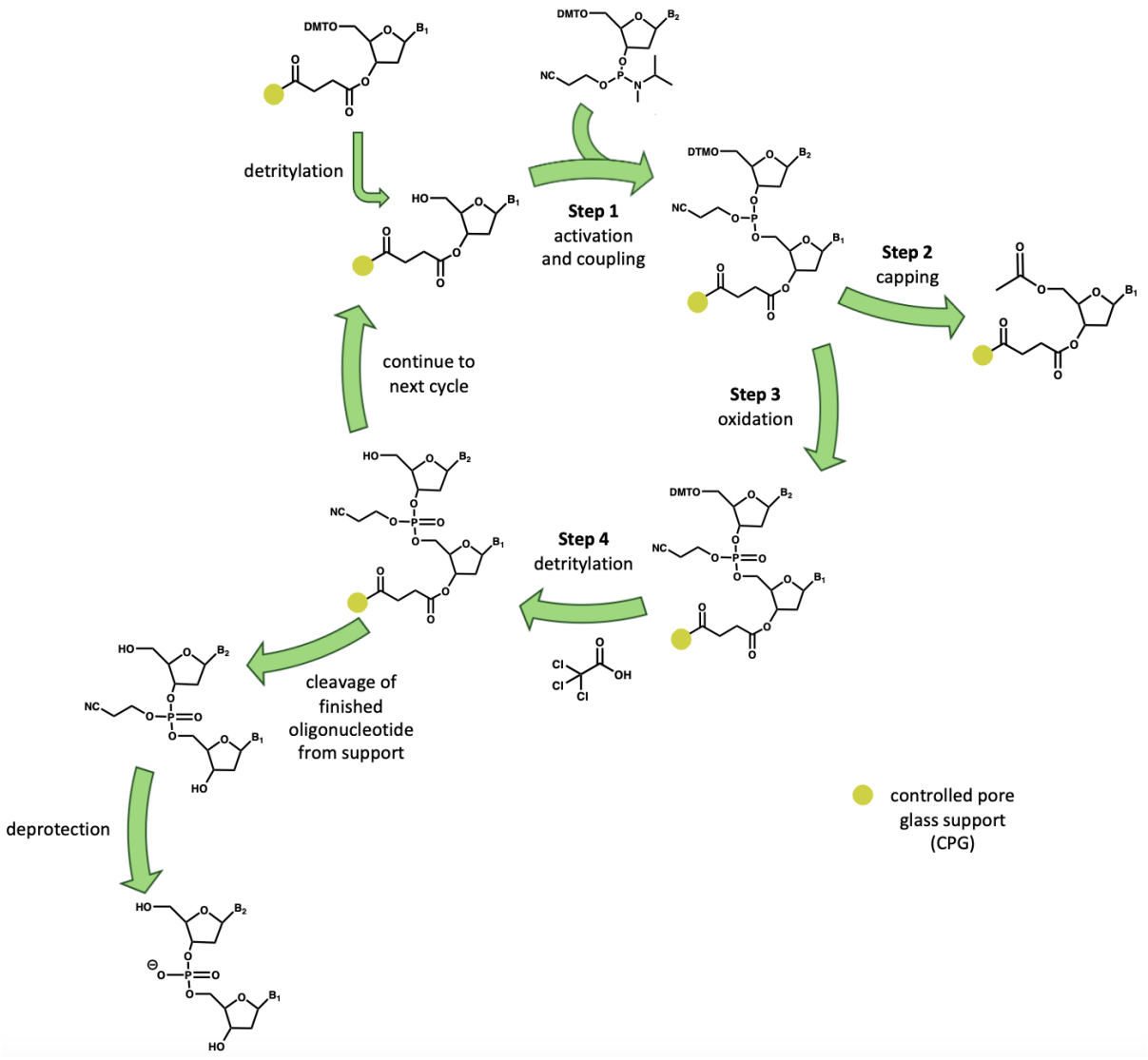

Figure 13 Generalised phosphoramidite oligonucleotide synthesis cycle. The stepwise cycle includes (1) activation and coupling of the phosphoramidite to the growing oligonucleotide chain, (2) capping to block unreacted hydroxyl groups, (3) oxidation to convert the unstable phosphite triester linkage to a stable phosphate linkage and (4) detritylation to remove the protecting group and expose a new hydroxyl group for the next cycle. After synthesis, the oligonucleotide is cleaved from the solid support and deprotected to yield the final product.

1.3.3.1 Detritylation

Before starting the synthesis, the 5'-Dimethoxytrityl (DMT) protecting group of the first nucleoside, which is bound to the solid support (CPG resin), must be removed in a step called detritylation. By protonating the 5' oxygen with trichloroacetic acid (3%) in DCM, the alcohol becomes a good leaving group and DMT cleaves from the sugar, shown in **Figure 14**. The resonance forms of the DMT cation provide a bright orange colour, which serves as a good estimation for the efficiency of the detritylation. Commonly, oligonucleotide synthesisers are equipped with a trityl monitor, which detects the absorption at 498 nm after each detritylation to track the efficiency of the previous coupling.

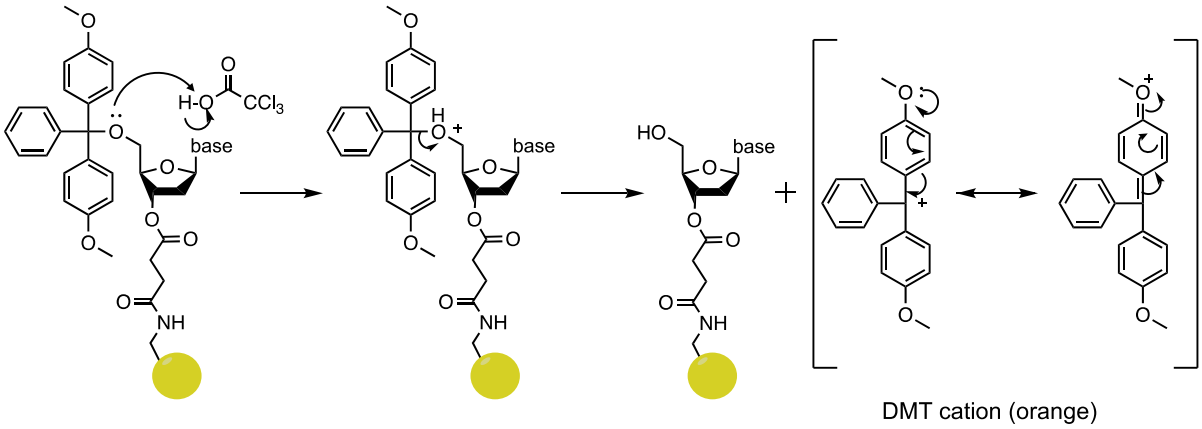

Figure 14 Mechanism of detritylation of an DMT-protected nucleoside through trichloroacetic acid (3%)

1.3.3.2 Activation and coupling

The free hydroxyl group of the ribose sugar situated at the 5' position is now available for the coupling. In an activation step, the next nucleoside phosphoramidite is mixed with an acidic activator, a tetrazole catalyst, in MeCN in order to protonate the diisopropylamino group to become a good leaving group. It is further replaced by the activator, which is then displaced

through nucleophilic substitution by the 5'-hydroxyl group of the support-bound nucleoside (**Figure 15**).

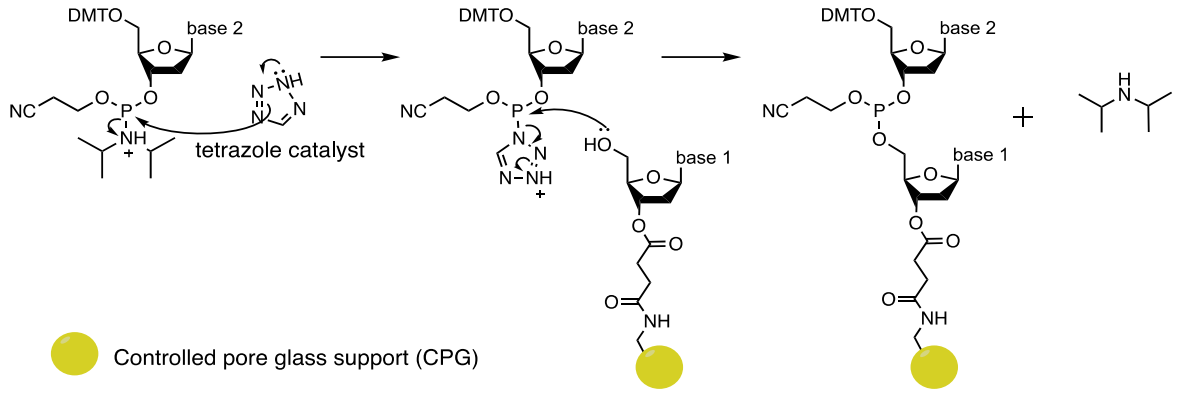

Figure 15 Activation and coupling mechanism

1.3.3.3 Capping

The next step, named capping, blocks 5'-hydroxyl groups of unreacted monomers through acetylation to prevent them from reacting in the next coupling step (**Figure 16**).

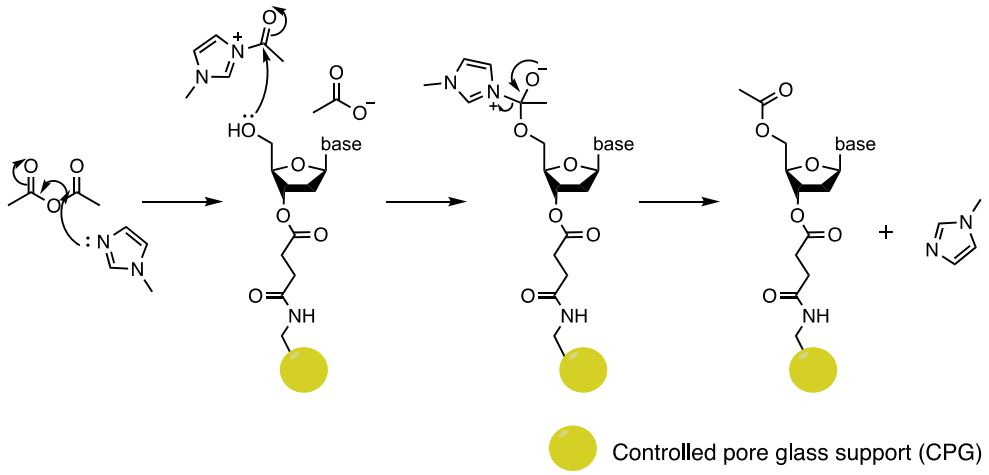

Figure 16 Capping mechanism for blocking unreacted monomers through acetylation

1.3.3.4 Oxidation

By treating the column with iodine in a THF and water mixture in the presence of a weak base (e.g. pyridine), the unstable phosphite-triesters (P(III)) are transformed into more stable phosphate triesters (P(V)) in an oxidation step, see **Figure 17**.

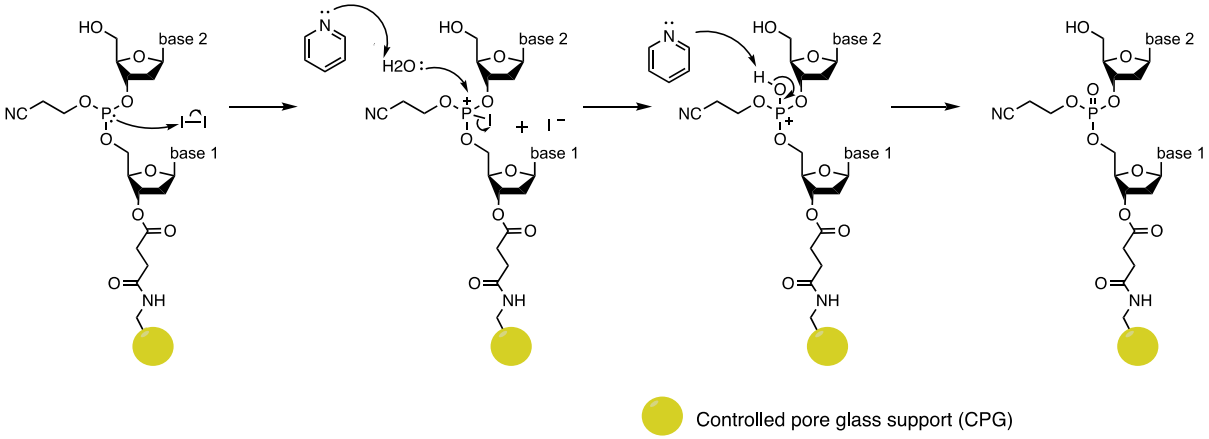

Figure 17 Iodine oxidation to convert unstable phosphite-triester into stable phosphate-triester

Finally, to continue the synthesis and to prepare the oligonucleotide for the addition of a next base, a detritylation step removes the DMT protecting group at the 5'-end of the chain to allow the hydroxyl group from the next nucleotide phosphoramidite to react.

1.3.3.5 Deprotection and cleavage

To finish the synthesis, the oligonucleotides must be removed from the solid support, since the first nucleoside at the 3'-end was pre-bound in most cases through a succinyl linker. The

cleavage is performed using concentrated ammonium hydroxide, which induces ester hydrolysis, as shown in **Figure 18**.

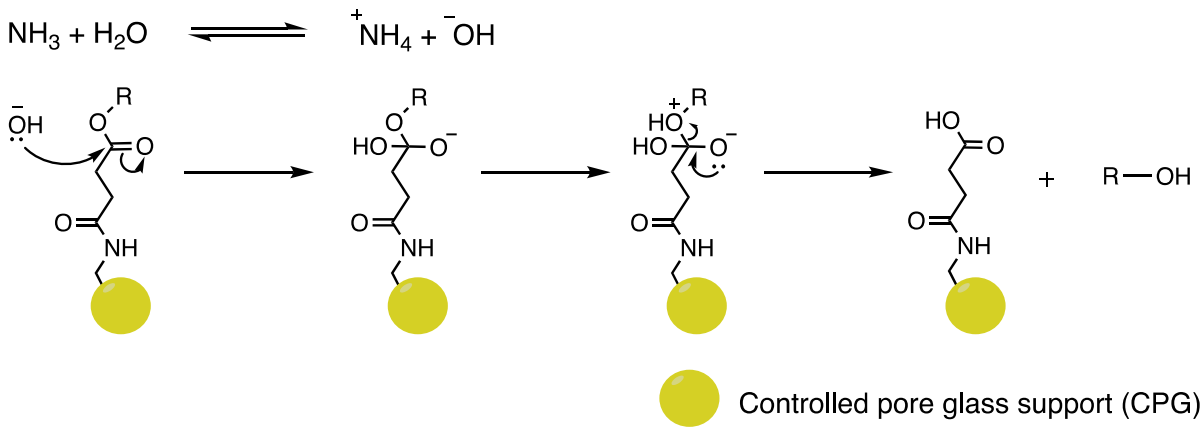

Figure 18 Cleavage from the solid support using concentrated ammonium hydroxide. R = DNA

Finally, before purifying the oligonucleotide, an additional deprotection step is introduced to remove the protecting groups from the heterocyclic bases and phosphodiester backbone. The deprotection is performed by heating the dissolved oligonucleotides in the concentrated aqueous ammonia solution from the cleavage step at around 55°C (**Figure 19**).

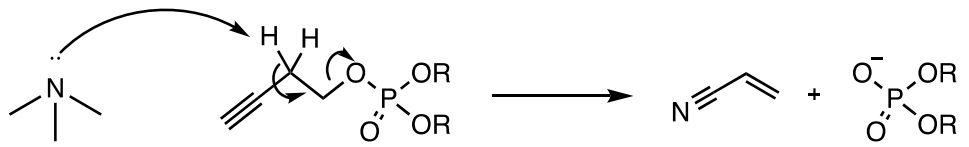

Figure 19 β-elimination mechanism for the deprotection of 2-cyanoethyl phosphotriester, resulting in the acrylonitrile by-product

In the deprotection step of the phosphate group, acrylonitrile results as a by-product, which serves as a Michael acceptor and possibly reacts with Michael donors (e.g. Thymine) under the strong basic conditions to form 2-cyanoethyl adducts, see **Figure 20**. To avoid the formation of these adducts, it is advised to perform the deprotection step before the cleavage from the solid support using a solution of a weak base e.g. 20% diethylamine in MeCN. In this case, the protecting groups are removed, and the acrylonitrile is deactivated in a process of

cyanoethylation of diethylamine and can subsequently be washed leaving the deprotected oligonucleotide on the solid support. The cleavage with concentrated aqueous ammonia solution can now be performed without the formation of 2-cyanoethyl adducts.

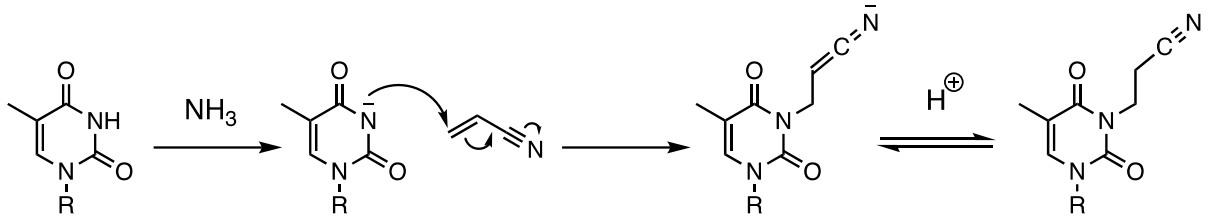

Figure 20 Formation of cyanoethyl adducts in the presence of acrylonitrile

Purification is performed through standard desalting method but may require further purification through gel electrophoresis or HPLC.

1.4 Antibody-drug conjugates

The field of antibody-drug conjugates (ADCs) has transformed the aspect of cancer treatment by offering highly specific targeting of cancer cell while sparing healthy tissue. Currently, there are 14 FDA-approved ADCs such as trastuzumab emtansine and brentuximab vedotin (**Figure 21**) which validate the clinical potential and evolving design strategies that make ADCs a promising innovation in modern oncology. By combining the tumour-targeting precision of monoclonal antibodies with potent cytotoxic payloads, ADCs deliver chemotherapeutic agents directly to cancer cells, thereby minimising systemic toxicity and enhancing therapeutic efficacy[36, 84-87].

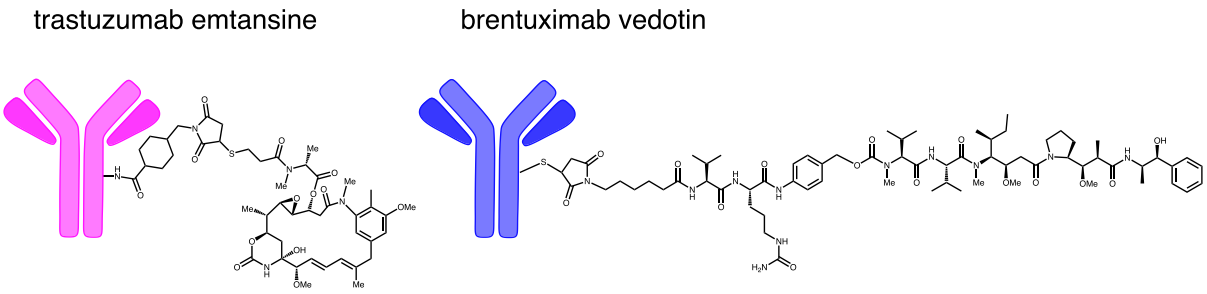

Figure 21 Chemical structure of trastuzumab emtansine (left) and brentuximab vedotin (right)

1.4.1 The concept of antibody-drug-conjugates

ADC technology has grown tremendously over the last years, with multiple generations of ADCs advancing beyond traditional chemotherapies. Each ADC typically includes three components: a monoclonal antibody targeting a specific tumour-associated antigen, a cytotoxic drug and a linker that controls drug release within the target cells (**Figure 22**). Continuous innovation in linker technologies and payload design have improved ADCs specificity, stability and potency of ADCs for treating cancers resistant to traditional therapies. The rapid development and clinical success of ADCs show their significant potential to reshape targeted therapy, not only expanding into various solid tumour types, but also pushing therapeutic boundaries in hematologic malignancies and beyond.

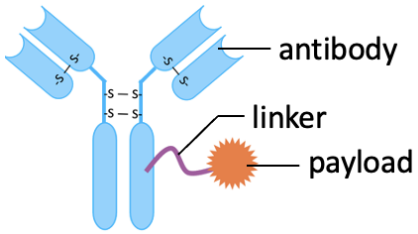

Figure 22 Schematic representation of the concept of antibody-drug conjugates (ADCs), illustrating the antibody for specific cell targeting, a linker that connects the payload to the antibody, and the cytotoxic payload responsible for exerting the therapeutic effect upon internalisation into the target cell.

1.4.2 Expanding the field with antibody-oligonucleotide conjugates

One promising addition to ADCs comes with antibody-oligonucleotide conjugates (AOCs) combining the targeting abilities of antibodies with the gene-silencing functions of oligonucleotides. Unlike ADCs, which rely on cytotoxic drugs in order to kill cancer cells, AOCs focus on modulating key biological pathways through the regulation of gene expression. This is fundamentally a different therapeutic approach that targets disease pathways at the genetic level. The potential for AOCs extends across oncology, rare genetic disorders, and inflammatory diseases, where gene modulation holds therapeutic promise. With the mechanism of action of ASOs elucidated in 1.3.2.1, AOCs are being explored for their efficacy in the treatment of genetic disorders either by correcting splicing errors or degrading harmful transcripts directly within target cells. In oncology, AOCs can silence oncogenic drivers like MYC or BCL-2, which play essential roles in tumor growth and survival. Moreover, they may interfere with inflammatory pathways by downregulating cytokine production or inhibiting immune checkpoints, making them valuable in autoimmune and inflammatory diseases. Despite their therapeutic potential, oligonucleotide therapeutics are inherently challenging to deliver due to their instability in biological environments and their potential to trigger immune responses. However, the antibody in AOCs improves the stability and specificity in the delivery of oligonucleotides directed at cell-specific antigens. *Malecova et al.* demonstrated that the administration of naked siRNA (siMstn) resulted in minimal uptake into skeletal muscle tissue due to rapid systemic clearance (plasma half-life <0.5 hours). In contrast, αTfR1-antibody conjugated siMstn (αTfR1-siMstn) demonstrated a significantly longer plasma half-life of approximately 6 hours, consistent with the pharmacokinetic profile of the antibody and confirming the stability of the antibody–siRNA complex, as evidenced by

comparable plasma exposure of both the antibody and siRNA moieties[88]. Similarly, *Dovgan et al.* reported that conjugation with antibodies significantly improved oligonucleotide stability, with a two-fold increase in the half-life of the antibody-conjugated oligonucleotide ($t_{1/2}$ of 1.1 days) compared to unconjugated oligonucleotides[89]. Furthermore, double-stranded constructs demonstrated even higher stability, with a half-life of up to 5.7 days, which further confirms that antibody shielding effectively protects oligonucleotides from nuclease degradation. In fact, two examples of successful AOCs targeting HER2 and EGFR were reported in the literature[90]. In one study, an AOC targeting HER2+ breast cancer cells with a single-chain variable fragment (scFv) antibody linked to Polo-like kinase 1 siRNA through protamine-based ionic conjugation was developed. This conjugate demonstrated significant tumour size reduction in HER2+ BT474 breast cancer mouse models. Another example is an EGFR-targeting AOC conjugated to KRAS siRNA via ionic interactions, which efficiently inhibited tumour growth in EGFR-positive cancer models through downregulation of KRAS expression, a critical driver of oncogenesis in various cancers.

Ongoing efforts in reserach continue to refine AOC technology with a focus on optimizing conjugation strategies, improving delivery efficiency and expanding their application across a broader range of diseases to fully exploit their therapeutic potential.

1.4.3 Conjugation strategies

A main component in AOC design is the careful selection of the linker strategy that suits both the antibody and the oligonucleotide cargo, ensuring stability, specificity and functionality within the target environment. Recent reviews emphasise that site-specific conjugation methods ensure homogeneity and retain antibody binding affinity which are essential factors

to be considered. For instance, one effective conjugation strategy for AOCs involves covalent linkers that bind specifically to reactive groups on antibodies, such as amines or thiols.

1.4.3.1.1 Maleimide linker chemistry

Maleimide linkers are widely used for thiol-targeted conjugation through a Michael addition with cysteine residues to form stable thioether bonds that are resistant to enzymatic degradation and hydrolysis under physiological conditions as schematized in **Figure 23**.

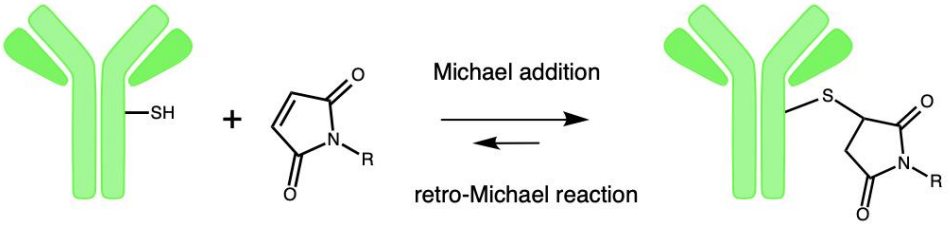

Figure 23 Maleimide linkers specifically react with thiol groups (-SH) present on cysteine residues of antibodies, forming stable thioether bonds, which are prone to retro-Michael reactions.

Since native antibodies generally lack free cysteines, the introduction engineered cysteine residues offers precise conjugation points for maleimide derivatives[91, 92]. Despite their conjugation efficacy, maleimide linkers can sometimes be unstable *in vivo* due to retro-Michael reactions and thiol exchange in glutathione-rich environments, such as the cytosol, which may result in early release of the payload. Strategies to overcome this challenge involved promoting the hydrolysis of the thiosuccinimide ring after conjugation, thereby converting the maleimide-thiol adduct into a more stable form not susceptible for retro-Michael deconjugation (**Figure 24**).

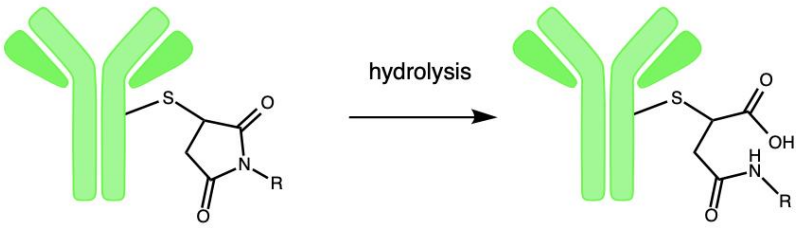

Figure 24 Schematic outline for improved stability of maleimide linkers through thiosuccinimide ring hydrolysis reducing susceptibility to retro-Michael reactions and thiol exchange.

This approach has been shown to improve the *in vivo* stability of maleimide-based conjugates and reduce the risk of early release of the payload. A notable example is AOC 1020 (**Figure 25**) by Avidity Biosciences, an AOC for the treatment of facioscapulohumeral muscular dystrophy. The construct comprises a non-cleavable maleimide linker with an undisclosed structure and a siRNA linked to a transferrin receptor antibody for stable delivery that withstands systemic circulation and achieves effective gene silencing in target muscle tissues[88].

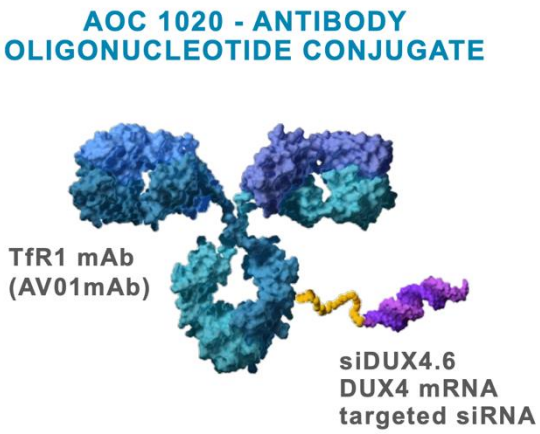

Figure 25 Structure of AOC 1020, an antibody-oligonucleotide conjugate designed for targeted gene silencing in facioscapulohumeral muscular dystrophy. AOC 1020 consists of a transferrin receptor 1 monoclonal antibody (TfR1 mAb, AV01mAb) conjugated to siDUX4.6, an siRNA specifically targeting DUX4 mRNA, which is implicated in FSHD pathology.[93]

1.4.3.1.2 N-hydroxysuccinimide-ester linker chemistry

N-hydroxysuccinimide (NHS) esters are also commonly used in protein conjugation due to their ability to form stable amide bonds with primary amine groups of lysine residues. As a result, this represents another simple strategy for antibody conjugation. The high and fast reactivity of NHS-esters to amine groups enable for strong and covalent linkage between oligonucleotides to antibodies. However, NHS-ester linkers typically result in heterogeneous conjugates as lysine residues are abundant and widely distributed on antibodies as seen on previous antibody-NP studies performed in our group and schematized in **Figure 26**[81].

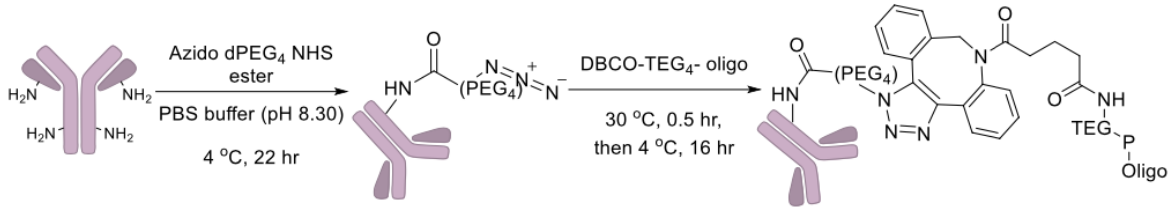

Figure 26 Schematised synthetic route for mAb-oligonucleotide conjugation targeting lysine residue using an azido-dPEG$_4$-NHS ester. The resulting azide-groups are reacted with DBCO-modified oligonucleotides via SPAAC. Reproduced with permission of the rights holder[81].

This variability may additionally result in a lack of site-specificity, which affects the structural integrity and binding properties of the antibody-oligonucleotide conjugate. Despite these challenges, NHS-ester linkers remain popular due to their ease of use and efficiency, especially for applications that can tolerate structural heterogeneity.

1.4.3.1.3 Cleavable linker strategies

Cleavable linkers offer improved the efficacy of AOCs for the controlled release of ASOs, siRNA or other therapeutic molecules at target sites. *Zavoiura et al.* reported that cleavable linkers in nanobody-siRNA conjugates targeting EGFR improved RNA interference effectiveness,

achieving knockdown rates above 60% in EGFR-positive cells, while non-cleavable linkers showed reduced efficacy[94]. Similarly, *Wang et al.* also developed novel photoresponsive and ROS-sensitive linkers (**Figure 27**) that release the attached siRNA upon exposure to specific triggers, such as light or reactive oxygen species, in the tumour microenvironment. This selective release strategy ensures that the therapeutic effects are directed against target cells, thus enhancing both safety and efficacy of the treatment[95].

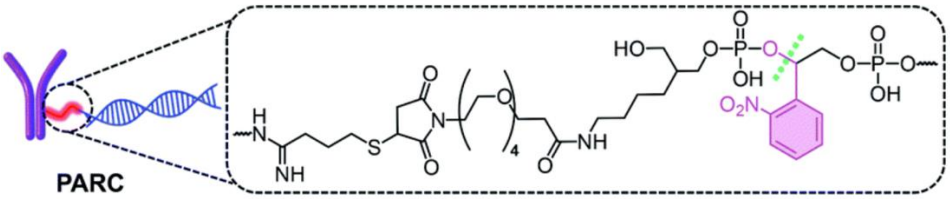

Figure 27 Schematic representation of a photoresponsive and ROS-sensitive linker system developed by *Wang et al*. The construct enables the controlled release of siRNA upon exposure to light or reactive oxygen species (ROS) within the tumour microenvironment. The green dashed lines indicate the ROS-sensitive moiety, which triggers linker cleavage in the presence of ROS, while the pink aromatic group represents the photoresponsive unit, allowing light-induced release of the therapeutic payload.[95]

1.4.3.1.4 Sortase-mediated enzymatic conjugation

Sortase-mediated conjugation has become valuable to afford precise, homogeneous AOCs, due to its specificity and compatibility with various biomolecules. Sortase A is a transpeptidase enzyme derived from *Staphylococcus aureus* and has been widely adopted in bioconjugation as it recognises a specific LPXTG amino acid motif, where X represents any amino acid at the C-terminus of peptides and proteins allowing it to catalyse a transpeptidation reaction with high specificity as illustrated in **Figure 28**[91]. However, despite these advantages, sortase-mediated conjugation does have limitations. Its application relies

on the presence of an LPXTG motif at the C-terminus of the antibody either introduced through genetic modification or peptide engineering which will introduce additional steps and complexity[96].

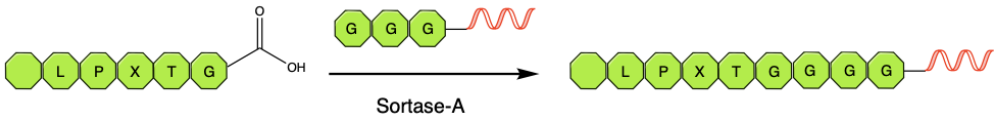

Figure 28 Schematic presentation of Sortase-A mediated conjugation of oligonucleotide payload (red) targeting LPXTG amino acid motif at the C-terminus of a protein or antibody.

1.4.3.1.5 Dibromopyridazinedione linker

Dibromopyridazinedione (diBrPD) linkers represent a recent addition in conjugation chemistry, bringing several unique advantages to the stable, site-specific conjugation methods of antibodies and oligonucleotides. Unlike conventional linkers, diBrPDs selectively target disulphide bonds within antibody structures, making it particularly effective for conjugation applications requiring conjugation with controlled attachment sites. Indeed, studies have shown that diBrPD linkers enable rebridging of interchain disulphides in antibodies to generate extremely stable conjugates suitable for both systemic circulation and the intracellular environments often encountered in therapeutic contexts[97, 98].

The conjugation mechanism of diBrPD linkers is characterised by its dual bromine groups, which facilitate the selective thiol reactivity in antibodies by rejoining the interchain disulphides without compromising antibody structure (**Figure 29**). This stability is advantageous in all applications including B-cell malignancies, where controlled and sustained therapeutic activity is critical.

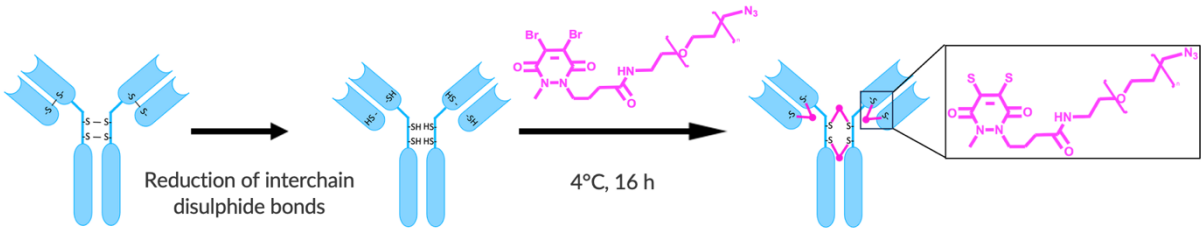

Figure 29 Schematic representation of the conjugation process using a disulphide-rebridging linker. The interchain disulphide bonds of the antibody are first reduced to generate free thiol groups, followed by incubation with the linker at 4°C for 16 hours, resulting in site-specific conjugation.

The mechanism of action for diBrPD linkers involves a Michael addition followed by an elimination reaction (**Figure 30**). After reduction of the interchain disulphide, the free thiol performs a nucleophilic attack on the electron-deficient double bond of the dibromopyridazinedione ring. This is followed by elimination of a bromine atom, which acts as a good leaving group, allowing for subsequent attack by a second thiol. This sequence enables rebridging of disulphide bonds in a site-specific and controlled manner without compromising antibody structure, contributing to the high stability of the resulting conjugates.

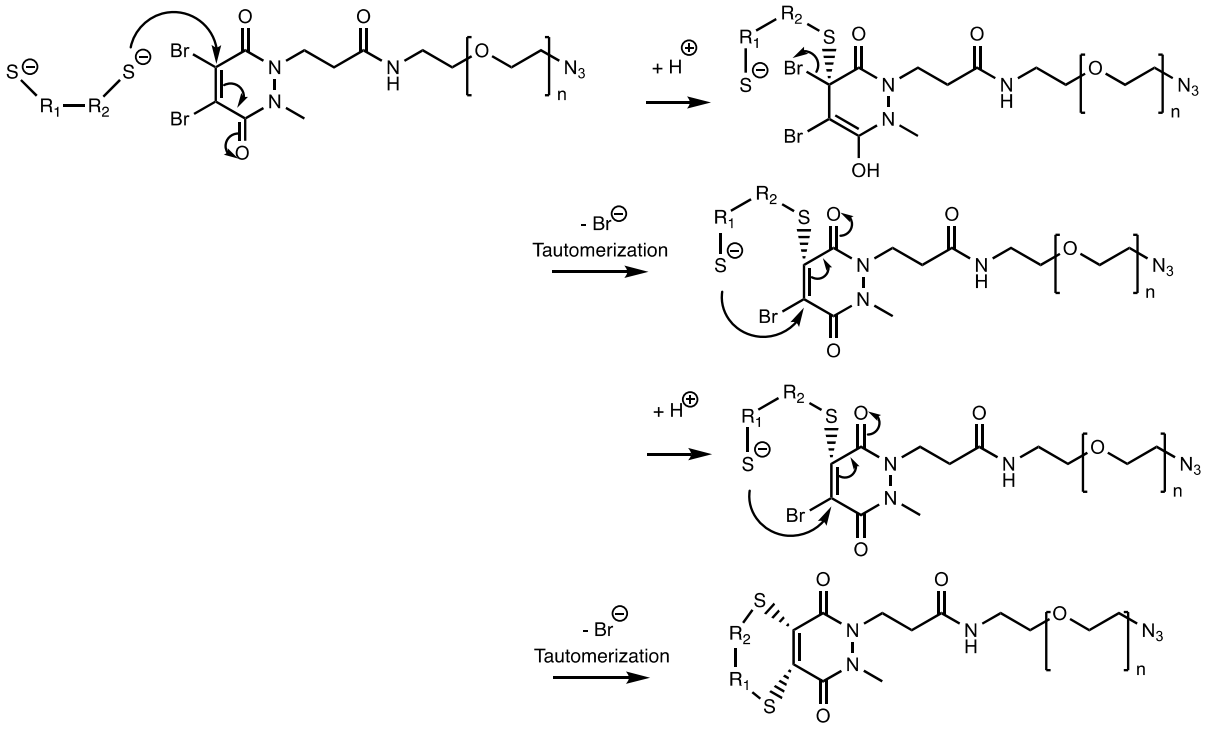

Figure 30 Proposed mechanism for disulphide rebridging using a dibromopyridazinedione (diBrPD) linker.

The reaction proceeds via a Michael addition-elimination mechanism. First, a thiol derived from a reduced disulfide bond attacks the electron-deficient double bond of the diBrPD and the bromine is removed as a good leaving group. A second thiol then undergoes a similar Michael addition at the remaining brominated position, displacing the second bromide and forming a stable bis-thioether adduct.

1.5 Scope of the project

This project focusses on the development and assessment of a novel modular therapeutic platform for the targeted therapy of B-cell malignancies by the conjugation of self-assembling NPs with the CD20-targeting monoclonal antibody, rtx. NPs have shown promising results in artificial lipid bilayers and cell membranes, demonstrating cytotoxicity in various cell lines[76-78]. Their assembly through specific base pairing, aqueous solubility and the commercial availability makes DNA an ideal building block for therapeutic NPs. These NPs interact with

the lipid bilayers like cell membranes by disrupting their structure and potentially leading to osmotic imbalances or inducing apoptotic pathways. It has been shown that hydrophobically modified NPs span cell membranes, forming stable channels that disrupt structural integrity and induce cell death[74, 75].

Building on recent advancements in self-assembled DNA nanostructures, our group has optimised a protocol for the formation of NPs with either four or six helical bundles, modified with HU for stable membrane insertion and exhibiting cell cytotoxicity in various cell lines. For this work, a new structure (6HB-NPx) was designed, consisting of ten DNA single strands forming a six-helix bundle with oligonucleotide sequences provided in **Appendix 2**; it was modified with two HUs pointing outward from the pore as illustrated in **Figure 31**.

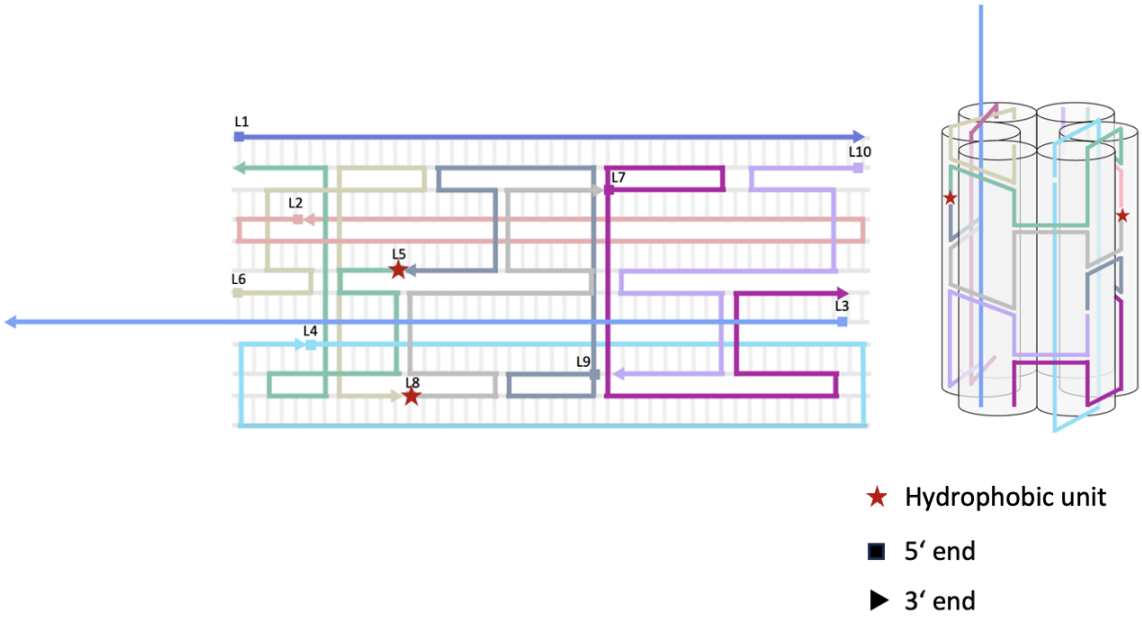

Figure 31 Schematic representation of 6HB-NPx-TH in caDNAno design. The left panel depicts the 2D assembly of 10 interconnected DNA oligonucleotides (L1–L10) with their respective 5′ and 3′ ends indicated. Hydrophobic units (red stars) are strategically incorporated to enable membrane insertion. The right panel illustrates the 3D model of the NP, demonstrating its cylindrical structure stabilised by DNA duplexes and featuring hydrophobic modifications for membrane anchoring.

In addition, the design included a DNA overhang (strand L3) that acts as the point of attachment site for a linker. The therapeutic efficacy of the NPs was assessed through *in vitro* studies with cell viability analyses conducted in CD20-expressing malignant B-cell lines such as Ramos cells to determine clinical translation.

mAbs, such as rtx targeting the CD20 antigen, have significantly improved treatment outcomes; however, their efficacy is often limited by resistance mechanisms and the inability to fully eliminate malignant cells. Therefore, novel strategies that combine targeted delivery with innovative mechanisms of action are urgently needed. By combining the precise targeting abilities of antibodies with the cytotoxic potential of membrane-spanning NPs[76, 78], this approach provides a promising dual-function strategy for the selective killing of malignant B cells.

A central aspect of the project is the site-specific conjugation of these NPs to rituximab through a diBrPD linker. This approach allows rebridging of the interchain disulphide bonds of the antibody[97], achieving site-specific and defined NP-to-antibody ratios while preserving the antibody's binding capacity. Conjugation efficiencys were evaluated by SDS-PAGE, SEC and flow cytometry to confirm the structural integrity and functional viability of the final construct. The therapeutic potential of modified rtx is assessed through *in vitro* functional validation with binding studies conducted in CD20-expressing malignant B-cell lines such as Ramos cells.

The modular design of the antibody-NP conjugate (**Figure 32**) builds on previous research in ADCs and DNA nanotechnology, addressing several critical limitations observed in conventional therapeutic approaches.

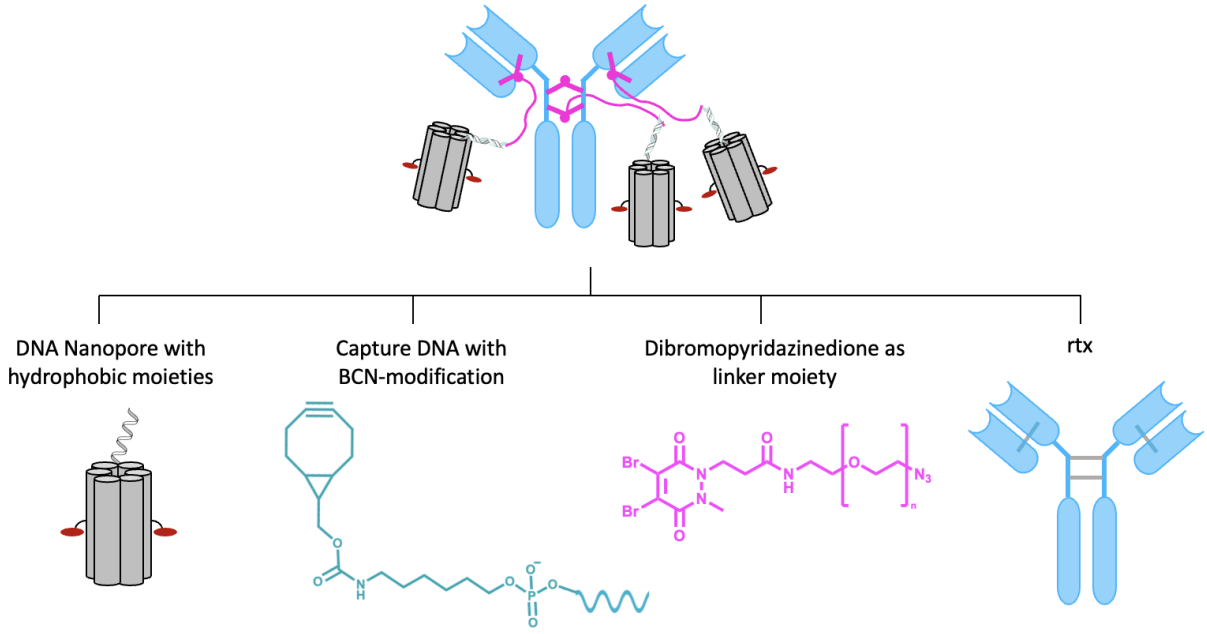

Figure 32 Schematic representation of the modular design of the antibody-nanopore conjugate. The construct consists of a DNA nanopore modified with hydrophobic moieties for membrane insertion, a capture DNA strand functionalised with a bicyclononyne (BCN) group for strain promoted azide alkyne cycloaddition to the terminal azide of the dibromopyridazinedione (diBrPD) linker that enables site-specific attachment to the anti-CD20 monoclonal antibody rituximab (rtx).

Unlike traditional ADCs, which are based on cytotoxic payloads that can eventually lead to systemic toxicity and resistance, the conjugate builds on these advances to offer an alternative approach that does not rely on intracellular uptake but rather induces cell death through direct disruption of the membrane (**Figure 33**). Furthermore, the use of a diBrPD linker represents a significant improvement over maleimide-based chemistries, which are prone to instability due to retro-Michael reactions and thiol exchange in glutathione-rich environments. Recent findings have demonstrated that the conjugation to antibodies significantly improves oligonucleotide stability by reducing susceptibility to nuclease degradation and additionally enhancing delivery to target tissues. The increased stability of

the proposed conjugate would ensure prolonged systemic circulation and sustained therapeutic activity at the tumour site.

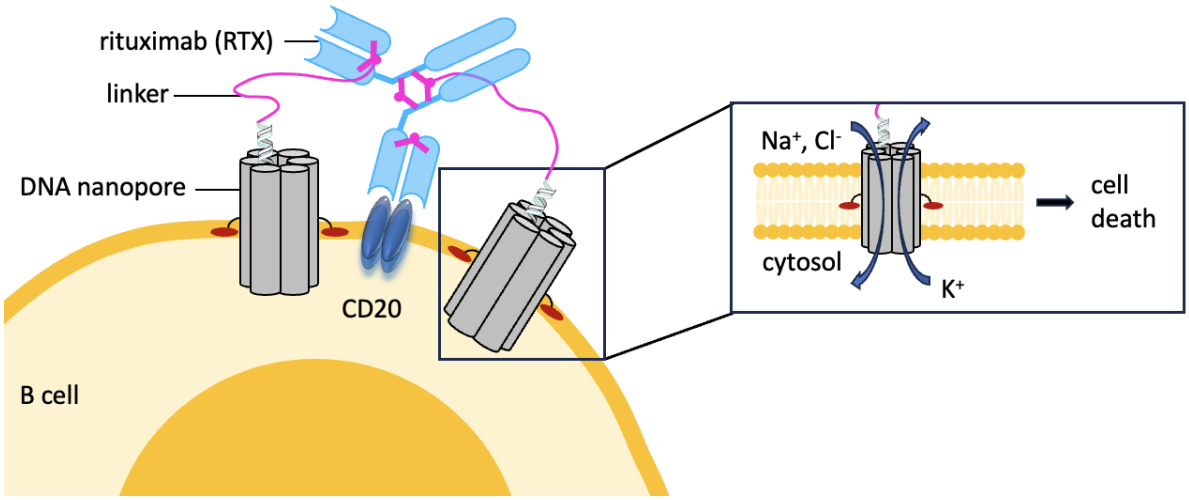

Figure 33 Schematic illustration of a rtx-linked NP targeting B cells via the CD20 receptor. NPs are conjugated to rtx through a linker, enabling receptor-specific binding and localization to the cell membrane. NPs which span the cell membrane, allowing uncontrolled ion flux (Na^+, Cl^- influx, and K^+ efflux), ultimately disrupting cellular homeostasis and inducing cell death.

The following sections summarize the results obtained and describing the design, synthesis and functional assessment of these antibody-NP conjugates, highlighting key findings in cytotoxicity evaluation, conjugation efficiency and structural stability. Additionally, challenges encountered during the characterisation process will be outlined, together with potential ways for optimization to provide a comprehensive understanding of the system's therapeutic potential and areas requiring further refinement.

This proof-of-concept study will establish, if successful, a strong foundation for future developments, allowing the modular platform across a wide range of cancer types and therapeutic targets. Indeed, the adaptability of this approach holds great promise for expansion into various malignancies and potentially offers a new avenue for personalised and targeted cancer therapies.

Chapter 2 Materials and Methods

2.1 General experimental details

2.1.1 Supplier

All reagents and solvents were obtained from commercial suppliers (BioRad, Fisher Scientific, Fluka, Fluorochem, Integrated DNA technologies, LGC Genomics, Promega, Qiagen, Sigma Aldrich, Thermofisher, VWR) and used as instructed by supplier. Rituximab was provided by the Southampton General Hospital as unused treatment leftover. AntiCD40 and antiHER2 bispecific antibodies were supplied by Strike Pharma. Air and moisture sensitive reactions were performed under an inert atmosphere.

2.1.2 pH measurements

pH measurements were performed at room temperature on a Thermo Scientific™ Eutech™ pH 5+ after a two-point calibration using pH Calibrations Buffer Solutions from Hanna Instruments™.

2.1.3 Column chromatography and thin layer chromatography

Column chromatography was carried out using Silica gel (60 μm particle Size) supplied by Merck Millipore.

All chemical reactions were monitored using thin layer chromatography (TLC) with aluminium supported TLC Silica gel 60 F_{254} obtained by Merck.

2.1.4 NMR Spectroscopy

NMR analyses were performed by the NMR Spectroscopy Facility in the School of Chemistry and Chemical Engineering on a Brucker AVII400 FT-NMR Spectrometer at room temperature. Chemical shifts are given in ppm and spectra are calibrated to the residual solvent peak.

2.1.5 Mass Spectrometry

Small molecule samples were analysed using a Waters (Manchester, UK) Acquity TQD mass tandem quadrupole mass spectrometer by the Mass Spectrometry service at the University of Southampton. Samples were introduced to the mass spectrometer *via* an Acquity H-Class quaternary solvent manager (with TUV detector at 254 nm, sample and column manager). Ultrahigh performance liquid chromatography was undertaken using Waters BEH C18 (or equivalent) column (50 mm x 2.1 mm 1.7 µm).

Gradient elution from 20% acetonitrile (0.2% formic acid) to 100% acetonitrile (0.2% formic acid) was performed over five minutes at a flow rate of 0.6 mL/min. Low resolution positive electrospray ionisation mass spectra were recorded.

DNA samples were analysed using a Waters (Manchester, UK) Acquity TQD mass tandem quadrupole mass spectrometer. Samples were introduced to the mass spectrometer *via* an Acquity H-Class quaternary solvent manager (with TUV detector at 260 nm, sample and column manager). Ultrahigh performance liquid chromatography was undertaken using Acquity UPLC® BEH C18 column (50 mm x 2.1 mm 1.7 µm). Gradient elution from 5% acetonitrile in 20 mM Triethylammonium acetate (TEAA) to 100% was performed over fourteen minutes at a flow rate of 0.250 mL/min.

2.1.6 IR Spectroscopy

Infrared spectra were recorded on a Thermo Scientific Nicolet is5. 16 scans of the wavelength range 4000-600 cm^{-1} were taken per spectrum with a resolution of 4 cm^{-1}. Absorption maxima (ν_{max}) are reported in wavenumbers (cm^{-1}).

2.1.7 Size exclusion chromatography (SEC)

Samples were analysed using a Shimadzu HPLC system and introduced to the HPLC *via* SIL-20A Autosampler (with SPD-20A UV/Vis detector at 280 nm and LC 20AD Liquid chromatographer) by Dr Tatyana Inzhelevskaya at the Centre for Cancer Immunology. Liquid chromatography was undertaken using Zorbax GF250 column (250 mm x 4.6 mm 4 µm) at a flow rate of 0.4 ml/min for 38 min.

Mobile phase was prepared by dropwise addition of 1.0 M DMF – 0.2 KH_2PO_4 to stirring 1.0 M DMF – 0.2 Na_sHPO_4 (1L) until the pH is adjusted to 7.0.

2.1.8 Protein concentration

Unmodified protein sample concentration measurements were performed on a NanoDrop Technologies ND-1000 Spectrophotometer in triplicates using PBS (137 mM NaCl, 2.7 mM KCl, 10 mM Na_2HPO_4, 1.8 mM KH_2PO_4) as blank. The absorbance at 280 nm was measured and the concentration is further calculated using $\varepsilon_{0.1\%}$ as the mass extinction coefficient for a 1 mg/ml solution of a reference protein measured in a 1 cm cuvette. When using mass extinction coefficients for the calculation of the protein concentration through Beer-Lambert law, the results are directly expressed as mass percentages of 0.1% (1 mg/ml).

$$c(0.1\%) = \frac{A}{\varepsilon(0.1\%)}$$

2.1.9 Bradford assay

For modified protein/antibody sample concentration, measurements were performed by diluting using Biorad Protein Assay Dye Reagent Concentrate (#5000006) in MQ water (1:5 dilution factor). A protein standard was prepared for 4 concentrations between 0.5 mg/ml and 0.0625 mg/ml. 10 μL of samples were placed on a 96-well plate and 200 μL of diluted dye reagent added to the well and mixed by pipetting up and down. After an incubation time of 5 min at RT the absorbance at 595 nm was measured using an Agilent BioTek Epoch microplate spectrophotometer.

2.2 Chemical synthesis

2.2.1 Synthesis of Di-tert-butyl-1-methylhydrazine-1,2-dicarboxylate (compound 1)

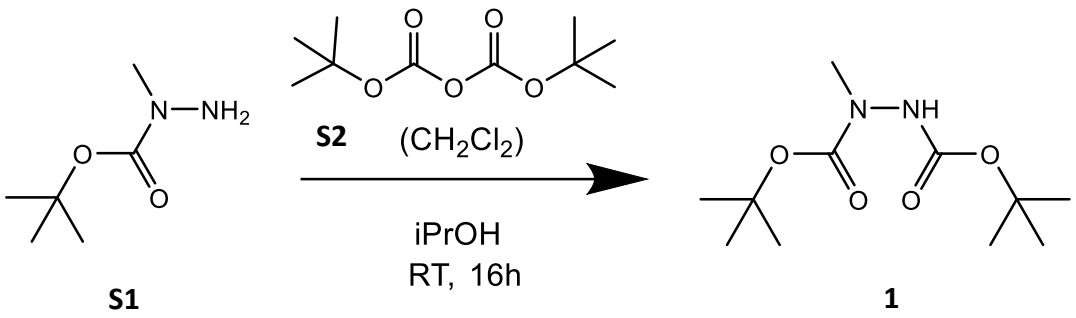

S1 **1**

To a solution of 1-Boc-1-methylhydrazine **S1** (2.1 ml, 14.1 mmol) in ^{i}PrOH (20.9 ml), was added a solution of di-tert-butyl decarbonate **S2** (3.9 ml, 17.0 mmol) in CH_2Cl_2 (7.8 ml) dropwise over 30 min and the reaction mixture was stirred for 16 h at room temperature. After this time, the solvent was removed *in vacuo* and the crude residue purified by flash column chromatography in 50% EtOAc:PE to recover di-tert-butyl-1-methylhydrazine-1,2-dicarboxylate **(compound 1)** as a white solid (3200 mg, 13.0 mmol, 92%). Analytical data were consistent with literature values.[97]

^{1}H NMR: (400 MHz, $CDCl_3$, rotamers) δ_H (ppm) 6.41–6.16 (m, 1H) 3.11 (s, 3H), 1.47–1.46 (2 s, 18H)

$^{13}C\{^{1}H\}$ NMR (101 MHz, $CDCl_3$) δ 155.8, 80.7, 37.2, 28.09, 28.1

ESI+ ($C_{11}H_{22}N_2O_4$): Monoisotopic mass: calcd. 246.16, observed m/z = 269.28 [M+Na^+]

2.2.2 Synthesis of Di-tert-butyl-1-(3-(tert-butoxy)-3-oxopropyl)-2-methylhydrazine-1,2-dicarboxylate (compound 2)

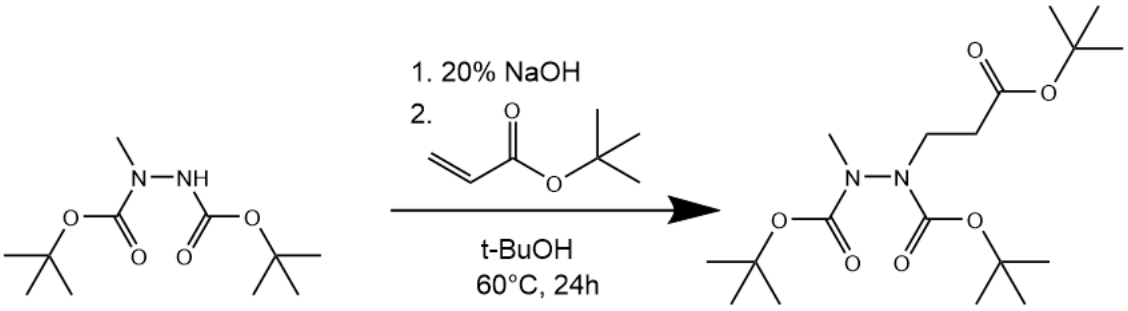

1 **2**

To a solution of **compound 1** (2000 mg, 8.1 mmol) in ^{t}BuOH (10 ml) was added freshly prepared 20% NaOH (aq) (0.33 ml) and the reaction stirred at room temperature for 30 min under a nitrogen atmosphere. After this time, tert-butyl acrylate (3.5 ml, 24.4 mmol) was added to the solution and the reaction mixture was heated to 60°C for 24h.

After the incubation time, the solvent was removed *in vacuo* and the crude residue dissolved in 5 ml EtOAc and washed with water (3 x 10 ml). The organic layer was concentrated *in vacuo* and the crude residue purified *via* flash column chromatography in 20% EtOAc:PE to recover di-tert-butyl-1-(3-(tert-butoxy)-3-oxopropyl)-2-methylhydrazine-1,2-dicarboxylate **(compound 2)** as a clear oil (1670 mg, 4.5 mmol, 55%). Analytical data were consistent with literature values[97].

^{1}H NMR (400 MHz, CDCl3, rotamers) δ 3.85–3.52 (m, 2H), 3.06–2.99 (m, 3H), 2.51 (t, J = 7.2 Hz, 2H), 1.48–1.43 (m, 27H)

$^{13}C\{^{1}H\}$ NMR (101 MHz, $CDCl_3$) δ 170.9, 155.3, 154.3, 81.0, 44.5, 36.6, 34.1, 28.3, 28.2, 28.2, 28.1, 28.0

ESI+ ($C_{18}H_{34}N_2O_6$): calcd. mass: 374.24, observed m/z = 397.37 [$M+Na^+$]

2.2.3 Synthesis of 3-(4,5-Dibromo-2-methyl-3,6-dioxo-3,6-dihydropyridazin-1(2H)-yl)propanoic acid (compound 3)

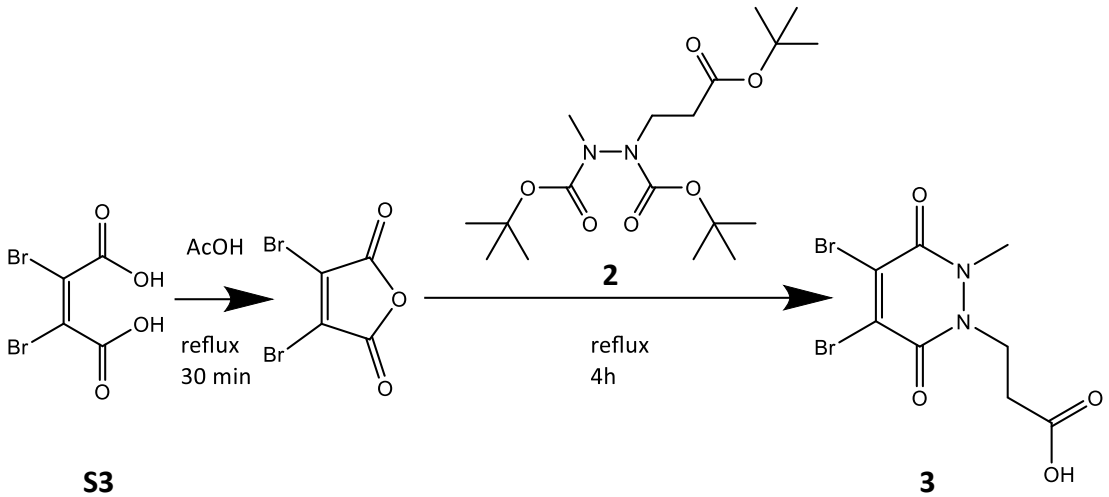

S3 **3**

Dibromomaleic acid **S3** (846 mg, 3.1 mmol) was dissolved in AcOH (25 mL) and heated under reflux for 30 min. To this solution **compound 2** (1000 mg, 2.67 mmol) was added and the reaction heated under reflux for a further 4 h. After this time, the reaction mixture was concentrated in vacuo with toluene co- evaporation as an azeotrope. Purification was performed via flash column chromatography (100% EA (1% AcOH)) to afford 3-(4,5-dibromo-2-methyl-3,6-dioxo-3,6-dihydropyridazin-1(2H)-yl)propanoic acid **(compound 3)** as a brown solid (951 mg, 2.68 mmol, 100%). Analytical data were consistent with literature values.[97]

^{1}H NMR (400 MHz, DMSO-d_6) δ 4.28 (t, J = 7.3 Hz), 2H), 3.56 (s, 3H), 2.63 (t, J = 7.3 Hz, 2H)

$^{13}C\{^{1}H\}$ NMR (101 MHz, DMSO) δ 171.8, 152.6, 152.3, 135.3, 134.9, 43.0, 40.1, 34.6, 31.6

ESI+ ($C_8H_8Br_2N_2O_4$): calcd. mass: 353.89, observed: m/z = 355.1 [$C_8H_8{}^{79}Br_2N_2O_4$]; m/z = 357.1 [$C_8H_8{}^{79}Br^{81}BrN_2O_4$]; m/z = 359.1 [$C_8H_8{}^{81}Br_2N_2O_4$]

2.2.4 Synthesis of 2,5-Dioxopyrrolidin-1-yl-3-(4,5-dibromo-2-methyl-3,6-dioxo-3,6-dihydropyridazin-1(2H)-yl)propanoate (compound 4)

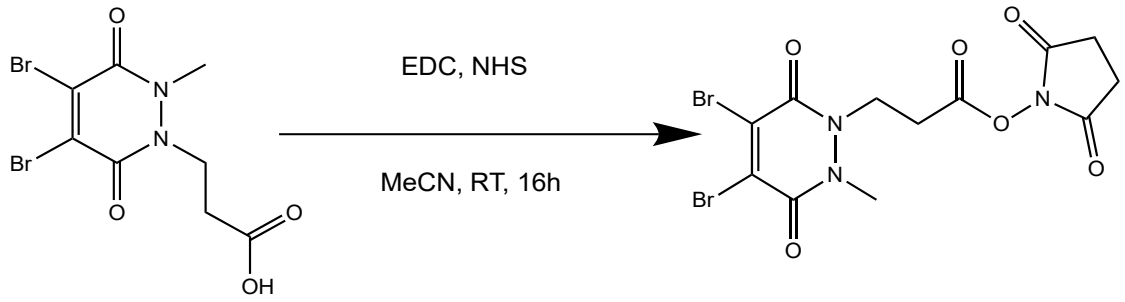

3 **4**

1-Ethyl-3-(3-dimethylamino-propyl)carbodiimide hydrochloride (EDC-HCl) (323 mg, 1.7 mmol) and NHS (194 mg, 1.7 mmol) were weighted into a round bottom flask and flushed with nitrogen. **Compound 3** (500 mg, 1.4 mmol) was dissolved in anhydrous MeCN (20 mL) and added to the round bottom flask. The reaction was stirred at room temperature for 16 h. After the reaction time, the solvent was removed *in vacuo* and the crude mixture dissolved in DCM (15 ml) and washed with water (3 x 15 ml). The organic layer was dried in vacuo and the crude mixture purified through flash column chromatography in 100% EA to afford 2,5-Dioxopyrrolidin-1-yl-3-(4,5-dibromo-2-methyl-3,6-dioxo-3,6-dihydropyridazin-1(2H)-yl)propanoate **(compound 4)** as a light yellow solid (150 mg, 0.33 mmol, 21%). Analytical data were consistent with literature values.[97]

^{1}H NMR (600 MHz, CDCl3) δ 4.48 (t, J = 6.9 Hz, 2H), 3.68 (s, 3H), 3.11 (t, J = 6.9 Hz, 2H), 2.85 (s, 4H)

$^{13}C\{^{1}H\}$ NMR (101 MHz, $CDCl_3$) δ 168.5, 165.9, 154.2, 135.2, 96.4, 42.9, 35.2, 29.0, 25.5

ESI+ ($C_{12}H_{11}Br_2N_3O_6$): calcd. mass: 450.9, observed: m/z = 452.1 [$C_{12}H_{11}{}^{79}Br_2N_3O_6$]; m/z = 454.1 [$C_{12}H_{11}{}^{79}Br^{81}BrN_3O_6$]; m/z = 456.1 [$C_{12}H_{11}{}^{81}Br_2N_3O_6$]

2.2.5 Synthesis of *N*-(26-azido-3,6,9,12,15,18,21,24-octaoxahexacosyl)-3-(4,5-dibromo-2-methyl-3,6-dioxo-3,6-dihydropyridazin-1(2H)-yl)propanamide (diBrPD-8)

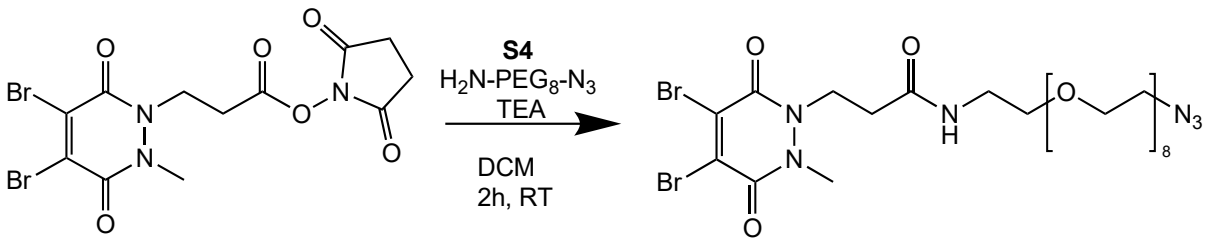

4 **diBrPD-8**

O-(2-Aminoethyl)-O'-(2-azidoethyl)pentaethylene glycol **S4** (101 mg, 0.231 mmol) was dissolved in anhydrous DCM (2.5 ml) and cooled on ice. Triethylamine (0.087 mL, 0.629 mmol) was added, and the mixture is stirred on ice for 10 min under a nitrogen atmosphere. Meanwhile **compound 4** (95 mg, 0.210 mmol) was dissolved in DCM (2.5 ml) and added dropwise to the mixture. The reaction was stirred at room temperature in the absence of light for 2 hours. After the reaction time, the mixture was diluted with DCM (5 ml) and extracted with water (3 x 10 ml). The organic phase is concentrated in vacuo, and purification through flash column chromatography in 4% MeOH:$CHCl_3$ afforded **diBrPD-8** as a yellow oil (35 mg, 0.045 mmol, 20%).

^{1}H NMR (400 MHz, CDCl3) δ 2.60 (t, J = 6.97 Hz, 2H), 3.36 – 3.39 (m, 2H), 3.40 – 3.43 (m, 2H), 3.49 – 3.54 (m, 2H), 3.59 – 3.69 (m, 32 H), 3.71 (s, 3H), 4.43 (t, J = 6.97 Hz, 2H), 6.77 (br s, 1H)

^{13}C NMR (101 MHz, $CDCl_3$) δ 169.1, 152.9, 152.7, 136.1, 135.3, 70.6, 70.6, 70.6, 70.5, 70.5, 70.5, 70.4, 70.4, 70.2, 70.0, 69.5, 50.6, 44.3, 39.4, 35.0, 33.8

ESI+ ($C_{26}H_{44}Br_2N_6O_{11}$): calcd. mass: 774.14, observed: m/z = 775.3 [$C_{26}H_{44}{}^{79}Br_2N_6O_{11}$]; m/z = 777.3 [$C_{26}H_{44}{}^{79}Br^{81}BrN_6O_{11}$]; m/z = 779.3 [$C_{26}H_{44}{}^{81}Br_2N_6O_{11}$]

2.2.6 Synthesis of *N*-(71-azido-3,6,9,12,15,18,21,24,27,30,33,36,39,42,45,48,51,54,57,60,63,66,69-tricosaoxahenheptacontyl)-3-(4,5-dibromo-2-methyl-3,6-dioxo-3,6-dihydropyridazin-1(2*H*)-yl)propanamide (diBrPD-23)

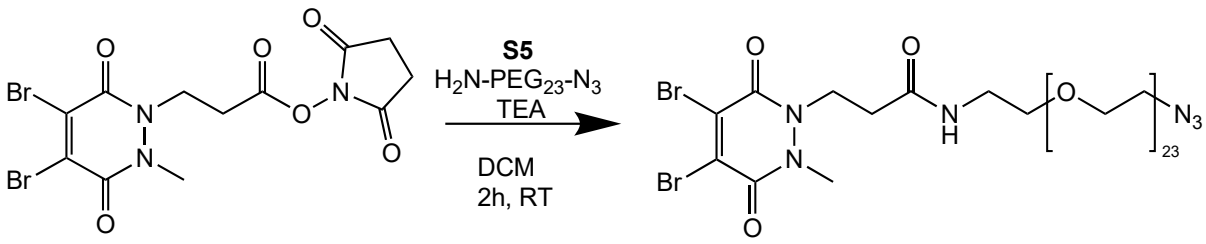

4 **diBrPD-23**

Azido-dPEG®$_{23}$-amine **S5** (100 mg, 0.091 mmol) was dissolved in anhydrous DCM (1 ml) and cooled on ice. Triethylamine (35 μL, 0.248 mmol) was added and the mixture is stirred on ice for 10 min under a nitrogen atmosphere. Meanwhile **compound 4** (37.5 mg, 0.083 mmol) was dissolved in DCM (1 ml) and added dropwise to the mixture. The reaction was stirred at room temperature in the absence of light for 2 hours. After the reaction time, the mixture was diluted with DCM (3 ml) and extracted with water (3 x 5 ml). The organic phase was concentrated *in vacuo* and purification through flash column chromatography in 7% MeOH:$CHCl_3$ afforded **diBrPD-23** as a yellow oil (26 mg, 0.018 mmol, 20%).

^{1}H NMR (400 MHz, CDCl3) δ 2.58-2.64 (m, 2H), 3.36 – 3.40 (m, 2H), 3.40 – 3.43 (m, 2H), 3.50 – 3.54 (m, 2H), 3.62 – 3.696 (m, 91 H), 3.72 (s, 3H), 4.43 (t, J = 6.91 Hz, 2H), 7.00-7.06 (m, 1H)

^{13}C NMR (101 MHz, $CDCl_3$) δ 169.2, 152.7, 136.1, 135.4, 77.3, 76.7, 70.6, 70.6, 70.6, 70.5, 70.4, 70.4, 70.1, 70.0, 69.5, 50.6, 44.3, 39.3, 35.0, 33.7

ESI+ ($C_{56}H_{104}Br_2N_6O_{26}$): calcd. mass: 1434.54, observed: m/z = 1435.9 [$C_{56}H_{104}{}^{79}Br_2N_6O_{26}$]; m/z = 1437.9 [$C_{56}H_{104}{}^{79}Br^{81}BrN_6O_{26}$]; m/z = 1439.9 [$C_{56}H_{104}{}^{81}Br_2N_6O_{26}$]

2.3 DNA experimental details

2.3.1 DNA Concentration determination

For the determination of DNA sample concentration, measurements were performed on a NanoDrop Technologies ND-1000 Spectrophotometer in triplicates using MQ water as blank. The absorbance at 260 nm was measured and the concentration is further calculated following the Lambert-Beer law.

$$A = \varepsilon \times c \times d$$

With *A* corresponding to the Absorption, *ε* to the extinction coefficient, *c* representing the concentration and finally *d* is the path length. The extinction coefficient was determined through IDT Oligo Analyser (**Appendix 2**).

2.3.2 DNA Synthesis

DNA oligonucleotides L1 – L10, L6c, L9c, L3-A594 L10-A647 were acquired from Integrated DNA Technologies (IDT). Other cholesterol-modified oligonucleotides (L2c, L4c, L5c and L8c) were provided from Quentin Vicentini at AstraZeneca (Sweden) and alkyl-modified oligonucleotides were provided by Brune Vialet from the National Institute of Health and Medical Research in Bordeaux (INSERM). C2 and M1 were synthesised and purified by Mónica Lopes at the Research Institutes of Sweden (RISE). pTagPNA samples were received by Jan H. Meffert (Ghent University). Selected 5'-modified oligonucleotides were synthesised and isolated inhouse, this applies to anti-L10, C1, L5c and L8c. The details of the synthesis are given below.

2.3.2.1 Synthesis of unmodified DNA strands before post-synthesis labelling

In this project, DNA oligonucleotides do not have backbone modifications, but if applicable contain 5' modifications. The unmodified strands were synthesised using a standard protocol and standard commercially available phosphoramidites on an Applied Biosystems Nucleic Acid Synthesis System using either 500 or 1000 Å pore CPG beads on a 1 µmol scale, depending on the length of the oligonucleotide with a final DMT on.

2.3.2.2 Post-synthesis functionalisation of oligonucleotides

2.3.2.2.1 Functionalisation with cholesterol

For the post-synthetic modification with cholesterol, the commercially available 5'-Cholesterol-TEG CE-Phosphoramidite was diluted in 1.5 ml anhydrous DCM and subsequently transferred to a pear-shaped flask compatible with the Expedite DNA synthesiser. A protocol involving an extended coupling time of 10 min was used for the functionalisation of the oligonucleotide and kept on the solid support. The resin was treated with diethylamine (20% in MeCN) for 20 min and further washed with MeCN in a first step, with water in a second step. Oligonucleotides were cleaved from the solid support (CPG resin) by incubating the resin in concentrated aqueous ammonia solution (30%) for about 1 hour. The resulting solution was then incubated at 50°C overnight or at 65°C for 5 hours to complete the deprotection. After incubation, the solvent was removed through lyophilization or using a DNA SpeedVac concentrator.

2.3.2.2.2 Functionalisation with (1R, 8S, 9S)-Bicyclo[6.1.0]non-4-yn-9-yl (BCN)

For the functionalisation of the oligonucleotide using (1R, 8S, 9S)-Bicyclo[6.1.0]non-4-yn-9-ylmethyl N-succinimidyl carbonate (BCN-NHS), first the oligonucleotide is labelled with a 5'-

TFA-6-Aminohexyl Amidite, which was diluted to a 0.2 M concentration. The coupling was performed with an extended coupling time of 10 min and without the capping step. The resin was treated with diethylamine (20% in MeCN) for 20 min and further washed with MeCN in a first step, with water in a second step. Oligonucleotides were cleaved from the solid support (CPG resin) by incubating the resin in concentrated aqueous ammonia solution (30%) for about 1 hour. The resulting solution is then incubated at 50°C overnight or at 65°C for 5 hours to complete the deprotection. After incubation, the solvent was removed through lyophilization or using a DNA SpeedVac concentrator. The dried samples were then dissolved in water and desalted using a NAP-10 column. For the coupling with BCN-NHS, the oligonucleotides were dissolved in 0.5 M $NaHCO_3/Na_2CO_3$ (pH 8.75) to a concentration of 0.5 mM. BCN-NHS (~ 30 eq) was dissolved in DMF and added to the oligonucleotide solution in a 1:1 volume ratio. The reaction mixture was incubated at room temperature for 5 hours and finally desalted twice using NAP-10 columns.

2.3.3 Purification through high-performance liquid chromatography

In-house synthesised oligonucleotide strands were purified using a Varian 920-LC Liquid Chromatography system. High-performance liquid chromatography was undertaken using XBridge® Oligonucleotide BEH C18 column (50 mm x 4.6 mm 2.5 µm).

Gradient elution from 5% Methanol in 8.6 mM Triethylammonium (TEA) and 100 mM Hexafluoro-2-propanol to 95% was performed over twenty-two minutes at a flow rate of 0.800 mL/min.

2.3.4 Formation of DNA nanopores

By pipetting the DNA strands in an equimolar mixture (1 to 6 μM) in 1X PBS into a PCR tube, the NPs are prepared for their assembly. The mixture was heated to 90°C then cooled at a rate of 1°C per minute to 4°C using a BioRad T-100 thermal cycler. If not stated otherwise, the constructs were stored at 4°C and vortexed for 1s before use.

2.3.5 Agarose gel electrophoresis

Agarose gels were prepared with 2% agarose and 11 mM $MgCl_2$ in 1X TB buffer (130 mM Tris base and 45 mM Boric acid, pH 8.3) and stained with SYBR Gold (10.000-fold dilution of SYBR® Gold stain). Electrophoresis was run at 55 V at room temperature for 70 min or at 4°C for 120 min to increased resolution. Images were obtained with a BioRad molecular Imager Gel Doc™.

2.3.6 Polyacrylamide gel electrophoresis (PAGE)

All PAGE gels were prepared by mixing the components outlined in each specific section, excluding the freshly prepared 10% ammonium persulfate (APS) solution. Polymerisation was initiated by adding the indicated volume of APS to the mixture, followed by thorough mixing and casting between the gel plates. A suitable comb was added and the gel left to set. Once polymerization was complete, the comb was removed and the gel was rinsed with water. If necessary, the gel was pre-run for 30 minutes at the chosen voltage before loading the samples. PAGE gels were run in a Bio-Rad Mini-Protean III electrophoresis chamber. Staining and destaining were performed using an IKA VXR S17 Orbital Shaker, and gel images were acquired with a Bio-Rad Molecular Imager Gel Doc™ system.

2.3.6.1 Native PAGE

10% Native gel composition

Component	Amount
40% SureCast Acrylamide Solution (29:1 Bis-acrylamide ratio)	2.50 mL
10X Tris-Borate buffer pH 8.3	1.00 mL
H_2O	6.39 mL
Tetramethylethylenediamine (TEMED)	0.01 mL
10% APS (fresh!)	0.10 mL

10X TB Running buffer (pH 8.3)

Component	Concentration	Amount
Tris-Base	89 mM	10.78 g
Boric acid	89 mM	5.50 g
H_2O		to 1 L

DNA samples (1 μM, 0.5 μL) were mixed with 2 μL 6X DNA Gel Loading Dye (0.25% bromophenol blue, 30% glycerol) and 9.5 μL water, before loading the sample into the well. Gels were run until the dye front reached three quarter of the gel. The gel removed from the casting plates and incubated in a 1X staining solution (10.000-fold dilution of SYBR® Gold stain in running buffer) for 10 min.

2.3.6.2 Denaturing PAGE

10% Denaturing PAGE gel composition

Component	Amount
40% SureCast Acrylamide Solution (29:1 Bis-acrylamide ratio)	2.50 mL
Urea	4.8 g
10X Tris-Borate-EDTA buffer pH 8.3	1.00 mL
H_2O	1.39 mL
TEMED	0.01 mL
10% APS (fresh!)	0.10 mL

10X TBE Running buffer (pH 8.3)

Component	Concentration	Amount
Tris-Base	1 M	121.1 g
Boric acid	1 M	61.8 g
EDTA	0.02 M	7.4 g
H_2O		to 1 L

DNA samples (1 μM, 2 μL) were mixed with 1 μL Gel Loading Buffer II (Thermofisher) and 7 μL water, before loading the sample into the well. Gels were run at 200V until the dye front reached three quarter of the gel. The gel removed from the casting plates, rinsed with DI

water and incubated in a 1X staining solution (10.000 fold dilution of SYBR® Gold stain in running buffer) for 10 min.

2.3.6.3 SDS-PAGE

Resolving PAGE gels were poured leaving roughly 2 cm from the top of the plate and isopropanol was added to remove bubbles and to maintain an even, horizontal surface. Once the gel is set, the isopropanol is removed, and the surface rinsed with water. Stacking PAGE gels were poured on top of the resolving gel. A suitable comb was added, and the gel left to set.

8% Resolving PAGE gel composition

Component	Amount
40% SureCast Acrylamide Solution (29:1 Bis-acrylamide ratio)	2.00 mL
1.50 M Tris-HCl pH 8.8	2.60 mL
10% SDS	0.10 mL
H_2O	5.19 mL
TEMED	0.01 mL
10% APS (fresh!)	0.10 mL

5% Stacking PAGE gel composition

Component	Amount
40% SureCast Acrylamide Solution (29:1 Bis-acrylamide ratio)	0.375 mL
1.00 M Tris-HCl pH 6.8	0.380 mL
10% SDS	0.100 mL
H_2O	2.112 mL
TEMED	0.003 mL
10% APS (fresh!)	0.030 mL

10X SDS-PAGE Running buffer (pH 8.3)

Component	Concentration	Amount
Tris-Base	0.250 M	30.3 g
Glycine	1.9 M	144.4 g
SDS	0.03 M	10 g
H_2O		to 1 L

Protein samples (0.5 μg) were mixed with 2.5 μL NuPAGE™ LDS Sample Buffer (ThermoFisher) and diluted to 10 μL with MQ water. Samples were heated to 90°C for 3 min in order to achieve complete unfolding of the antibody. The samples were cooled for 3 min and centrifuged before loading into the wells. Gels were run at 250 V until the dye front reached three quarter of the gel. The gel was removed from the casting plates and stained using

Coomassie Brilliant Blue G250 stain for 10 min on the rocker. The gel was then washed with water and left in water for destaining overnight.

SDS-PAGE Staining solution

Component	Concentration	Amount
Coomassie Blue R350	0.1%	0.1 g
Methanol	40% (v/v)	400 mL
Acetic acid	10% (v/v)	100 mL
H_2O		to 1 L

2.4 Antibody construct assembly

2.4.1 Antibody disulphide rebridging protocol

DiBrPD-8 or diBrPD-23 (50 mM, 30 eq.) was added to a solution of rituximab (1-5 mg/ml, 1 eq.) in PBS and the solution incubated on ice for 30 min. Freshly prepared TCEP-HCl (50 mM, 10 eq.) was added to the solution and incubated at 4°C for 16h. Excess reagents were removed by ultrafiltration (3x 100.000 MWCO, Amicon® Ultra 0.5, Millipore). Successful conjugation was assessed through SDS-PAGE and SEC.

2.4.2 SPAAC reaction: antibody-linker conjugation to oligonucleotides

Oligonucleotides (80 eq.) were added to the antibody-linker mixture (1 eq.) and pipetted up and down to mix. The resulting solution is then incubated at 30°C for at least 4 hours. Excess reagents were removed by size exclusion chromatography in PBS and afforded antibody-

oligonucleotide conjugates (antibody-ssDNA). Successful conjugation was assessed through SDS-PAGE and SEC.

2.4.3 Assembly of antibody-dsDNA construct

Single oligonucleotides were dissolved in MQ water to a concentration of approximately 5 mM and heated to 90°C for 3 min. The oligonucleotides (80 eq., 1.1 μL) were added to the antibody-ssDNA constructs (100 μg/ml, 10 μL) and mixed by pipetting up and down. The mixture was placed in at 4°C for at least 30 min to allow hybridisation. Successful conjugation was assessed through flow cytometry.

2.4.4 Assembly of antibody-NP construct

Previously assembled NP constructs (6 μM, 200 μL) were freeze dried using a Labconco FreeZone Benchtop freeze dryer. The samples are resuspended in a solution of antibody-linker (100 ug/ml, 45 μL) with 10 μL of 1M TEAA and incubated at 30°C overnight to allow SPAAC.

2.4.5 Assembly of modular antibody-oligonucleotide construct with peptide tag and PNA

MALAT1 oligonucleotide (M1) and peptide-tag-PNA (pTagPNA) were pipetted in an equimolar mixture (100 μM) in 1X PBS to a final volume of 20 μL. This mixture is briefly vortexed and centrifuged before heated to 90°C for 5 min and allowed to cool down on ice for 30 min. The annealed oligonucleotides were stored at 4°C until use. Previously annealed oligonucleotides were incubated with Strike2001 or SP032 at a final concentration of 2.5 μM for 30 minutes at

room temperature. Successful conjugation was verified by Size-exclusion chromatography (SEC) (Zorbax GF-250) and by native SEC-ESI MS.

2.5 Cell culture experimental details

Ramos and Daudi cell lines, both human B-cell lymphoma cell lines, were obtained from the American Type Culture Collection (ATCC) and cultured at 37°C with 5% CO_2 in an appropriately sized Corning flask. The Ramos cell line originates from a 3-year-old male patient diagnosed with Burkitt's lymphoma and is Epstein-Barr virus (EBV)-negative. In contrast, the Daudi cell line was derived from a 16-year-old male patient with Burkitt's lymphoma and is EBV-positive. Roswell Park Memorial Institute (RPMI) 1640 Medium was supplemented with 50 ml fetal calf serum (FCS), 5 ml Penicillin-Streptomycin, L-Glutamine and Sodium Pyruvate filtered through a 0.20 μM filter.

2.5.1 Cell thawing

Cell aliquots were removed carefully from the -80°C freezer and immediately placed in a water bath (37°C) for 1 min. Once the aliquot is thawed, the suspension is transferred to a universal with 10 ml RPMI 1640 medium. The universal is centrifuged for 5 min at 1500 rpm and the supernatant discarded. The pellet is carefully resuspended in fresh RPMI 1640 media, transferred to a T75 corning flask and placed in an incubator. Cells were passaged at least 3 times before experiments are conducted.

2.5.2 Cell counting

Cell counting was performed using an automatic cell counter or a haemocytometer (described under 2.5.3.1). For automatic cell counting, 10 μL of cell suspension was mixed with 10 μL

DeNovix Acridine Orange / Propidium Iodide (AO/PI) by pipetting up and down. The mixture is then analysed on a DeNovix CellDrop™.

2.5.3 Cell binding assay

Antibody samples were prepared in a stock of 30 μg/ml to make a serial dilution (7-8 steps) with a chosen dilution factor (either 1:3 or 1:2). Cells were resuspended, counted and pelleted (1500 rpm, 5 min). The supernatant was discarded and cells were resuspended in FACS buffer to a concentration of $4*10^6$ cells/ml. 50 μL of cell suspension was placed in a FACS tube in a 1:1 volume ratio and incubated for 30 min in the dark at 4°C. After incubation time, the samples are washed two times with 3 ml FACS buffer to remove unbound antibody. A 1/10 dilution of the secondary antibody (R-Phycoerythrin-conjugated AffiniPure F(ab')2 Fragment Goat Anti-Human IgG, Fcγ Fragment specific, Jackson ImmunoResearch) was prepared. 10 μL were added to the FACS tubes and incubated at 4°C for 30 min in the dark. The samples were washed two times with 3 ml FACS buffer before analysis on a BD FACSCanto™ II Flow Cytometer or a CytoFlex Flow Cytometer.

2.5.4 Cell viability assays

Prior to performance of cell viability assays, NP samples were prepared and diluted in PBS to a 1 μM concentration. Cells were resuspended, counted and diluted to a concentration of $1*10^6$ cells/ml using RPMI. 100 μL cell suspension was placed on a flat bottom 96-well plate and 100 μL NP sample added to the well. The plate was placed in an incubator for the time points, indicated in the results section.

2.5.4.1 Trypan Blue staining

10 μL cell suspension was diluted with Trypan Blue Solution 0.4% (Gibco) in a separate Eppendorf tube. 10 μL of the mixture was placed on a haemocytometer and analysed under a microscope at 20X magnification. Cells were counted in the corner quadrants manually and calculated using the formula below.

$$\frac{\text{Sum of cells counted in quadrants}}{\text{Number of quadrants}} \times \text{Dilution factor} \times 10^4 = \text{Number of cells per ml}$$

Cell viability in percentage was calculated by dividing the number of live cells counted by the total number of cells multiplied by 100.

2.5.4.2 Annexin V / Propidium Iodide assay

Cells were treated in capped FACS tubes. After incubation time (24h or 48h), tubes were removed from the incubator and 100 μL of freshly prepared 2X Annexin V/PI stain was added to each tube. The tubes were agitated and incubated for 15 min at room temperature in the dark before analysis on a BD FACSCanto™ II Flow Cytometer or a CytoFlex Flow Cytometer.

2.5.4.3 LiveDead Cell Stain

After incubation time (24h or 48h), treated cells were resuspended and transferred to FACS tubes. The cells are washed two times with azide- and serum/protein-free PBS and finally resuspended to $1*10^6$ cells/ml. Fixable Viability Dye (1 μL per 1 ml cell suspension) was added and vortexed immediately. The tubes were incubated at 4°C for 30 min in the dark. The reaction was quenched by washing the cells with 3 ml FACS buffer before analysis on a BD FACSCanto™ II Flow Cytometer or a CytoFlex Flow Cytometer.

2.5.4.4 CellTiter Glo®

CellTiter-Glo® Buffer and lyophilised CellTiter-Glo® Substrate was equilibrated to room temperature prior to use. The CellTiter-Glo® Buffer was transferred from the original bottle to the amber bottle containing the CellTiter-Glo® Substrate and mixed by inverting the bottle a few times to make a homogeneous solution. The CellTiter Glo® Reagent was divided into 10 x 1 ml aliquots and stored at -20°C until further use.

An aliquot was equilibrated to room temperature an hour before use. In an opaque-walled 96-well plate, 25,000 cells were seeded per well and supplemented with complete RPMI to 50 μL. One control well with 50 μL RPMI 1640 was added as a background measurement. 50 μL of CellTiter Glo® Reagent was added, the plate immediately shaken for 2 min and incubated for 10 min at room temperature before reading of the luminescent signal on a VarioskanFlash.

2.5.5 Confocal microscope

Cells were cultured in capped FACS tubes in solution at $1*10^6$ cells/ml in a final volume of 550 μL. Alexa Fluor 647-labelled NPs were added in solution at a concentration of 0.5 μM and incubated for indicated time points at 37°C, 5% CO_2. After incubation, cells were washed with PBS twice and fixed with 2% paraformaldehyde for 10 min at RT. After fixation, cells were washed twice with PBS and stained with Wheat Germ Agglutinin (WGA) Rhodamine (1:100 dilution in PBS) for 10 min at RT. After staining, cells were washed twice with PBS and subsequently stained with 4',6-diamidino-2-phenylindole (DAPI) (1:5000 dilution in PBS) for 10 min at RT. Cells were washed with PBS twice and transferred to a poly-D-lysine covered μ-Slide 18 well microscopy chamber slide (Ibidi) and centrifuged at 300xg for 15 min at RT.

Confocal microscopy pictures were acquired using an ONI Nanoimager (ONI Oxford) and analysed using ImageJ software.

2.5.6 Gene knockout assay

Cells were plated at a concentration of $2*10^5$ cells/ml on a 24-well plate in 0.5 ml working volume. The cells were left to settle in the incubator for at least 16h before treatment. The next day, the antibody constructs were added to the appropriate wells and resuspended gently. The plate was returned to the incubator for 24 or 48h incubation.

2.5.6.1 RNA extraction

After incubation time, cells were resuspended, transferred to labelled Eppendorf tubes and stored on ice to stop the transfection. The cells were centrifuged at 4°C for 5 min at 1500 rpm and washed with PBS. The cell pellets were lysed by adding QIAzol™ Lysis Reagent (750 μL/$5*10^6$ cells). After a 5 min incubation time, 20% of the final volume of $CHCl_3$ was added, vortexed and incubated for another 5 min. The Eppendorf tubes were centrifuged at 4°C for 10 min at 12000xg to separate the phases. The aqueous phase was removed with a pipette and transferred to a fresh Eppendorf tube. The same volume of isopropanol and 1 μL of Glycogen Blue was added to precipitate the RNA. After an incubation time of 15 min at room temperature, the RNA was pelleted by centrifuging the sample at 4°C for 15 min at 12000xg. The precipitated RNA is washed twice with 1 ml of 75% EtOH (kept at -20°C). The supernatant was carefully removed and the pellet was briefly air-dried before resuspension in RNase-free water. The RNA concentration and quality were assessed using a NanoDrop Technologies ND-1000 Spectrophotometer by measuring the absorbance at 260 nm (A260). An absorbance of 1 unit at 260 nm corresponds to 40 μg/ml of RNA, provided the measurements are conducted

in water. To ensure reliable quantification, absorbance readings were taken at both 260 nm and 280 nm, as the 260/280 ratio serves as an indicator of nucleic acid purity. A ratio of ~2.0 is generally considered pure for RNA, while a lower ratio may indicate protein contamination.

2.5.6.2 Complementary DNA (cDNA) synthesis

cDNA was generated using the "High-Capacity cDNA Reverse Transcription Kit" from Applied Biosystems with addition of RNAse OUT as RNAse inhibitor. Reaction volumes were reduced to 15 μL. The following is a general protocol for the preparation of the cDNA Mastermix and sample.

1. The 2X Mastermix was prepared by pipetting the following components into an Eppendorf and mixed gently. The tube was placed on ice until further use.

Components	Volume for 1 sample (μL)
10X RT Buffer	1.5
25X dNTP Mix (100 mM)	0.6
10X RT Random primers	1.5
MultiScribe RT	0.75
RNase OUT	0.3
Nuclease-free H_2O	2.85
Total per reaction	7.5

2. 1.5 μg RNA was pipetted into a PCR tube or PCR strip and RNAse free water was added to a volume of 7.5 μL.

3. 7.5 μL of the cDNA Mastermix was added and mixed by gently pipetting up and down.
4. The tubes were closed with appropriate lids and spun down to remove bubbles.
5. Samples were placed on a Veriti Pro thermal cycler and heated to 25°C for 10 min, then to 37°C for 120 min, and further to 85°C for 5 min, before cooling down to 4°C with an indefinite hold at 4°C.
6. After the cDNA synthesis, the tubes were either placed on ice or in the fridge until further use.

2.5.6.3 Quantitative Polymerase Chain Reaction (qPCR)

2.5.6.3.1 qPCR plate preparation

In this project, reverse transcription qPCR (RT-qPCR) analysis was performed using MALAT1 Taqman assays (human Hs00273907_s1, Thermofisher) normalised against GAPDH (human Hs02786624_g1, Thermofisher) as housekeeping gene.

The plates were prepared on ice as the reagents are temperature sensitive.

1. 60 μL RNAse-free water was added to the cDNA samples and controls.
2. Primer aliquots were prepared by pipetting 1 part primer to 4 parts RNAse-free water.

The following instructions are for 384-well PCR plates to make a working reaction volume of 10 μL; when using 96-well PCR plates the working volume is 20 μL.

3. Taqman™ Fast Advanced Mastermix (5 μL) was pipetted into each well.
4. Primer aliquots (2.5 μL) were pipetted into relevant rows/columns as triplicates (housekeeping gene first, then gene of interest)
5. Samples (2.5 μL) were added into relevant rows.
6. Each plate was run with a water control, no-template control and control.

7. The plate is sealed using self-adhesive sealing film for PCR plates.
8. The plate was centrifuged for 2 min at 3000 rpm.

2.5.6.3.2 Running the qPCR plate

The qPCR plates were run on a Biorad CFX 96 with the following programme:

1. Holding stage: 50°C for 2 minutes followed by 95°C for 2 minutes
2. PCR stage: 95°C for 15 seconds followed by 60°C for 30 seconds for 40 cycles

On last cycle, plate will then be cooled to 4°C.

2.5.6.3.3 qPCR data analysis using delta-delta Ct

Relative gene expression of the gene of interest was calculated by utilizing the ΔΔCt method developed by Livak and Schmittgen[99], a formula that calculates the relative fold change in gene expression by assessing the difference between a control and a gene of interest. The formula assumes maximal efficiency of duplication at each cycle, hence it is $2^{-\Delta\Delta Ct}$. ΔCt values were calculated for mean Ct scores for each treatment type to calculate ΔΔCt for the gene of interest.

Chapter 3 Design and synthesis of mAb-NP constructs

3.1 NP studies

This modular system is based on NP with HU, which allow for stable membrane insertion and have demonstrated cytotoxic effects across various cell lines[76]. Although previous work in the group suggested focusing on smaller NPs due to their more pronounced cytotoxicity in studied cell lines[78], this project instead focused on a 6HB-NPx containing two outward-facing hydrophobic moieties. The construct with a targeting moiety was selected in order to explore specific targeting potential in bioconjugation studies. A well-characterised antibody like rtx was selected due to its well-characterized and functional properties in B cell malignancies. The design was adapted from the work by *Lauren Entwistle*, based on a different original strand arrangement used by *Göpfrich et al.*[100]. These modifications enhanced handling efficiency and also allowed the addition of other functional groups (e.g. fluorophores), that further expanded the analytical and functional capabilities of the NP (**Figure 34**).

Further structural modifications were made in the process with the aim of improving functionality. Particularly, the hydrophobic moieties added were positioned at about the same level and slight structural re-adjustments were necessary (**Figure 34**). The L2 and L4 strands were split into two segments and rearranged to enable modifications on their 3' and 5' ends respectively to face outwards from the pore for uniform orientation and function.

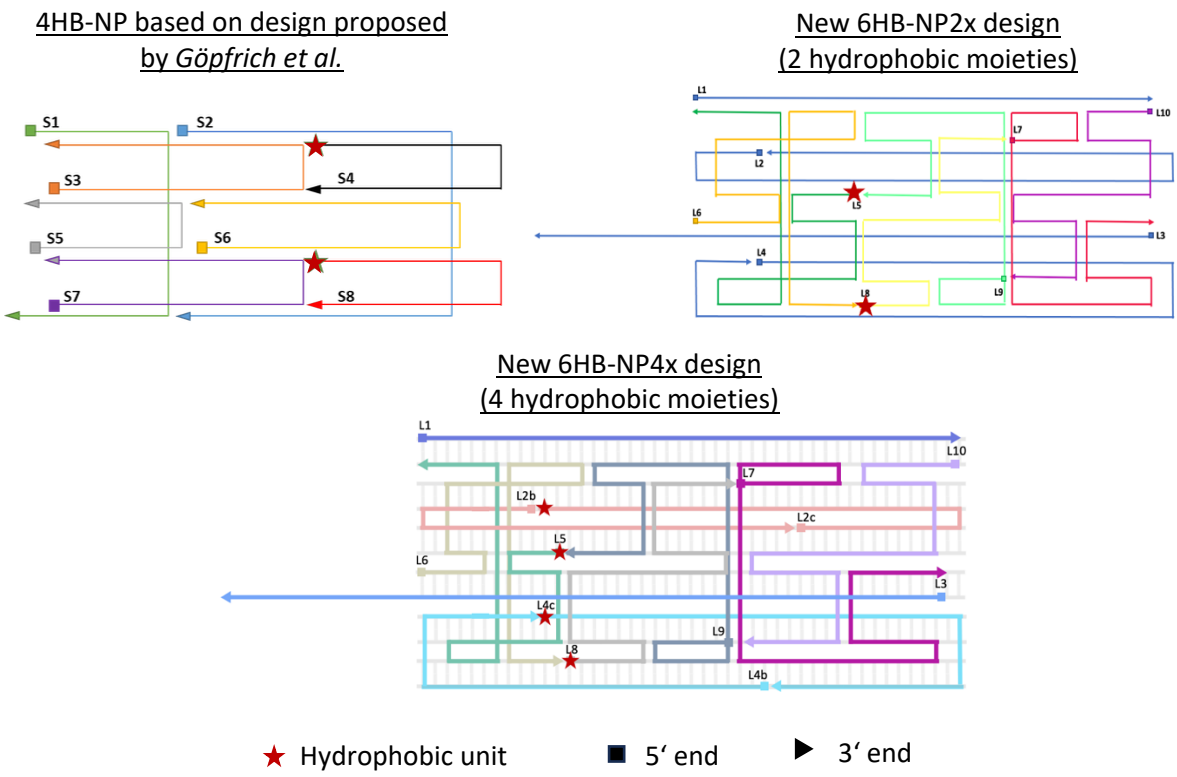

Figure 34 Schematic representation of previously used 4HB-NP[81], newly designed 6HB-NPx with two and four hydrophobic moieties used in this project

To investigate the membrane-spanning efficiency and aggregation behaviour, several hydrophobic modifications were prepared as shown in **Figure 35**, and these are denoted by suffixes to the NP name. For example, NPs modified with two cholesterol moieties are named as 6HB-NP2c, while those with four cholesterol moieties are labelled 6HB-NP4c. Similarly, structures containing one single C18 alkyl chain or a ketal with dual alkyl chains are designated as 6HB-NP1C18 and 6HB-NPk, respectively.

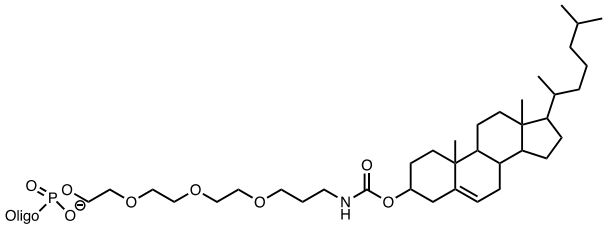

Cholesterol (c)

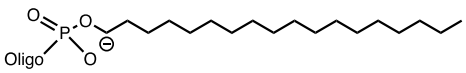

C18 alkyl chain (1C18)

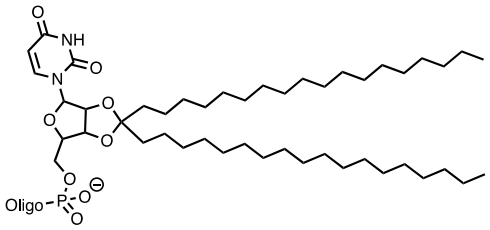

Ketal with dual alkyl chains (k)

Figure 35 Chemical structure of hydrophobic modifications employed in this project

By comparing these modifications, this project aims to identify the optimal hydrophobic moieties for stable and efficient membrane integration. Whereas cholesterol-modified NPs offer a balance between stability and efficient insertion, alkyl chain modifications provide a different option and explore alternative interactions. These insights contribute to the successful design of nanostructures tailored for therapeutic applications, such as targeted B-cell membrane disruption.

3.1.1 Synthesis of cholesterol-modified DNA strands

Due to the low yields expected in the synthesis and purification of oligonucleotides with 3'-end modifications on strands L6 and L9, the cholesterol modification was moved to the 5'-end of strands L5 and L8. Initial synthesis was unsuccessful, as analysis via LC-MS and denaturing PAGE failed to detect the modified DNA. This failure may have been caused by incomplete dissolution of the phosphoramidite in DCM or losses during its transfer from the supplier's bottle to the pear-shaped flask, compatible with the Applied Biosystems Nucleic Acid Synthesis System. To address these issues, a second synthesis was performed with an

extended coupling time of 10 minutes using a different line on Expedite DNA Synthesiser, previously validated during another synthesis. After deprotection and resin cleavage, the products were analysed by denaturing PAGE and LC-MS.

The denaturing PAGE in **Figure 36** showed partial success in cholesterol coupling. There are two clear bands: the lower band represented the unmodified DNA reference, while the upper band indicated a higher molecular weight product consistent with cholesterol-modified DNA. However, there was no consistent pattern in the coupling efficiency, as the detritylation steps looked very similar between the two syntheses.

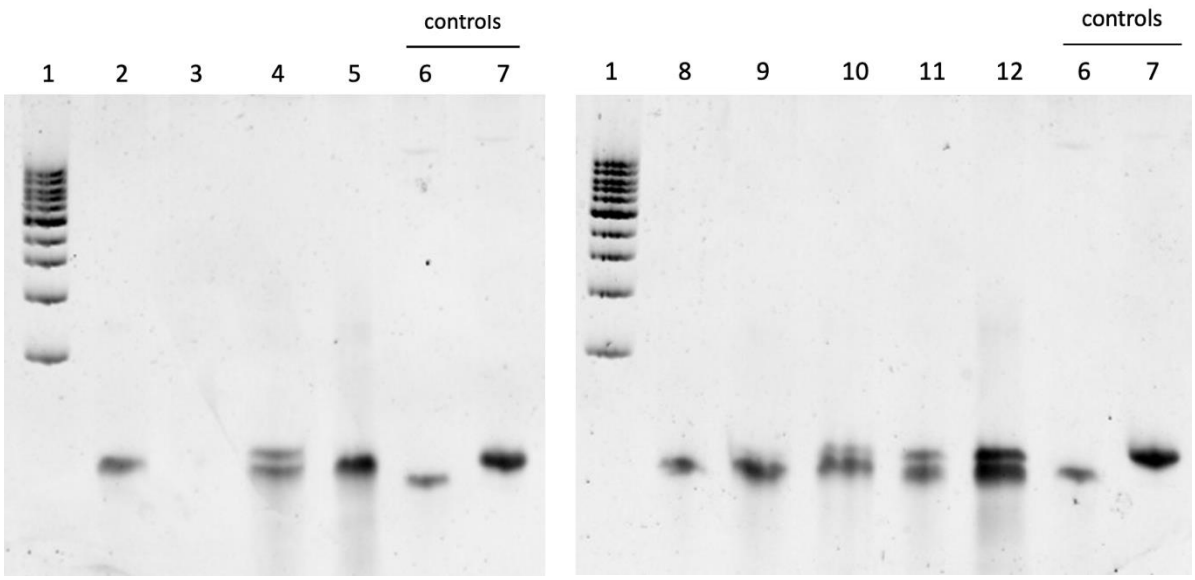

Figure 36 10% denaturing PAGE gels (120 V, 120 min, 1X TBE)

Left: Synthesis of L5c strands; lane 1: 100 bp DNA ladder, lane 2: L5 single strand (unmodified), lane 3: L5c single strand coupling 1, lane 4: L5c single strand coupling 3, lane 5: L5c single strand coupling 5, lane 6: L9 single strand (unmodified, received from IDT), lane 7: L9c single strand (cholesterol-modified, received from IDT)

Right: Synthesis of L8c strands; lane 1: 100 bp DNA ladder, lane 8: L8 single strand (unmodified), lane 9: L8c single strand coupling 2, lane 10: L8c single strand coupling 4, lane 11: L8c single strand coupling 6, lane 12: L8c single strand coupling 7, lane 6: L9 single strand (unmodified, received from IDT), lane 7: L9c single strand (cholesterol-modified, received from IDT)

LC-MS analysis using a gradient from 5% to 40% acetonitrile in 20 mM TEAA did not elute the cholesterol-modified DNA, suggesting that the presence of the hydrophobic tag required a change in the method. After several attempts with various buffer systems, a reliable purification method of cholesterol-modified oligonucleotides was established. A revised method, using a gradient from 5% to 100% acetonitrile over 15 minutes at a flow rate of 0.250 mL/min, successfully eluted the expected product (**Figures 37 and 38**). The use of this acetonitrile gradient is particularly suitable for hydrophobically modified oligonucleotides as it gradually increases the solvent's elution strength and therefore allows efficient separation based on hydrophobic interaction.

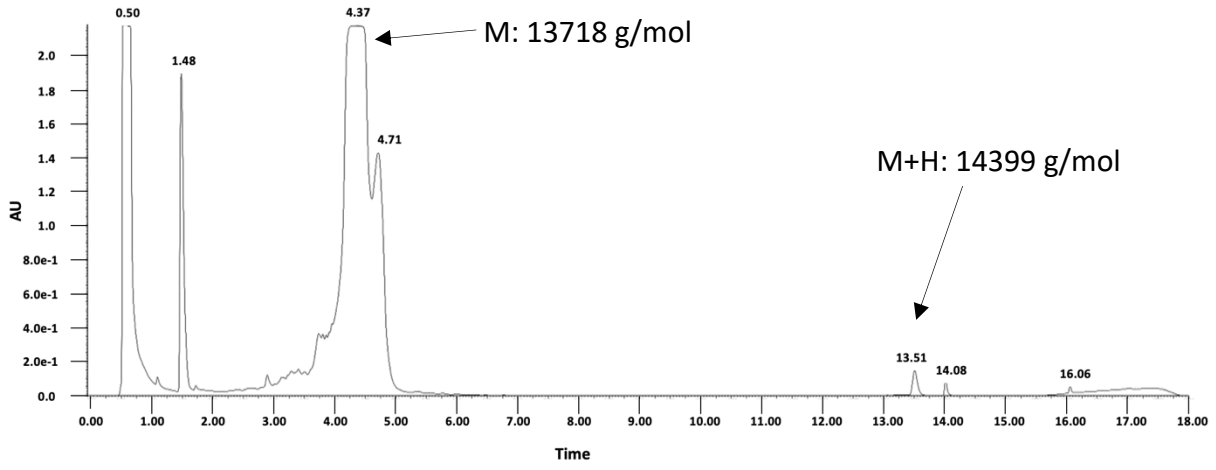

Figure 37 UV-Trace of LC-MS for single strand L5c coupling 3, Monoisotopic mass L5: 13718 g/mol, Monoisotopic mass L5c: 14398 g/mol

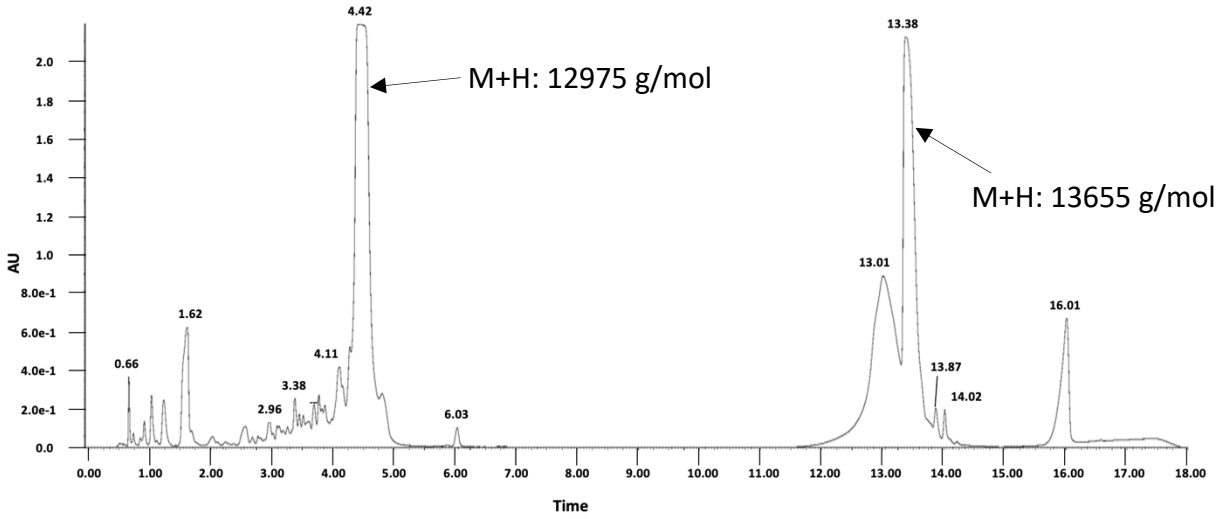

Figure 38 UV-Trace of LC-MS for single strand L8c coupling 6, Monoisotopic mass L8: 12974 g/mol, Monoisotopic mass L8c: 13654 g/mol

Unfortunately, the HPLC fraction collector had a delay between the displayed fraction and the actual collection point, leading to the collection of incorrect fractions and significantly reducing the yield. Fortunately, collaboration within the OLIGOMED network enabled the acquisition of these oligonucleotides through Quentin Vicentini at AstraZeneca, who synthesised and purified them efficiently in one large batch. This collaboration ensured that high-quality cholesterol-modified oligonucleotides would be available for subsequent experiments.

3.1.2 Synthesis of BCN-modified DNA strands as capture DNA

Another component of the NP system is the capture DNA strand (C1) designed with a 5'-BCN modification enabling SPAAC, commonly known as click chemistry. Allowing the effective conjugation of the NP to the linker unit via its terminal azide. Initially, a 15-base oligonucleotide was synthesised and labelled at the 5'-end using a commercially available BCN CE-phosphoramidite. The product was then purified using Glen-Pak™ DNA Purification

Cartridges and analysed by LC-MS to verify its purity and confirm the presence of the modified DNA. However, the gradient applied (5% to 40% acetonitrile in 20 mM TEAA) detected only unmodified DNA, with no peaks corresponding to the modified strand. A repeated synthesis under identical conditions, but with an extended coupling time did not provide the desired product either.

After reviewing alternative methods for obtaining BCN-modified oligonucleotides, a new approach was used (outlined in **Figure 39**). In this method, the oligonucleotides were first synthesised and finally coupled to a 5'-TFA-Amino-Modifier C6 CE phosphoramidite. The conditions were adjusted from the supplier's instruction to a 0.2 M dilution, extending the coupling time to 10 min and omitting the capping step during synthesis. After cleavage and deprotection in ammonium hydroxide, the resulting oligonucleotides carried a terminal amino group (NH_2-DNA), as confirmed by LC-MS. The next step was to functionalise NH_2-DNA with a BCN-NHS ester under standard coupling conditions for 5 hours to afford the BCN-modified oligonucleotide (BCN-DNA).

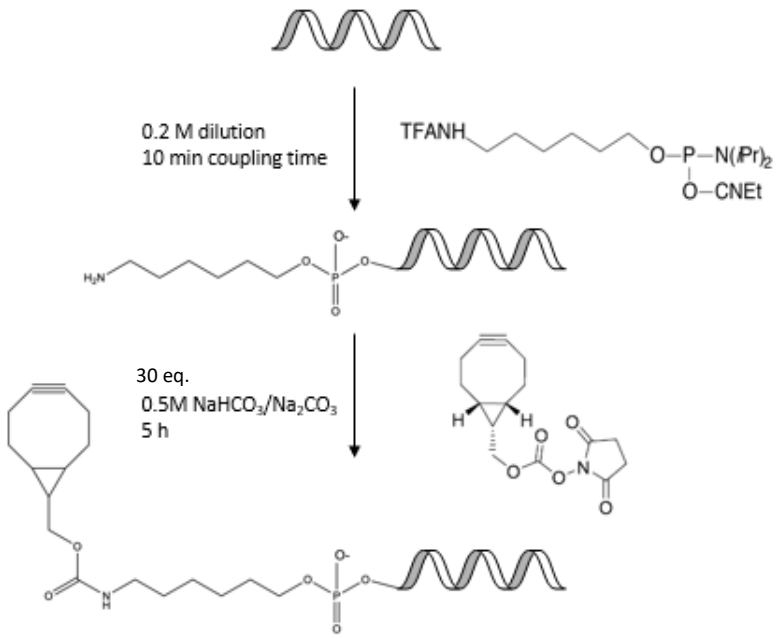

Figure 39 Schematic outline of BCN-DNA synthesis. The process begins with the modification of the oligonucleotide using a 5'-TFA-Amino-Modifier C6 phosphoramidite, introducing a terminal amino group. This amino group is subsequently reacted with a BCN-NHS ester to form a BCN-modified oligonucleotide.

Successful coupling was confirmed by LC-MS, using a gradient from 5% to 100% acetonitrile in 20 mM TEAA over 15 minutes at a flow rate of 0.250 mL/min. No peaks corresponding to NH_2-DNA were detected in the chromatogram, suggesting that the coupling reaction was quantitative (**Appendix 3**). To purify BCN-DNA from truncated and uncoupled strands, we utilised a C18 column with a gradient from 5% to 95% methanol in 8.6 mM TEA and 100 mM HFIP over 22 minutes at a flow rate of 0.800 mL/min, effectively isolating the pure BCN-DNA (**Appendix 4**).

Adjustments to the analytical gradient for detecting hydrophobic DNA modifications were introduced at a later stage, suggesting that earlier syntheses using 5'-BCN CE-

phosphoramidite might have been successful but remained undetected due to inappropriate gradient conditions. However, collaborators at the Research Institutes of Sweden (RISE, Sweden) consistently reported close to 0% yields with 5'-BCN CE-phosphoramidites, reinforcing the likelihood the likelihood that initial attempts were indeed unsuccessful.

Two different oligonucleotide strands which have 5'-BCN modifications according to **Appendix 2**, were synthesised in this study. The efficiency of phosphoramidite coupling varied significantly between sequences. While the 'anti-L10' sequence demonstrated highly efficient coupling during the synthesis, much lower coupling efficiencies of the 'C1' sequence have been observed. The presented variability highlights that the oligonucleotide sequence plays an important role on the conjugation efficiency of chemical modifications. For instance, some nucleotide sequences may hinder the accessibility of reactive sites or affect the local microenvironment in a way that impacts coupling efficiency. Repeated sequences, such as homopolymeric runs, can lead to synthesis errors like slippage or incomplete elongation, while GC-rich regions are prone to forming stable secondary structures (e.g. hairpins or duplexes) that physically block reactive sites. Additionally, purines such as adenine and guanine, due to their bulkier structures, pose steric hindrance, especially when present in consecutive stretches, which can further reduce coupling yields. The choice and efficiency of base-protecting groups also plays a crucial role, for instance bulky groups like benzoyl (for adenine) or isobutyryl (for guanine) may be more difficult to remove completely and can interfere with downstream reactions.

3.1.3 Formation and characterisation of NPs

The formation of NPs has been previously investigated[101, 102], confirming successful assembly in various buffer systems and biological media. Since the NP of interest (6HB-NPx) were newly

designed, preliminary studies on their assembly were required and performed initially without hydrophobic modifications. Phosphate-buffered saline (PBS) was identified as the optimal medium for stable nanostructure formation, outperforming TBE buffer.

To confirm successful assembly, a polyacrylamide gel (**Figure 40**) was loaded with single-stranded oligonucleotides of varying lengths that were used to construct the NPs, along with a positive control, the 4-helix bundle NP, as studied by Joanna Fish and Jianing Zhang[81, 102]. A 6-helix bundle nanopore (6HB-NP), the structure of interest, was also included. The oligonucleotides for 4HB-NPs are labelled S1-S8. A DNA ladder (Invitrogen 100 bp DNA ladder) was run as a control to validate the gel's running and staining of the gel; however, the indicated molecular weight should not be used as a reference for the NP constructs, since secondary and tertiary structures affect their mobility compared to linear single strands. The electromobility shift assay confirmed the successful assembly of unmodified 6HB-NPs (lane 8), as evidenced by the differential migration patterns.

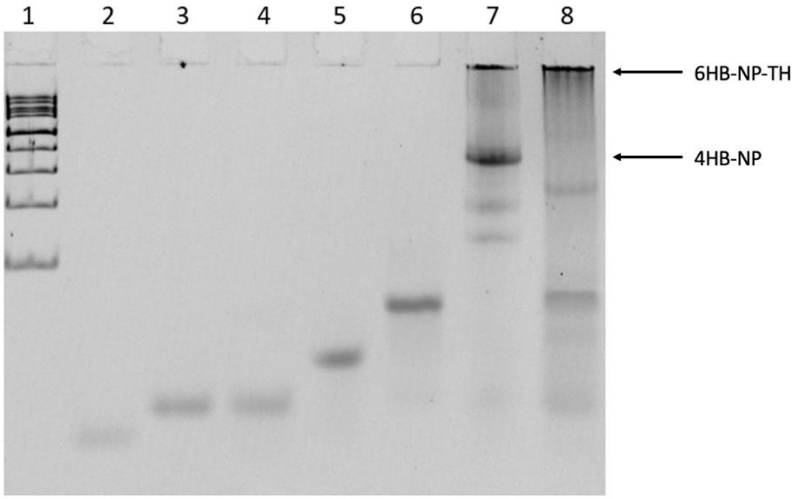

Figure 40 10% native PAGE gel (90V 105 min 1X TB), lane 1: Invitrogen 100 bp DNA ladder, lane 2: S1 single strand 28 b, lane 3: S2 single strand 42 b, lane 4: L10 single strand 42 b, lane 5: L3 single strand 59 b, lane 6: L4 single strand 92 b, lane 7: 4HB-NP, lane 8: 6HB-NP

Following verification of the general assembly of the NPs, the hydrophobically modified nanostructures were also assembled and analysed using an electromobility shift assay on a 2% agarose gel with 11 mM $MgCl_2$, run at 55V for 120 minutes (**Figure 41A**). As expected, lane 5, loaded with the unmodified 6HB-NP, demonstrates a shift toward the cathode, reflecting changes in charge and size relative to the single strands in lanes 2-4. This shift in lane 5 provides a baseline for understanding how structural modifications impact the NP's charge and mobility in the electrophoretic field. Interestingly, the modified NPs containing two cholesterol moieties 6HB-NP2c (lane 6) did not present a significant shift in migration compared to the unmodified 6HB-NP, which could indicate that the cholesterol moieties, despite being hydrophobic, have minimal impact on the overall charge and size of the structure. However, the presence of a faint streaking pattern indicates that the hydrophobic moieties interact with the agarose matrix or are partially retained, which aligns with previously reported results in the literature[73, 76, 78, 103]. This observation may reflect a slight aggregation tendency or a unique interaction of the cholesterol-modified NPs with the gel matrix, possibly because of transient self-associations between hydrophobic groups. These interactions may affect the stability and homogeneity of the NPs, which is critical in their applications toward targeting cell membranes.

In contrast, the NPs modified with single (6HB-NP1C18) and double alkyl chains (6HB-NPk) in lanes 7 and 8 respectively showed both a noticeable band shift and streaking patterns. This increased streaking may suggest that alkyl chain modifications promote stronger or more varied interactions with the agarose, possibly due to increased hydrophobicity and flexibility of the alkyl chains compared to cholesterol. The aggregation observed could pinpoint a potential limitation, as excessive aggregation in physiological environments could impact the

NPs' ability to stably insert into cell membranes or interfere with their delivery and targeting efficiency.

Indeed, the NPs modified with four cholesterol moieties, 6HB-NP4c, loaded in lane 9, migrated more uniformly and further towards the cathode compared to both the 2-cholesterol construct and the 92mer in lane 4 (**Figure 41B**). This observation highlights that electrophoretic mobility in an EMSA is not solely dependent on size, but also on shape, compactness, and charge distribution of the structure. The 6HB-NP4c, which does not contain any 92mer strands, appears to adopt a more compact conformation, facilitating faster migration through the gel matrix. The addition of two extra cholesterol units likely enhances hydrophobic interactions within the construct, contributing to a tighter packing of the DNA strands and reduced structural fraying.

This behavior aligns with findings from *Ohmann et al.*, who demonstrated that cholesterol-modified DNA nanostructures exhibit sequence-dependent aggregation, and that increased cholesterol content can promote more compact and stable assemblies[104]. Furthermore, *Langecker et al.* reported that hydrophobic modifications, such as cholesterol, can induce hydrophobic collapse in DNA nanostructures[73], leading to enhanced structural integrity and uniformity. These studies support the notion that the incorporation of additional cholesterol moieties can enhance the compactness and stability of DNA nanostructures, thereby influencing their electrophoretic mobility.

The sharp, streak-free band observed for 6HB-NP4c supports this, suggesting improved structural integrity and reduced aggregation. This increase in compactness and stability, coupled with efficient membrane anchoring capabilities, makes the 4-cholesterol variant a promising candidate for applications requiring robust and sustained membrane insertion.

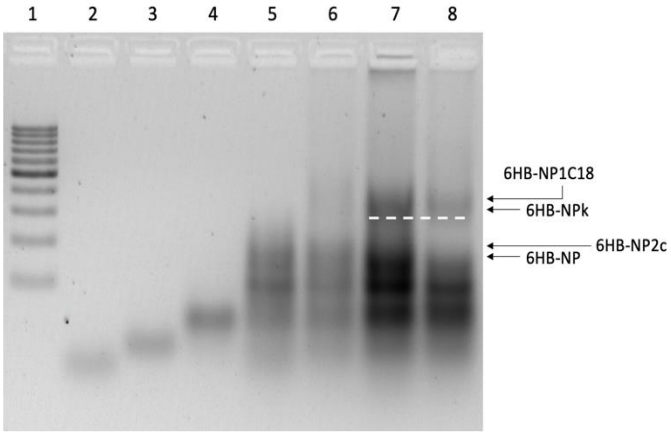

Figure 41A 2% agarose gel (55V 120 min 1X TB), lane 1: 100 bp DNA ladder, lane 2: L10 single strand 42 b, lane 3: L3 single strand 59 b, lane 4: L2 single strand 92 b, lane 5: 6HB-NP, lane 6: 6HB-NP2c, lane 7: 6HB-NPk, lane 8: 6HB-NP1C18

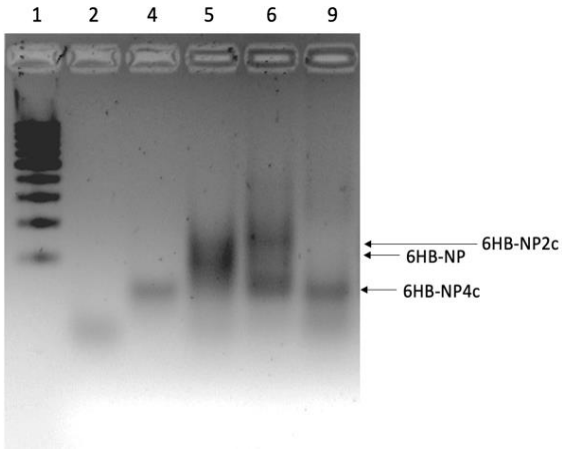

Figure 41B 2% agarose gel (55V 120 min 1X TB), lane 1: 100 bp DNA ladder, lane 2: L10 single strand 42 b, lane 4: L2 single strand 92 b, lane 5: 6HB-NP, lane 6: 6HB-NP2c, lane 9: 6HB-NP4c

These results also raise questions about the balance of hydrophobic modification and the stability of NPs. Compared with the alkyl-modified variants, the cholesterol-modified NPs showed much less aggregation and streaking, which indicate that cholesterol might be a preferable choice for our intended application. The present work explored how variable hydrophobic moieties impacted the NP behaviour and additionally provides insights into the optimal hydrophobic modifications for stable and efficient membrane insertion.

3.2 From synthesis to assembly: a modular approach to antibody-nanopore conjugates

The group previously established a protocol for synthesising mAb-oligonucleotide conjugates by targeting lysine residues on the antibody[81]. This protocol involved a two-step reaction: first, the addition-elimination of an azido-pegylated-NHS ester to the terminal amino group, followed by an azide-alkyne cycloaddition with alkyne-modified oligonucleotides, as illustrated in **Figure 42**.

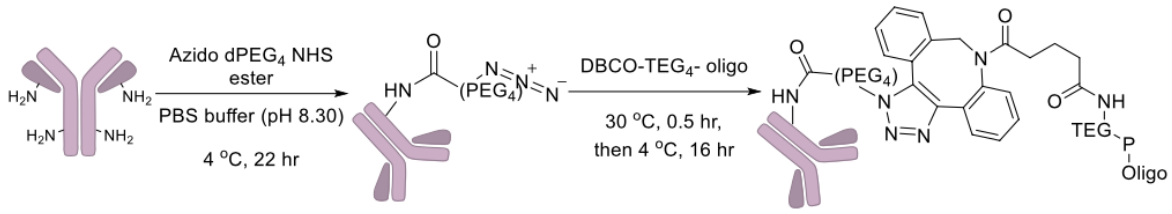

Figure 42 Schematic synthetic route for mAb-oligonucleotide conjugation targeting lysine residues using an azido-dPEG$_4$-NHS ester. The resulting azide-groups are reacted with DBCO-modified oligonucleotides via SPAAC. Reproduced with permission of the rights holder[81].

However, this approach led to non-site-specific conjugation, and cell-binding assays demonstrated reduced binding affinity to the CD20 receptor compared to the unconjugated rtx[3]. To address these limitations, this project adopts an improved method for mAb-NP conjugation reported by *Bahou et al.*[97] enabling high site-specificity alterations (**Figure 43**). This approach targets interchain disulfides bonds located in the junctional region of the mAb, avoiding interference with its binding sites and preserving binding affinity.

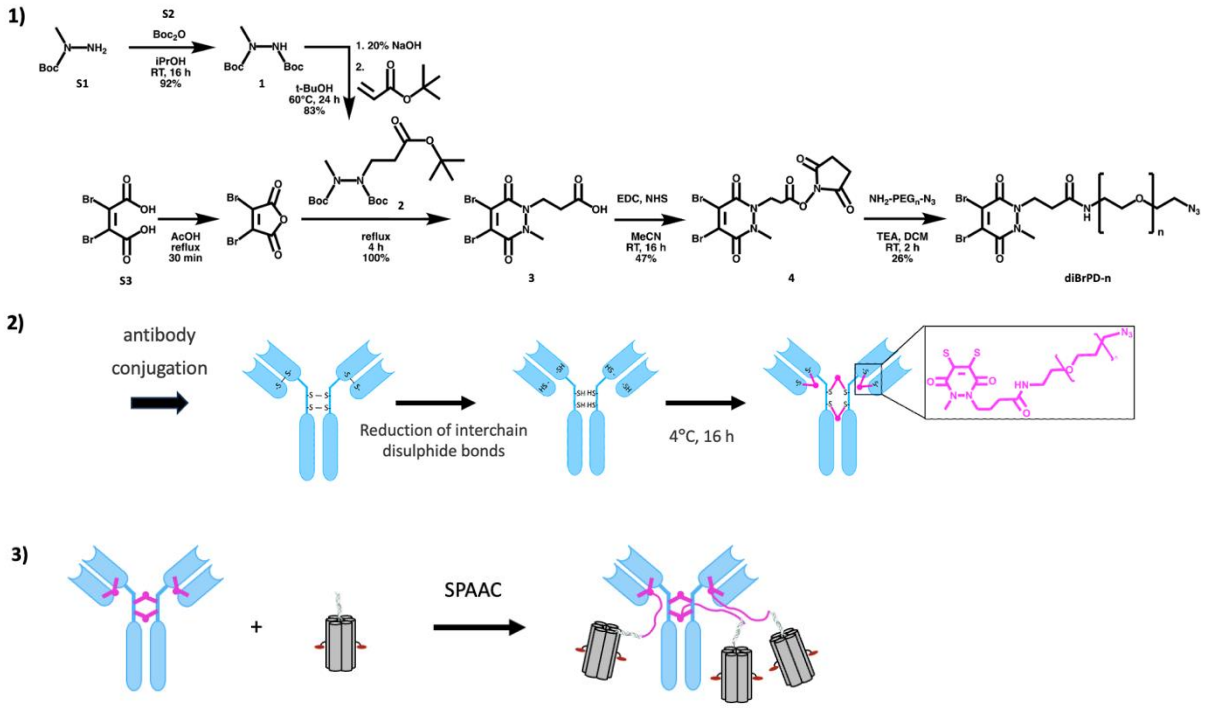

Figure 43 Optimised synthetic route for mAb-oligonucleotide conjugation via disulphide bonds. A diBrPD-linker with a terminal azide was synthesised through a five-step process and subsequently used for the rebridging of reduced interchain disulfides. The terminal azide of the linker was then conjugated to BCN-containing NPs through SPAAC.

3.2.1 Synthesis of diBrPD-linkers for antibody-disulphide rebridging

Synthesis of diBrPD-linker was conducted in a five-step reaction. Each step was carefully optimised to ensure maximum yield and purities. The linker includes a flexible PEG chain and a terminal azide group which is specifically designed for bioorthogonal conjugation via SPAAC. In this project, two PEG lengths were selected based on the commercial availability of starting materials. The final products, diBrPD-8 and diBrPD-23, correspond to PEG chains with 8 and 23 repeating units, respectively.

3.2.1.1 Synthesis of di-tert-butyl-1-methylhydrazine-1,2-dicarboxylate (compound 1)

In the reported method[97], methyl hydrazine was used as starting material; however, since it was not commercially available, 1-Boc-1-methylhydrazine was chosen as an alternative. In the first step this compound was reacted with di-tert-butyl dicarbonate in order to form a Boc-protected amine, yielding di-tert-butyl-1-methylhydrazine-1,2-dicarboxylate (compound 1). The proposed flash column chromatography method (0% to 15% EtOAc/PE) was modified to 50% EtOAc which successfully isolated the desired product. This step was highly efficient, as 92% of the desired product was afforded. The reaction conditions were mild, with no signs of decomposition or side reactions. Flash column chromatography was used with an optimised solvent gradient to ensure efficient purification. Analytical data confirmed the successful formation of the expected product with no impurities.

3.2.1.2 Synthesis of di-tert-butyl-1-(3-(tert-butoxy)-3-oxopropyl)-2-methylhydrazine-1,2-dicarboxylate (compound 2)

The synthesis step involved the Michael addition of tert-butyl acrylate to compound 1. Initial attempts using the conditions proposed in the protocol were unsuccessful, failing to synthesise compound 2. Several test reactions, while optimizing conditions to an anhydrous environment, led to the establishment of a successful protocol. Compound 1 was dissolved in ^{t}BuOH and stirred for 10 min under nitrogen. Instead of the initially suggested 10% NaOH solution, a freshly prepared 20% NaOH solution was added, and the reaction mixture was stirred for 30 minutes instead of 10 minutes. Increasing the base concentration and extending reaction time improved the yield and reaction completeness. However, the reaction required careful monitoring to prevent overreaction or degradation. The reaction also demonstrated high selectivity, as no side products were observed in the NMR analysis. After purification *via*

flash column chromatography in 20% EtOAc:PE analytical data confirmed the successful formation of the desired product with no impurities.

3.2.1.3 Synthesis of 3-(4,5-Dibromo-2-methyl-3,6-dioxo-3,6-dihydropyridazin-1(2H)-yl)propanoic acid (compound 3)

Dibromomaleic acid was heated under reflux in AcOH for 30 min to form 3,4-dibromofuran-2,5-dione for the synthesis of compound 3. The previously synthesised compound 2 was then added and the reaction mixture was stirred under reflux for another 4 hours. The reproducibility of this reaction was challenging as not all performed reactions showed the same result. In favourable cases, the reaction was quantitative, leaving no starting material or side products and no purification was needed. However, in other cases, purification was required using flash column chromatography with a solvent system of EA containing 1% AcOH.

The presence of acid in the purification process led to product streaking across multiple fractions. The drying process was therefore labour-intensive and resulted in significant product loss with overall lower yields. While reactions that proceeded quantitatively were efficient, cases requiring purification demonstrated the limitations of the solvent system. The use of preparative HPLC could potentially optimize the purification process to achieve cleaner separation. Nevertheless, structural analysis confirmed the successful formation of the desired product.

3.2.1.4 Synthesis of 2,5-Dioxopyrrolidin-1-yl 3-(4,5-dibromo-2-methyl-3,6-dioxo-3,6-dihydropyridazin-1(2H)-yl)propanoate (compound 4)

This step aimed for the synthesis of a stable NHS-ester derivative, specifically 2,5-dioxopyrrolidin-1-yl-3-(4,5-dibromo-2-methyl-3,6-dioxo-3,6-dihydropyridazin-1(2H)-yl)

propanoate (compound 4). The NHS-ester is essential for effective amide bond formation with primary amines, such as azido-PEG_n-amine in further conjugation reactions.

Small-scale test reactions, carried out as previously described[97], were successful in producing the desired product by dissolving compound 3 in THF on ice, followed by addition of DCC and stirring for 30 minutes. Then, NHS was added and the reaction mixture was stirred at room temperature for 30 hours. Filtration, concentration *in vacuo* and purification using flash column chromatography with 100% EA resulted in the isolation of a pure product.

However, attempts to scale up the reaction resulted in inconsistent results. TLC analysis confirmed the presence of the product, although NMR analysis failed to verify the observations. Crude NMR analysis was conducted to assess the reaction progress prior to purification, but repeated attempts using the same conditions yielded unreliable results. Problems related to handling, such as temperature fluctuations or the use of outdated DCC, were suspected as contributing factors. Despite replacing DCC with a fresh batch, these issues persisted, necessitating a re-evaluation of the approach.

Since the root cause of these inconsistencies could not be identified, alternative methods were pursued. The direct couplings of carboxylic acids with primary amines were initated using two common strategies: HATU-mediated coupling[105] and EDC/HOBt-mediated coupling[106] as described in the literature. Test reactions using methyl-6-aminohexanoate hydrochloride as a model amine were conducted to evaluate the efficiency of these methods. HATU-mediated coupling was performed in DMF using TEA as a base. While TLC analysis revealed several minor spots indicative of intermediate products or side reactions, NMR analysis confirmed that HATU remained attached to the starting material and the desired amide bond was not formed.

EDC-mediated coupling with HOBt as an additive to suppress side reactions, showed more promising results. EDC activated the carboxylic acid, while HOBt facilitated efficient coupling with the test amine. TLC analysis showed fewer spots, suggesting a more complete reaction. Subsequent purification via flash column chromatography isolated the desired product and NMR and mass spectrometry analyses confirmed the findings.

Based on test reactions, the coupling was attempted with O-(2-Aminoethyl)-O'-(2-azidoethyl)pentaethylene glycol as a model azide-functionalised PEG. Unfortunately, this reaction failed to produce the desired product and due to supply limitations of azido-PEG_n-amine compounds, further optimizations were not carried out. Instead, the focus was directed towards the synthesis of the NHS-ester (compound 4).

Following an extensive literature review, reactions were performed to form the NHS ester using TSTU as a coupling agent[107-109]. While this approach successfully produced the desired product, the reaction was not reproducible and failed to achieve significant yields. In an alternative approach, EDC was selected as the carboxyl-activating agent with the addition of NHS. EDC is water soluble, facilitating removal during an aqueous work-up and reducing contamination risks.

In the optimized protocol, compound 3 was reacted with EDC and NHS in an anhydrous solvent system. After aqueous work-up, the crude product was purified by flash column chromatography using 100% EA. This yielded the NHS-ester (compound 4) as a light yellow foamy solid with a yield of 21%.

The synthesis of NHS esters is widely recognised as challenging due to their instability, particularly due to their susceptibility to hydrolysis during synthesis and storage. Hydrolysis of NHS esters can easily occur in the presence of moisture or during an aqueous work-up, which leads to reverting to the carboxylic acid and lowering yields significantly. Factors such

as solvent selection, pH control, and reaction time play critical roles in avoiding hydrolysis and optimizing yields.

Reported yields for NHS ester formation from literature vary between 50-90%, depending on substrate, reagents and conditions employed. The 21% yield achieved in this study is lower than the reported numbers, likely due to a combination of factors e.g. hydrolysis during the reaction or purification losses.

Literature procedures often emphasise rigorous drying procedures and controlled pH conditions in order to maximise yields. While the current protocol demonstrated reproducibility and produced a pure product for subsequent conjugation steps, this step could be further optimized in the future to increase overall yields.

3.2.1.5 Synthesis of N-(26-azido-3,6,9,12,15,18,21,24-octaoxahexacosyl)-3-(4,5-dibromo-2-methyl-3,6-dioxo-3,6-dihydropyridazin-1(2H)-yl)propanamide (diBrPD-8) and N-(71-azido-3,6,9,12,15,18,21,24,27,30,33,36,39,42,45,48,51,54,57, 60,63,66,69-tricosaoxahenheptacontyl)-3-(4,5-dibromo-2-methyl-3,6-dioxo-3,6-dihydropyridazin-1(2H)-yl)propanamide (diBrPD-23)

Test reactions were conducted using O-(2-Aminoethyl)-O'-(2-azidoethyl)-pentaethylene glycol (S5) and the NHS-ester (compound 4) under reported conditions[110], using TEA in DMF overnight. Both NMR and LC-MS analysis of the crude reaction mixture confirmed the formation of the desired product. Interestingly, in contrast to the reported literature, the reaction was completed after 2 hours, leaving no detectable starting material. This observation suggests that some structural features of the NHS ester (compound 4) impact the reactivity of the ester, making the coupling more efficient. These results were further

supported by NMR analysis which showed evidence of the rapid and efficient nature of this reaction under the modified conditions.

Purification of the product was challenging, primarily due to poor separation seen on TLC. Flash column chromatography using a silica-to-sample ratio of 100:1 successfully yielded the purified product with a moderate yield of approximately 20%. The presence and purity of the product were verified through NMR and LC-MS analyses, while IR spectroscopy confirmed the presence of the azide group with a characteristic absorption at 2100 cm^{-1} (**see Appendix A.6**).

The same reaction conditions were applied to Azido-dPEG®23-amine, with slight adjustments to the purification solvent system by increasing MeOH concentration from 4% to 7% which afforded the product with a slightly higher yield of 22%. Again, purity of the product was analysed by NMR and LC-MS and confirmed the product's purity. IR spectroscopy validated the presence of the azide group at 2100 cm^{-1} (**see Appendix A.8**).

The higher reactivity observed in these reactions compared to reported conditions may indicate that some specific structural features of the NHS-ester (compound 4) contribute to its rapid activation and coupling efficiency. Electron-withdrawing bromine substituents on the pyridazinedione core could be responsible for an increase of the electrophilicity of the activated ester and thus allow faster amide bond formation. Structural effects like these likely explain the reduced reaction time compared to similar NHS-esters reactions described in the literature.

Although the efficiency of the reaction was promising, the overall yields of 20%–22% point towards the challenges associated with product isolation and purification. Poor separation on silica gel which is a common issue for PEGylated compounds, likely contributed to material

losses during chromatography. In fact, the presence of highly polar PEG chains often results in streaking and broader elution bands. Future improvements could involve exploring alternative purification techniques, such as preparative HPLC, to minimise product loss and improve recovery rates.

With the confirmation of the presence of the azide through IR analysis after isolation, this synthesis step demonstrated the compatibility of these reaction conditions with biorthogonal moieties, which is an essential characteristic for subsequent SPAAC applications.

3.2.2 Antibody-linker conjugation: the first step in modular assembly

Site-specific conjugation to our target antibody rtx was conducted after the successful synthesis and isolation of the two diBrPD-linkers with different polyethylene glycol (PEG) lengths: diBrPD-8 and diBrPD-23. These newly synthesized linkers were designed for selective rebridging interchain-disulphide bonds in the antibody structure. Whereas the original conjugation was performed using borate buffered saline (BBS)[97], in this reaction PBS was employed without effects on the yields, showing that buffers can be variable in this case. In addition, it was observed that experiments using pre-dissolved TCEP-HCl as the reducing agent were less efficient. The protocol was further optimized by using freshly prepared TCEP-HCl solutions which significantly improved the reproducibility and yields of the conjugation process.

Successful conjugation was initially confirmed by SDS-PAGE (**Figure 44**) with subtle but notable shifts in antibody mobility. Specifically:

- For the diBrPD-8 conjugate (rtx-diBrPD-8), there is a slight shift observed in the band which is associated with the addition of a lower molecular weight linker.

- A more pronounced shift for the rtx-diBrPD-23 was identified, consistent with the addition of a higher molecular weight linker.

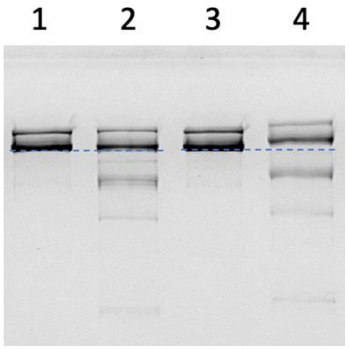

Figure 44 8% non-reducing PAGE gel (300V 45 min 1X SDS-PAGE buffer), lane 1: rituximab unmodified, lane 2: rtx-diBrPD-8, lane 3: rituximab unmodified, lane 4: rtx-diBrPD-23

These observations were further supported by SEC analysis using an HPLC system (**Figure 45**) which showed that conjugated samples eluted earlier compared to the unconjugated antibody. Also, a slightly higher UV signal was observed, which can potentially be attributed to the aromatic dibromopyridazinedione core of the linker.

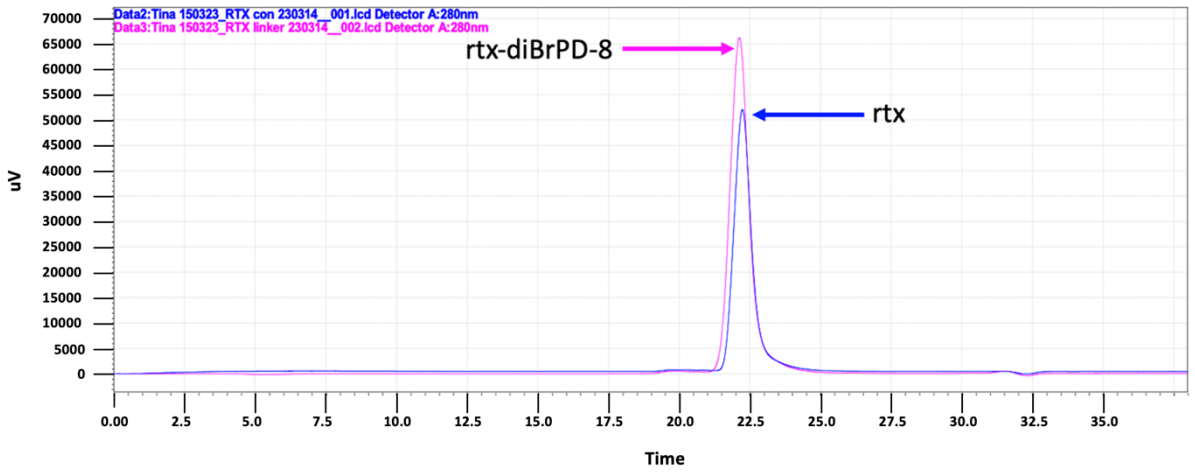

Sample	Retention time	Height
rtx	22.240	51411
rtx-diBrPD-8	22.135	65878

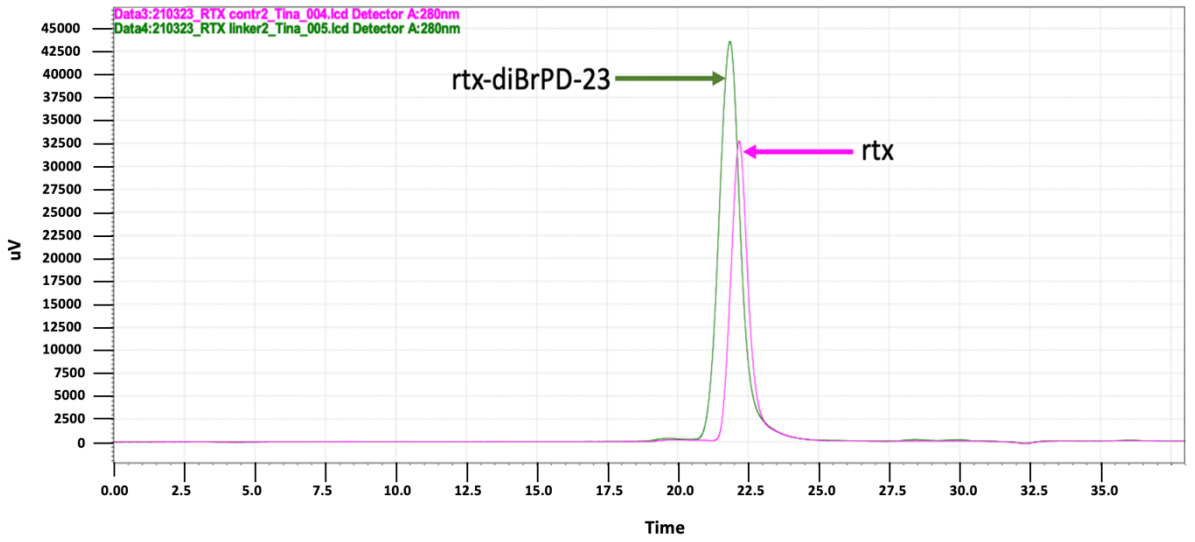

Sample	Retention time	Height
rtx	22.187	32572
rtx-diBrPD-23	21.858	43284

Figure 45 Size exclusion chromatography trace on a HPLC system of rtx-diBrPD-8 in comparison with rtx including the retention time and height (upper graph). Size exclusion chromatography trace on an HPLC system of rtx-diBrPD-23 in comparison with rtx including the retention time and height (lower graph)

A collaboration with RISE allowed for more precise characterisation of the antibody-linker constructs by liquid chromatography-mass spectrometry (LC-MS). From the LC-MS data (**Appendix 4**), it was observed that mainly constructs with three diBrPD linkers attached to the antibody were formed. This observation strongly supports the hypothesis that steric hindrance is a major factor driving the conjugation efficiency in this approach. In particular, when one diBrPD linker occupies a disulphide bridge, the steric bulk of the attached PEG chain potentially obstructs access to adjacent disulphide bonds, thus preventing additional linkers from binding. The LC-MS results not only confirm the specificity of the conjugation reaction but also provide evidence for the observed stoichiometry, pointing to the spatial limitations of the antibody's structure.

3.2.3 Oligonucleotide conjugation via SPAAC

To form oligonucleotide-linker conjugates, SPAAC was initiated between BCN-modified oligonucleotide (C1) and the terminal azide of the diBrPD-linker. Preliminary experiments were performed at low oligonucleotide and linker concentrations with a 1:1 molar ratio which resulted in unsuccessful outcomes. The failure was likely due to poor reaction kinetics, as lower reactant concentrations and equimolar ratios can lead to low coupling efficiency in SPAAC reactions, especially in cases of steric hindrance or with suboptimal solvent systems.

A successful coupling protocol was developed during a research visit at Sixfold Biosciences in London. The reactions were carried out in a 1M TEAA buffer at a final oligonucleotide concentration of 400 µM and with the azide in a fivefold molar excess. These adjustments improved the reaction kinetics and resulted in a quantitative conversion within 4 hours. The resulting linker-oligonucleotide conjugate was then purified by HPLC allowing separation of

the desired product from truncated or unmodified oligonucleotide strands. The final construct was confirmed through LC-MS and verified successful conjugation (**Appendix 7**).

These observations align with reports from the literature that SPAAC reactions proceeded with high efficiency under buffered conditions and excess reactants. TEAA buffer has been used as it has demonstrated to maintain oligonucleotide stability and reaction pH which are critical for successful conjugation[111].

After the successful synthesis and isolation of the oligonucleotide-linker product, the conjugation to rtx was sought using the disulphide-rebridging protocol. This approach was unsuccessful, and it was hypothesised that steric hindrance introduced by the oligonucleotide-linker construct or potential incompatibilities in reaction conditions, prevented efficient binding to the antibody.

Instead, the antibodies were first conjugated to the linker moieties to form rtx-diBrPD-8 and rtx-diBrPD-23 constructs. Subsequently, the linker-modified antibodies were reacted with the BCN-modified C1 oligonucleotide through SPAAC. This strategy proved to be more efficient as it afforded the desired antibody-oligonucleotide conjugates.

The conjugation of rtx-diBrPD-8 and rtx-diBrPD-23 with oligonucleotides was confirmed by SDS-PAGE and SEC using an HPLC system. An 8% SDS-PAGE performed under non-reducing conditions revealed the presence of a heterogeneous mixture with differently labelled antibody species, as evident from multiple distinct shifted bands (**Figure 46A**). These shifts represent the conjugation of different numbers of oligonucleotides (1–3) per antibody molecule, supporting the hypothesis that steric hindrance and spatial constraints limit quantitative conjugation. In a follow-up experiment, efforts were made to push the conjugation reaction towards a homogeneous product by increasing the molar equivalents of oligonucleotides relative to the antibody-linker construct. However, increasing to 80

equivalents of oligonucleotides resulted in constructs bearing higher numbers of oligonucleotides (**Figure 46B**) and a homogeneous mixture with a single construct was not achieved. In conclusion, these findings highlight how steric and spatial hindrances in the antibody structure may prevent uniform attachment, even at high concentrations of oligonucleotides.

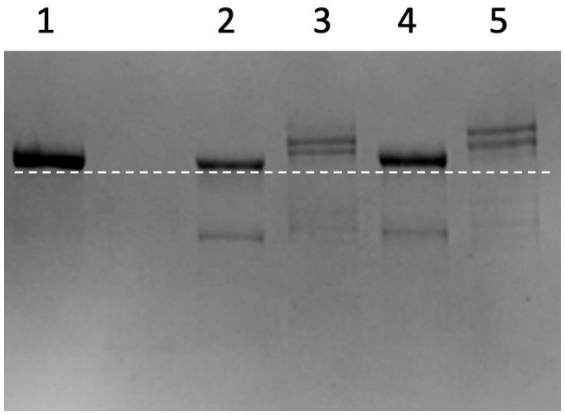

Figure 46A 8% SDS-PAGE under non-reducing conditions (250 V, 30 min), lane 1: rtx, lane 2: rtx-diBrPD-8, lane 3: rtx-diBrPD-8-C1, lane 4: rtx-diBrPD-23, lane 5: rtx-diBrPD-23-C1

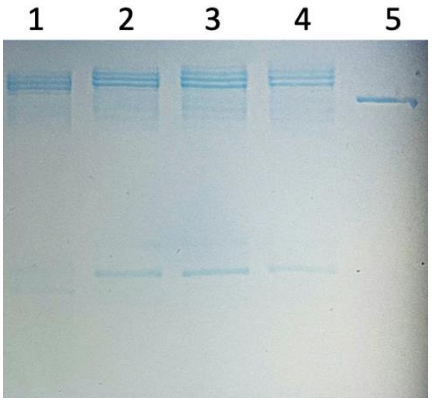

Figure 46B 8% SDS-PAGE under non-reducing conditions (250 V, 30 min), lane 1: rtx-diBrPD-8-C1 10 eq., lane 2: rtx-diBrPD-8-C1 20 eq., lane 3: rtx-diBrPD-8-C1 40 eq., lane 4: rtx-diBrPD-8-C1 80 eq., lane 5: rtx

In contrast, the SEC results presented only one broad peak corresponding to the conjugated products. Poor resolution of distinct antibody-oligonucleotide constructs by the SEC column

may be due to low resolution, especially for constructs of similar hydrodynamic radii. Literature on SEC of antibody conjugates indicates challenges of separating closely related species, especially when the attached moieties contribute minimal differences to the overall molecular size.

Further analysis, in collaboration with RISE, using LC-MS was inconclusive for determining the exact number of oligonucleotides attached to each antibody molecule. The negatively charged phosphate backbone of the oligonucleotides likely interfered with ionization and mass detection, a known limitation in the LC-MS analysis of nucleic acid-protein conjugates. Furthermore, the complex nature of the conjugates with heterogeneous labelling added challenges to spectral deconvolution.

These limitations encountered here are consistent with reported challenges in characterising antibody-oligonucleotide conjugates by mass spectrometry. Previous studies have emphasised the importance of specialised MS methods to overcome such issues[112].

3.2.4 Building the antibody-nanopore conjugate

The next efforts were thus directed towards the assembly of the final antibody-NP conjugates as successful attachment of one to three oligonucleotides to the antibody validated the feasibility of this approach. Two different approaches were chosen to evaluate the kinetics of the conjugation strategy for attachment of nanostructures to the antibody.

1. **NP assembly first approach:** The 6HB-NP construct was assembled with the capture strand C1, forming 6HB-NP-C1. Test reactions confirmed that the BCN-modification is stable under assembling conditions and still reactive in SPAAC. The 6HB-NP-C1 was incubated with rtx-diBrPD-8 to allow the SPAAC reaction affording rtx-NP-C1.

2. **Stepwise SPAAC approach:** Here, C1 oligonucleotide was first conjugated to rtx-diBrPD-8 through SPAAC, forming rtx-diBrPD-8-C1, followed by the addition of pre-assembled 6HB-NP constructs. This mixture was then incubated at 37°C, allowing hybridisation between the DNA overhangs of L3 and C1 attached to the antibody to create rtx-C1-NP.

Characterisation of such large and complex structures had significant limitations using standard analytical techniques. SDS-PAGE was not suitable for characterisation of the constructs as there was no suitable method found to run NP on SDS-PAGE. Native PAGE is not a viable method as antibodies do not migrate through the gel matrix, because of their large size, heterogeneous charge distribution and isoelectric point (~9.1 in the case of rtx). The previously employed SEC method using a Zorbax GF-250 column (4–400 kDa range) was not suitable to separate the formed constructs, which have an estimated molecular weight of ~660 kDa (antibody: 150 kDa; 3 linkers: 3 × 776 Da; 3 NPs: 3 × 170 kDa) and most likely passed through the column without retention.

In the literature, agarose gel electrophoresis with a Histidine-(2-(N-morpholino)ethanesulfonic acid) (HIS/MES) running buffer at pH 6.1 was employed to characterise antibodies[113, 114]. These conditions enable the positively charged antibodies to migrate towards the cathode.

To evaluate detection sensitivity, Coomassie Brilliant Blue and silver staining were tested. Coomassie staining proved to be more sensitive, detecting as little as 0.3 µg protein, compared to 1.25 µg for silver staining. Preliminary runs (**Figure 47, left**) were performed on 2% agarose gels in 30 mM HIS/MES buffer at pH 6.1 running at 100 V for 30 min. Rtx was

loaded in a 1:2 dilution steps starting from 5 ug to 0.078 ug. One gel was stained with Coomassie Brilliant Blue G250, while the other was visualised using silver staining (**Figure 47, right**). Results clearly show that silver staining is less sensitive than Coomassie: the detection limit is 1.25 µg of protein compared to Coomassie which can detect protein quantities as little as 0.3 µg.

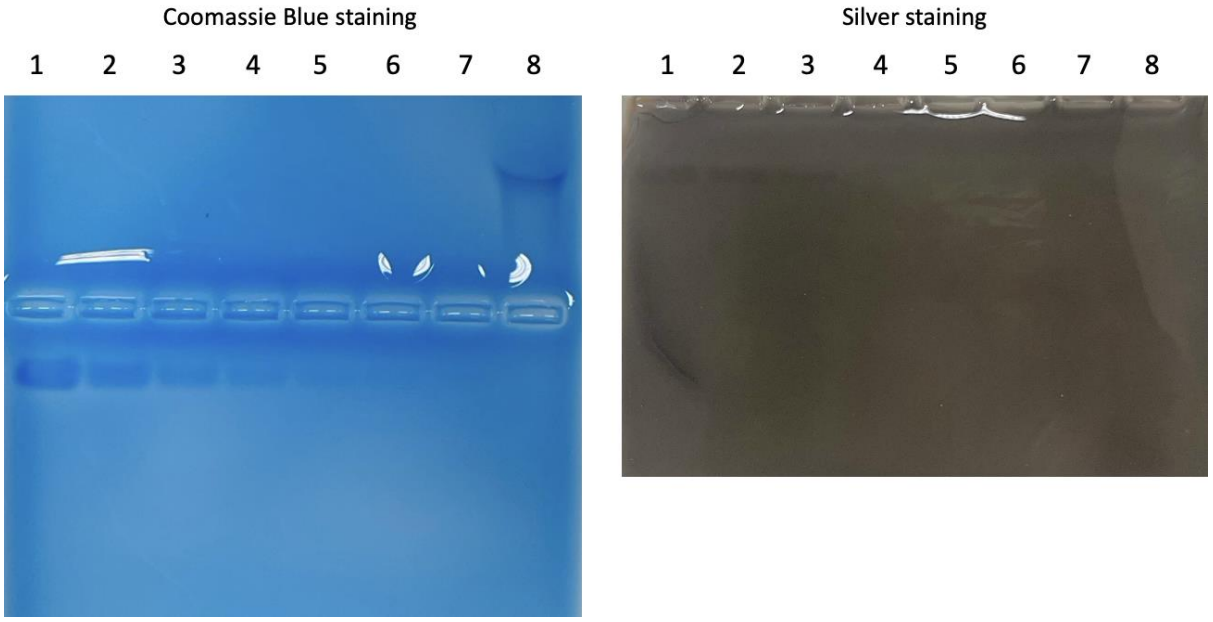

Figure 47 1% agarose gel (100V, 30 min, 30 mM HIS/MES buffer pH 6.1), both gels have the same samples loaded as followed. Lane 1: 5 µg rtx, lane 2: 2.5 µg rtx, lane 3: 1.25 µg rtx, lane 4: 0.63 µg rtx, lane 5: 0.31 µg rtx, lane 6: 0.16 µg rtx, lane 7: 0.08 µg rtx, lane 8: Novex™ Sharp Pre-stained Protein Standard

The desired antibody-NP conjugates were prepared according to previous descriptions on a 1.5 µg scale. After the completion of the reactions, the entire sample was loaded onto an agarose gel and stained by silver staining for visualisation. However, neither the proteins nor the NPs were detectable, since no material was observed on the gels. A major limitation in these experiments was the availability of oligonucleotides, particularly of C1, whose preparation and purification is both labour-intensive and costly. For example, conjugating 1.5

µg of antibody required 40 molar equivalents of NPs, corresponding to 0.4 nmol of oligonucleotides. These practical limitations interfere with the possibility either to scale up reactions or develop optimized conditions.

To overcome these limitations, two highly sensitive staining methods were therefore used Coomassie Blue for proteins and SYBR Gold for DNA. The reactions were run on the same gel and subjected to identical running conditions, with the samples loaded into separate wells. After electrophoresis, the gel was carefully cut into two parts using a scalpel: one portion was stained with SYBR Gold which is used to visualise DNA, while the other part was stained with Coomassie Blue to enable the detection of proteins. The presence of a band in the same position on both gels will strongly indicate successful conjugation. However, SYBR Gold and Coomassie Blue have different detection limits, therefore some bands may only show up on one gel, given the nature and concentration of the conjugate.

Agarose gel electrophoresis (**Figure 48**) provided preliminary evidence for conjugate formation with sensitivity limitations. Coomassie staining showed obvious changes in migration behaviour for rtx-diBrPD-8-C1 (lane 2) compared to unmodified rtx (lane 1), indicating that oligonucleotide attachment altered the antibody's net charge significantly.

In samples where NPs were hybridised to the rtx-diBrPD-8-C1 (lane 4), a streaking pattern was observed which suggests the presence of a heterogeneous mixture of conjugates with varying numbers of NPs attached. On the SYBR Gold-stained gel, lane 4 showed a minor shift compared to lane 3, likely reflecting a slower or less efficient reaction.

In the second approach, where NPC1s were conjugated to the antibody-linker construct through SPAAC, Coomassie staining (lane 3) revealed the presence of unreacted rtx, indicating

incomplete conjugation. In the SYBR Gold-stained gel, lane 3 migrated further toward the cathode compared to the NP reference in lane 5 potentially accountable to increased negative charges caused by multiple NPs attached to the antibody. This indicated the formation of antibody-NP conjugates with larger size and multiple DNA nanostructures attached accounting for an increase in electromobility towards the cathode. Future optimisation, such as increasing the incubation time, the molar excess of NPs or refining reaction conditions, may enhance the conjugation efficiency.

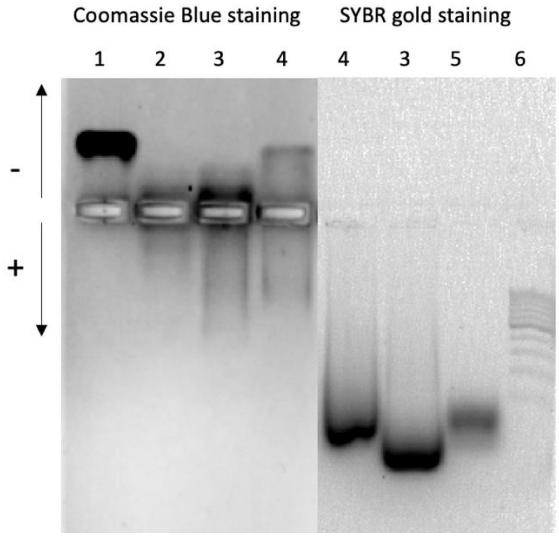

Figure 48 2% agarose gel (60 V, 90 min, 4°C, 30 mM HIS/MES buffer pH 6.1). Lane 1: rtx, lane 2: rtx-diBrPD-8-C1, lane 3: rtx-diBrPD-8-C1-NP, lane 4: rtx-diBrPD-8-NPC1, lane 5: NP, lane 6: GeneRuler 100 bp DNA ladder

To further validate the formation of these conjugates, a microscopy experiment was conducted. For this, 6HB-NPx constructs (6HB-NP2c and 6HB-NP4c) were assembled using L10 oligonucleotides labelled with AlexaFluor647 (L10-A647). The stepwise assembly was conducted as described above: conjugation of C1 to the rtx to afford rtx-diBrPD-8-C1 through SPAAC, followed by hybridisation of the NPs to C1. The constructs were then incubated with Ramos cells for 30 minutes at 4°C in order to prevent internalisation. Unbound constructs

were removed through a washing step and an antibody specific for rtx (MB2A4) labelled with AlexaFluor488 was added to the Ramos cells for a 30 min incubation. In a subsequent washing step, unbound antibodies were removed. Fluorescence microscopy (**Figure 49**) showed colocalizing signals for AlexaFluor647 (NPs) and AlexaFluor488 (antibody), confirming successful conjugation of the two components.

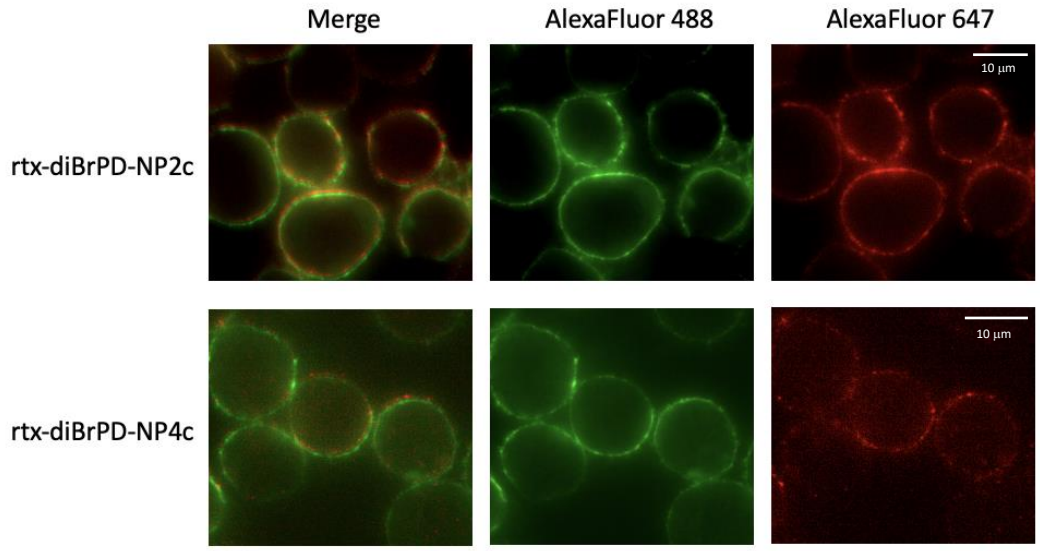

Figure 49 Colocalisation assay of the antibody-nanopore conjugates on Ramos cells. The microscopy images showed overlapping fluorescence signals from AlexaFluor647 (NPs, red) and AlexaFluor488 (antibodies, green) that confirm the co-localisation of the two components and serves as validation for the conjugation process.

This work, even though important, needs further optimization in reaction efficiency along with more viable characterisation methods. Streaking in the gels would suggest polydispersity in the number of NPs bound to each antibody, possibly as a result of steric hindrance or poor reaction conditions. Analytical techniques such as cryo-electron microscopy or native MS could reveal more detailed information on the structure and composition of the conjugates. Additionally, further optimization of staining protocols or the use of more sensitive fluorescence-based methods could even improve the detection and characterisation of such

complex constructs. Herein, preparation and characterization of antibody-NP conjugates have been outlined as a first approach that probably offers a good foundation for their further development. Continued refinement of the assembly step and analytical techniques will enable the production homogeneous and well-characterised constructs.

Chapter 4 Functional characterisation of NPs and antibody constructs

Functional assays were performed to assess the NPs effectiveness and therapeutic potential. This chapter describes the general characterisation of the designed constructs using several *in vitro* assays to evaluate their potential in targeted delivery, cellular uptake and cytotoxic effects. The assays provide insight into its intracellular behaviour and therapeutic potential.

The described assays explore membrane association, internalization kinetics, cytotoxicity and receptor binding. With these outcomes we are able to evaluate if the modular constructs are able to perform efficiently in cell killing and therefore offer a new option as a potential cancer therapeutic. The data in this chapter offers insight into the design and use with a functional readout of the construct's potential and indicating areas of possible optimization.

4.1 Cytotoxicity evaluation of NP constructs

Following the successful assembly of the NPs with different hydrophobic moieties, their cytotoxicity was evaluated *in vitro*. The proposed mechanism of action involves membrane association which disrupts the protective barrier and subsequently induces uncontrolled ion flux across the cell membrane. This ionic imbalance ultimately leads to cell death. A range of assays were employed to determine their suitability for measuring any cytotoxic effects.

4.1.1 Annexin V/Propidium Iodide (PI) assay for apoptosis detection

The Annexin V/PI assay is a widely used method for the detection of apoptotic cells and assessment of membrane integrity. Propidium iodide (PI) is a DNA intercalator that binds to

the cell's DNA in the nucleus upon membrane damage and therefore serves as a marker for late-stage apoptosis or necrosis. In cells with intact cell membranes, phosphatidylserine is located to the inner leaflet of the plasma membrane but flips to the outer surface during apoptosis as a recognition signal for macrophages to induce phagocytosis. Annexin V binds to externalised phosphatidylserine and thus, indicates early apoptosis, while a positive PI signal suggests late apoptosis or necrosis. Data processing included the entire cell population leaving debris out as shown in **Figure 50**.

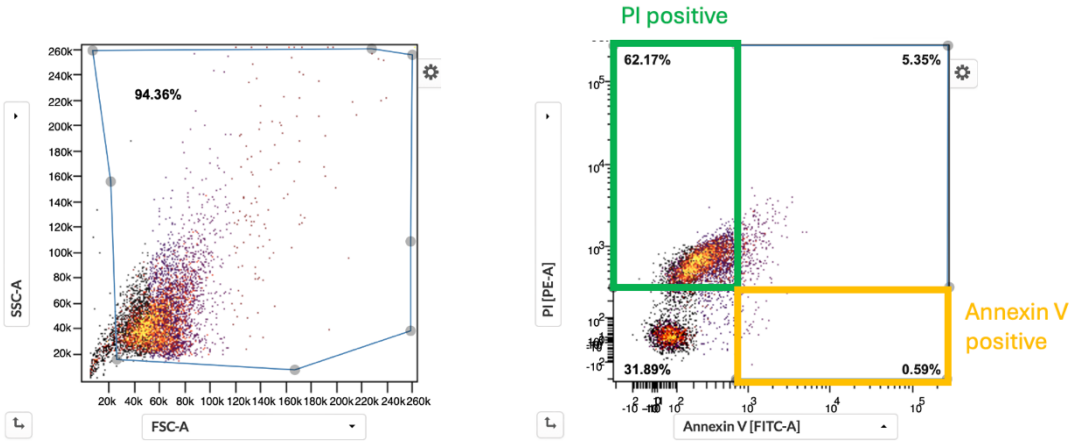

Figure 50 Left: Gating strategy for flow cytometry analysis in the Annexin V/PI assay, excluding cell debris. Right: Distribution of PI-positive (necrotic/late apoptotic) and Annexin V-positive (early apoptotic) cells.

This study involved the cytotoxicity testing of four constructs: 6HB-NP, 6HB-NP2c, 6HB-NP4c and 6HB-NPk. Constructs and Ramos cells were co-cultured at five NP concentrations, diluted in a 1:5 series, under standard conditions (37°C, 5% CO_2) in RPMI supplemented with 10% FCS. Cells were stained with Annexin V/PI and analysed using flow cytometry after 24 and 48 hours of incubation.

Previous studies showed that unmodified NPs had no significant impact on cell viability, as the negatively charged backbone prevents insertion into lipid bilayers like cellular membranes[76]. In this study, unmodified 6HB-NPs were included as a control to measure for background cell death and to confirm that assembly conditions were non-cytotoxic.

A consistently positive PI signal was observed across the dilution series, including in cells treated with unmodified 6HB-NPs (**Figure 51**). This unexpected observation may indicate a potential interference in the assay. Reviewing of the protocol noted that the Annexin V/PI stain was added directly to the samples without any intermediate washing steps. Given that PI binds to DNA, it is hypothesised that PI may have intercalated the DNA nanostructures themselves, rather than exclusively staining nuclear DNA from apoptotic cells. This hypothesis explains the positive PI signal observed in every sample, regardless of treatment which suggests that the Annexin V/PI assay is not suitable for assessing the cytotoxicity of DNA nanostructures like NPs. The structural properties of the nanostructures seem to interfere with PI staining which likely generates false-positive signals and makes the read-out of this assay unreliable for this application.

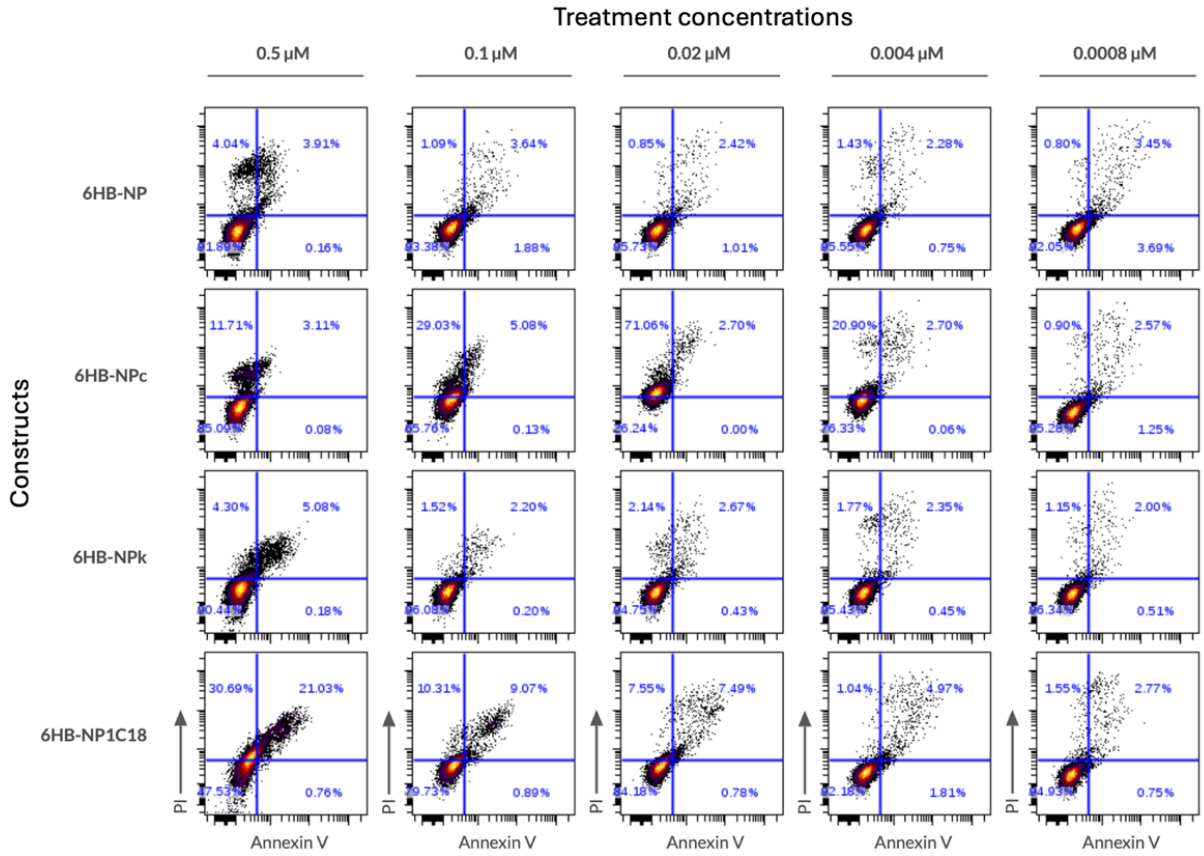

Figure 51 Flow cytometry panels of Annexin V/PI-stained samples. Positive PI signals were detected across all samples, with consistently higher signals in more concentrated samples, suggesting PI intercalation into the NPs. This is further supported by the detection of positive PI signals in unmodified 6HB-NP-treated samples, indicating potential NP staining.

4.1.2 Hypotonic PI assay for apoptosis and cell cycle analysis

The hypotonic PI assay detects apoptotic cell death as well as variations in the cell cycle. This technique involves the lysis of the cell population to expose their nuclear DNA and this DNA is then stained with PI[115]. Through flow cytometry, the fluorescence intensity of PI-stained nuclei is measured which is proportional to the DNA content and identifies apoptotic cells.

Apoptosis causes the fragmentation of nuclear DNA which is measurable through reduced staining and a characteristic sub-G1 peak on the left-hand side of the fluorescence intensity graph. On the other hand, cells in the G2/M phase with higher DNA content, exhibit stronger fluorescent signals and will appear on the right-hand side of the fluorescence intensity graph. This allows for accurate assignment of cell cycle phases and enable identification of any changes in cell proliferation or DNA integrity (**Figure 52**).

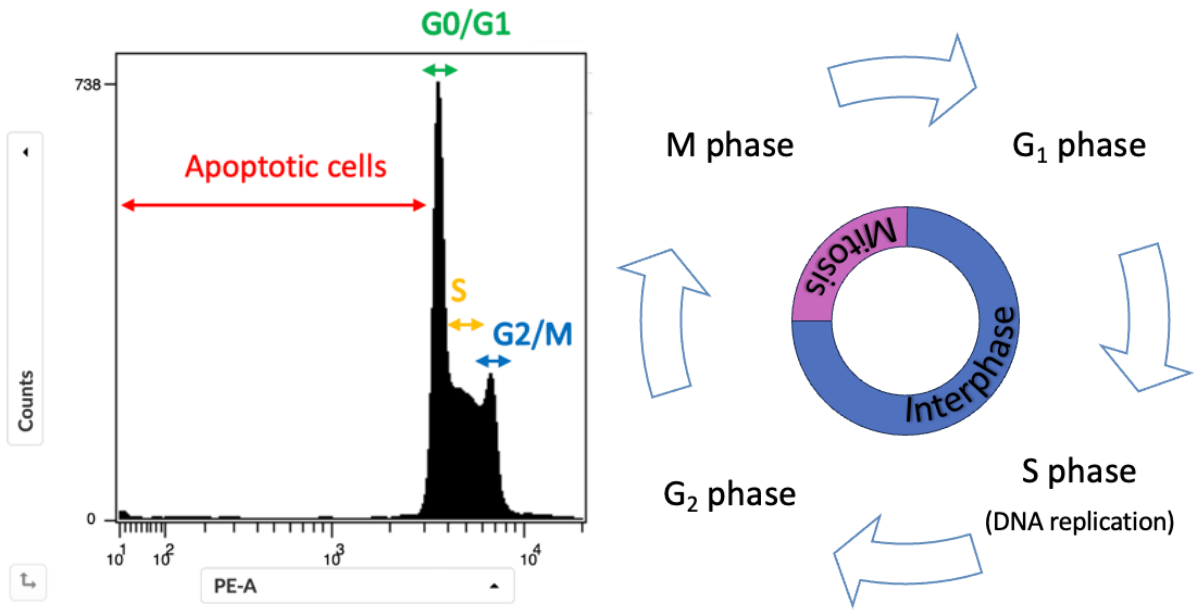

Figure 52 Left: Histogram showing DNA content stained with PI, analysed via flow cytometry. The DNA content in the nucleus is correlated with the respective cell cycle phases. Right: Schematic overview of cell cycle phases

6HB-NP2c-treated samples showed no evidence of apoptotic cell death with the absence of a sub-G1 peak, which indicates that the nanostructures do not induce apoptosis under the tested conditions. However, the data showed a reduced number of cells in the G2 phase, suggesting an impact on cell proliferation (**Figure 53, right panel**). This observation stipulates a potential cell cycle arrest in earlier phases, such as G1 or S, or a delayed progression through the cell cycle.

A reduced number of cells in G2 phase may indicate that the 6HB-NP2cs disrupt cellular processes necessary for the preparation for mitosis. Such effects could be attributed to structural interactions with the cell membrane or indirect impacts on signalling pathways that regulate cell cycle progression. Further investigations are needed to confirm whether these observations result from specific 6HB-NP2c activities or from secondary effects related to the experimental setup.

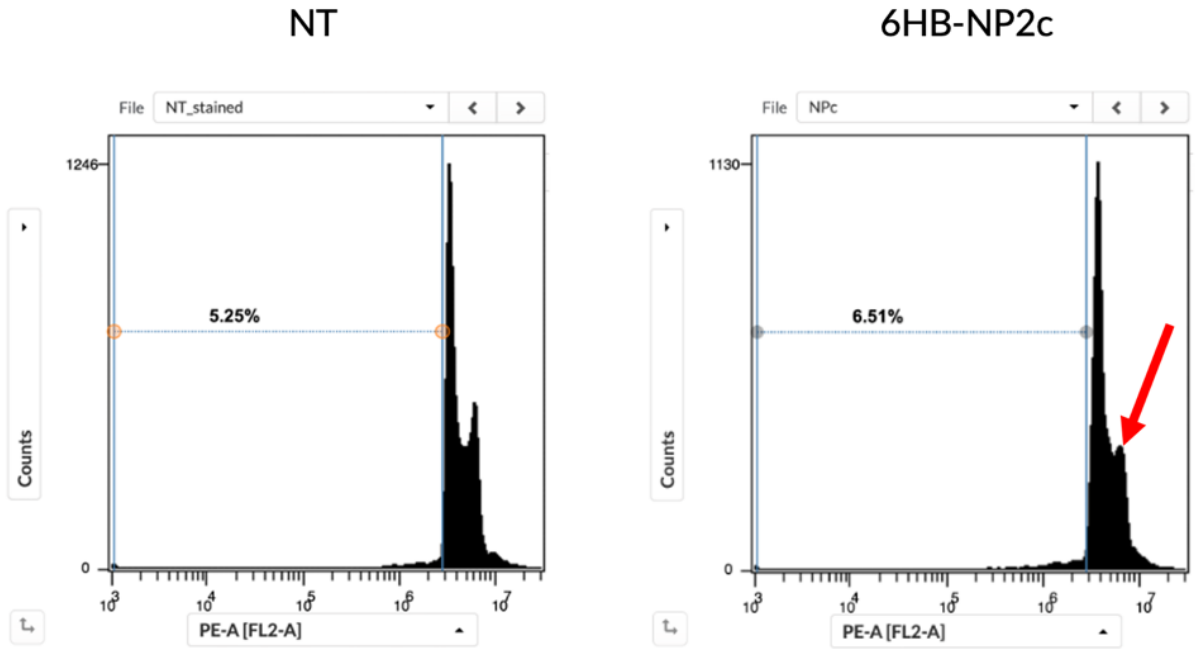

Figure 53 Flow cytometry histograms of hypotonic PI assay. Left: Non-treated (NT) control cells showing 5.25% sub-G1 population, indicating baseline levels of DNA fragmentation. Right: Cells treated with 6HB-NP2c after 24 hours, showing an increased sub-G1 population of 6.51% and a reduced population in G2/M-phase (highlighted by the red arrow), suggesting potential effects on cell proliferation.

4.1.3 Trypan Blue exclusion assay for cell viability

The Trypan Blue dye exclusion test is a common approach to measure cell viability among many approaches to assess cytotoxicity. Damaged cell membranes allow Trypan Blue to enter

and stain cells, whereas healthy cells are impermeable to the dye which can be quickly assessed under a microscope. However, the permeability of the membrane to the dye occurs only when significant disintegration of the membrane proceeded at a later stage of cell death. The simplicity, cost-effectiveness and reliability are the key advantages of this method. However, manual counting of cells introduces the potential for human error and may not be the most time-efficient option for analysing a large number of samples.

This assay studied the effects of 6HB-NPs on multiple cell lines, including Daudi and Ramos cells as well as peripheral blood mononuclear cells (PBMCs), at two different concentrations. The first experiments measured how the constructs affected cell viability after 24-hour incubation. Further experiments investigated the longer-term effects, using extended incubation periods of 48 and 72 hours, thus offering a better understanding of the sustained impact of NPs over time. However, in some cases, Ramos cells exhibited significant cell death before assessments could be performed and led to missing data for certain time points. The short lifespan of PBMCs, generally less than 48h hours under standard culture conditions, limited the studies to 24-hour and 48-hour time points.

First investigations of 6HB-NP2c effects in Ramos cells revealed a promising data showing a 30% reduction in cell viability at a concentration of 0.5 μM (**Figure 54A**) compared to NT controls (**Figure 54B**). However, we could observe that unmodified 6HB-NP construct also caused a statistically non-significant viability decrease of 7%, which results in a more precise quantification of 6HB-NP2c's cytotoxic effect of around 23%, consistent with reports in the literature[76]. Unfortunately, further repetitions of this experiment did not result in consistent findings and showed minimal impact overall on cell viability, as shown in **Appendix 6** and summarized in **Figure 54A**.

Similar observations were made for cells co-cultures with 6HB-NPk (**Figure 54C**), where cells exhibited a decrease in cell viability of up to 15% after 72 hours in some experiments, while other repetitions showed no notable effects. In the conditions tested, 6HB-NP1C18 showed no significant cytotoxicity (**Figure 54D**).

As to improve the cytotoxic potential of the 6HB-NPxs, the design of the structure was altered to carry an additional cholesterol moiety, creating the 6HB-NP3c construct. In Ramos cells, this construct reduced cell viability by 9% after 24 hours, 16% after 48 hours, and up to 33% after 72 hours of incubation compared to NT control (**Figure 54E**). Material limitations restricted the continuation and repetition of further experiments, and the promising observations could not be confirmed. As an additional structure, 6HB-NP4c with 4 cholesterol moieties was proposed and resulted from in only a 5% decrease in viability upon co-culture (**Figure 54F**).

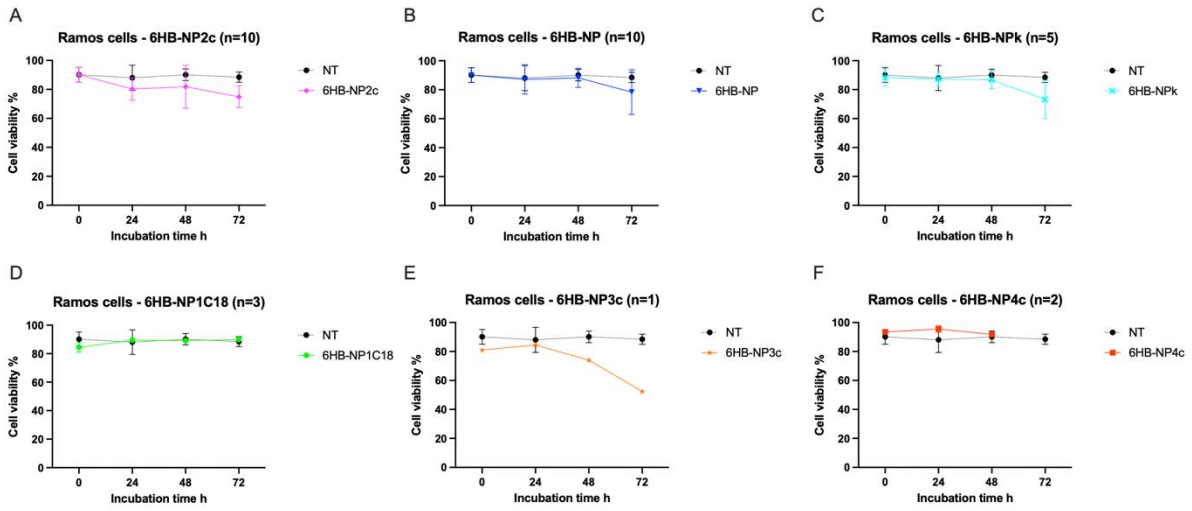

Figure 54 Graphical presentation of cell viability assays using Trypan Blue dye exclusion test for constructs 6HB-NP, 6HB-NP1C18, 6HB-NPk, 6HB-NP2c, 6HB-NP3c and 6HB-NP4c. Cell viability percentages are plotted over different incubation times (0, 24, 48, and 72 hours), with significant variations observed between individual experimental runs associated with large error bars.

The viability of Daudi cells remained largely unchanged when cultured with the diverse 6HB-NP constructs, except for samples treated with 6HB-NPk. After 48h, a decreased cell viability by 6% at concentrations of 0.25 µM and 0.5 µM was noted; this 6% decrease lasted at 0.25 µM up to 72h, showing a consistent effect on cell viability related to the dose (**Figure 55**). Cytotoxicity assays in PBMCs did not reveal any significant effects, though minor decreases in viability (8–15%) were observed with 6HB-NP2c and 6HB-NP4c (**Figure 55**).

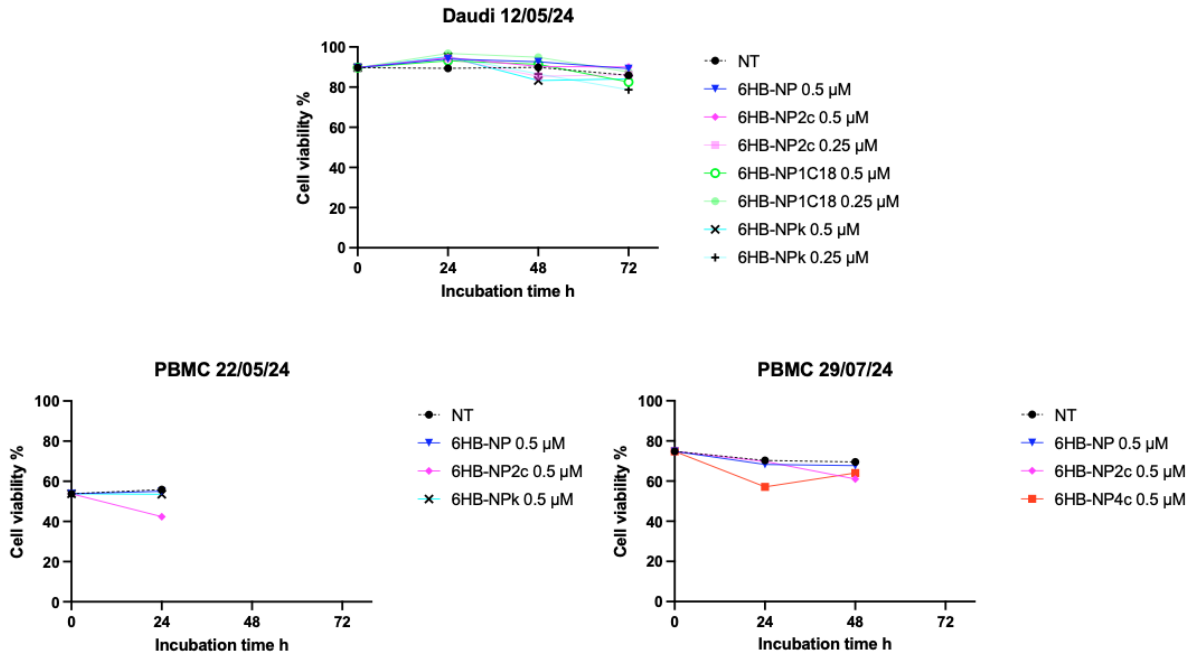

Figure 55 Graphical representation of cell viability assays in Daudi cells (top) and PBMCs (bottom) using the Trypan Blue dye exclusion test. No significant effects on cell viability were observed across all tested constructs (6HB-NP, 6HB-NP2c, 6HB-NP3c, 6HB-NP4c, 6HB-NPk) at the indicated concentrations (0.25 µM and 0.5 µM). Cell viability percentages are shown over different incubation times (0, 24, 48, and 72 hours), with consistent viability levels observed in both Daudi cells and PBMCs.

The variability in the cytotoxic effects of the NPs observed across different cell types may be attributed to differences in cell membrane composition, the NP design or the choice of hydrophobic modification. While prior studies demonstrated significant cytotoxicity of similar NPs in HeLa cells[76], their effect in B-cell-derived lines (Daudi and Ramos cells) and PBMCs was

less consistent. The lipid and protein composition of the membranes in these cells likely plays a critical role. B-cell membranes, for instance, are enriched with cholesterol and sphingolipids[116], which enhance membrane stability and may reduce susceptibility to NP-mediated disruption. Similarly, PBMC membranes are highly heterogeneous and resilient due to their functional diversity as immune cells.

The findings by *Jones et al.* showed that hydrophobically modified DNA nanostructures, such as those used in this study, rely on interactions with lipid bilayers to exert their effects[117]. Modifications like cholesterol and alkyl-phosphorothioate (PPT) enhance membrane tethering and insertion but can also cause clustering and localised membrane rearrangements. These effects are influenced by the specific lipid composition of the target membrane. In epithelial cell membranes, like HeLa cells, these interactions may result in effective membrane disruption. However, in the more complex and dynamic membranes of B cells and PBMCs, these interactions may be less efficient, leading to variability in cytotoxic effects induced by these nanostructures.

The inconsistent effects observed with constructs like 6HB-NP2c and 6HB-NPk may also result from variability in NP stability and behaviour. Hydrophobic modifications, while enhancing membrane interactions, can destabilise the NP structure in biological environments. *Jones et al.* noted that longer hydrophobic chains provide more stable anchoring but may also induce stretching or destabilization of the DNA duplex. Aggregation or dissociation of NPs during incubation could further reduce their efficacy.

Additionally, studies by *Ohmann et al.* have shown that DNA nanostructures can actively induce membrane flipping, a process wherein lipids are translocated between the inner and outer leaflets of the bilayer[118]. This enzyme-like activity, mediated by DNA nanostructures, creates disruptions in membrane asymmetry, potentially leading to cytotoxic effects.

However, the extent to which this phenomenon occurs in the context of NPs used in this study remains unclear. More experiments are required to determine whether the observed effects are due to membrane flipping induced by NPs or other mechanisms of interaction with the bilayer.

The promising results observed with 6HB-NP3c with a 33% reduction in Ramos cell viability after 72 hours, point towards the increased benefit of additional hydrophobic modifications on the structure. However, the reduced efficacy seen with 6HB-NP4c suggests that there might be a structural limitation when adding hydrophobic moieties. Excessive hydrophobicity may lead to aggregation or improper insertion and would thereby limit the NP's ability to interact with the membrane.

This study underscores the potential of hydrophobically modified DNA NPs as cytotoxic agents, while highlighting variability in efficacy due to differences in membrane composition and nanopore stability. Future work should focus on real-time mechanistic studies, improved nanopore design to enhance stability and specificity, and expanded cytotoxicity assays across diverse cell types. These efforts will refine the therapeutic potential of NPs and advance their application in nanomedicine.

4.1.4 ATP-based cell viability analysis using CellTiter-Glo® assay

To further confirm the cytotoxic effects observed in the Trypan Blue exclusion assay, a luminescence-based CellTiter-Glo® assay was performed in parallel. This method measures adenosine triphosphate (ATP), an indicator of metabolically active and viable cells. Luciferase, an enzyme, converts luciferin to oxyluciferin in the presence of ATP and oxygen. This reaction emits light as a measurable output proportional to ATP levels provided from viable cells. For this assay, aliquots of 25,000 cells were taken from the same cell suspensions used for Trypan

Blue exclusion assay. The CellTiter-Glo® reagent was added to the cell aliquots and the luminescent signal was recorded for all samples along with an ATP standard curve to validate the assay's accuracy and ensure proper calibration of the luminescence readings. Although precautions were taken, the results were highly variable and inconsistent. The three replicates showed significant differences, and the findings did not correlate with the Trypan Blue dye exclusion assay (**Figure 56**).

The CellTiter-Glo® protocol recommends using up to 50,000 cells per well as linearity up to this cell number between ATP and luminescence readings is given. The aliquots in this study were each precisely designed to contain 25,000 cells and should ideally fall within the defined linear range. However, variations in cell density as well as ATP levels among the samples could still lead to differences. Additionally, deviations in pipetting or cell suspension homogeneity may have impacted the results. On the other hand, the relatively low cytotoxic effects observed with 6HB-NPs in this study may not have caused sufficient differences in ATP levels to exhibit clear luminescent differences. CellTiter-Glo® might not be a sensitive method to detect subtle changes in cell viability compared to methods like Trypan Blue.

Based on these findings, the CellTiter-Glo® assay may not be suitable for this specific experimental setup due to the variability and lack of reproducibility in luminescence readings.

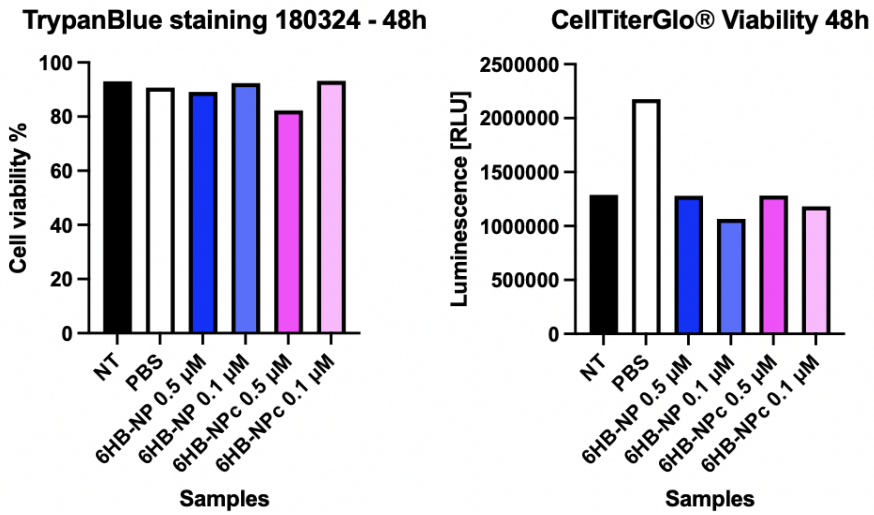

Figure 56 Comparative analysis of cell viability in Ramos cells using Trypan Blue dye and CellTiter-Glo® assay at 48h. The Trypan Blue assay shows cell viability percentages, while the CellTiter-Glo® assay measures ATP levels as an indicator of metabolic activity. Despite running the assays in parallel, the CellTiter-Glo® results display variability and lack of reproducibility, failing to correlate with the Trypan Blue findings.

4.1.5 Live/Dead staining with eFluor® 506 viability dye

In the exploration of additional methods for assessing cell viability in NP-treated samples, the fixable viability dye eFluor® 506 was investigated. This highly reactive dye has a strong attachment to amines present on the cell surface proteins. It penetrates cells through damaged cell membranes and therefore binds to interior and exterior amines in dead cells which results in higher fluorescent signals. The staining protocol included two washing steps to remove unbound nanostructures and serum proteins that could interfere with the staining procedure. After resuspension of the cell pellet in PBS, the dye was added and the cell suspension vortexed. To allow efficient binding, the samples were incubated for 30 minutes in the dark at 4°C. The samples were then analysed using flow cytometry.

The results revealed no significant differences in cell viability between treated and untreated samples which is shown in **Figure 57**. However, it should be noted that this approach was implemented later in the project for samples where the Trypan Blue exclusion assay revealed only light decreases in cell viability in Ramos cells and PBMCs. The observations from the eFluor® 506 assay suggest that the method may not be sensitive enough to detect subtle differences in cell viability resulting from NP treatments either similarly to the CellTiter-Glo® assay as described in section 4.1.4. It also had some difficulty in detecting subtle changes in metabolic activity. Moving forward, these limitations and findings should be considered for future investigations on cell viability.

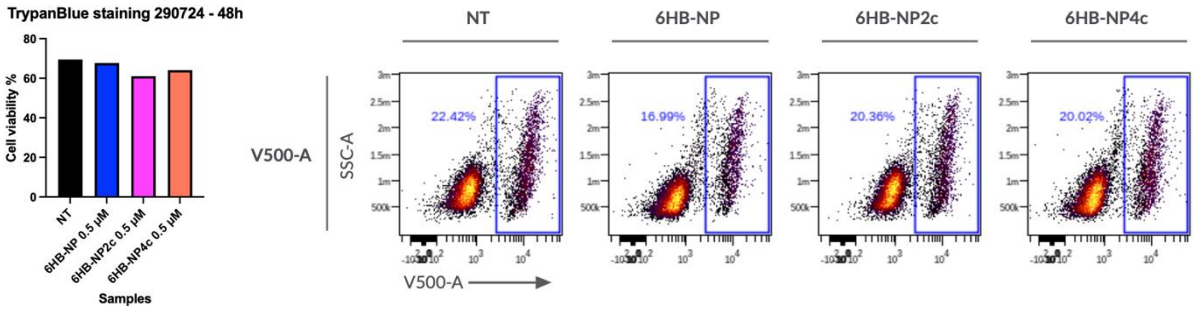

Figure 57 Comparative analysis of cell viability in PBMCs using Trypan Blue dye and fixable viability dye eFluor® 506 at 48h. The Trypan Blue assay provides cell viability in percentages, while the eFluor® 506 assay detects fluorescent signals amine-residues on proteins. Both methods revealed minimal differences in cell viability between treated and untreated samples.

One potential explanation might be that the NP treatments may only induce small changes that do not considerably compromise membrane integrity or ATP levels, thereby preventing these methods to detect any significant viability differences. As seen from the Annexin V/PI assay, the structural characteristics of the NPs may interfere with the staining process itself,

especially if any residual nanostructures remain in solution and no washing step is included in the procedure.

The absence of statistically significant differences in cell viability between treated and untreated groups indicates the need for additional assays to detect subtle cytotoxic effects that will translate into the main goal of killing cancer cells. Advanced imaging techniques, for example confocal microscopy, could provide real-time insights into interactions between NP and cell membranes and therefore offer a more precise understanding of their impact and behaviour.

4.2 Membrane integration and intracellular localisation of NPs

This study aimed to investigate the inter- and intracellular behaviour of NPs with the focus on their ability to span cell membranes and to track their localisation over time.

NPs were assembled according to established protocols with one Alexa647-labeled oligonucleotide (L10-A647) to enable fluorescent tracking. The resulting nanostructures were then co-cultured with Ramos cells under standard conditions (37°C, 5% CO_2) in RPMI medium supplemented with 10% FCS. At predetermined time points (15 min, 2h, 5h and 24h), the cells were washed twice to remove any unbound NP constructs and further stained with WGA-Rhodamine to label the membrane and DAPI, a DNA intercalator, to visualise the nucleus. The stained cells were subsequently analysed on a fluorescence microscope, called Nanoimager.

4.2.1 Control experiments with AlexaFluor647-labeled oligonucleotides

In control experiments using Alexa647-labelled oligonucleotides (L10-A647) alone, we observed that membrane penetration could not solely be attributed to hydrophobically

modified oligonucleotides, consistent with findings by *Lacroix et al.*[119]. They observed that labelled oligonucleotides (Cy3 and Cy5) have the tendency to penetrate cells and to accumulate in mitochondria. A formaldehyde fixation would wash them away, leaving punctual signals associated with endosomes or lysosomes, as well as diffuse cytoplasmic fluorescence. Our study revealed similar behaviour with Alexa647-labelled oligonucleotides shown in **Figure 58**. After a 15 min incubation time, aggregated fluorescence signals were observed at the edge of the cell membrane which indicates initial membrane association. By 6 hours co-culture, fluorescent signals were mainly localised in the cell which is associated with cell penetration and internalization. These observations align with the reported dynamics of Cy3 and Cy5 dyes. Also, the punctual signal pattern, resulting from the cell fixation process, was observed as described by *Lacroix et al*. Therefore, the interpretation of localisation data should be careful under consideration of these fixation artifacts, particularly when evaluating intracellular trafficking pathways.

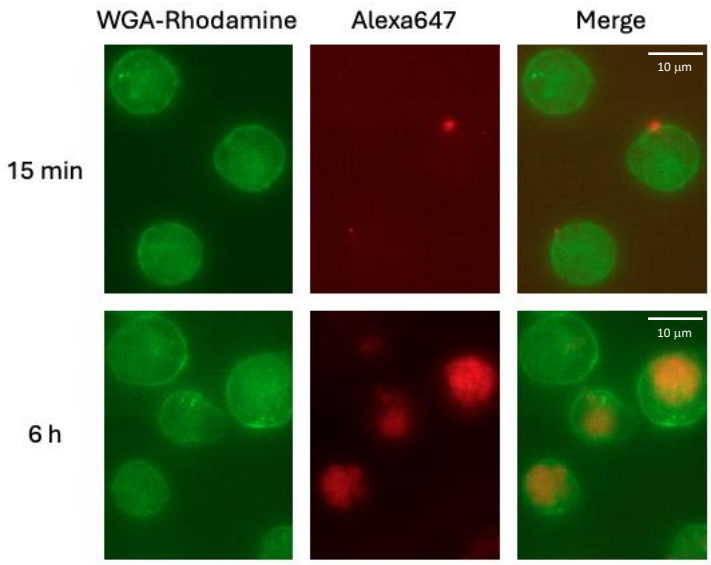

Figure 58 Control experiment with Alexa647-labelled oligonucleotides (L10-A647). Representative microscopy images showing the behaviour of L10-A647 in Ramos cells. At 15 minutes, strong and aggregated fluorescence signals localise at the cell membrane, indicating association. By 6 hours, the signal is predominantly internalised which demonstrates cellular uptake.

Analysis of samples was performed at 15 minutes, 2 hours, 5 hours and 24 hours to precisely track NP integration and intracellular localisation. These time intervals enabled observations of membrane association, and they also revealed information of subsequent intracellular movement over time.

To investigate potential interactions between NPs and DAPI, several samples were imaged before as well as after DAPI staining (**Figure 59**). While clear DAPI fluorescence was observed in the nucleus, no detectable DAPI signal was observed in regions where Alexa647-labeled nanostructures were localized on the membrane. These findings suggest that either DAPI does not intercalate into the NPs or that any potential interaction results in fluorescence signals too weak to be detected under the given imaging conditions.

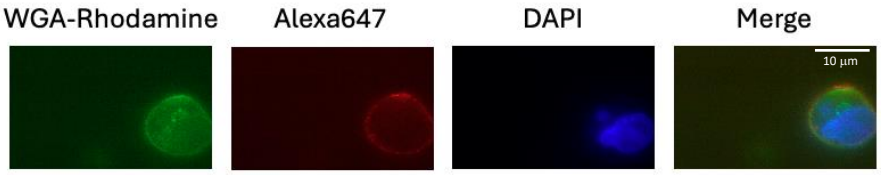

Figure 59 Analysis of nanopore interactions with DAPI: Microscopy images comparing fluorescence signals after DAPI staining. Fluorescence signals from Alexa647-labelled nanopores were observed only at the membrane and no detectable DAPI signal colocalizing on the membrane.

4.2.2 Time-course analysis of unmodified nanopore localisation (6HB-NP)

This study evaluated several NP constructs: 6HB-NP, 6HB-NP2c, 6HB-NP4c and 6HB-NPk. The localization patterns were observed at selected time points (15 min, 2h, 5h and 24h).

- **Unmodified NPs (6HB-NP)** – **Figure 60**
    - At 15 min incubation, some little non-specific membrane binding was observed.
    - At 2h, many unmodified NPs were near the nucleus with some punctual localisation on the cell membrane.
    - After a 5h incubation time, the NPs were predominantly found in the cytosol and nucleus.
    - After 24h, the NPs were aggregated in the cytosol close to the cell nucleus.

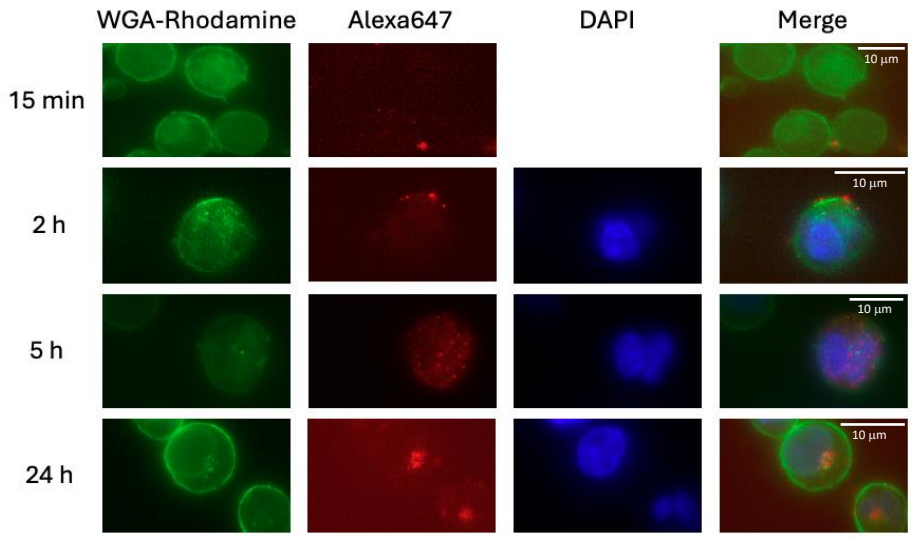

Figure 60 Time-course localisation of 6HB-NPs. Microscopy images illustrating the intracellular behaviour of unmodified nanopores at different time points. At 15 minutes, weak membrane association is visible. By 2 hours, fluorescence is detected near the nucleus with some signals on the membrane. At 5 hours, nanopores are distributed in both the cytosol and nucleus, while at 24 hours, fluorescence clusters are observed close to the nucleus.

These findings provide valuable insights into NP behaviour in *in vitro* settings without the influence of hydrophobic moieties, but the interpretation of the data is challenging. One possible explanation for the observed intracellular fluorescence patterns at 5h and 24h time points is that it might be associated with the dissociation of NPs during the co-culture. In this case the fluorescence signal observed within the cytosol or nucleus could originate from constituent oligonucleotides of the NPs rather than intact NPs. This hypothesis might be supported by our previous studies where fluorescently labelled oligonucleotides have shown to diffuse freely and localise within cellular compartments such as the nucleus. However, the fluorescence patterns of single oligonucleotides (**Figure 58**) show significant differences

compared to the observed pattern in this study (**Figure 60**) which suggests that the NPs may have retained their structural integrity. In this case, as highlighted in section 4.2.1., the influence of the fixation process must also be taken into consideration. It is known that fixation, particularly with paraformaldehyde, alters the localisation of fluorescent signals. The observed clustering of fluorescent signal in close proximity to the nucleus after the 24-hour incubation period may be a consequence of fixative-induced disruption of their natural distribution, as previously discussed.

4.2.3 Hydrophobically modified NPs membrane association and uptake

- **Hydrophobically Modified NPs**:
    - **6HB-NP2c**: After 15 minutes, irregular binding patterns on the cell membrane were observed with areas of higher and lower fluorescence suggesting potential aggregation or variability in membrane interaction efficiency. After 2- and 5-hours incubation time, the nanostructures remained bound to the cell surface on the membrane, showing colocalised regions of fluorescence intensity. Minor membrane disruptions could be identified, though no significant cell death was observed. After 24h, most NPs remained on the membrane, with strong and clustered fluorescence signals also detected inside the cell near the nucleus (**Figure 61**).

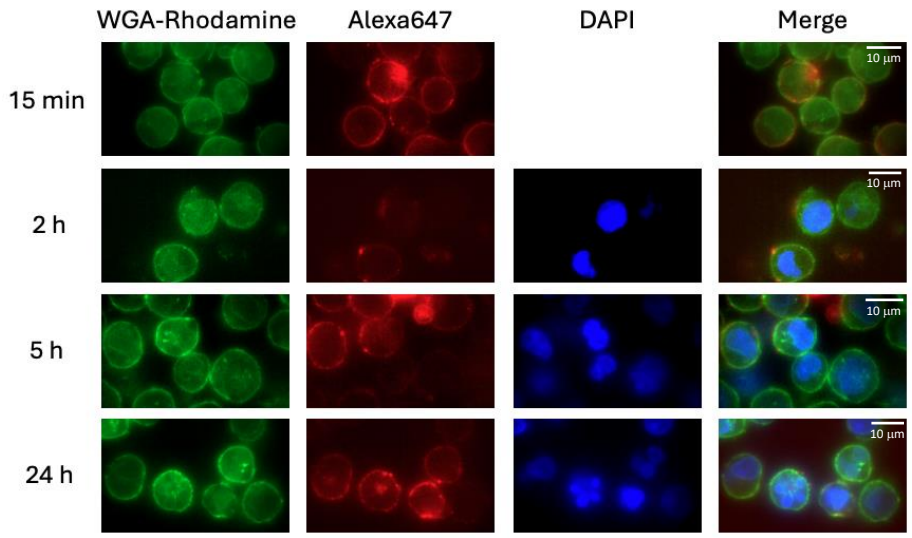

Figure 61 Membrane association and internalisation of 6HB-NP2c constructs. Microscopy images showing 6HB-NP2c treated cells at 15 minutes, 2 hours, 5 hours and 24 hours. At 15 minutes, irregular fluorescence patterns on the membrane suggest potential aggregation. By 2 and 5 hours, nanostructures remain associated with the membrane, with localised regions of high fluorescence intensity. After 24 hours, additional strong clustered fluorescence signals appear near the nucleus, indicating internalization and stability on the membrane without induction of significant cell death.

- **6HB-NP4c**: Uniform membrane binding was observed compared to 6HB-NP2c, with regular fluorescence patterns on the cell membrane at the 15 minutes time point. By 5 hours, fluorescence was detected both on the membrane and inside cells, suggesting internalisation. At 24 hours, the NPs appeared stable on the membrane and with some clustered signals observed near the nucleus. Importantly, the cells remained intact which supports the results from the cell

viability assay that 6HB-NP4c does not induce immediate cytotoxic effects (**Figure 62**).

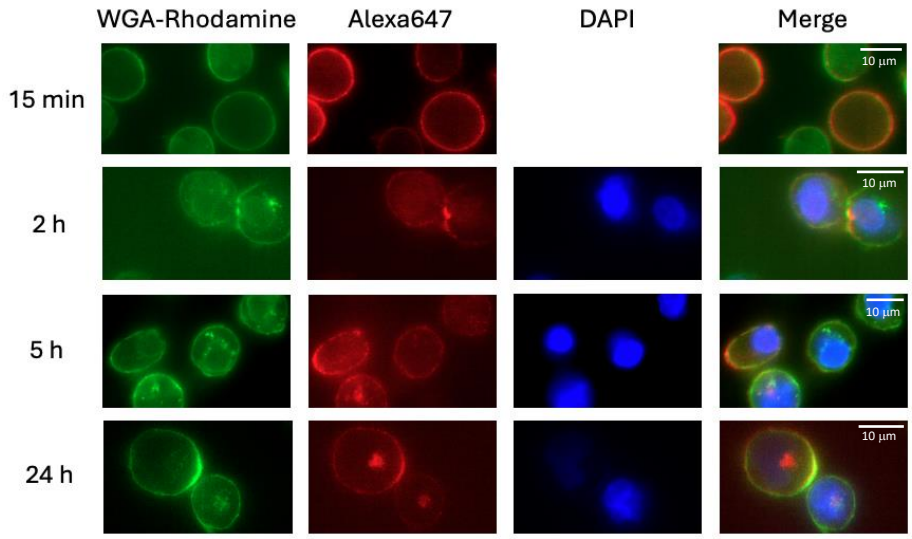

Figure 62 Membrane association and internalisation of NP4c constructs. Microscopy images demonstrating the time-dependent behaviour of NP4c nanopores. At 15 minutes, uniform membrane association is observed. By 5 hours, fluorescence is detected both at the membrane and within the cell. At 24 hours, the nanopores remain stably associated with the membrane, and clustered signals near the nucleus indicate partial internalisation.

- **6HB-NPk:** Limited and ineffective membrane binding was observed, suggesting poor interaction with the cell membrane after 15 minutes incubation time. After 2 hours, fluorescent signals were primarily detected inside the cell, suggesting that 6HB-NPk may lack the stability or assembly required for effective membrane spanning. At 24h, few cells exhibited punctate

fluorescence on the membrane, further indicating the unsuitability of this construct for membrane spanning activities (**Figure 63**).

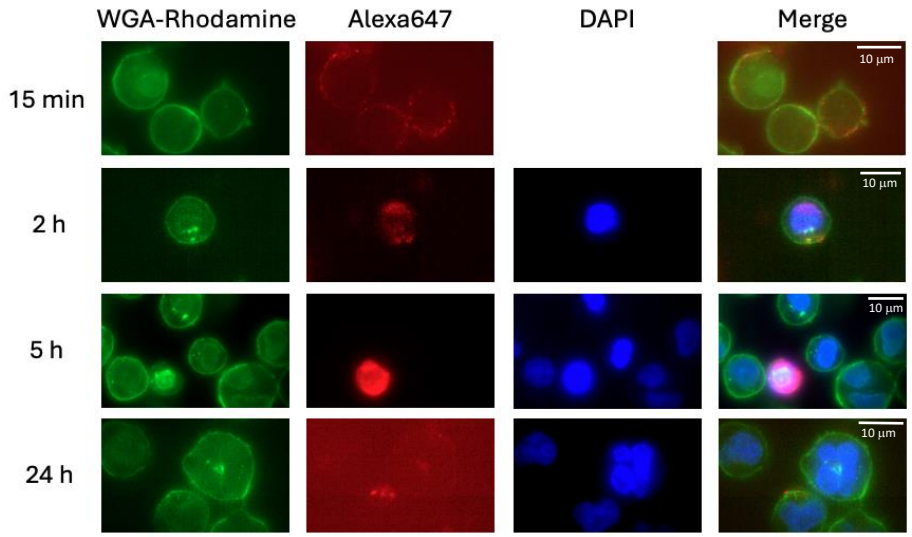

Figure 63 Assessment of 6HB-NPk nanopore constructs. Microscopy images showing limited membrane interaction of 6HB-NPk constructs. At 15 minutes, weak and inconsistent membrane association is observed. After 2 hours, fluorescence signals were predominantly detected inside the cells which suggests potential dissociation or instability of the constructs. By 24 hours, only a few cells exhibit punctate membrane fluorescence, indicating poor membrane integration and limited suitability of 6HB-NPk as a functional nanopore construct.

The cholesterol-modified nanostructures, 6HB-NP2c and 6HB-NP4c, had intense and persistent membrane association up to 24 hours. The anchoring property of the nanostructures into lipid bilayer is attributed to the hydrophobic properties.

The uniform binding pattern of 6HB-NP4c compared to 6HB-NP2c indicates that the number of attached hydrophobic parts may considerably improve its membrane binding and stability. However, no notable cell death was observed, raising the question of whether NP are too

small or present at insufficient concentrations to disrupt the membrane efficiently. Future studies should involve redesigning of the constructs into larger nanopore constructs (> 6 nm diameter) and potentially increasing their hydrophobicity to enhance ion flow and induce membrane destabilisation more efficiently which ultimately would lead to cell death.

In contrast, the poor performance of 6HB-NPk considerably points out the importance of precise structural assembly for effective membrane integration. The internalisation and clustered fluorescence signals observed, particularly after 2 hours, may be attributed to nanopore aggregation or dissociation. While control experiments show some differences in labelled single oligonucleotide behaviour, further experiments using live-cell imaging, could clarify whether intact NP or free oligonucleotides are responsible for the observed localisation patterns.

The observations from this microscopy study can be directly correlated with the results from the cytotoxicity assays, described in 4.1. Cholesterol-modified constructs 6HB-NP2c and 6HB-NP4c exhibited clear membrane association along with little internalization over time; however, these constructs did not induce meaningful cell death, as indicated by low cytotoxicity in the viability assays.

The findings revealed that despite successful membrane anchoring, these NPs may not efficiently disrupt the membrane to trigger uncontrolled ion flux and ultimately leading to cell death. Cholesterol seemed to be the most suitable moiety for the modification of NPs which is also undermined by the commercial availability of the oligonucleotide modifier. In addition, this assay demonstrated the unsuitability of alkyl chains as hydrophobic modification in NPs, because only limited and inconsistent membrane interaction in combination with a lack of notable cytotoxicity was observed for the 6HB-NPk construct bearing the double alkyl-chain modification.

4.3 Binding assays of antibody constructs

While the conjugation strategy employing diBrPD linkers seeks to preserve antibody integrity through the rebridging of reduced interchain disulphides, this introduced modification could result in compromised binding affinity and capacity. For this purpose, once the antibody-linker conjugates were formed, a binding assay was conducted to determine their binding capacity. For instance, the constructs were cocultured with Ramos cells for 30 min at 4°C to prevent the internalisation of the constructs. Unbound antibodies are first washed away and then the cells are stained with a Fcγ-fragment specific antibody that is fluorescently labelled with Phycoerythrin (PE) to detect surface-bound antibodies. After a 30 min incubation at 4°C in the dark, the cells are washed, followed by analysis using flow cytometry.

4.3.1 Evaluation of antibody-linker conjugates

After successful assembly of antibody-linker conjugates (see section 3.2.2), the resulting constructs, rtx-diBrPD-8 and rtx-diBrPD-23, were evaluated for their binding efficiency using a flow cytometry-based binding assay. A 1:3 serial dilution was prepared, starting from a saturation concentration of 15 µg/ml. CD20-expressing Ramos cells were incubated with the constructs for 30 minutes at 4°C to allow binding. Cells were washed to remove unbound antibodies, then stained with a PE-conjugated and Fcγ-specific secondary antibody for the detection of bound primary antibodies. The mean fluorescence intensity (MFI) was measured as an outcome value to determine antibody binding levels with elevated values indicating a high number of antibodies bound to the surface, while a lower value stipulating fewer bound antibodies. The unmodified rtx antibody served as a reference to compare the binding activities between the different constructs.

The results demonstrated a clear dose-dependent decrease in MFI across all constructs, confirming that the observed signal originated from bound antibodies (**Figure 64**). Compared to the unmodified rtx control, both modified constructs exhibited reduced MFI values at equivalent concentrations, indicating that conjugation of the linker negatively affects antibody binding efficiency.

Closer analysis of the two constructs revealed significant differences based on PEG linker length. The construct with the longer PEG chain (rtx-diBrPD-23) showed lower MFI values compared to rtx-diBrPD-8 at the same concentrations. This suggests that the longer PEG chain may introduce steric hindrance, obstructing the rtx's binding site or the secondary antibody's binding site and therefore interfering with its ability to recognise the receptor epitope. In contrast, the shorter PEG linker (rtx-diBrPD-8) retained relatively better binding, though still reduced compared to the unmodified antibody.

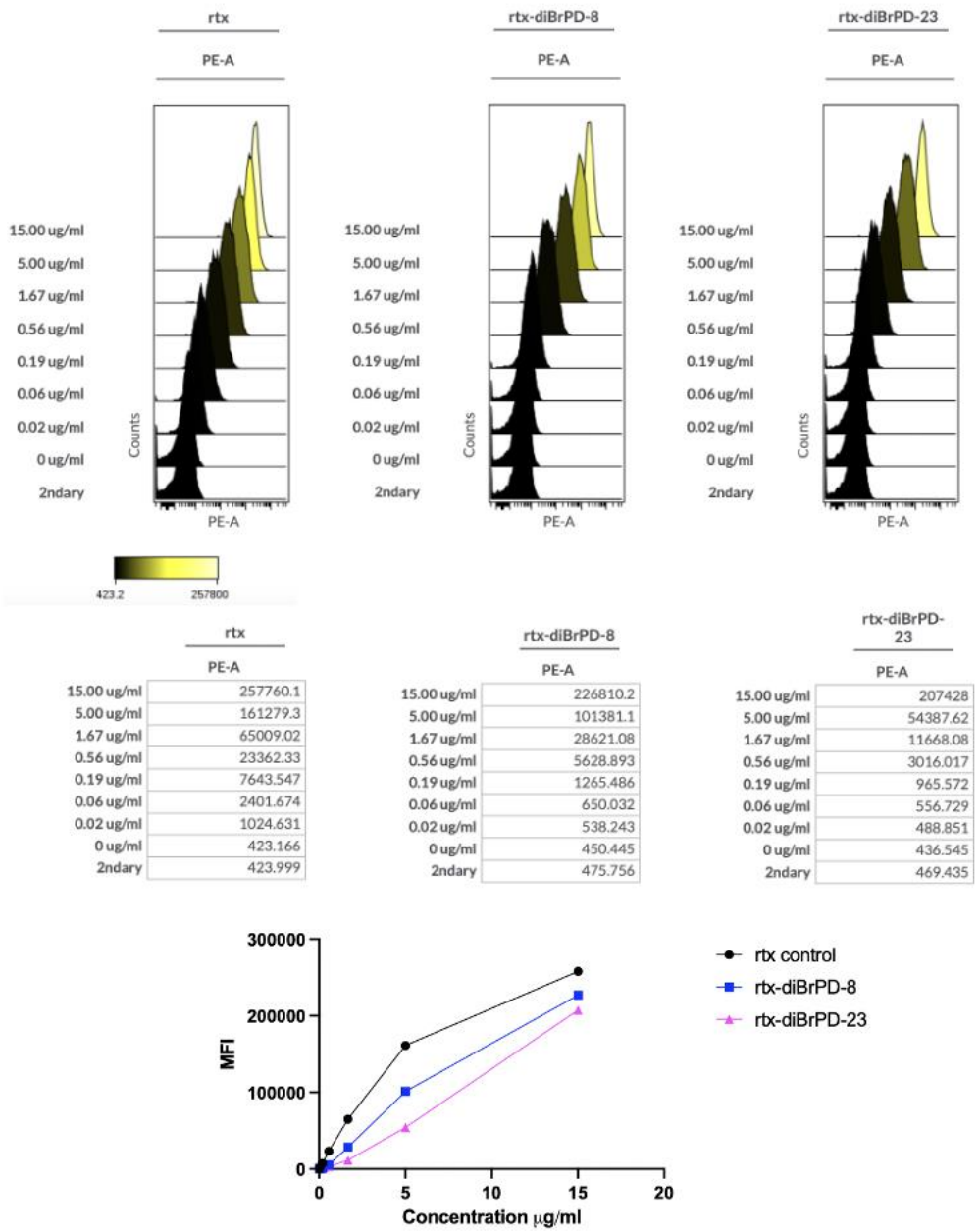

Figure 64 Binding assay of rtx-diBrPD-8 and rtx-diBrPD-23 in Ramos cells. Histograms (top) display PE signal intensity across 1:3 serial dilution series for control antibody rtx, rtx-diBrPD-8 and rtx-diBrPD-23 incubated with Ramos cells. MFI values (bottom) are plotted against antibody concentration, showing dose-dependent binding curves for both constructs.

With the introduction of the PEGylated linkers, a reduced binding activity of the antibody was observed which spotlights the importance of linker design in antibody modification.

PEGylation is often used to improve solubility, stability, and pharmacokinetics, but it can also introduce structural limitations and thereby considerably interfere with receptor interactions. A longer PEG chain in rtx-diBrPD-23 likely obstructs epitope accessibility due to increased steric hindrance. In the case of rtx-diBrPD-8, the decrease in binding was less pronounced, though still noticeable which can be attributed to the shorter PEG length and its lower potential to obstruct the epitope.

Previous reports on linker studies have demonstrated that very linker length or bulkiness has the ability to impair antibody functionality and receptor binding[120-122]. Achieving a balance between linker stability and minimal structural interference is therefore essential for maintaining binding efficacy. Despite the observed reductions, this assay confirms that the modified antibodies retain measurable binding to the CD20 receptor, providing a solid foundation for further functionalisation.

4.3.2 Evaluation of antibody-oligonucleotide conjugates

To further assess the functional behaviour of the constructs, in the next step we examined if conjugating an oligonucleotide to the antibody-linker construct would influence the binding activity as observed with the linker-modified antibodies. The same binding assay was conducted as described in section 4.3.1. A 1:3 serial dilution of the antibody-oligonucleotide conjugates was prepared, starting at 15 µg/ml, and Ramos cells were incubated with the constructs for 30 minutes at 4°C. After the washing step to remove unbound antibodies, cells were stained with a PE-conjugated and Fcγ-specific secondary antibody, and MFI was recorded *via* flow cytometry.

The results revealed a dose-dependent decrease in MFI across all constructs, consistent with earlier observations (**Figure 65**). As previously seen, the rtx-diBrPD-8 construct exhibited lower MFI values compared to the unmodified rtx control which reconfirmed that the linker attachment influences the binding of the antibody to its receptor. However, an interesting observation was made for the antibody-oligonucleotide construct rtx-diBrPD-8-C1 since the measured MFI was higher compared to rtx-diBrPD-8.

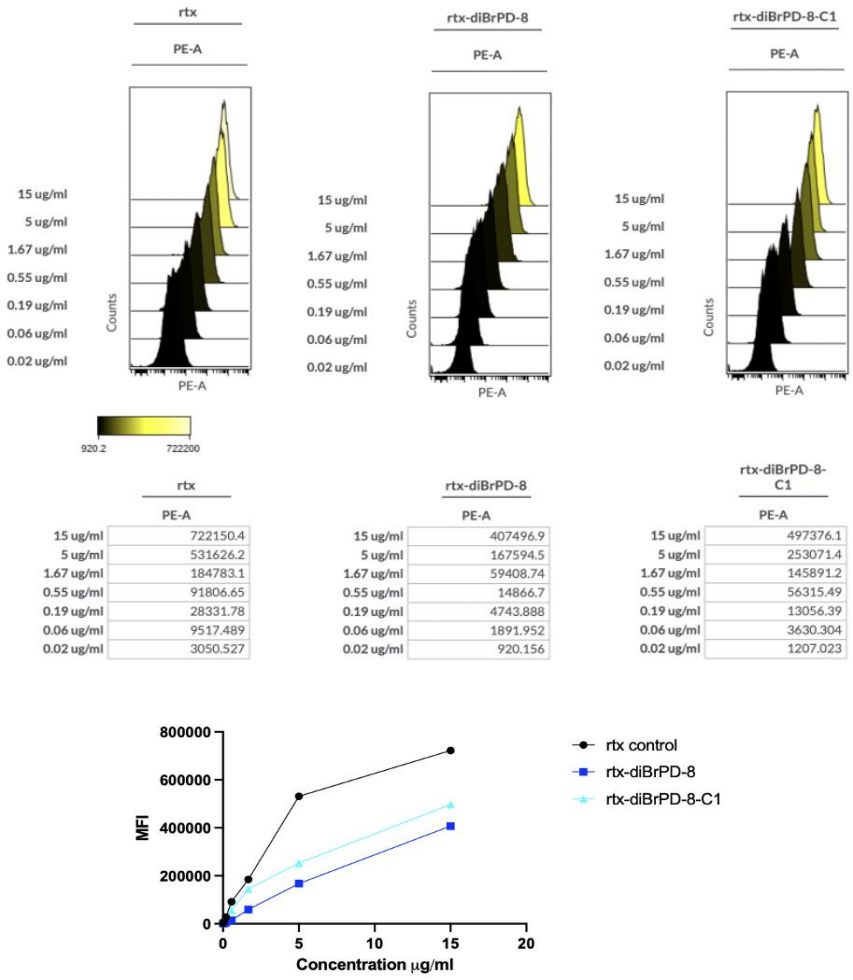

Figure 65 Binding assay of rtx-diBrPD-8 and rtx-diBrPD-8-C1 in Ramos cells. Histograms (top) display PE signal intensity across 1:3 serial dilution series for control antibody rtx, rtx-diBrPD-8 and rtx-diBrPD-8-C1 incubated with Ramos cells. MFI values (bottom) are plotted against antibody concentration.

The observed increase in MFI with the antibody-oligonucleotide conjugate could be potentially caused by the negatively charged backbone of the oligonucleotide that interacts electrostatically with amino acid residues on the antibody. Based on these interactions, the charges from the amino acids may repel the charges of the oligonucleotides that would otherwise sterically obstruct the epitope and thereby partially restoring accessibility to the receptor-binding site.

These findings provide further insights into the behaviour of the construct and the chosen design approach. While the conjugation of the diBrPD linker initially compromises binding, oligonucleotide attachment appears to stabilise or partially reduce these effects. To investigate binding kinetics, surface plasmon resonance (SPR) could be employed and these additional biophysical studies would provide further information on the receptor-antibody interaction of these constructs.

4.3.3 Stability and functionality of antibody-duplex constructs

In the next step, we aimed to further evaluate the stability and functionality of the rtx-diBrPD-8 construct, therefore we investigated if adding a complementary oligonucleotide that hybridises to the attached single-stranded oligonucleotide would form a stable double-stranded DNA (dsDNA) construct in *in vitro* conditions. With this approach successful oligonucleotide conjugation would be additionally validated. For this purpose, an additional BCN-modified oligonucleotide was designed and synthesised following the procedure described in section 3.1.2. named antiL10 (analytical data in **Appendix 5 and 6**). The sequence was selected to afford a 15mer that is complimentary to the 3' end of L10-A647, see **Appendix 2**. After the successful synthesis and isolation of the BCN-modified antiL10 oligonucleotides, they were combined with rtx-diBrPD-8 in an aqueous mixture following the assembly protocol

described in section 3.2.3 to form rtx-diBrPD-8-antiL10. To produce the desired antibody construct with the dsDNA attached, L10-A647 was heated to 90°C for 3 min to remove secondary structures and further added to rtx-diBrPD-8-antiL10 to enable hybridisation at 4°C for at least 30 min. The resulting construct was labelled rtx-diBrPD-8-dsDNA and the synthesis route outlined in **Figure 66**.

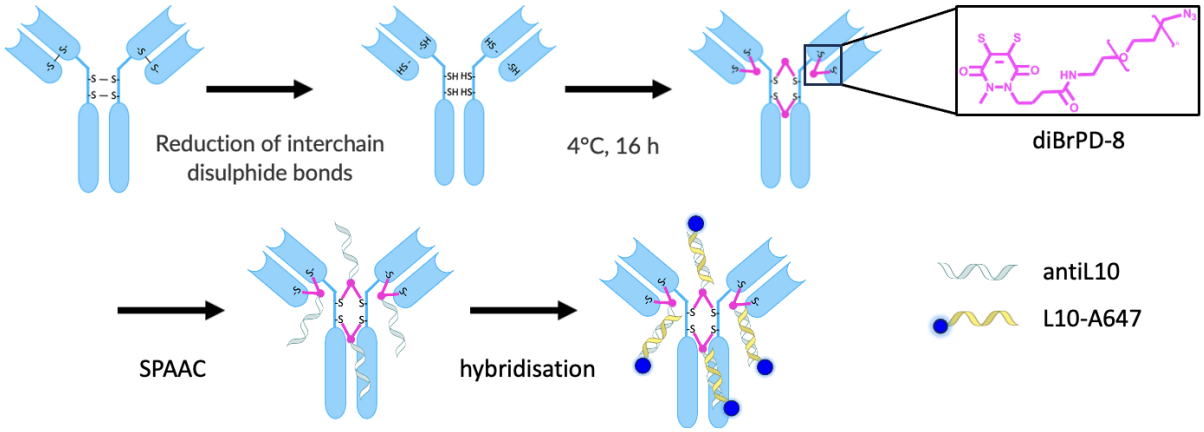

Figure 66 Schematic representation of assembly process for rtx-diBrPD-8-dsDNA. To generate the rtx-linker construct, the interchain disulphides were reduced and rebridged with diBrPD-8. Through SPAAC antiL10 oligonucleotides were attached to the rtx-linker construct and the fluorescently labelled oligonucleotides L10-A647 were hybridised to the attached antiL10.

The dsDNA-antibody constructs were prepared in an 8-point serial dilution (1:2) starting from 10 µg/ml and then incubated with Ramos cells for 30 minutes at 4°C in the dark to maintain fluorophore stability. Through a washing step unbound constructs were removed and the cells analysed on the flow cytometer. Two control samples with L10-A647 alone and additional PE-conjugated Fcγ-specific secondary antibody were included in the analysis as background fluorescence measurement (L10-A647) and to verify the integrity of the antibody (secondary antibody). MFI was used as the outcome measure.

Strong fluorescent signal originating from the AlexaFluor 647-labeled oligonucleotides (L10-A647) were detected for all rtx-diBrPD-8-dsDNA and rtx-diBrPD-23-dsDNA samples (**Figure 67**). The signals decreased in a dose-dependently and therefore confirms that both constructs retain binding to the CD20 receptor on the Ramos cell surface with the dsDNA attached.

Importantly, in control samples where the PE-conjugated Fcγ-specific secondary antibody was added, a positive PE signal was also detected. This observation demonstrates that the antibody's Fc region remains intact where the secondary antibody specifically binds to. Together, these results confirm that the dsDNA constructs maintains both structural antibody integrity and receptor-binding capacity after the addition of the complementary oligonucleotide L10-A647.

This assay also confirms the successful formation of the dsDNA-antibody construct, a significant and important advancement in the project. The observed dose-dependent fluorescent signals from the AlexaFluor 647-labelled oligonucleotides are correlated to stable hybridisation of L10-A647 to rtx-diBrPD-8-C1 or rtx-diBrPD-23-C1. These findings establish a good starting point for the conjugation of NPs to the antibody as stable attachment of dsDNA to the antibody through the diBrPD linker without dissociation was demonstrated. Additionally, retained CD20 receptor binding was validated.

The detection of a PE signal from the secondary antibody further validates the intactness of the antibody, particularly the Fc region, which is critical for maintaining the antibody's functional properties, such as effector functions or additional modifications in therapeutic applications[123]. In conclusion, we demonstrated that linker conjugation and addition of dsDNA do not compromise rtx' binding to the CD20 receptor which is a key characteristic in our proposed construct and plays an important role in the project for targeted cell killing.

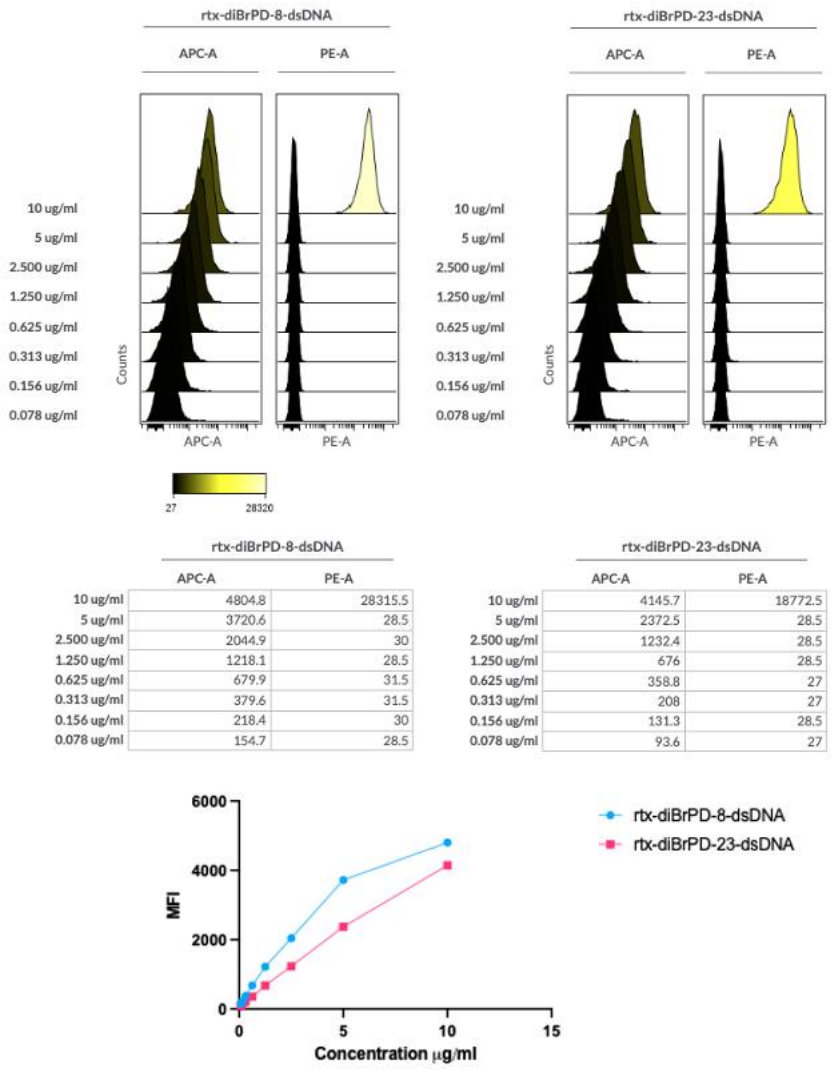

Figure 67 Binding assay of rtx-diBrPD-8-dsDNA and rtx-diBrPD-23-dsDNA in Ramos cells. Histograms (top) display the AlexaFluor 647 signal intensity across a 1:2 serial dilution series for rtx-diBrPD-8-dsDNA and rtx-diBrPD-23-dsDNA incubated with Ramos cells. MFI values (bottom) are plotted against antibody concentration, showing dose-dependent binding curves for both constructs.

4.4 Discussion and Conclusion

This chapter presents a comprehensive evaluation of NPs and antibody constructs with a focus on their cytotoxic effects in cell lines, intercellular as well as intracellular behaviour and

receptor-specific binding capacities. Through *in vitro* assays, the functionality of these constructs was analysed across multiple biological contexts.

Different hydrophobic modifications for the DNA nanostructures were explored for their potential to enhance membrane insertion. Cholesterol has been widely utilised in the context of nanostructures due to its natural affinity for lipid bilayers and its commercial availability. Cholesterol-modified DNA nanostructures insert into lipid membranes based on the hydrophobic interactions between cholesterol and the lipid bilayer that facilitate stable integration. This modification has been shown to enhance membrane binding efficiency and stability of the nanostructures[73, 104, 124]. This project also explored the use of alkyl chains as hydrophobic modifications which present another approach for membrane-nanostructure interactions. The *Barthélémy* group has performed extensive studies on nucleolipids with alkyl chains which indicated that chain length and saturation have a great influence on the self-assembly and membrane-spanning properties of nanostructures[125, 126]. However, their observations suggest that alkyl chains enhance membrane association, but they also induce aggregation which potentially affects structural uniformity and functional performance.

The cytotoxicity assays were inconclusive and raised multiple questions about the design of the construct as significant variability in the efficacy was observed. The cholesterol-modified constructs (6HB-NP2c and 6HB-NP3c) initially showed promising reductions in cell viability, but these findings were not reproducible in subsequent repetitions. In parallel, observations from the microscopy studies revealed time-dependent localisation patterns of NPs. 6HB-NP2c and 6HB-NP4c demonstrated consistent and regular membrane association with little internalisation activity into the cell, whereas 6HB-NPk showed very limited membrane interactions and proved its unsuitability as membrane targeting compound. In these

microscopy studies no notable cell killing upon membrane association of the NPs was observed at 24h co-culture.

The binding assays demonstrated how the attachment of the linker and oligonucleotide conjugation impacted antibody-receptor binding. It was hypothesized that the reduced binding capacity of the antibody-linker constructs is due to steric hindrance which was improved with the addition of oligonucleotides. The successful formation of dsDNA-antibody constructs, with maintained receptor binding and structural integrity, was an immense step forward toward the full assembly of the antibody-nanopore construct.

All the presented findings in this chapter have contributed to the continued development of antibody-nanopore constructs. It became apparent that the redesign of the nanopore should be the focus of future studies to improve their functionality as cell killing moieties. Potential approaches could involve the synthesis of larger or multifunctional NPs that may improve membrane disruption and induce cytotoxic effects. Additionally, including real-time imaging approaches, such as live-cell microscopy, will provide valuable insights into the dynamics of NP integration, internalisation and intracellular trafficking.

In this project, a reliable and suitable characterisation method to identify the real composition of the generated antibody conjugates was not established. These methodologies are essential in determining the precise number of nanostructures attached to each antibody and will ultimately provide the needed information to determine the optimal concentration ranges for optimal functionality. Additionally, the characterisation methods will validate the reproducibility of this approach for conjugating diverse molecules to antibodies.

To pave the way for clinical applications, once a stable construct is established, *in vivo* studies will be essential to evaluate systemic efficacy, biodistribution, and safety as important factors in the therapeutic development.

Future investigations and studies should address key challenges to enhance the potential of the described constructs for the development of next-generation therapeutic platforms with precise targeting and functional cytotoxicity.

Chapter 5 Towards novel antibody-oligonucleotide conjugates

5.1 Cobalamin conjugates

Building on the successful conjugation of oligonucleotides to rtx using diBrPD-8 as the linker, the potential application of this technology for ASO delivery was explored. In collaboration with RISE, Sixfold Bioscience, the Polish Academy of Sciences and Ghent University, a novel construct was conceptualised to investigate enhanced nuclear delivery of ASOs.

The central hypothesis of this project was that oligonucleotides could be uptaken through the natural cobalamin (Cbl) pathway for cellular internalization.

5.1.1 The cobalamin pathway and proposed constructs

In the bloodstream, Cbl binds to transcobalamin (TC) to form a Cbl-TC complex. This complex is recognised by ubiquitously expressed transcobalamin receptors (TCblR) on cell surfaces. This receptor-ligand interaction initiates endocytosis, allowing the complex to enter the cell. Inside the lysosome, cobalamin is released and subsequently directed to the cytoplasm and mitochondria, where it is metabolised into its active forms, methylcobalamin and adenosylcobalamin.

Two constructs were developed for testing (**Figure 68**):

- **Construct 1**: This construct comprises rtx, the diBrPD-8 linker, a capture oligonucleotide (C2) with a 5’ DBCO-modification, and a MALAT1-mRNA targeting ASO (M1) functionalised with a 5’-Cbl modification (Cbl-M1). The DBCO modification

enables conjugation through SPAAC with the terminal azide of diBrPD-8. M1 was equipped with two cleavable TCA sequences and an 8-mer complementary part to C2.

- **Construct 2**: This design includes a CD20-targeting nanobody, a 5-hydroxy-1,5-dihydro-2H-pyrrol-2-one (5HP2O) linker conjugated through an NHS ester to a terminal amine on C2. M1, with the same capture sequence and TCA cleavage site, was employed similarly to construct 1.

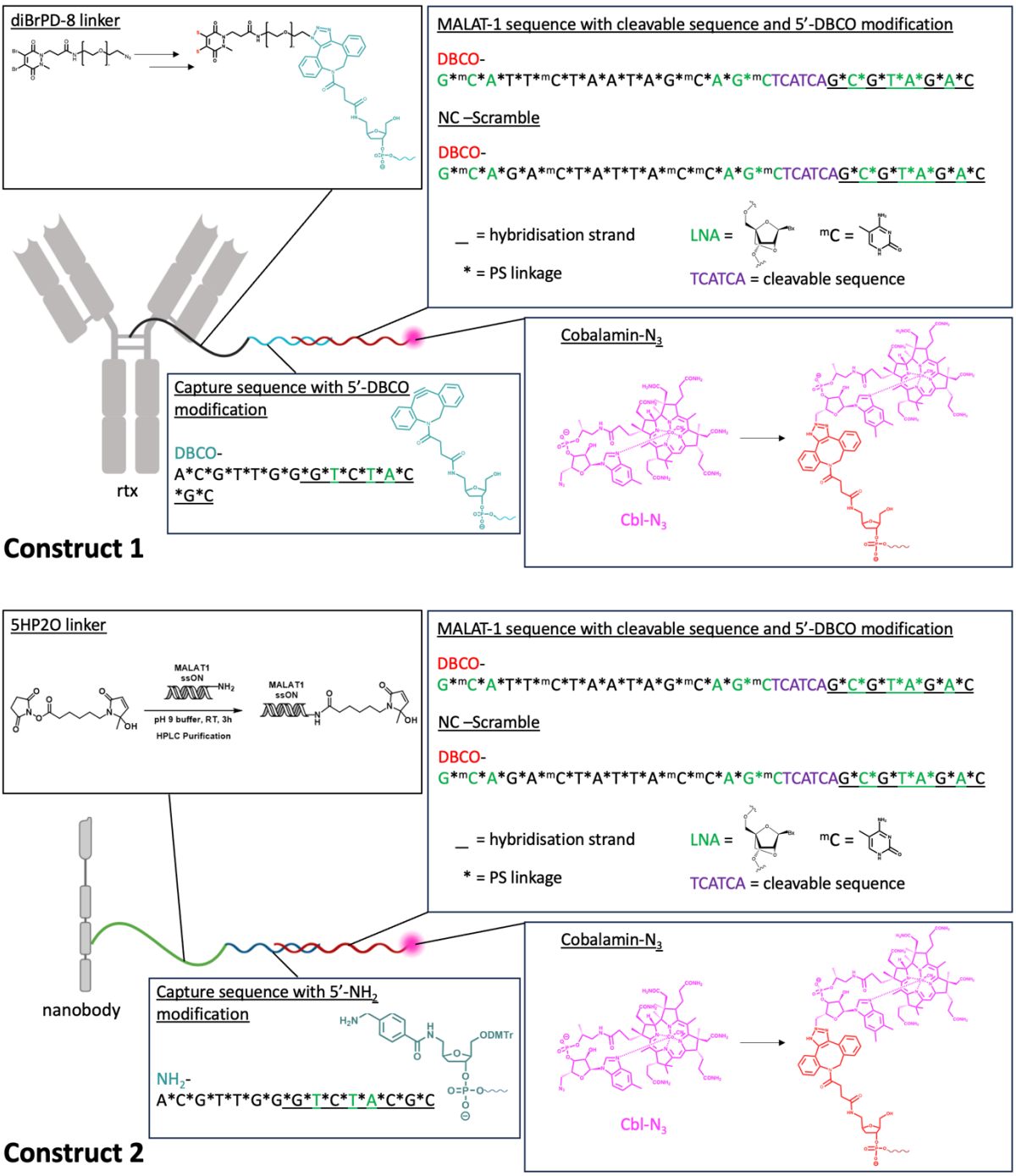

Figure 68 Schematic representation of the proposed cobalamin-based delivery constructs. Construct 1 with rtx conjugated via a diBrPD-8 linker to C2, hybridised with a M1 functionalised with a 5'-Cbl modification. Construct 2 incorporates a CD20-targeting nanobody linked to the capture sequence using a 5HP2O linker. Both designs use Watson-Crick base pairing for hybridisation and include cleavable TCA sequences for efficient ASO release.

In the proposed construct, each component was carefully selected to fulfil a specific role. The antibody rtx is specifically targeting the CD20 receptor on B cells, while the diBrPD-8 linker rebridged interchain disulphide bonds to maintain the integrity of the antibody and enable SPAAC conjugation through the terminal azide. C2 is a capture strand that hybridises to M1 *via* Watson-Crick base pairing to minimise the complexity of modifying both oligonucleotide termini.

The selection and design of the therapeutic ASO sequence M1 was based on previously validated constructs commonly used at AstraZeneca[127, 128]. A few modifications were introduced for functionality, for example M1 incorporated two TCA sequences to enable endonuclease cleavage and therefore ensuring efficient release of the ASO. The therapeutic segment of the ASO was designed as a gapmer with a fully phosphorothioated (PS) backbone for nuclease resistance. This modification ensures prolonged stability and enables efficient binding to the target RNA. Additionally, the sequence was extended by 8 nucleotides on the 3' side to allow hybridisation to the capture strand C2. C2 comprised three locked nucleic acid (LNA) nucleotides to ensure duplex stability under physiological conditions at 37°C.

In comparison to previous reports, the ASO synthesised at RISE incorporated LNA modifications instead of constrained ethyl (cET) modifications. This decision was driven by availability of phosphoramidites at RISE.

The development and evaluation of the proposed AOCs involved contributions from multiple collaborators, each fulfilling specific functions for distinct aspects of the project. Oligonucleotide synthesis and characterisation was performed by Mónica Lopes at RISE. Monica Fresta at Ghent University was responsible for functionalisation and purification of

Cbl to produce Cbl-M1 conjugates. The constructs behaviour was evaluated in serum and cellular environments, stability and cleavage assays were conducted by Laura Reyes Fraile at Sixfold Bioscience. The University of Southampton was responsible for the assembly of the final construct and led *in vitro* testing to investigate its functionality and therapeutic efficacy. Despite the efforts made, the synthesis and assembly of construct 2 at Ghent University was faced with significant challenges and could not afford the desired nanobody which hindered the successful assembly of construct 2.

5.1.2 Characterisation of the construct

The successful assembly through hybridisation of C2 and M1 was verified using native PAGE (**Figure 69A**), and melting curve analysis revealed a Tm of 69.05°C (**Figure 69B**) which confirms duplex stability under physiological conditions at 37°C.

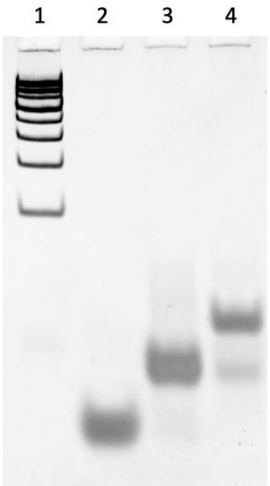

Figure 69A 10% native PAGE gel (80V 90 min 1X TB), lane 1: 100 bp DNA ladder, lane 2: C2 single strand 15 b, lane 3: M1 single strand 30 b, lane 4: C2-M1 duplex

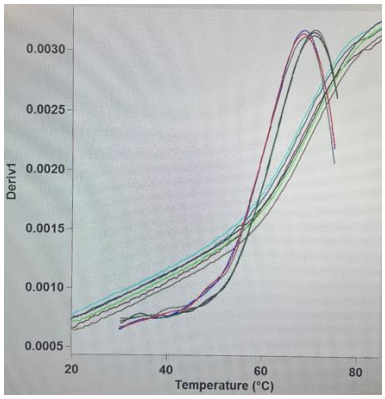

Figure 69B Melting curve analysis of the C2-M1 duplex, demonstrating a Tm of 69.05°C. The high melting temperature indicates robust duplex stability under physiological conditions.

At Sixfold Biosciences, Laura Reyes Fraile evaluated the behaviour of the C2-M1 duplex in various conditions to validate its stability for subsequent assays. In the first instance, studies aimed at the evaluation of the susceptibility to degradation of the duplex in environments mimicking physiological and intracellular conditions and thereby provides insights into the longevity of the oligonucleotide construct.

The stability evaluation in extracellular conditions was assessed through the incubation of the C2-M1 duplex in 55% fetal calf serum (FCS) in RPMI medium[129, 130]. After 24 hours of incubation, the construct was run on a PAGE gel to identify potential degradation. The gel revealed no significant degradation of the duplex which indicates duplex stability in extracellular environments. These findings validate the stability of the oligonucleotide design incorporating the PS backbone and LNA which are both known to enhance nuclease resistance.

For investigations mimicking the intracellular environment, Fraile incubated the single oligonucleotides with tritosomes which are subcellular fractions enriched with endonucleases, lysosomal enzymes, and other proteolytic components. This model simulates

the conditions that the construct would encounter after endocytosis. After an incubation period of 72h, the single oligonucleotides showed minimal degradation which can be attributed to the chemical modifications. However, when the C2-M1 duplex was analysed, partial degradation was detected at 72h incubation time. The assay involved the analysis of the samples through mass spectrometry and for the C2-M1 duplex specific cleavage patterns indicative of enzymatic processing by endonucleases at both the TCA cleavage site and within the therapeutic region of the ASO were observed. These findings suggests that the duplex remains mostly intact over short periods, but prolonged exposure to intracellular nucleases eventually leads to fragmentation. Despite this observed degradation, the functional efficacy of the ASO should hypothetically remain unaffected as the primary mechanism of action relies on rapid hybridisation of the ASO to target RNA. This process is likely to occur before significant degradation takes place.

The conjugation of rtx to diBrPD-8 (rtx-diBrPD-8) followed the established protocol described in section 3.2.2. The SPAAC reaction was performed using C2 which comprises a DBCO modification. The successful assembly was confirmed through SDS-PAGE (**Figure 70A**) and SEC (**Figure 70B**).

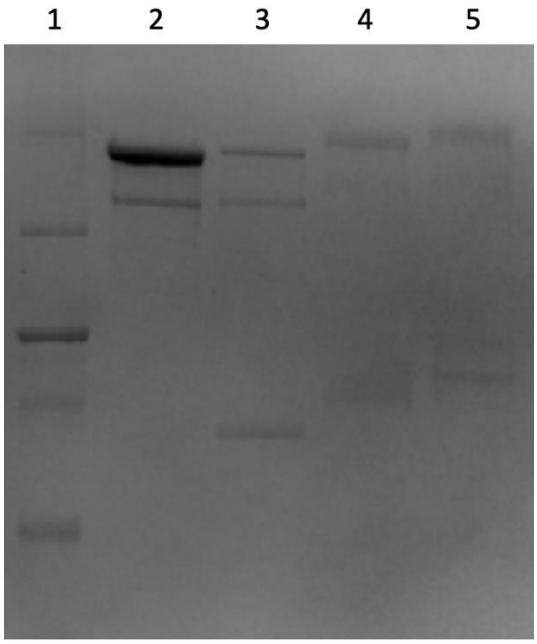

Figure 70A 8% SDS-PAGE under non-reducing conditions (250 V, 30 min), lane 1: Novex™ Sharp Prestained Protein Standard, lane 2: rtx, lane 3: rtx-diBrPD-8, lane 4: rtx-diBrPD-8-C2, lane 5: rtx-diBrPD-8-C1

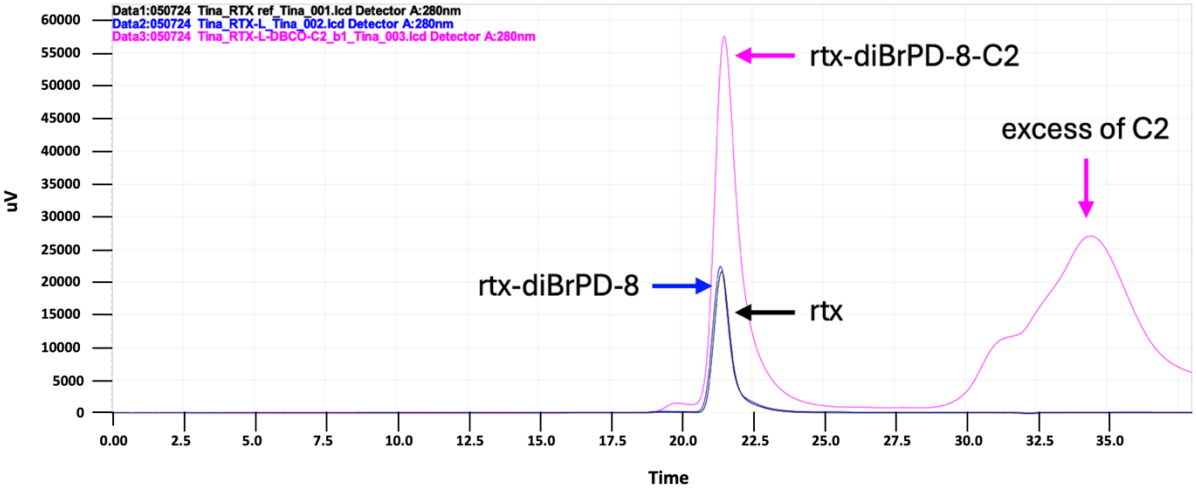

Figure 70B Size exclusion chromatography trace on a HPLC system of different rtx constructs. The black trace represents the unmodified rtx and the blue trace shows rtx-diBrPD-8. The pink trace corresponds to rtx-diBrPD-8-C2. The peak at ~35 min represents excess of unreacted C2.

After conjugation, rtx-diBrPD-8-C2 was purified by SEC in PBS, and post-purification analysis confirmed the absence of unconjugated antibody and excess of C2 (**Figure 71**).

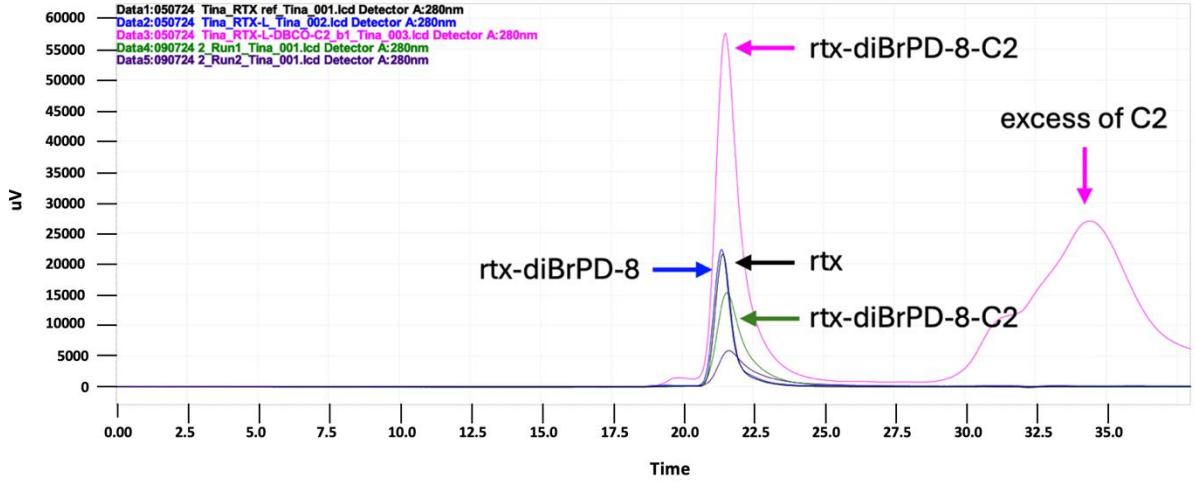

Figure 71 Size exclusion chromatography trace on a HPLC system of different rtx constructs after purification. The black trace represents the unmodified rtx and the blue trace shows rtx-diBrPD-8. The pink trace corresponds to rtx-diBrPD-8-C2. The peak at ~35 min represents excess of unreacted C2. The additional green line represents the purified rtx-diBrPD-8-C2 without the excess of C2.

To evaluate the binding efficiency of the oligonucleotide-conjugated construct, a binding assay was performed as previously described in section 4.3.2. Similarly to the evaluation of previous AOCs, this assay was used to evaluate the influence on receptor binding capacity caused by conjugation of C2 to rtx-diBrPD-8.

As previously seen, the results revealed a minimal decrease in binding across all tested concentrations following conjugation (**Figure 72**) which indicates that the addition of the oligonucleotide did not significantly impair the receptor recognition of the antibody. It is hypothesized that the slight reduction in binding efficiency may be attributed to steric hindrance introduced by the oligonucleotide C2. However, the observed binding levels

remained sufficiently within the expected functional range which should not negatively affect effective receptor targeting during future experiments.

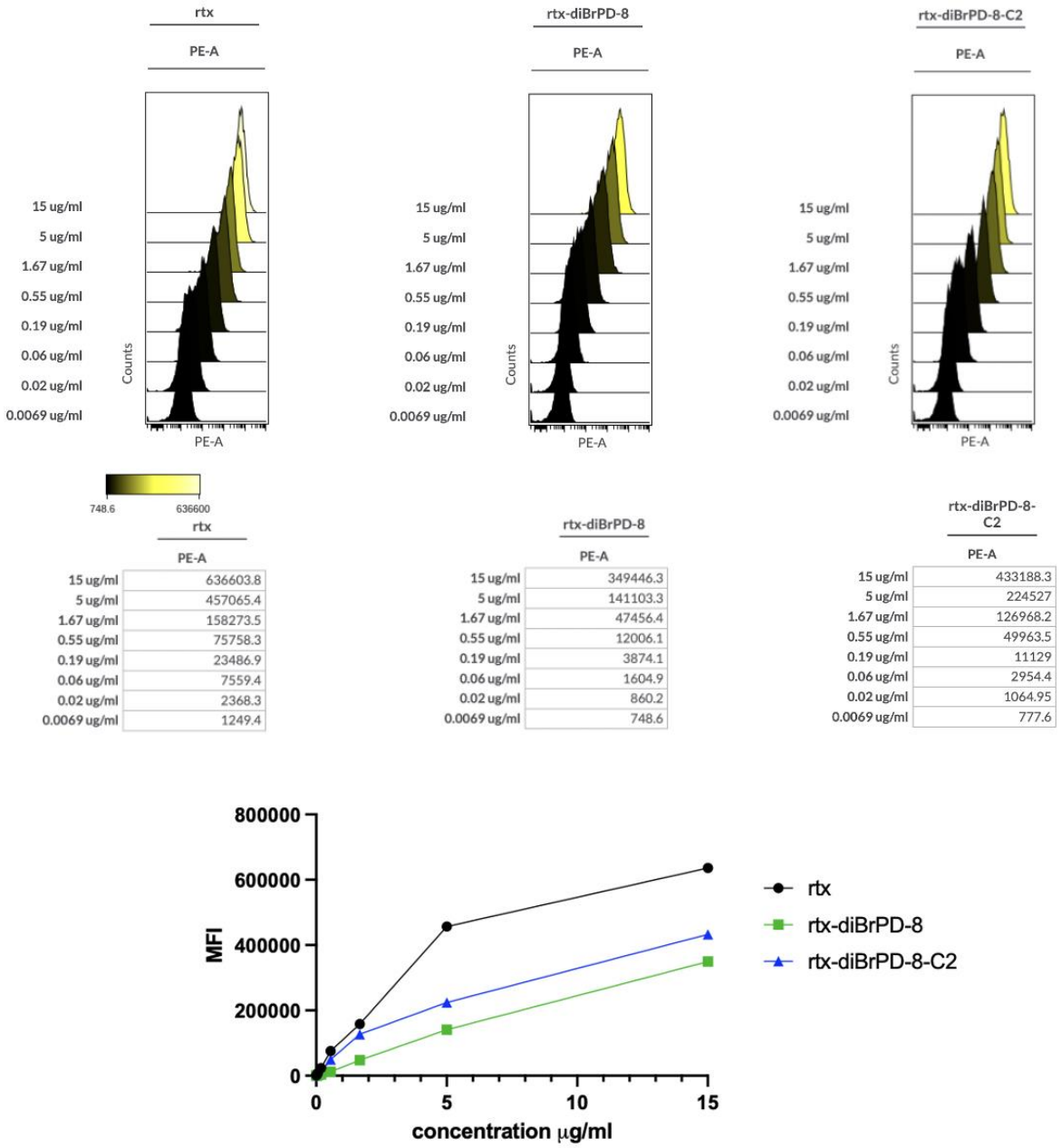

Figure 72 Binding assay of rtx-diBrPD-8 and rtx-diBrPD-8-C2 in Daudi cells. Histograms (top) display PE signal intensity across 1:3 serial dilution series for control antibody rtx, rtx-diBrPD-8 and rtx-diBrPD-8-C1 incubated with Ramos cells. MFI values (bottom)

are plotted against antibody concentration, showing dose-dependent binding curves for both constructs.

5.1.3 Functional assessment of the construct

Before the assembly and testing of the complete antibody-oligonucleotide construct, preliminary assays were conducted to determine a suitable concentration range at which the ASO would exert a downregulating effect on MALAT1 RNA using a transfection agent to ensure nuclear delivery. In the first experiments, four concentrations were tested, starting at 10 nM and increasing by tenfold to 10 µM. Cells were incubated with the M1 ASO at the given concentrations while one set utilised Lipofectamine 3000 and enhancer P3000 for efficient transfection and the other set only involved coculture with the naked M1 to explore any passive gymnotic uptake. After a 24h co-culture, the cells were lysed and the RNA extracted. The RNA was then converted to cDNA and analysed in a RT-qPCR assay to evaluate MALAT1 gene expression (**Figure 73**). The results indicated that at 10 nM, no measurable effect was observed for gymnosis and transfected samples. At 100 nM, a slight downregulation was noted in transfected samples which suggest that this concentration might serve as an initial starting point for further experiments. However, the error bars indicate that these preliminary findings required optimisation, and these results should be interpreted cautiously.

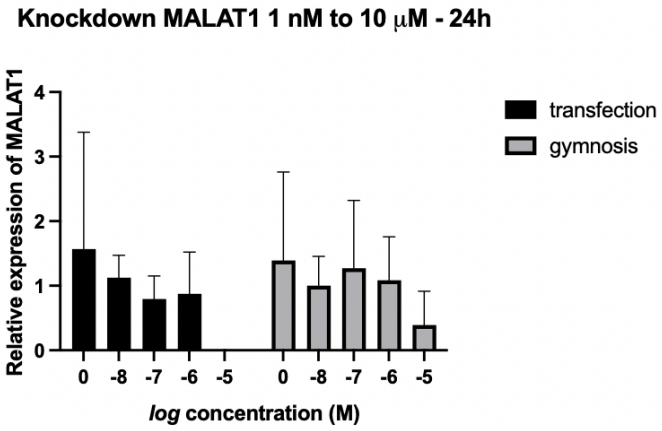

Figure 73 Quantification of MALAT1 knockdown following 24-hour treatment with antisense oligonucleotide M1 (ASO) across a concentration range of 1 nM to 10 μM (n=1). Relative MALAT1 expression levels were assessed under two delivery conditions: transfection (black bars) and gymnosis (grey bars). Data are presented as mean ± standard deviation from triplicates (three biological replicates and each with three technical replicates), showing a dose-dependent knockdown effect, with transfection achieving a higher downregulating effect in MALAT1 expression compared to gymnotic uptake.

In subsequent experiments, we explored the uptake and functional efficacy of Cbl-M1, transfected M1, and gymnotic M1 and compared their effectiveness at a treatment concentration of 100 nM. After 24 hours of incubation, we observed minimal downregulation of MALAT1 for all samples with no statistical significance compared to untreated controls. These observations led to the extension of the incubation period to 48 hours led and a significant downregulating effect in transfected samples was perceived and no notable effect was observed for either Cbl-M1 or gymnotic M1 constructs (**Figure 74**). These findings suggested that the treatment concentration might have been insufficient to induce uptake through the Cbl pathway and therefore the ASO was not delivered to the nucleus to exert its

function. Thus, treatment concentration was increased to 1 µM in the next set of experiments. The results showed significant downregulation of MALAT1 was achieved in both transfected and Cbl-M1-treated samples after 24h incubation time. By 48h, almost complete gene knock-down was achieved for transfected samples, while Cbl-M1-treated cells showed higher relative MALAT1 expression levels than at 24h. The reduced MALAT1 expression levels for gymnosis samples at 48h indicate the uptake of the oligonucleotide in the absence of transfection reagents over time.

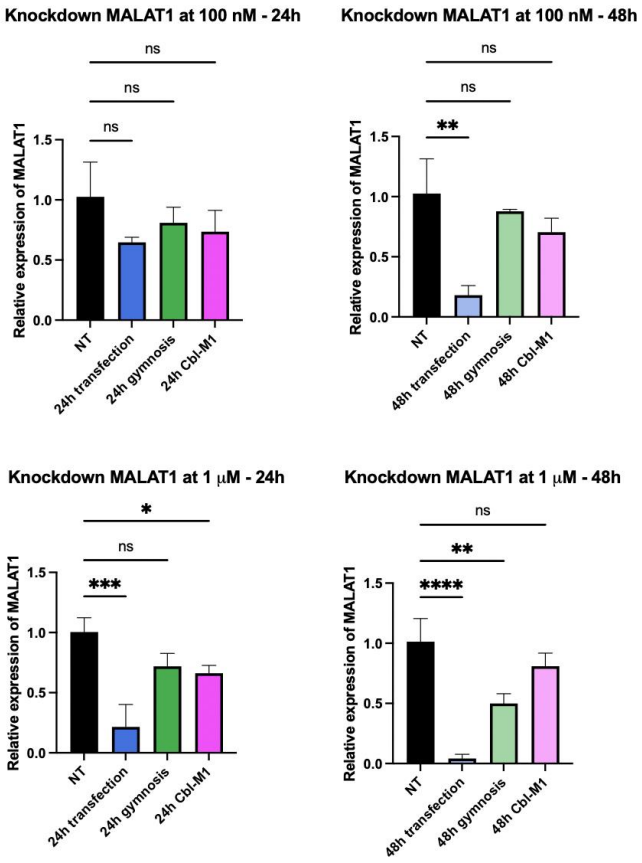

Figure 74 RT-qPCR results for MALAT1 downregulation using Cbl-M1 constructs, gymnotic uptake, and transfection with Lipofectamine 2000. No significant knockdown was observed at lower concentrations (100 nM; n=1), but at 1 µM (n=2), significant downregulation was achieved in transfected and Cbl-M1-treated samples.

Repeated experiments confirmed these findings and revealed a consistent pattern: naked oligonucleotide M1 achieved a downregulation effect comparable to Cbl-M1 at the same treatment concentration. This unexpected result led to a thorough literature review with the hypothesis that the uptake of M1 was mediated through gymnosis instead of the proposed Cbl pathway.

5.1.4 Discussion

A report[131] on cobalamin receptors and their saturation levels indicated that cobalamin receptors are rapidly saturated at relatively low Cbl-TC complex concentrations. It has been suggested that following internalisation, the receptor-ligand complex undergoes endocytosis and then degradation in the lysosome without supporting evidence of receptor recycling back to the cell surface. In previous studies[131], treatment with 22 pM of the Cbl-TC complexes resulted in receptor saturation at a cell seeding concentration of 10^6 cells/ml across diverse cell lines such as HL60, K562 and HEK293. In our experiments, 0.4×10^6 cells/ml were treated with 1 µM Cbl-M1, representing approximately 2/5 of the cell density used in the prior work and with a 100,000-fold higher ligand concentration. This excess likely led to rapid receptor saturation on all cells which limited the uptake of our therapeutic cargo *via* the cobalamin pathway. Based on these calculations, it is hypothesised that the downregulation observed in our experiments was mainly due to gymnotic uptake of M1 and that only a very small amount (<0.0001%) was entering the cells *via* the proposed Cbl pathway.

Due to these encountered limitations of receptor saturation the cobalamin-mediated strategy was not pursued further in the context of ASO delivery. Since rtx is known to undergo receptor-mediated internalization, we tested whether the assembled antibody-oligonucleotide construct could achieve functional knockdown independently of cobalamin.

Despite these efforts, 24-hour co-culture with the antibody-oligonucleotide complex did not show any significant downregulation of the target mRNA and therefore the project was not further investigated.

While the hypothesis of exploiting the cobalamin pathway for oligonucleotide delivery presented an innovative approach, the saturation dynamics of TCblR limited its practical application. The extensive time and resources invested gave valuable insights and proved the unsuitability of this approach for the delivery of ASOs. In the search of further approaches to deliver ASOs efficiently, alternative receptor-mediated pathways with more abundant or recyclable surface receptors should be considered and may offer benefits.

This subproject demonstrated how important the critical evaluation of receptor expression levels and ligand-receptor dynamics, such as receptor saturation and turn over, during the design phase is and highlights a key characteristic for receptor-targeted approaches. Although this particular idea did not afford the desired results, the knowledge gained is very beneficial for future strategies and can be applied for other design approaches.

5.2 Bispecific antibody conjugates

While exploring Cbl-mediated delivery contributed to important findings and indicated main limitations including receptor saturation and limited recycling, a new opportunity for an alternative strategy exploiting receptor-specific internalisation mechanisms arose. Bispecific antibody-oligonucleotide conjugates were presented as a promising approach to enable the targeted delivery of ASOs.

With the dual specificity of bispecific antibodies, benefits like simultaneous engagement of target antigens and payload internalisation could be combined. The internalising properties

of antiCD40 antibodies were taken advantage of to develop a modular and adaptable oligonucleotide delivery platform. The design was based on previous constructs explored by Strike Pharma (antiCD40) and employed the Adaptive Drug Affinity Conjugate (ADAC) technology[132, 133], conceptualised by Ulf Tedebark and Jan H. Meffert.

This construct was engineered to include two anti-peptide Tag single-chain variable fragments (antipTag scFv) which allow the non-covalent attachment of peptide Tags (pTag). The inclusion of the anti-pTag scFv ensure high-affinity and site-specific binding of the pTag, while the antibody retains its structural integrity and agonistic activity. Previously published results showed successful application in the delivery of cancer-specific peptides which resulted in improved T Cell proliferation and anti-tumour immunity in mice[132]. In this project, it was investigated whether this platform is equally suitable for the delivery of ASOs in the context of gene modulation. RNase H1-dependent ASO gapmer M1 designed to target MALAT1 RNA was selected as the therapeutic cargo. Optimised protocols for the *in vitro* evaluation were established previously. The included 8-mer DNA overhang is complementary to a peptide nucleic acid (PNA) strand that is directly connected to the pTag, named pTagPNA. The full construct could be seamlessly assembled through hybridisation between M1 and the pTagPNA to form a duplex that non-covalently binds to anti-pTag scFv of the bispecific antibody forming antiCD40-pTagPNA:M1 (**Figure 75**).

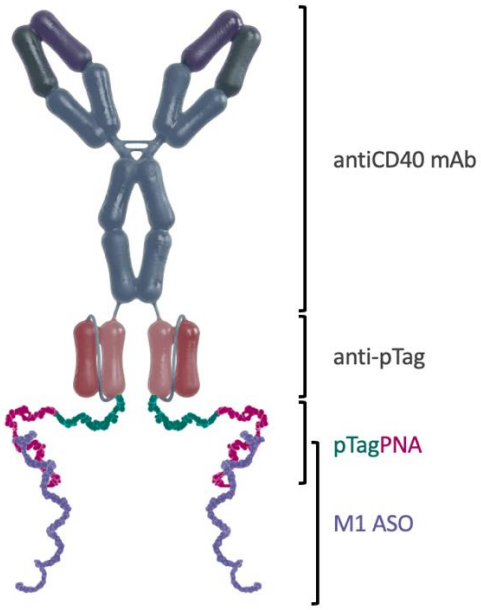

Figure 75 Schematic presentation of antiCD40-pTagPNA:M1. The construct incorporates a CD40-targeting bispecific antibody with high-affinity anti-pTag scFv fragments, hybridised with M1 through pTagPNA for stable oligonucleotide attachment. Reproduced with permission of the rights holder (Jan H. Meffert).

The known stability across a broad spectrum of pH and temperature ranges, low immunogenicity and higher resistance to enzymatic degradation guided the choice of PNA as the hybridising moiety in this construct. These characteristics make PNA well-suited for the use in biological environments where DNA or RNA are prone to degradation. Furthermore, PNA:DNA duplexes demonstrated increased stability compared to DNA:DNA duplexes as the neutral backbone of PNA reduces electrostatic repulsion between the hybridising strands. The PNA:DNA hybrid forms a more compact duplex, which could be beneficial for construct stability and oligonucleotide delivery in cellular environments. Additionally, practical considerations also played a role in the selection of PNA over DNA. The pTagPNA was synthesised and purified in a single step using automated Fmoc solid-phase peptide synthesis which bypassed required more complex conjugation strategies to connect DNA with peptides.

The isolated PNA strands were characterised using LC-MS by Jan H. Meffert at Ghent University.

Additionally, the modular nature of this design enables a simple assembly process which does not involve any complex chemistries typically required in covalent conjugation strategies. This strategy reduces preparation time and increases the scalability of AOCs.

5.2.1 Conjugate assembly and characterisation

The final AOC, antiCD40-pTagPNA:M1, was assembled using a two-step approach. First, M1 was hybridised to the pTagPNA and then attached to the antibody (antiCD40) through affinity conjugation (**Figure 76**). The hybridisation was performed at equimolar concentrations by heating to 95°C followed by cooling on ice to ensure stable duplex formation. The resulting PNA:DNA duplex was characterised by a melting experiment and revealed a Tm of 47°C which confirmed thermal stability under physiological conditions. The second step involved the high-affinity conjugation between the anti-pTag fragment of the bispecific antibody and the pTagPNA, enabling the non-covalent attachment of the hybridised pTagPNA:M1 duplex. Affinity loading was performed at controlled molar ratios (1:1 and 1:2). Two variants of the pTag peptide were evaluated in this study: pTag(K), which includes a positively charged lysine at position 8 and pTag(L), containing a hydrophobic leucine instead at the same position. These variants were carefully selected in order to investigate if and how differences in amino acid properties would influence conjugation efficiency, binding behaviour, and overall functionality.

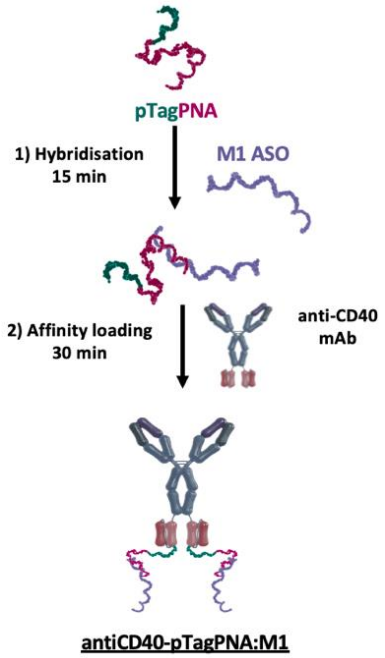

Figure 76 Schematic representation of the assembly process for the antiCD40-pTagPNA:M1 construct. In the first step, the M1 antisense oligonucleotide (ASO) is hybridised to the complementary pTagPNA sequence for 15 minutes to form a stable duplex. In the second step, the hybridised duplex is loaded onto the antiCD40 monoclonal antibody (mAb) *via* high-affinity binding to the anti-pTag scFv fragments, completing the assembly within 30 minutes at room temperature. Reproduced with permission of the rights holder (Jan H. Meffert).

The constructs were characterised using SEC performed on HPLC and native SEC-MS to confirm successful conjugation, the latter performed at Recipharm by Matthijs Pijnappel. Simple SEC analysis was unable to resolve or confirm successful conjugation as only an increase of aggregated antibody was detected (**Figure 77**).

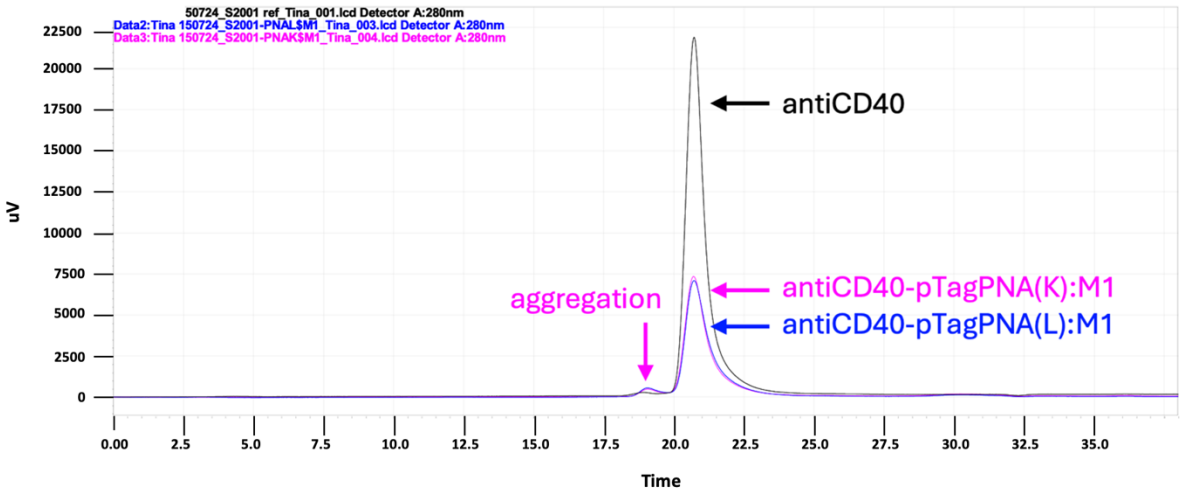

Figure 77 Size exclusion chromatography trace on an HPLC system of antiCD40-pTagPNA(K) and antiCD40-pTagPNA(L) in comparison with antiCD40 with increased aggregation observed after affinity loading.

Native SEC-MS analysis was able to resolve unmodified antibodies, single-loaded, and double-loaded conjugates when investigating antiCD40-pTagPNA (**Figure 78**). With 1:2 loading ratios, for the pTag(K) variant nearly no signal was detected corresponding to unbound antibody indicating high conjugation efficiency. In contrast, the pTag(L) variant showed detectable peaks for unbound antibody, likely due to weaker binding interactions. This difference might be explained by the positive charge of the lysine side chain which promotes stronger electrostatic interactions with the anti-pTag fragment. Leucine is a hydrophobic amino acid and relies on weaker van der Waals interactions which might lead to reduced binding affinity.

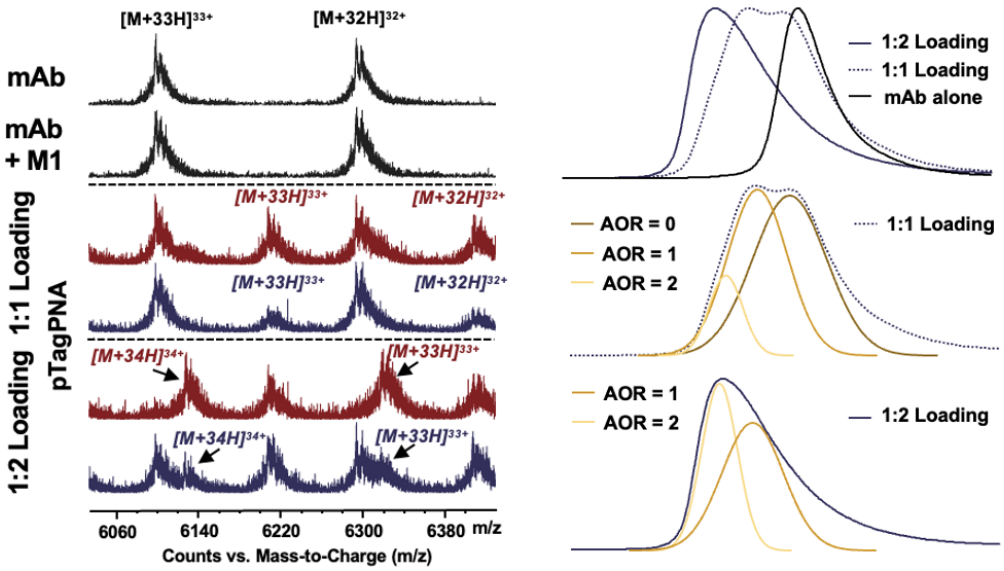

Figure 78 Left: Mass spectra of affinity loading reactions for bispecific antibody constructs with pTag(K)PNA (red) and pTag(L)PNA (blue). Loading was performed using one (1:1) and two (1:2) equivalents of pTagPNA. Peaks representing the mass fragments of the antiCD40 and antiCD40-pTagPNA:M1 are highlighted.

Right: Size-exclusion chromatography (SEC) chromatograms of the loading reactions for both pTagPNA:M1 hybrids at one (1:1) and two (1:2) equivalents. The distinct shifts indicate successful hybrid formation and mAb loading. Reproduced with permission of the rights holder (Jan H. Meffert).

The analysis using native SEC-MS of affinity loading of the pTagPNA:M1 duplex onto antiCD40 showed peak shifts indicating successful loading of the duplex onto the antibody. However, due to overlapping SEC signals (**Figure 79**), a fully quantitative comparison of antibody-oligonucleotide ratios was challenging. While the results confirmed efficient conjugation, they also revealed that complete loading of all anti-pTag binding sites was not consistently achieved. However, this incomplete loading was found acceptable for the purposes of the presented *in vitro* study.

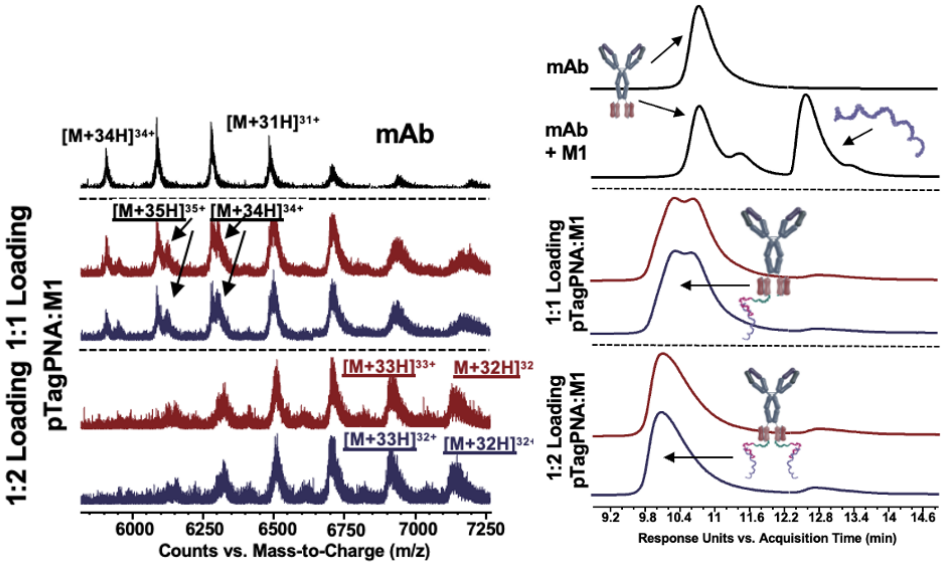

Figure 79 Left: Mass spectra extracted from SEC chromatograms comparing loading efficiency for pTagPNA:M1 hybrids at one (1:1) and two (1:2) equivalents with pTagPNA(K) (red) and pTagPNA(L) (blue). Key mass fragments corresponding to the loaded antibody constructs confirm distinct loading profiles for lysine and leucine-containing pTagPNAs.

Right: Overlaid SEC chromatograms of the naked mAb and crude loading reactions of pTagPNA(L):M1 hybrids at 1:1 and 1:2 equivalents, illustrating the shifts corresponding to different AORs. Reproduced with permission of the rights holder (Jan H. Meffert).

5.2.2 Functional assays: evaluating gene knockdown and antibody-binding specificity

In vitro experiments were conducted to assess the functionality of these constructs and to confirm the receptor-specific targeting and internalizing capabilities of the bispecific antibody platform in delivering ASOs.

While looking for a suitable cell model for the evaluation of CD40-mediated delivery, three lymphoma cell lines were investigated for their CD40 expression levels. Two of these were malignant B-cell lines: Daudi cells, derived from the peripheral blood of a 16-year-old male

patient with Burkitt's lymphoma, and Ramos cells, isolated from a 3-year-old male patient with Burkitt's lymphoma. Additionally, JeKo-1 mantle cells, originating from a 78-year-old female patient with a large-cell variant of mantle cell lymphoma and leukemic conversion, were included in the evaluation.

CD40 expression levels were quantified using an antiCD40 antibody conjugated to allophycocyanin (APC) to measure MFI. The results (**Figure 80**) revealed significant differences in CD40 expression among the cell lines. Daudi cells displayed the highest levels of CD40, with MFI values approximately double those from Ramos cells and substantially higher than those from JeKo-1 cells.

Based on these findings, we chose Daudi cells as the primary model for subsequent assays. Their high CD40 expression makes them an optimal choice for investigating the efficacy and specificity of CD40-targeted antibody-oligonucleotide constructs.

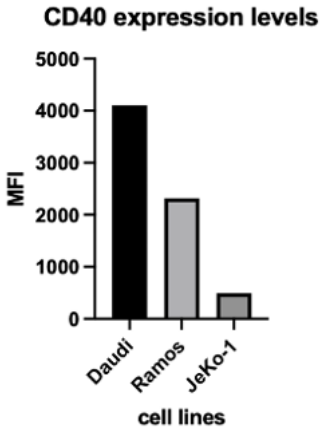

Figure 80 CD40 expression levels in lymphoma cell lines (n=1). Flow cytometry analysis quantifies relative CD40 expression in Daudi, Ramos, and JeKo-1 cells, with Daudi cells exhibiting the highest expression levels.

Reverse transcription quantitative PCR (RT-qPCR) was used to evaluate gene knockdown activity by measuring relative MALAT1 RNA levels. We investigated various conditions, including transfection, gymnotic uptake and incubation with the bispecific antibody-oligonucleotide conjugates (antiCD40-pTagPNA:M1) at different incubation times and different AORs.

5.2.2.1 Gene knockout assays

As discussed in section 5.1.3 (**Figure 73**), the knockdown experiments demonstrated a clear concentration-dependent downregulation of MALAT1 target RNA. At a concentration of 1 µM, transfection with Lipofectamine 2000 induced significant knockdown of MALAT1 after 24 hours, with a greater gene knockout effect seen after 48 hours. Knockdown was also achieved through gymnotic uptake at this concentration resulting in moderate, but statistically significant downregulation after 48 hours.

At a lower concentration of 100 nM, the knockdown effect was less pronounced. Transfected samples exhibited statistically significant silencing, whereas gymnosis did not achieve any significant effect on relative gene expression.

Initial experiments with the antiCD40-pTagPNA:M1 constructs aimed to simulate a 1:1 binding ratio of antibody and pTagPNA:M1 using a final oligonucleotide concentration of 50 nM. However, a calculation error during the hybridisation step resulted in an excess of PNA(L), with approximately 1.5 times more added than intended. This miscalculation led to the possibility of unhybridised PNA(L) binding to the antibody during the affinity binding step, creating variability in the conjugation outcome. Additionally, while the intention was to achieve a single pTagPNA:M1 per antibody, the inherent stochastic nature of the conjugation

process likely resulted in a mixture of antibodies bearing no, one, or two pTagPNA:M1 molecules.

Despite these limitations, initial findings (**Figure 81**) showed that both antiCD40-pTagPNA(L):M1 and antiCD40-pTagPNA(K):M1 constructs were able to achieve a reduction in relative MALAT1 expression compared to the NT control. Interestingly, antiCD40-pTagPNA(L):M1 showed a slightly more pronounced effect which could be due to the excess PNA(L) added during hybridisation. The following experiments explored whether increasing the equivalents of pTagPNA:M1 on the antibody could increase knockdown efficiency. All samples displayed statistically non-significant MALAT1 downregulation compared to the NT control (**Figure 81**). Encouragingly, antiCD40-pTagPNA(K):M1 at a 1:1 ratio consistently demonstrated a comparable downregulation effect across repeated experiments. The increased activity of antiCD40-pTagPNA(L):M1 observed in earlier experiments was likely due to variations in conjugation from the initial calculation error.

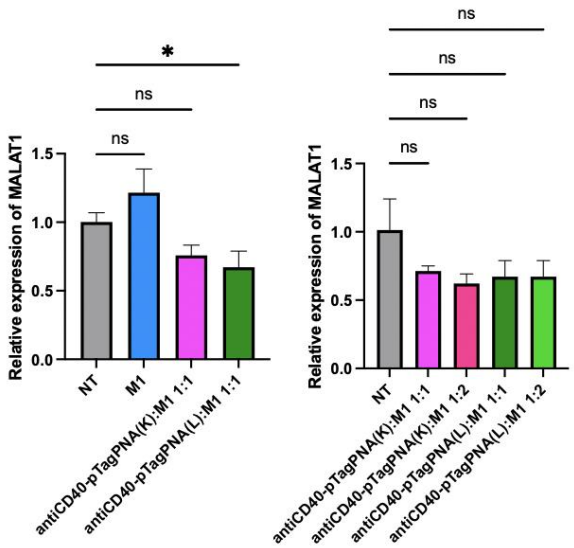

Figure 81 RT-qPCR results for MALAT1 knockdown using bispecific constructs at 50 nM and 100 nM concentrations. Both antiCD40-pTagPNA(K):M1 and antiCD40-

pTagPNA(L):M1 constructs achieved approximately 60% MALAT1 downregulation at 50 nM. Error bars represent standard deviations from three independent experiments. Statistical significance was assessed using one-way ANOVA (ns = not significant).

When comparing 1:1 and 1:2 AORs, no significant differences in MALAT1 downregulation were observed. To refine the experimental setup, longer incubation times were included in subsequent assays, as well as scrambled sequence controls (antiCD40-pTagPNA(L):Scr or antiCD40-pTagPNA(K):Scr). Gymnotic uptake of free pTagPNA(L):M1 and pTagPNA(K):M1 was also evaluated. In these experiments the hybridisation miscalculation from the earlier assays was noted and corrected. However, the results were less consistent, with a weaker downregulation effect across all samples compared to the NT control (**Figure 82**). There was no clear benefit observed for the 1:2 constructs, leading to a focus on the 1:1 ratio for future experiments. Subsequent assays were conducted using fixed antibody concentrations of 50, 100, and 150 nM with a standardised incubation time of 24 hours as extended incubation times showed no additional benefit either.

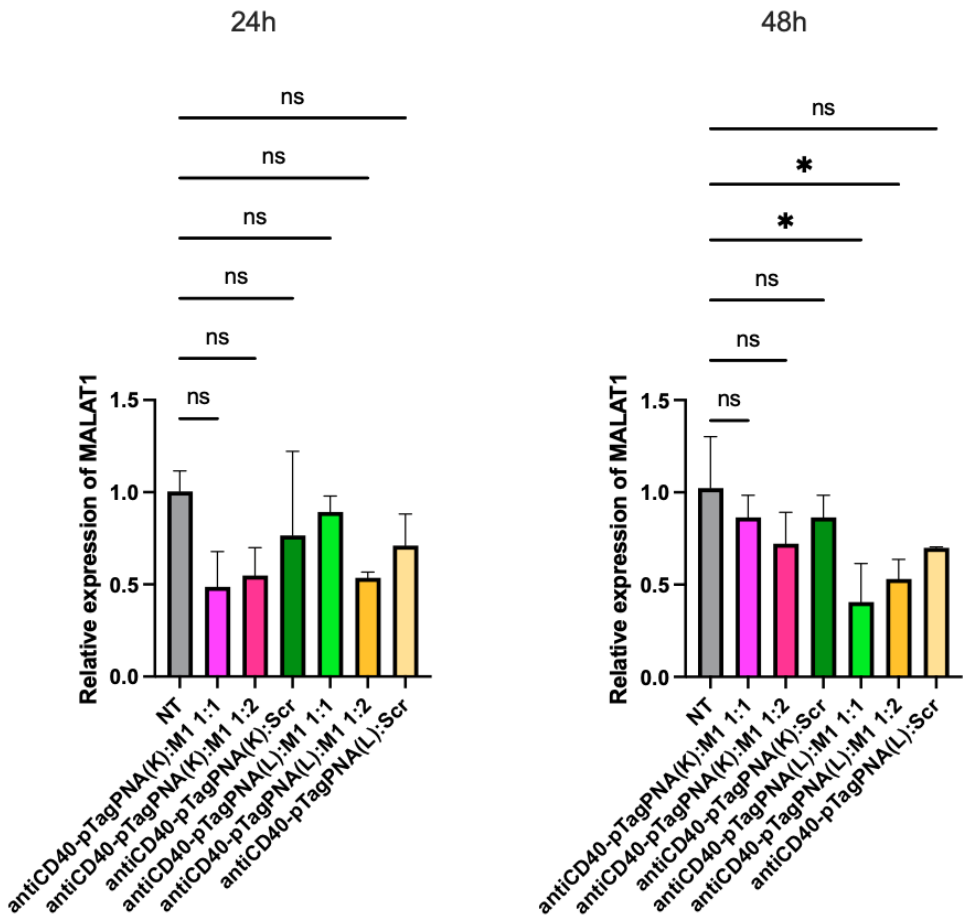

Figure 82 Comparison of MALAT1 knockdown across different antibody-oligonucleotide ratios. No significant differences were observed between 1:1 and 1:2 loading conditions, with both achieving effective silencing at lower concentrations. Error bars represent standard deviations from three independent experiments. Statistical significance was assessed using one-way ANOVA (ns = not significant).

Treated cells were now compared to cells stimulated with the antiCD40 antibody alone. Stimulated cells exhibited a slight but statistically insignificant increase in MALAT1 expression relative to the NT control. To provide a more accurate baseline, it was found appropriate to evaluate the effects of the antiCD40-pTagPNA:M1 constructs in relation to stimulated cells rather than to NT control. Although individual experiments suggested minor benefits at higher treatment concentrations (100 and 150 nM), pooled data from five independent experiments consistently revealed that only the 50 nM concentration achieved statistically significant

MALAT1 downregulation (**Figure 83**). Importantly, controls treated with antiCD40-pTagPNA:Scr constructs showed no changes in relative MALAT1 expression. In contrast, both antiCD40-pTagPNA(L):M1 and antiCD40-pTagPNA(K):M1 constructs achieved approximately 50% downregulation at 50 nM. Despite differences in conjugation efficiency observed during MS characterisation of the pTag variants, they did not translate into functional differences in MALAT1 downregulation. The findings indicate that both constructs effectively deliver sufficient therapeutic oligonucleotides to achieve robust gene silencing.

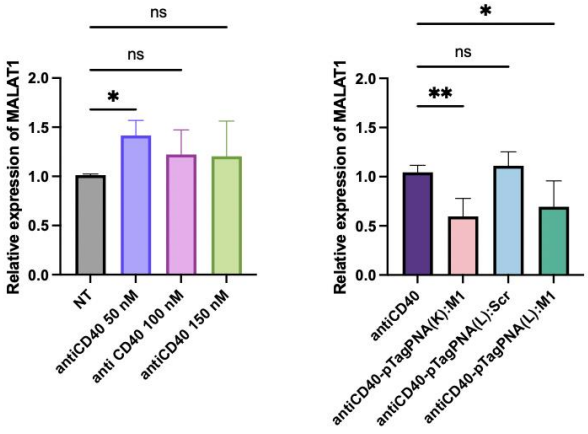

Figure 83 Relative expression of MALAT1 following treatment with antiCD40 and antiCD40-pTagPNA:M1 constructs at various concentrations. The first graph shows the influence on relative MALAT1 expression upon antiCD40 stimulation. The second graph highlights the specific knockdown achieved by antiCD40-pTagPNA(L):M1 and antiCD40-pTagPNA(K):M1 compared Scr controls, with significant silencing by antiCD40-pTagPNA(K):M1 (**$p < 0.01$) and antiCD40-pTagPNA(L):M1 (*$p < 0.05$). Error bars represent standard deviations from three independent experiments. Statistical significance was assessed using one-way ANOVA (ns = not significant).

5.2.2.2 Receptor specificity

To verify the specificity of these constructs for CD40-mediated delivery, an antiHER2 antibody with the same anti-pTag fragments was conjugated to pTagPNA(L):M1 and pTagPNA(K):M1 as controls. Upon co-culture with Daudi cells, no reduction in MALAT1 expression was observed (**Figure 84**) which supports the hypothesis that gene silencing was mediated by the CD40 receptor and its associated internalization pathway.

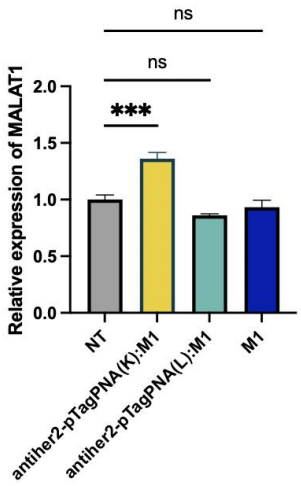

Figure 84 Functional evaluation of antiHER2-pTagPNA:M1 controls. No MALAT1 downregulation was observed in Daudi cells treated with antiHER2 constructs, confirming CD40-specific delivery of therapeutic oligonucleotides.

5.2.2.3 Internalisation assay

Receptor-mediated internalisation of the constructs was evaluated using flow cytometry in Daudi cells. Constructs were incubated with cells at 150 nM, and the internalisation process was monitored at 30 and 90 minutes at 37°C. Unbound antibodies were removed in two washing steps. Non-internalised, but bound antibodies were stained with a secondary PE-conjugated and Fcγ-specific secondary antibody which translates into measure MFI. A marked

reduction in surface fluorescence was observed at both time points compared to control samples maintained at 4°C, indicating temperature-dependent, receptor-mediated endocytosis (**Figure 85**). Over 80% of receptors were internalised within 90 minutes which is a confirmation for efficient uptake of the antiCD40-pTagPNA:M1 constructs via CD40-mediated pathways.

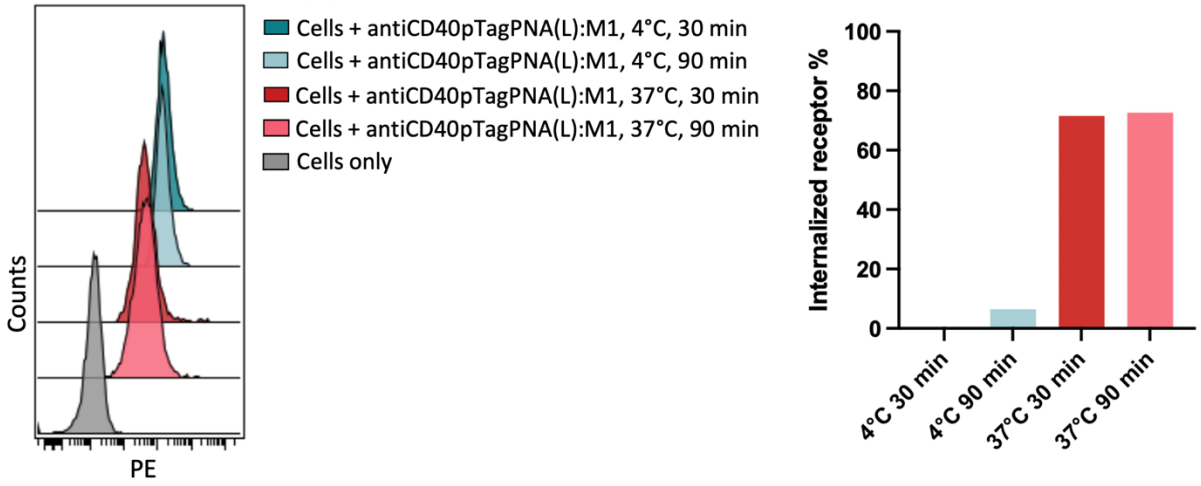

Figure 85 Internalization of bispecific constructs via CD40-mediated pathways. Flow cytometry data show time-dependent receptor-mediated endocytosis of antiCD40-pTagPNA:M1 constructs at 150 nM, with around 80% of receptors internalised within 90 minutes.

The chosen concentration of 150 nM may not represent the optimal range for all experimental conditions, but together with the knockdown data provided previously, these observations validate the functionality of the proposed construct. This assay represents additional evidence that confirms the effective engagement of the receptor and the delivery of the therapeutic oligonucleotide payload into cells. Despite potential limitations in representing other concentrations, these findings reinforce the capacity of the constructs to mediate gene silencing through receptor-specific internalisation.

5.2.3 Discussion

The modular design of the bispecific AOCs presented in this study represents a significant advancement in the field of targeted oligonucleotide delivery, particularly for challenging cell types like B cells. The high-affinity interaction between the anti-pTag scFv fragment and the pTag coupled to a PNA which hybridised to the therapeutic cargo M1, is a non-covalent, adaptable platform for therapeutic oligonucleotide delivery. The introduction of pTag variants (pTag(K) and pTag(L)) allowed to investigate how amino acid substitutions influence conjugation efficiency and functional performance, ultimately demonstrating the robustness and flexibility of the platform across variants.

The non-covalent approach simplifies the assembly of AOCs by eliminating the need for labour-intensive purification steps associated with covalent conjugation methods. The integration of the pTag system enables precise, site-specific loading of therapeutic oligonucleotides, dividing the process into two straightforward steps: annealing the pTagPNA with the ASO, followed by affinity loading onto the antibody. Native SEC-MS confirmed the successful assembly of constructs with a defined AOR. The system demonstrated efficient oligonucleotide loading without the need of excess reagents distinguishing it from classical covalent conjugation approaches that often require large excesses of oligonucleotide and higher protein concentrations for successful assembly.

The pTag(K) variant exhibited superior conjugation efficiency compared to pTag(L), likely due to its positively charged lysine residue enhancing electrostatic interactions with the anti-pTag fragment. Despite these differences, the functional performance of both variants in MALAT1 downregulation assays was close to equivalent.

The platform's efficacy in delivering MALAT1-targeting ASOs was validated through *in vitro* assays. In Daudi cells, which have high CD40 expression levels, the constructs successfully induced significant MALAT1 downregulation, with comparable results observed for both pTag variants. Interestingly, increasing the antibody-oligonucleotide ratio from 1:1 to 1:2 had no impact on knockdown efficiency. However, the constructs achieved levels of gene silencing comparable to lipofection-based transfection methods but at half the oligonucleotide concentration. Here, the potential of antiCD40pTagPNA:M1 as efficient delivery vehicles by minimise oligonucleotide dosage was clearly demonstrated.

One critical observation was the variability in knockdown efficiency across experimental replicates. This inconsistency may stem from limitations in endosomal escape or intracellular processing of the constructs. While extending the incubation time to 48 hours was hypothesised to positively impact delivery efficiency by allowing repeated receptor recycling cycles, the findings did not show significant improvements which indicates that the limitation was not based on receptor trafficking dynamics. Instead, the variability may arise from suboptimal endosomal escape of the oligonucleotide or delayed dissociation from the antibody construct.

Flow cytometry analyses demonstrated efficient internalization of the constructs within 30 minutes of incubation with an increase by 90 min incubation time. The quick internalization efficiency observed is another advantage of the construct and underlines the suitability of CD40 as a target for antibody-based delivery systems.

The findings of this study establish bispecific AOCs as a promising platform for targeted oligonucleotide delivery to B cells, with potential applications extending beyond MALAT1

silencing. The modularity of the system allows for seamless adaptation to other targets by simply modifying the oligonucleotide payload or the targeting antibody.

Future efforts shall focus on optimising endosomal escape mechanisms to further enhance oligonucleotide delivery efficiency. Incorporating endosomatic agents or modifying the linker region between the pTag and the PNA could facilitate oligonucleotide release into the cytosol. Additionally, exploring variations in the pTag sequence and their impact on binding affinity, conjugation efficiency, and intracellular trafficking dynamics will provide valuable insights for fine-tuning the platform for specific therapeutic applications.

Chapter 6 Summary and outlook

This work has explored the design, synthesis and functional characterisation of modular therapeutic platforms, focussing on antibody conjugates as targeted delivery systems in the context of cancer therapy. With the integration of innovative nanotechnology and bioconjugation strategies, this work has contributed to the growing field of DNA-based technologies and their application in precision medicine.

The key findings demonstrate the potential of these systems in targeted therapies. The design and functional assessment of NPs demonstrated their ability to insert into cellular membranes and exhibit cytotoxic effects at a concentration of 0.5 μM. Hydrophobic modifications enabled membrane spanning, while conjugation with rtx, an anti-CD20 monoclonal antibody would add specificity to B-cells. AOCs, assembled through diBrPD linkers, achieved site-specific conjugation with defined AORs. Functional assays confirmed the retention of the antibody's binding capacity and stability in tested conditions (summarized in **Figure 86**). Despite these promising findings, variability in cytotoxic effects seen from the different NP constructs could not achieve reproducible and reliable results. The need of further optimization in both NP design and functional assay methodologies is therefore strongly encourage to improve the functionalities of these nanostructures.

For NPs, future studies should focus on addressing structural stability and enhancing the reproducibility of cytotoxic effects. Real-time mechanistic studies, such as live-cell imaging, would provide additional insights into the interactions between NPs and the cellular membrane. Furthermore, increasing the size of the NPs could increase their activity and broaden their applicability to a wider range of cell types.

Construct	Names	Analysis performed
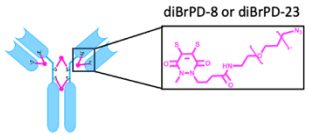	rtx-diBrPD-8 rtx-diBrPD-23	LC-MS SEC on HPLC SDS-PAGE Binding assay
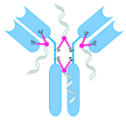	rtx-diBrPD-8-C1 rtx-diBrPD-23-C1 rtx-diBrPD-8-C2	SEC on HPLC SDS-PAGE Binding assay
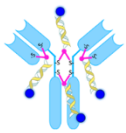	rtx-diBrPD-8-dsDNA rtx-diBrPD-23-dsDNA	Binding assay
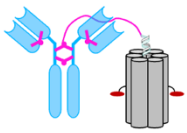	rtx-6HB-NP2c rtx-6HB-NP4c	Agarose gel electrophoresis Co-localisation assay (microscopy)
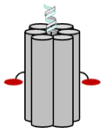	6HB-NP2c 6HB-NP3c 6HB-NP4c 6HB-NP1C18 6HB-NPk	Agarose gel electrophoresis Native PAGE Cytotoxicity assays Membrane association (microscopy)

Figure 86 Summary and overview of all tested constructs and the analysis performed

The technology of the proposed modular design was integrated into a parallel project exploring ASO delivery via the Cbl-pathway. While the assembly of these constructs was successfully confirmed and characterised through SDS-PAGE and LC-MS for antibodies conjugated to single oligonucleotides, significant challenges were encountered for the full characterisation of antibodies with dsDNA. An additional encountered limitation became apparent from receptor saturation at low concentrations which severely restricted the uptake of sufficient ASOs to achieve significant gene downregulation.

The exploration of bispecific antibodies with engineered tags enabling precise and controlled cargo attachments led to a significant advancement in the field of ASO delivery. Through antibody-mediated receptor internalisation, this approach demonstrated therapeutic potential, achieving around 50% gene knockdown at a treatment concentration of 50 nM

after 24 hours of incubation. With these results, this delivery method showed superior efficiency compared to conventional transfection agents, which required a higher concentration of 100 nM to achieve comparable results. Therefore, these findings introduce bispecific antibodies for the first time as a viable delivery platform for ASOs.

From a translational perspective, the modularity and adaptability of these constructs offer significant promise for clinical applications. The ability to attach therapeutic cargos in a site-specific and controlled manner introduces a level of precision that is critical for drug development. Scaling up these systems while maintaining structural fidelity and efficacy will be a key step in transitioning from preclinical to clinical settings.

Future studies could expand the applications of this modular platform beyond oncology. For example, the delivery systems described in this thesis holds promise for addressing unmet medical needs in genetic disorders, autoimmune diseases, and infectious diseases. Their compatibility with gene-editing tools, such as CRISPR/Cas systems, or RNA-based therapeutics could further enhance their utility across diverse therapeutic areas. Advanced real-time imaging techniques will provide further insights into construct stability, cellular interactions, and intracellular behaviour.

In conclusion, this thesis establishes a robust framework for the development of modular therapeutic platforms. The findings not only advance the current understanding of DNA nanotechnology and antibody engineering but also set the stage for future innovations in targeted therapeutic delivery. By continuing to refine these therapeutic platforms, future work would position them as transformative tools in precision medicine, with the potential to impact not only cancer treatment but also a broad spectrum of diseases.

Appendix 1 2016 WHO classification of mature lymphoid, histiocytic, and dendritic neoplasms[134]

Mature B-cell neoplasms	Mature T and NK neoplasms	Hodgkin lymphoma	Posttransplant lymphoproliferative disorders (PTLD)	Histiocytic and dendritic cell neoplasms
Chronic lymphocytic leukemia/small lymphocytic lymphoma Monoclonal B-cell lymphocytosis* B-cell prolymphocytic leukemia Splenic marginal zone lymphoma Hairy cell leukemia *Splenic B-cell lymphoma/leukemia, unclassifiable* *Splenic diffuse red pulp small B-cell lymphoma* *Hairy cell leukemia-variant* Lymphoplasmacytic lymphoma Waldenström macroglobulinemia Monoclonal gammopathy of undetermined significance (MGUS), IgM* μ heavy-chain disease γ heavy-chain disease α heavy-chain disease	T-cell prolymphocytic leukemia T-cell large granular lymphocytic leukemia *Chronic lymphoproliferative disorder of NK cells* Aggressive NK-cell leukemia Systemic EBV^{+} T-cell lymphoma of childhood* Hydroa vacciniforme–like lymphoproliferative disorder* Adult T-cell leukemia/lymphoma Extranodal NK-/T-cell lymphoma, nasal type Enteropathy-associated T-cell lymphoma Monomorphic epitheliotropic intestinal T-cell lymphoma* *Indolent T-cell lymphoproliferative disorder of the GI tract** Hepatosplenic T-cell lymphoma	Nodular lymphocyte predominant Hodgkin lymphoma Classical Hodgkin lymphoma Nodular sclerosis classical Hodgkin lymphoma Lymphocyte-rich classical Hodgkin lymphoma Mixed cellularity classical Hodgkin lymphoma Lymphocyte-depleted classical Hodgkin lymphoma	Plasmacytic hyperplasia PTLD Infectious mononucleosis PTLD Florid follicular hyperplasia PTLD* Polymorphic PTLD Monomorphic PTLD (B- and T-/NK-cell types) Classical Hodgkin lymphoma PTLD	Histiocytic sarcoma Langerhans cell histiocytosis Langerhans cell sarcoma Indeterminate dendritic cell tumour Interdigitating dendritic cell sarcoma Follicular dendritic cell sarcoma Fibroblastic reticular cell tumour Disseminated juvenile xanthogranuloma Erdheim-Chester disease*

Monoclonal gammopathy of undetermined significance (MGUS), IgG/A* Plasma cell myeloma Solitary plasmacytoma of bone Extraosseous plasmacytoma Monoclonal immunoglobulin deposition diseases*–Monoclonal immunoglobulin deposition diseases*–Monoclonal immunoglobulin deposition diseases*–Monoclonal immunoglobulin deposition diseases*– Extranodal marginal zone lymphoma of mucosa-associated lymphoid tissue (MALT lymphoma) Nodal marginal zone lymphoma *Pediatric nodal marginal zone lymphoma* Follicular lymphoma In situ follicular neoplasia* Duodenal-type follicular lymphoma* Pediatric-type follicular lymphoma* *Large B-cell lymphoma with IRF4 rearrangement**	Subcutaneous panniculitis-like T-cell lymphoma Mycosis fungoides Sézary syndrome Primary cutaneous CD30$^+$ T-cell lymphoproliferative disorders Lymphomatoid papulosis Primary cutaneous anaplastic large cell lymphoma Primary cutaneous γδ T-cell lymphoma *Primary cutaneous CD8$^+$ aggressive epidermotropic cytotoxic T-cell lymphoma* *Primary cutaneous acral CD8$^+$ T-cell lymphoma** *Primary cutaneous CD4$^+$ small/medium T-cell lymphoproliferative disorder** Peripheral T-cell lymphoma, NOS Angioimmunoblastic T-cell lymphoma *Follicular T-cell lymphoma** *Nodal peripheral T-cell lymphoma with TFH phenotype** Anaplastic large-cell lymphoma, ALK$^+$			

Primary cutaneous follicle center lymphoma Mantle cell lymphoma In situ mantle cell neoplasia* Diffuse large B-cell lymphoma (DLBCL), NOS Germinal center B-cell type* Activated B-cell type* T-cell/histiocyte-rich large B-cell lymphoma Primary DLBCL of the central nervous system (CNS) Primary cutaneous DLBCL, leg type EBV$^+$ DLBCL, NOS* *EBV$^+$ mucocutaneous ulcer** DLBCL associated with chronic inflammation Lymphomatoid granulomatosis Primary mediastinal (thymic) large B-cell lymphoma Intravascular large B-cell lymphoma ALK$^+$ large B-cell lymphoma Plasmablastic lymphoma Primary effusion lymphoma *HHV8$^+$ DLBCL, NOS** Burkitt lymphoma	Anaplastic large-cell lymphoma, ALK$^-$* *Breast implant–associated anaplastic large-cell lymphoma**			

*Burkitt-like lymphoma with 11q aberration** High-grade B-cell lymphoma, with *MYC* and *BCL2* and/or *BCL6* rearrangements* High-grade B-cell lymphoma, NOS* B-cell lymphoma, unclassifiable, with features intermediate between DLBCL and classical Hodgkin lymphoma				

Appendix 2 Oligonucleotide sequences and their biophysical properties

Name	Sequence 5’ to 3’	Length	Molecular weight (g/mol)	Extinction coefficient ($M^{-1}cm^{-1}$)
L1	TTCGCCCTTTGACGTTGGAGTCCACGTTCTTTAATAGCGGACTC	44	13455.7	401600
L2	TGAAAGATGATAGACGGTTTTTCGCCCTTTGACGTTGGAGTCCACGTTCTTTAAA CTGGAACAACACTCAACCCTATCTCGGGCTATTCTTT	92	28242.3	864800
L3	AGTGGACTCTTGTCCCAAACTGGAACAACACTCAACCCTATCTCGGGCTATTCTTT TGA	59	18015.7	552300
L4	TGATAGACGGTTTTTCGCCCTTTGACGTTGGAGTCCACGTTCTTTAATAGTTGACT CTTGTTCCAAACTGGACCAACACTCAACCCTATCTC	92	28129.2	851600
L5	GAAAAACTTGAGTGCCGTCTATCAGAGAGTTGAGTAAGGGCGAA	44	13718.0	452200
L6	GAGATAGGGCGTCTATTTTCAAAAGAATAGAACGTCAGTTGGTC	44	13658.9	446100
L7	GAGTGTTCTATTAAAGTCAACTATTAAAGTGGACTGTCCACT	42	12926.4	415000
L8	CAGTTTGCGAAAAATTGTTCCAGTTTGGCAACGTCTAGGGTT	42	12974.4	403000
L9	CAAAGGGGAACAAGAGAACGTGGACTCCCCCGAGAAAAGGGC	42	13058.5	429400
L10	GAGTCCGGTTCCAGAAGAACGTGGACTCGACAAGACCAACGT	42	12966.4	417400

Name	Sequence 5’ to 3’	Length	Molecular weight (g/mol)	Extinction coefficient ($M^{-1}cm^{-1}$)
L2b	TTCTTTGAAAGATGATAGACGGTTTTTCGCCCTTTGACGTTGGA	44	13573.8	417500
L2c	GTCCACGTCTTTAAACTGGAACAACACTCAACCCTATCTCGGGCTA-TEGChol	47	15058.3	441800
L4b	ACTCTTGTTCCAAACTGGACCAACACTCAACCCTATCTCTGATAGA	46	13957.1	434900
L4c	CholTEG-CGGTTTTTCGCCCTTTGACGTTGGAGTCCACGTTCTTTAATAGTTG	46	14790.1	419100
L5c	CholTEG-GAAAAACTTGAGTGCCGTCTATCAGAGAGTTGAGTAAGGGCGAA	44	14398.0	452200
L8c	CholTEG-CAGTTTGCGAAAAATTGTTCCAGTTTGGCAACGTCTAGGGTT	42	13654.4	403000
L5-1C18	1C18-GAAAAACTTGAGTGCCGTCTATCAGAGAGTTGAGTAAGGGCGAA	44	14051.0	452200
L8-1C18	1C18-CAGTTTGCGAAAAATTGTTCCAGTTTGGCAACGTCTAGGGTT	42	13307.0	403000
L5-k	k-GAAAAACTTGAGTGCCGTCTATCAGAGAGTTGAGTAAGGGCGAA	44	14540.4	460200
L8-k	k-CAGTTTGCGAAAAATTGTTCCAGTTTGGCAACGTCTAGGGTT	42	13796.4	412300
C1	BCN-TCAAAAGAATAGCCC	15	4909.0	153500
antiL10	BCN-ACGTTGGTCTTGTCG	15	4945.0	137600

Appendix 3 **Representative LC-MS traces for amino-modified and BCN-modified C1 oligonucleotide**

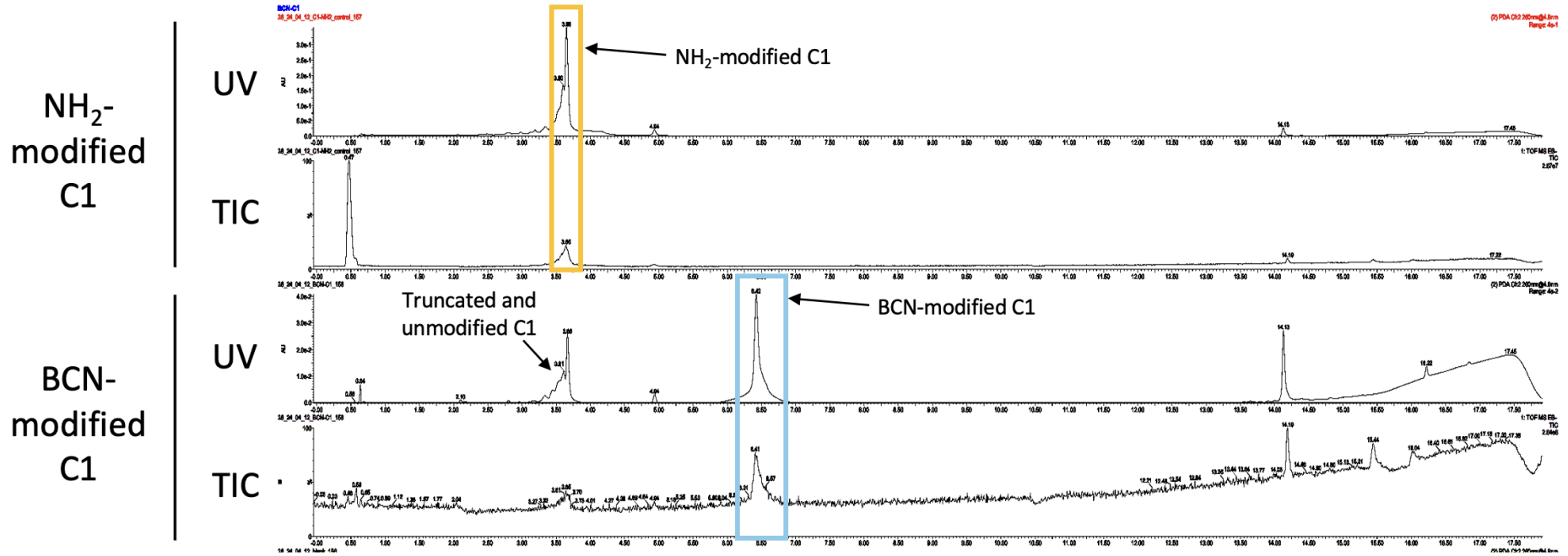

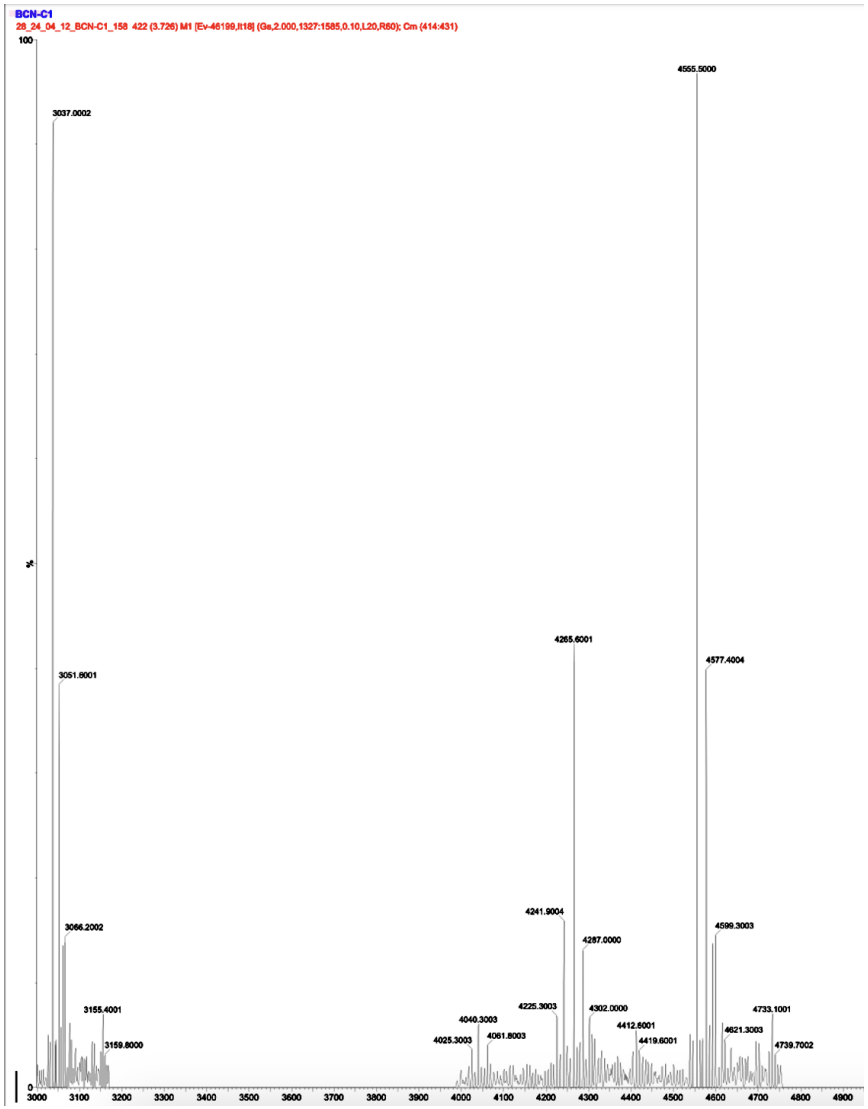

Deconvoluted mass at RT 3.736 corresponding to mass of unmodified C1 (calcd. 4554 g/mol)

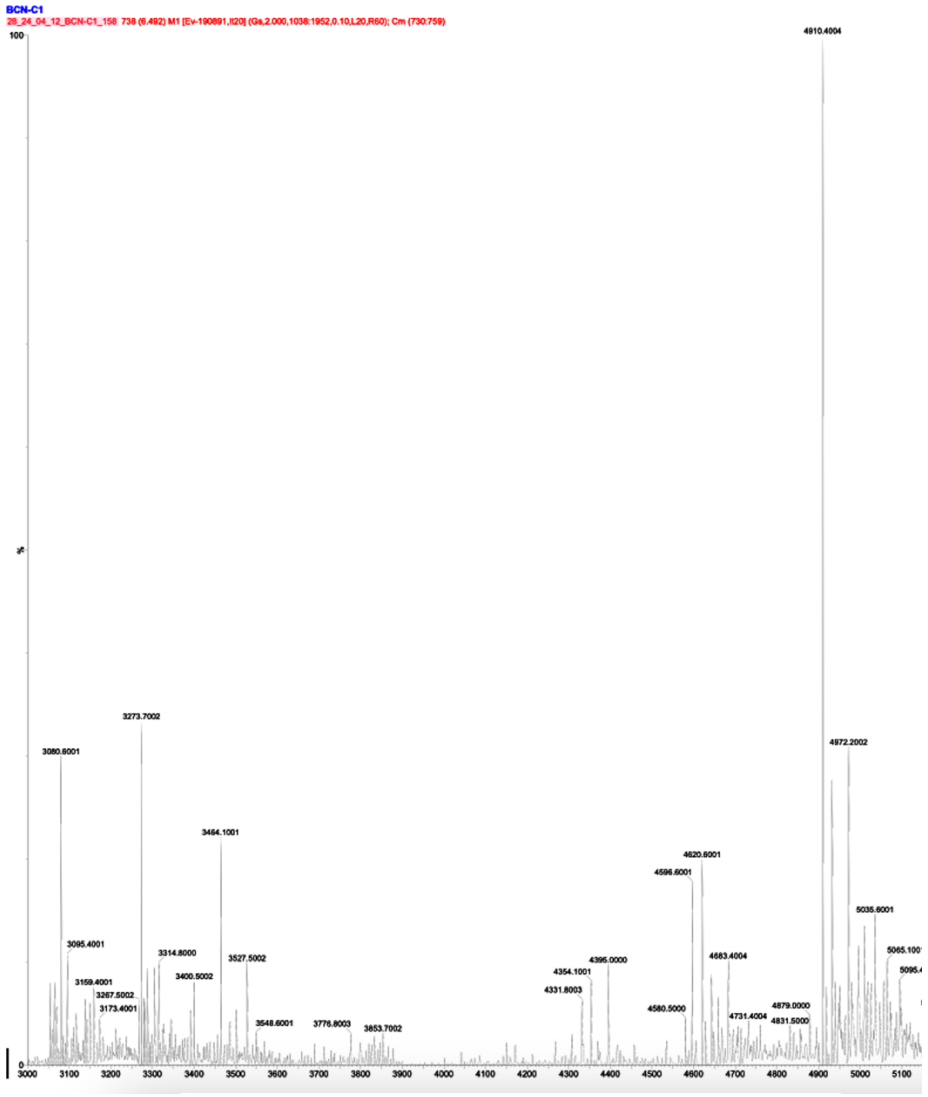

Deconvoluted mass at RT 6.492 corresponding to mass BCN-modified C1 (calcd. 4909 g/mol)

Appendix 4 **Representative HPLC trace for the purification of BCN-modified C1 oligonucleotide and LC-MS trace for purified C1**

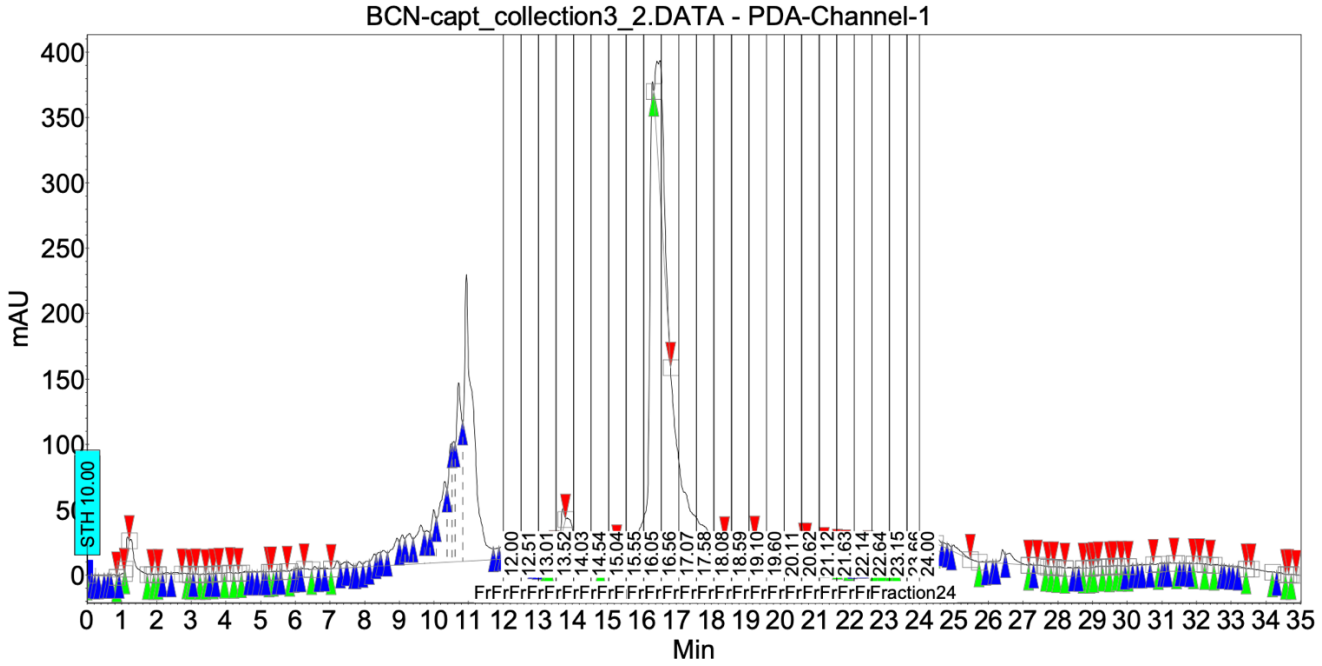

Appendix 5 **Representative LC-MS traces for amino-modified and BCN-modified antiL10 oligonucleotide**

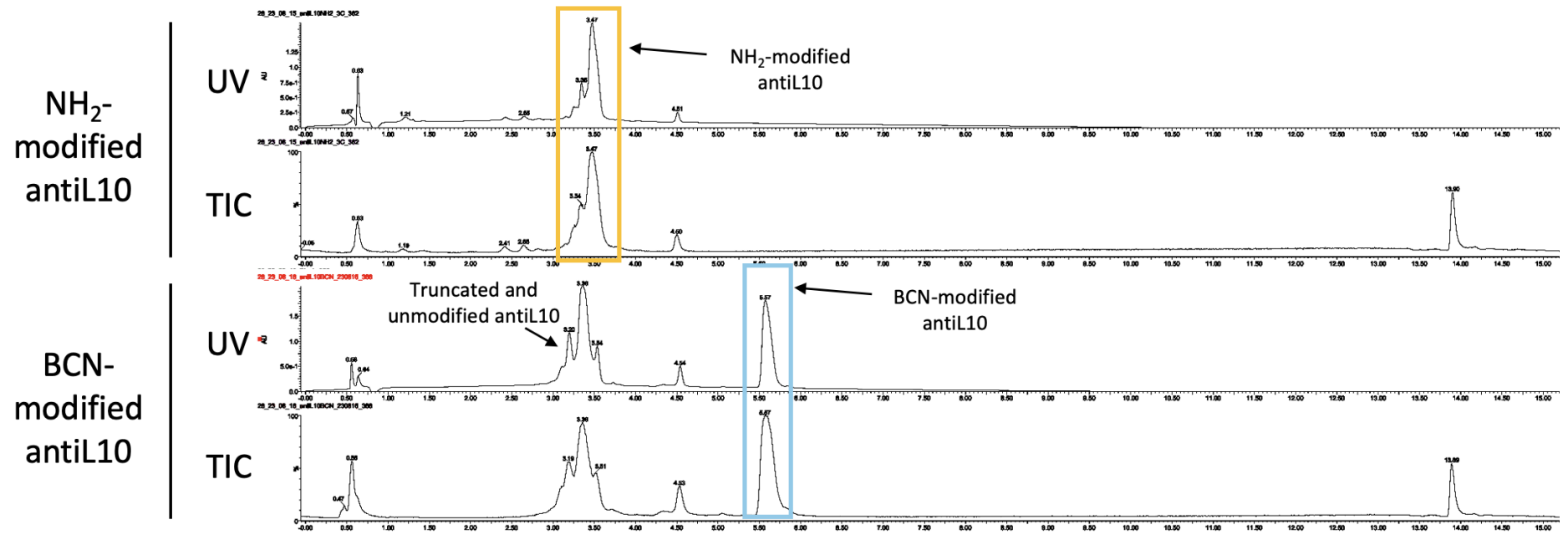

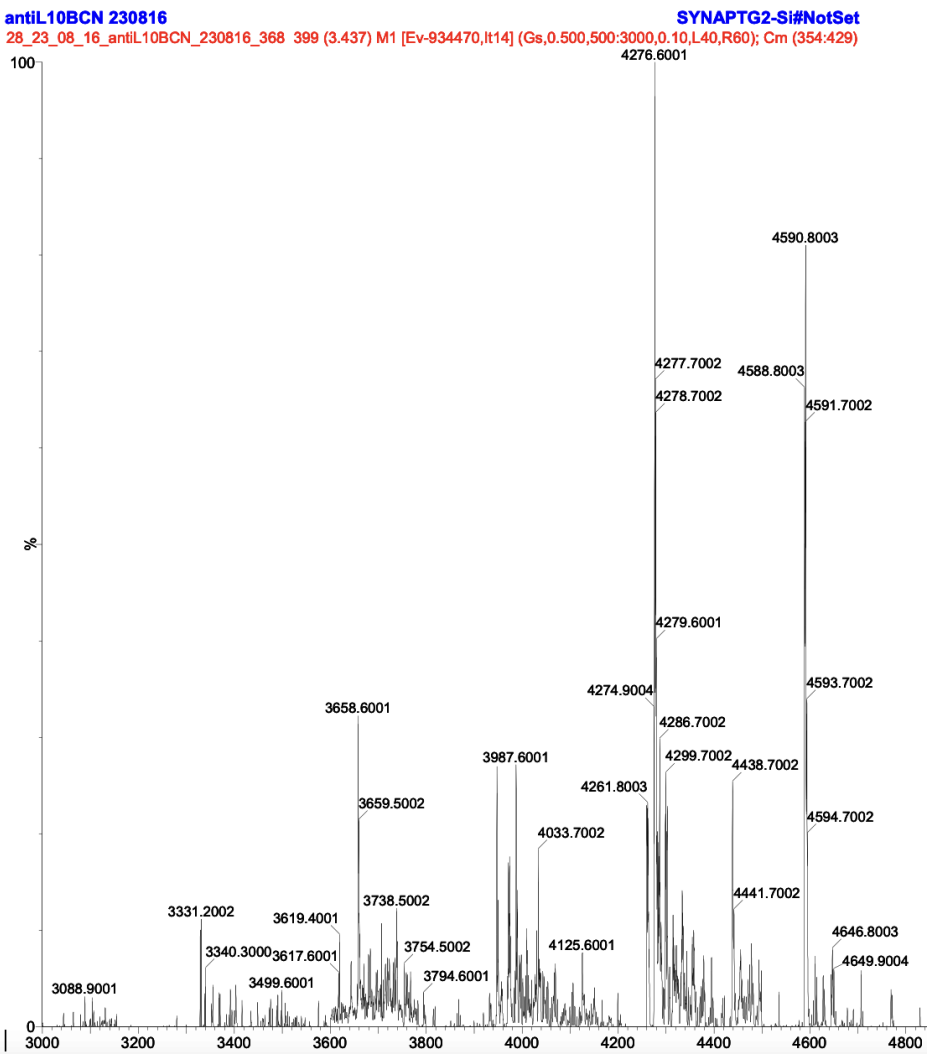

Deconvoluted mass at RT 3.437 corresponding to mass of unmodified antiL10 (calcd. 4590 g/mol)

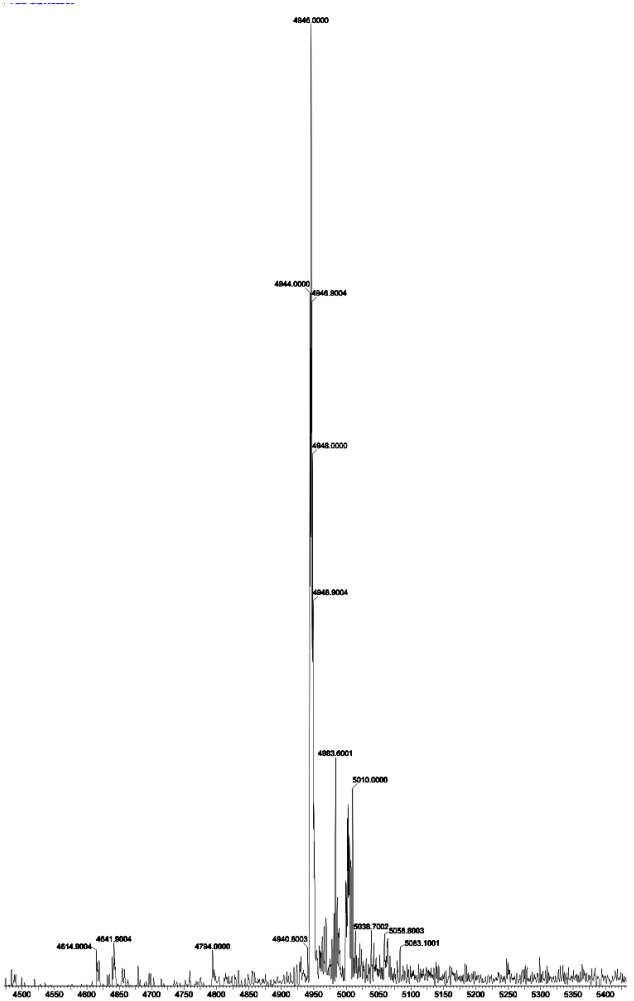

Deconvoluted mass at RT 5.649 corresponding to mass BCN-modified antiL10 (calcd. 4945 g/mol)

Appendix 6 Representative HPLC trace for the purification of BCN-modified antiL10 oligonucleotide and LC-MS trace for purified anti-L10

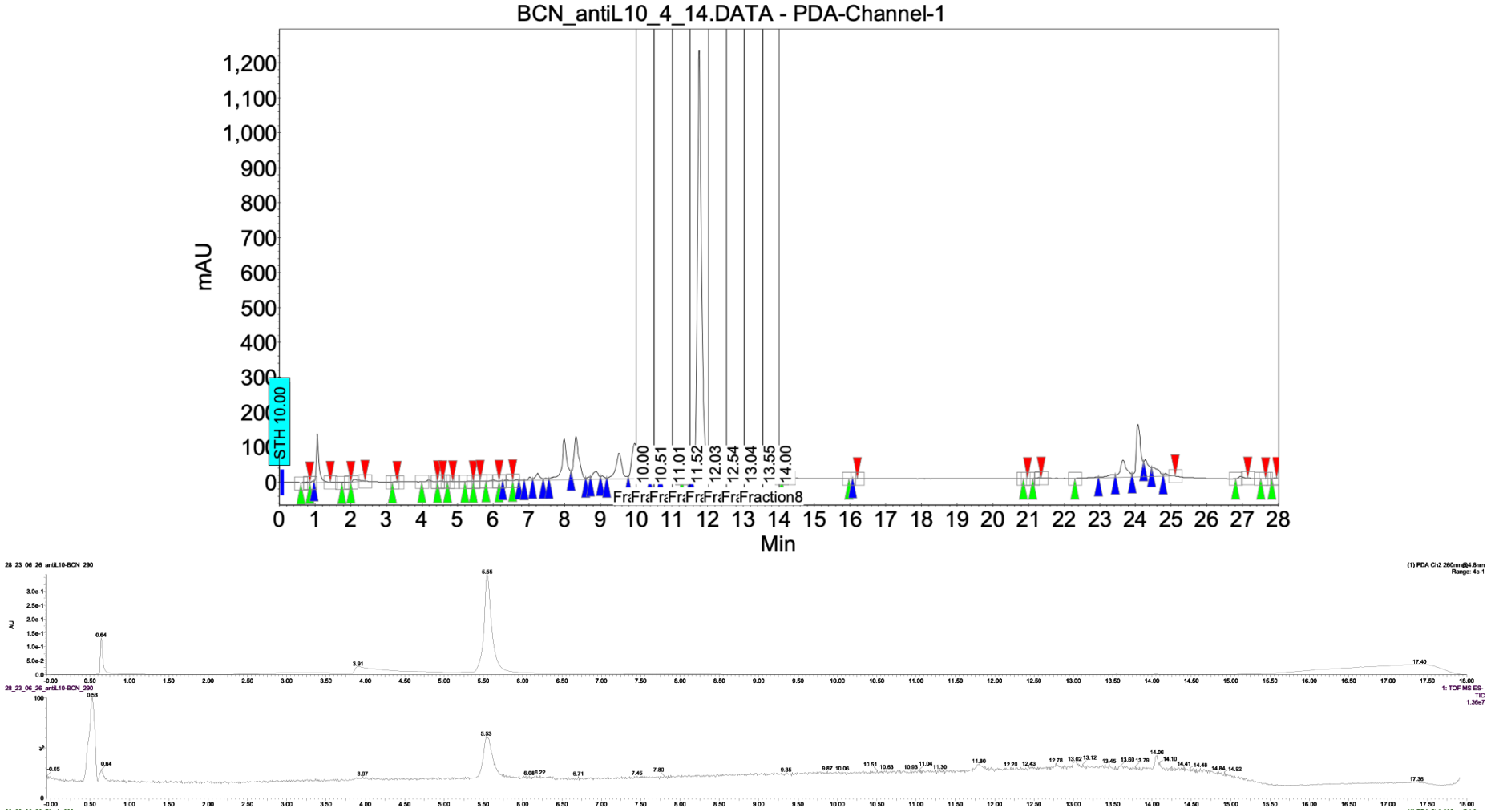

Appendix 7 Representative LC-MS UV trace for the linker-modified oligonucleotides

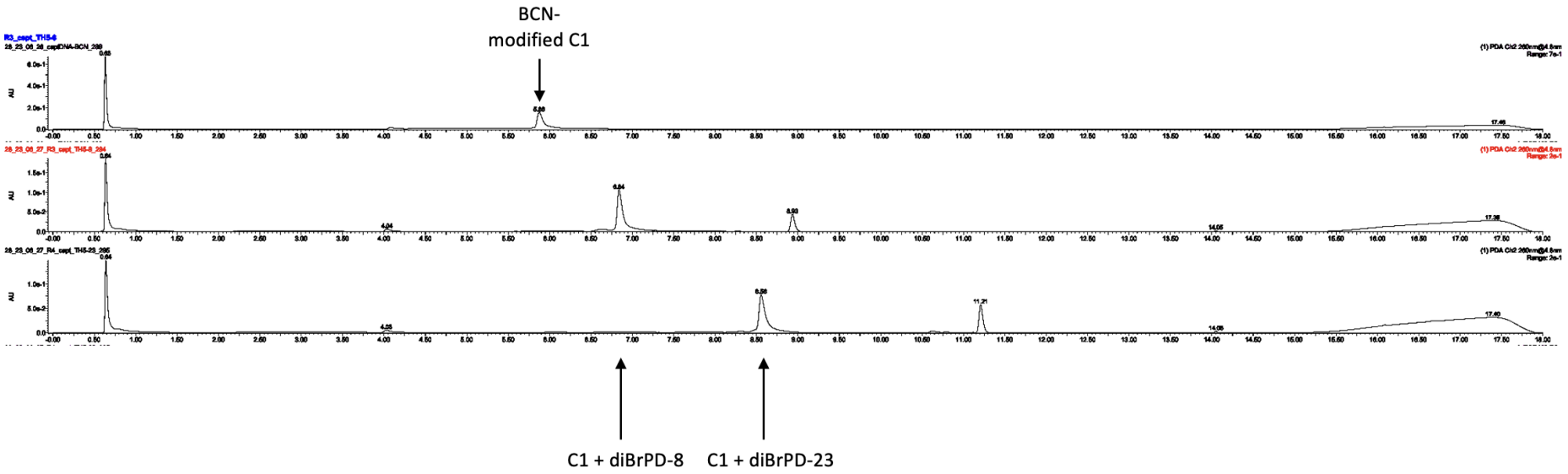

Appendix 8 NMR spectra

A.1 ^{1}H and ^{13}C JMOD NMR spectrum of compound 1 in $CDCl_3$

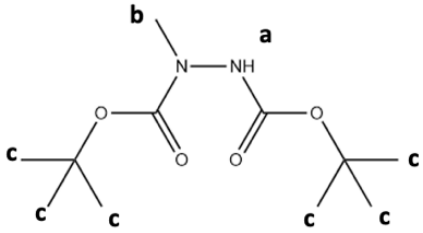

^{1}H NMR (400 MHz, $CDCl_3$) δ 6.51 – 6.00 (m, J = 113.5 Hz, 1H), 3.11 (s, 3H), 1.47 (d, J = 5.9 Hz, 18H).

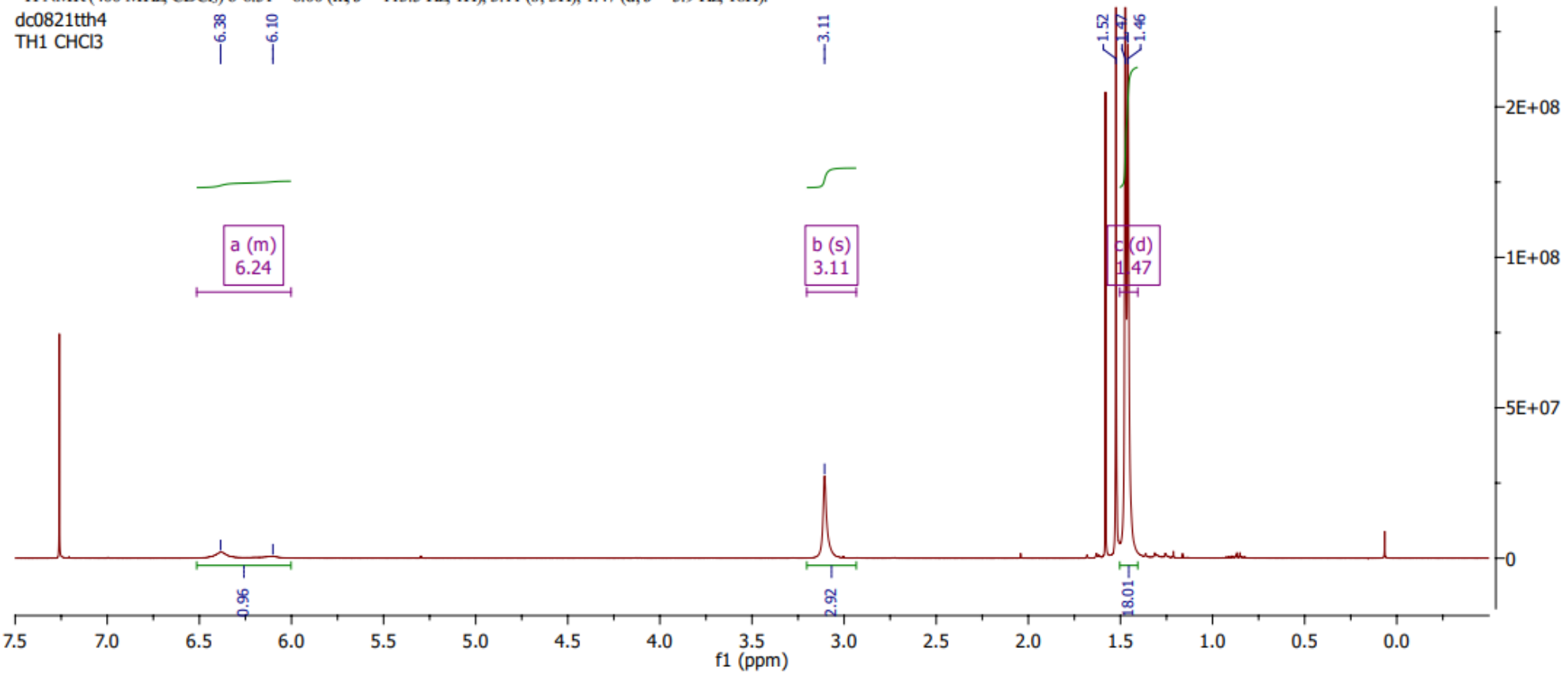

^{13}C NMR (101 MHz, $CDCl_3$) δ 155.77, 80.67, 37.19, 28.09, 28.05.

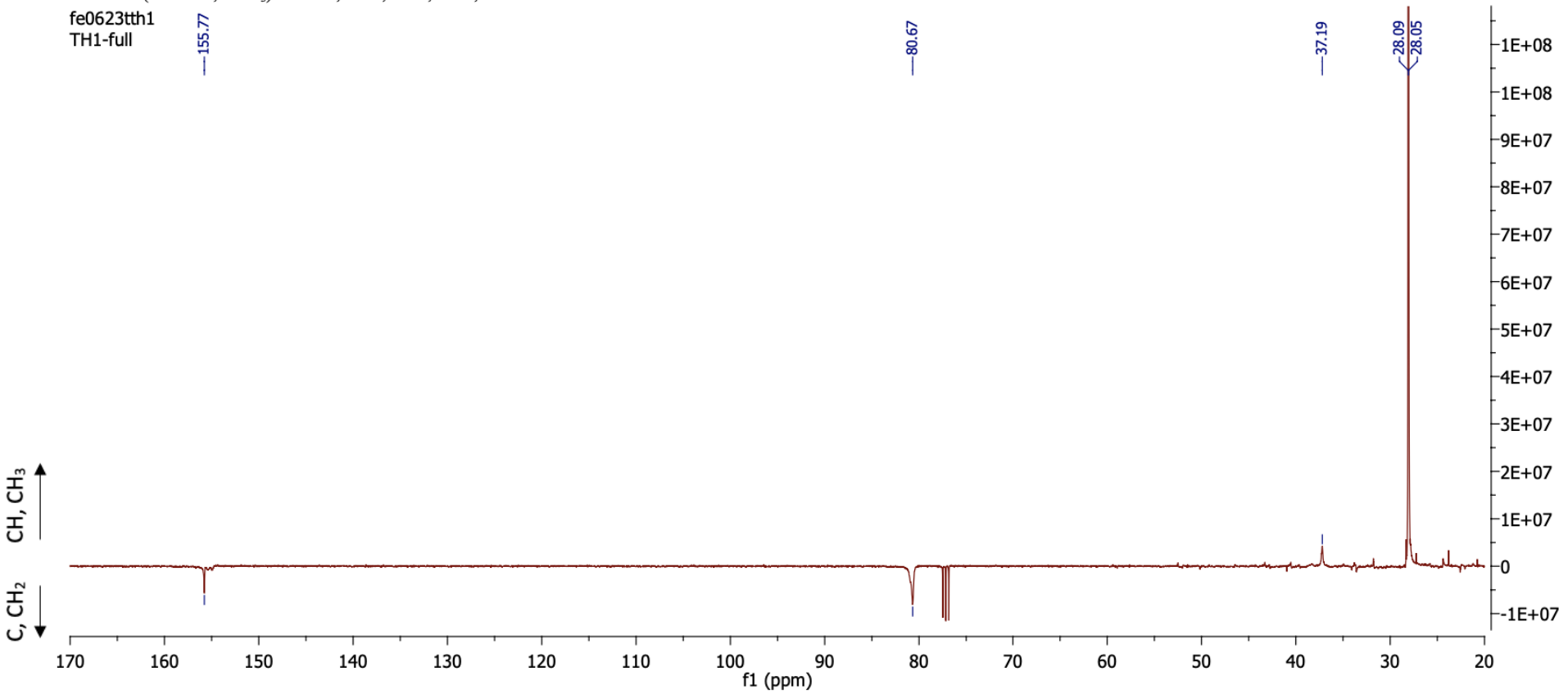

A.2 ^{1}H and ^{13}C JMOD NMR spectrum of compound 2 in $CDCl_3$

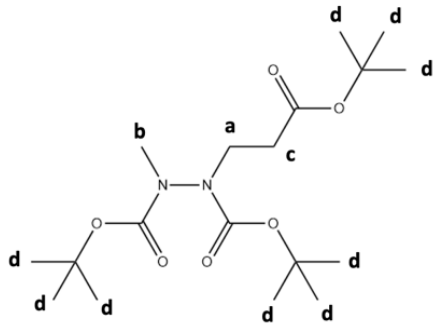

Full spectrum

^{1}H NMR (400 MHz, $CDCl_3$) δ 3.86 – 3.51 (m, 2H), 3.08 – 2.95 (m, 3H), 2.51 (t, J = 7.2 Hz, 2H), 1.51 – 1.42 (m, J = 9.5, 6.5, 2.9 Hz, 28H).

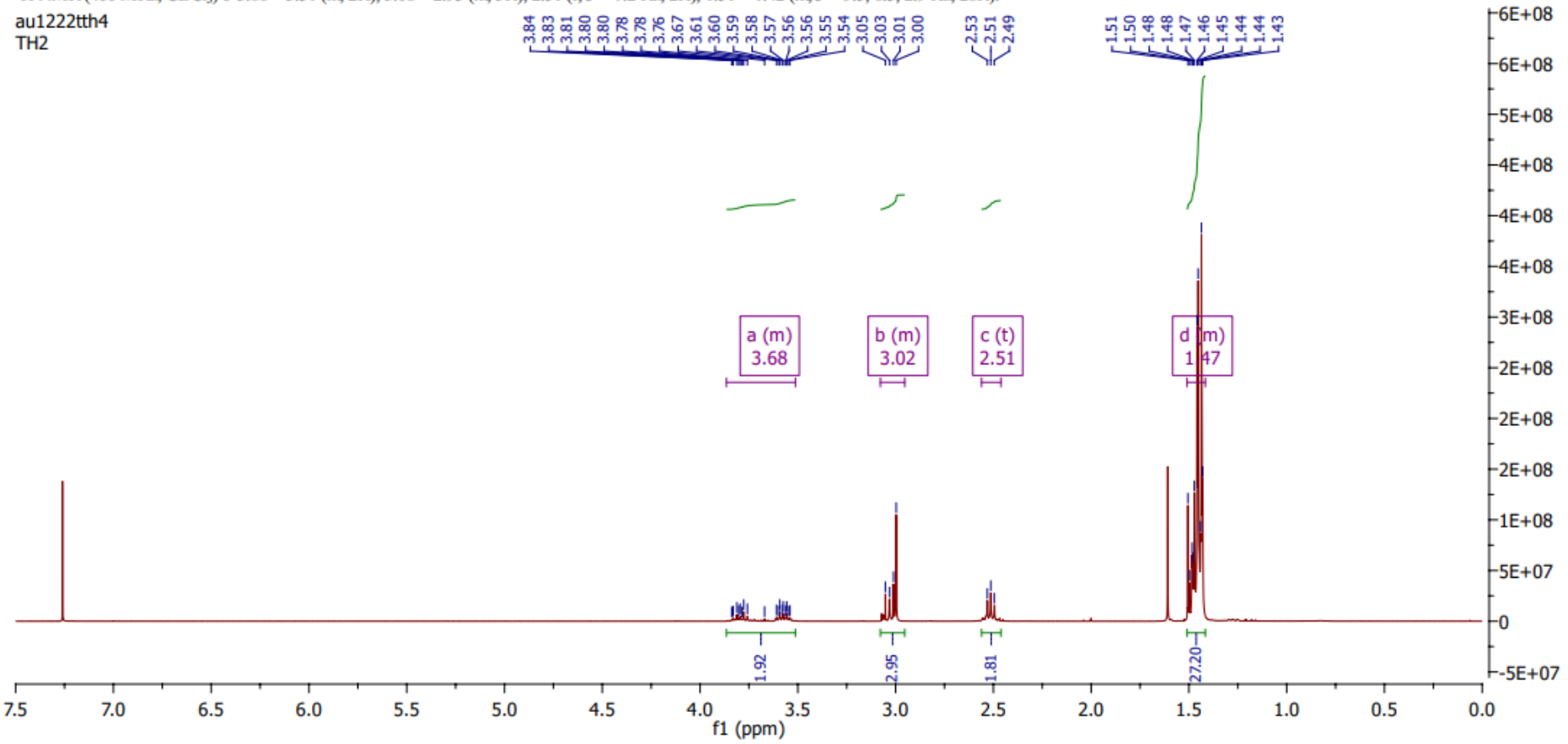

Zoomed region

^{1}H NMR (400 MHz, $CDCl_3$) δ 3.86 – 3.51 (m, 2H), 3.08 – 2.95 (m, 3H), 2.51 (t, J = 7.2 Hz, 2H), 1.51 – 1.42 (m, J = 9.5, 6.5, 2.9 Hz, 28H).

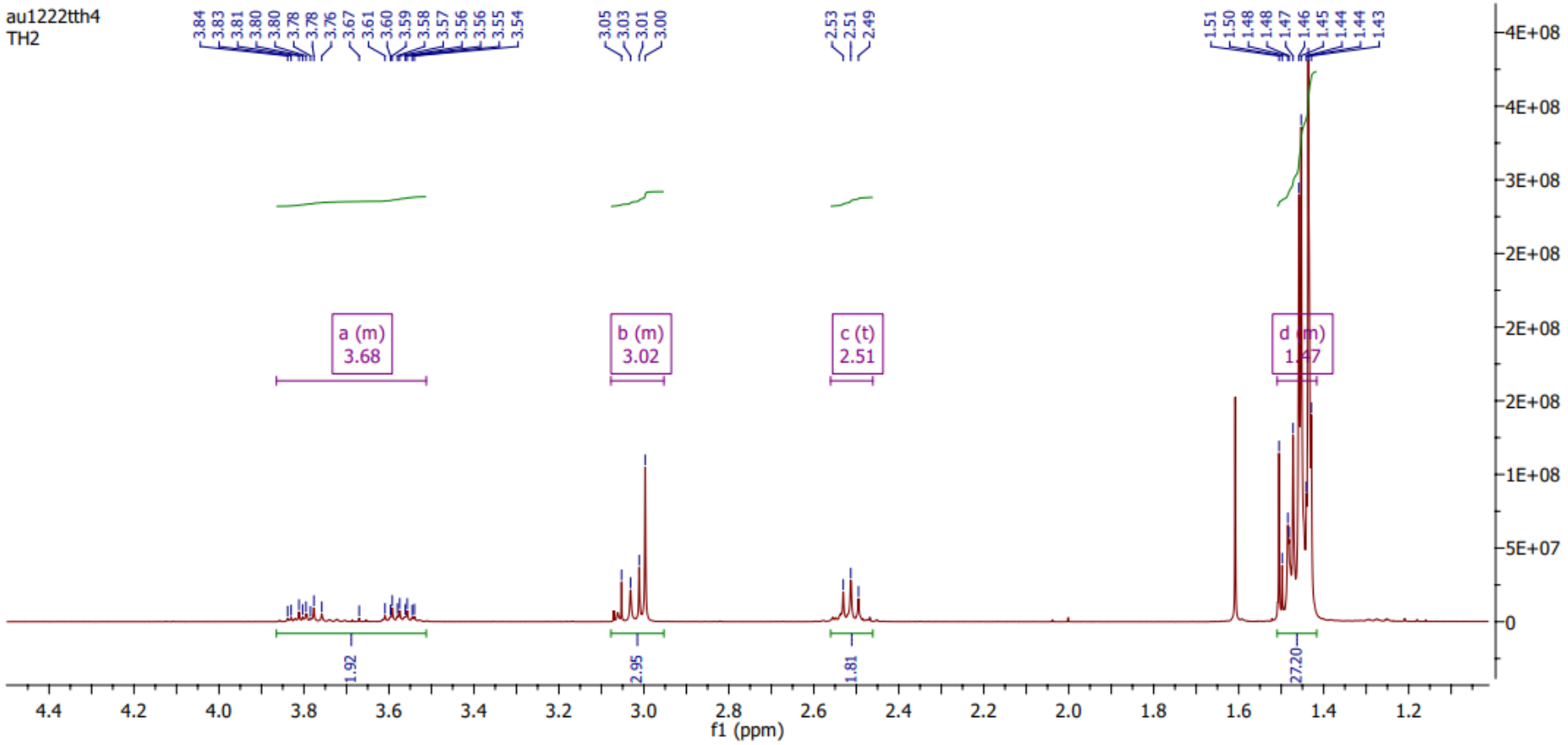

^{13}C NMR (101 MHz, $CDCl_3$) δ 171.08, 155.50, 154.48, 81.11, 80.86, 44.83, 44.68, 38.32, 36.71, 34.51, 34.38, 34.24, 28.42, 28.36, 28.31, 28.23, 28.19, 28.11.

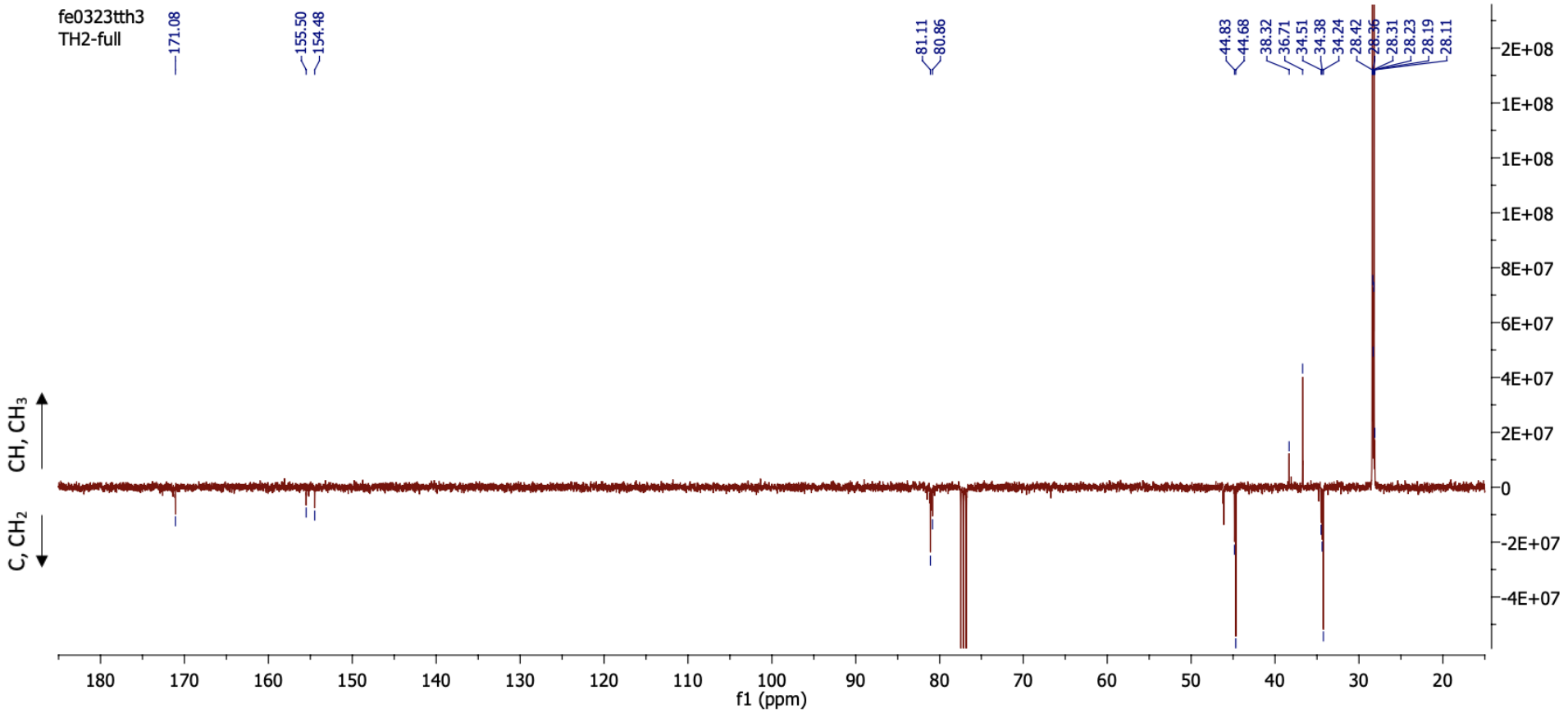

A.3 ^{1}H and ^{13}C JMOD NMR spectrum of compound 3 in DMSO

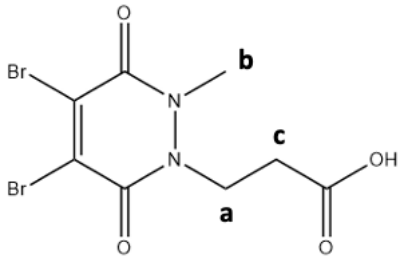

Full spectrum

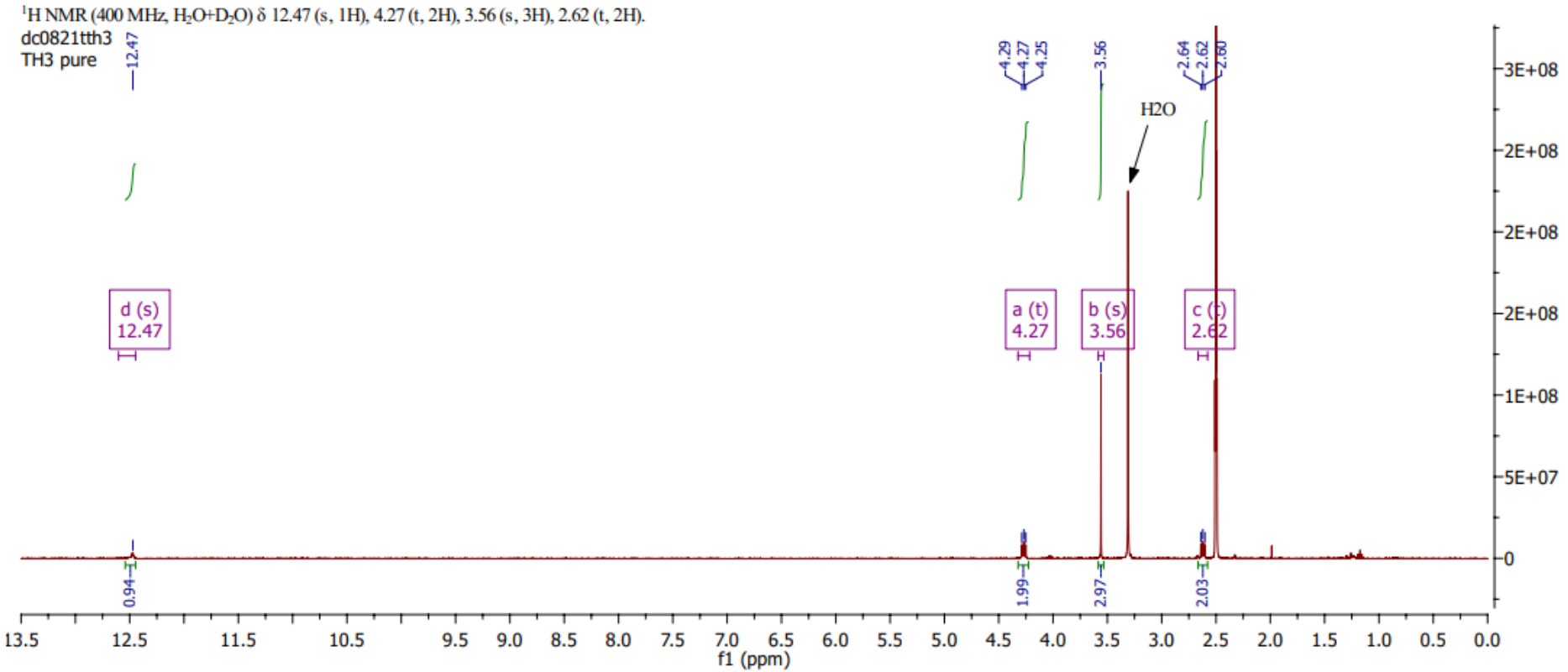

Zoomed region

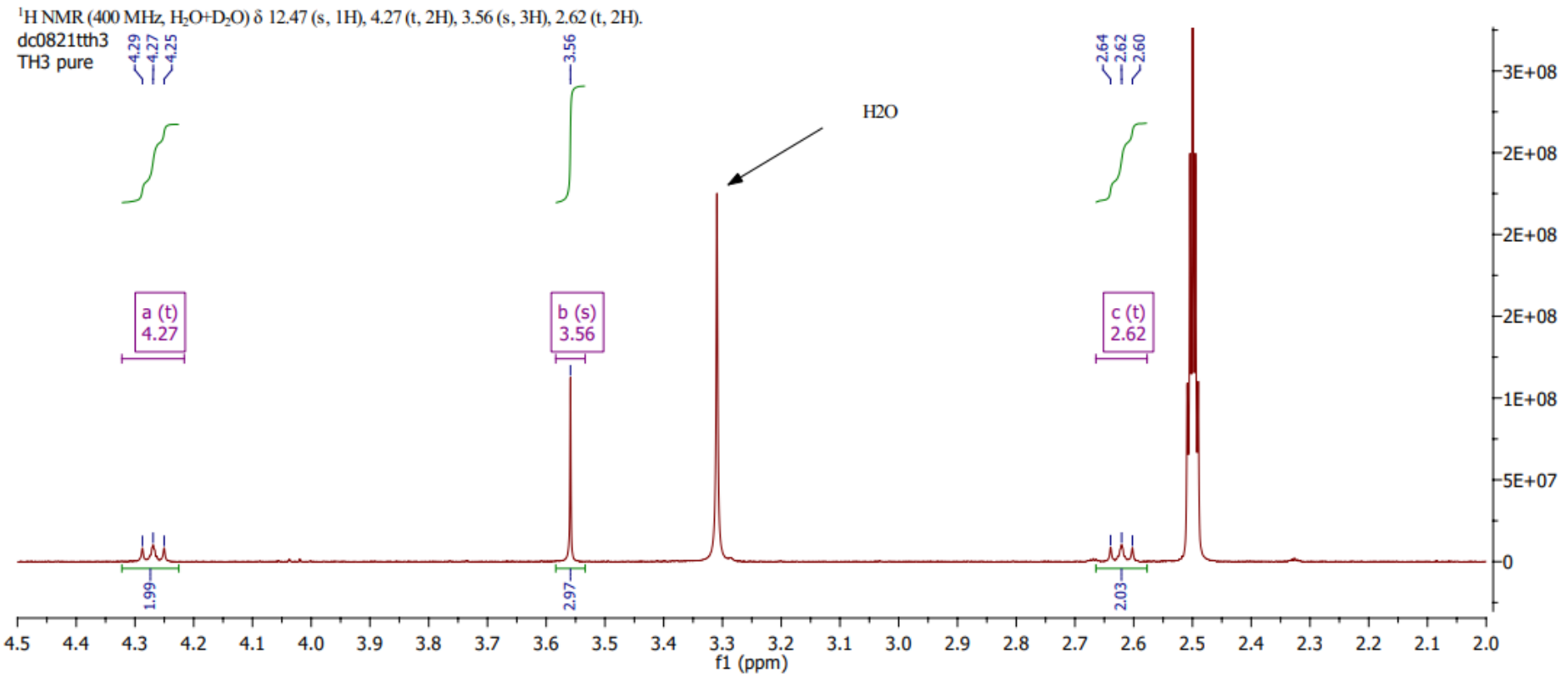

^{13}C NMR (101 MHz, DMSO) δ 171.85, 152.65, 152.32, 135.27, 134.94, 43.05, 40.15, 39.94, 39.73, 39.52, 39.31, 39.10, 38.89, 34.65, 31.60.

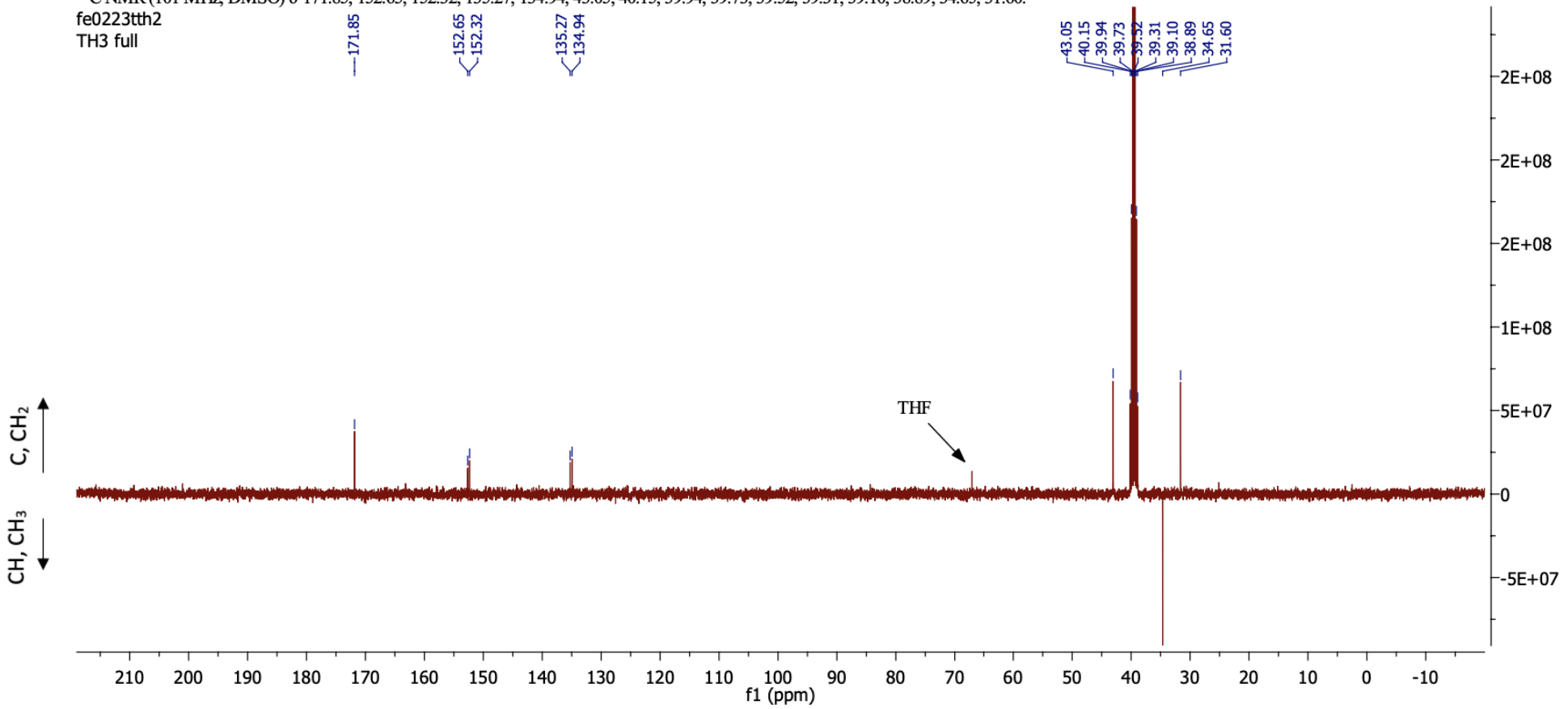

A.4 ^{1}H and ^{13}C JMOD NMR spectrum of compound 4 in $CDCl_3$

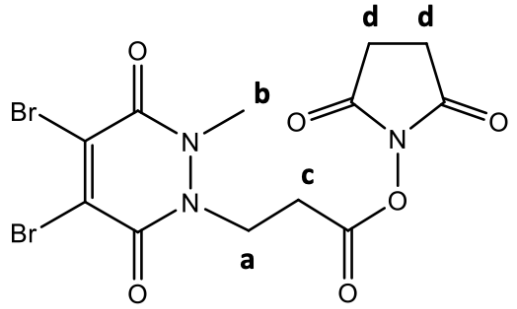

Full spectrum

^{1}H NMR (400 MHz, $CDCl_3$) δ 4.48 (t, J = 6.9 Hz, 2H), 3.67 (s, 3H), 3.10 (t, J = 6.9 Hz, 2H), 2.84 (s, 4H).

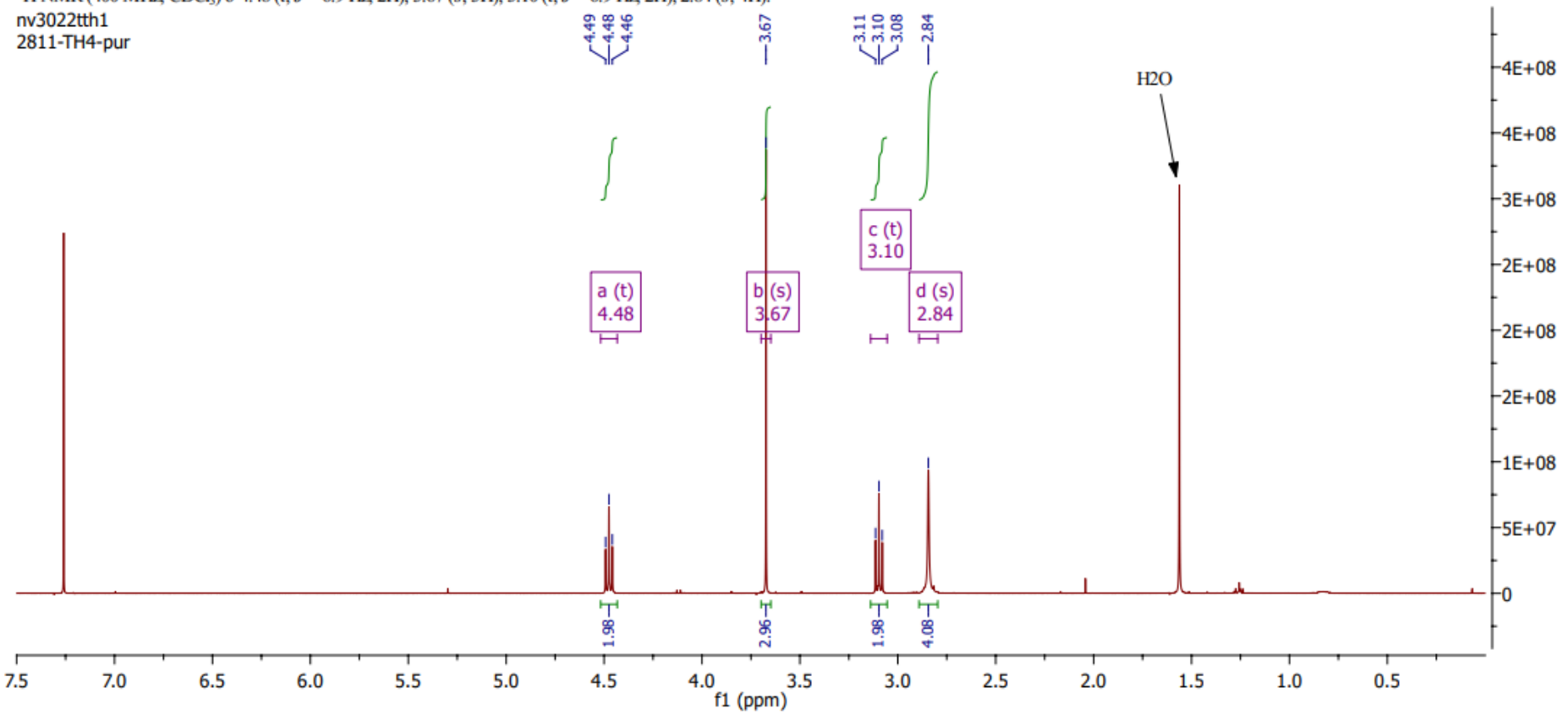

Zoomed region

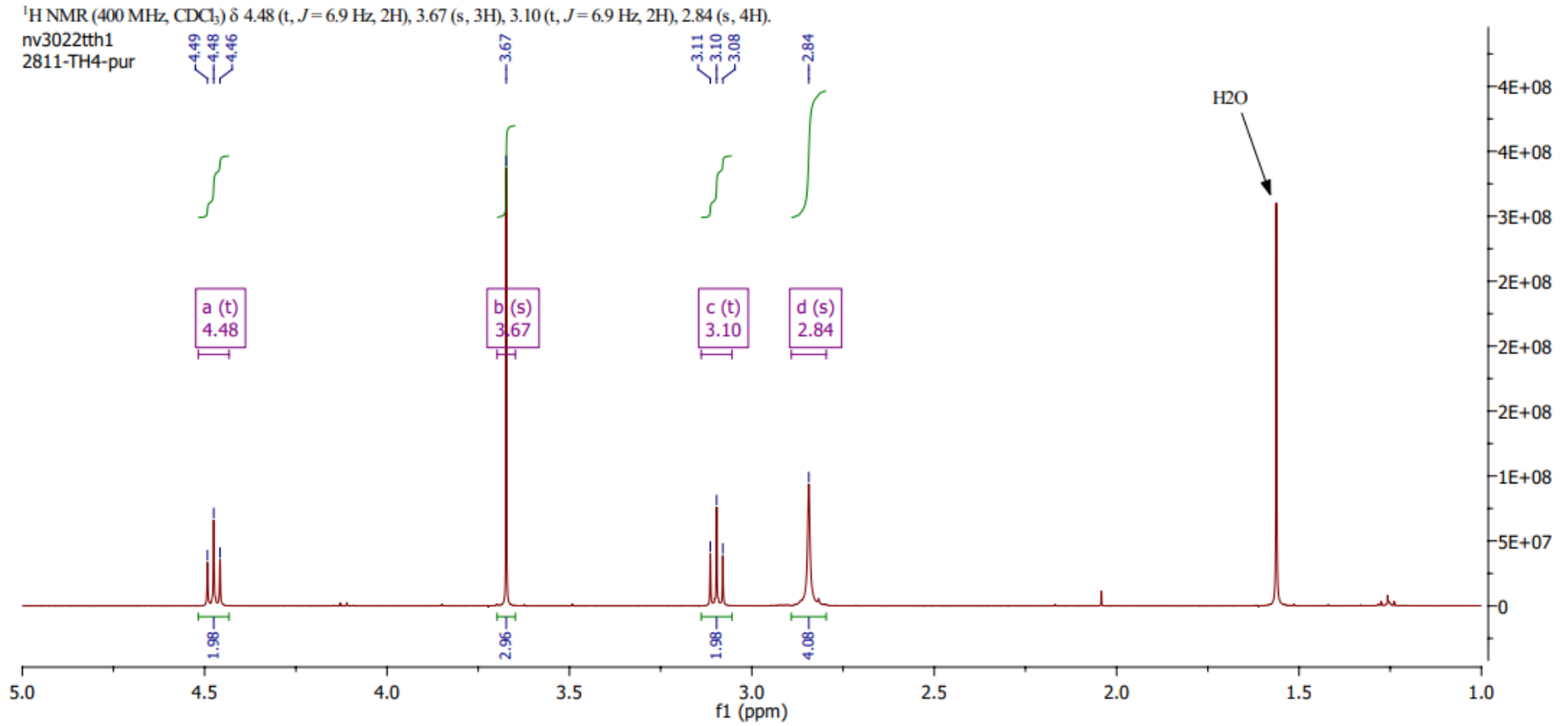

^{13}C NMR (101 MHz, $CDCl_3$) δ 168.70, 165.83, 152.97, 136.84, 135.11, 117.51, 43.06, 35.31, 29.16, 25.69.

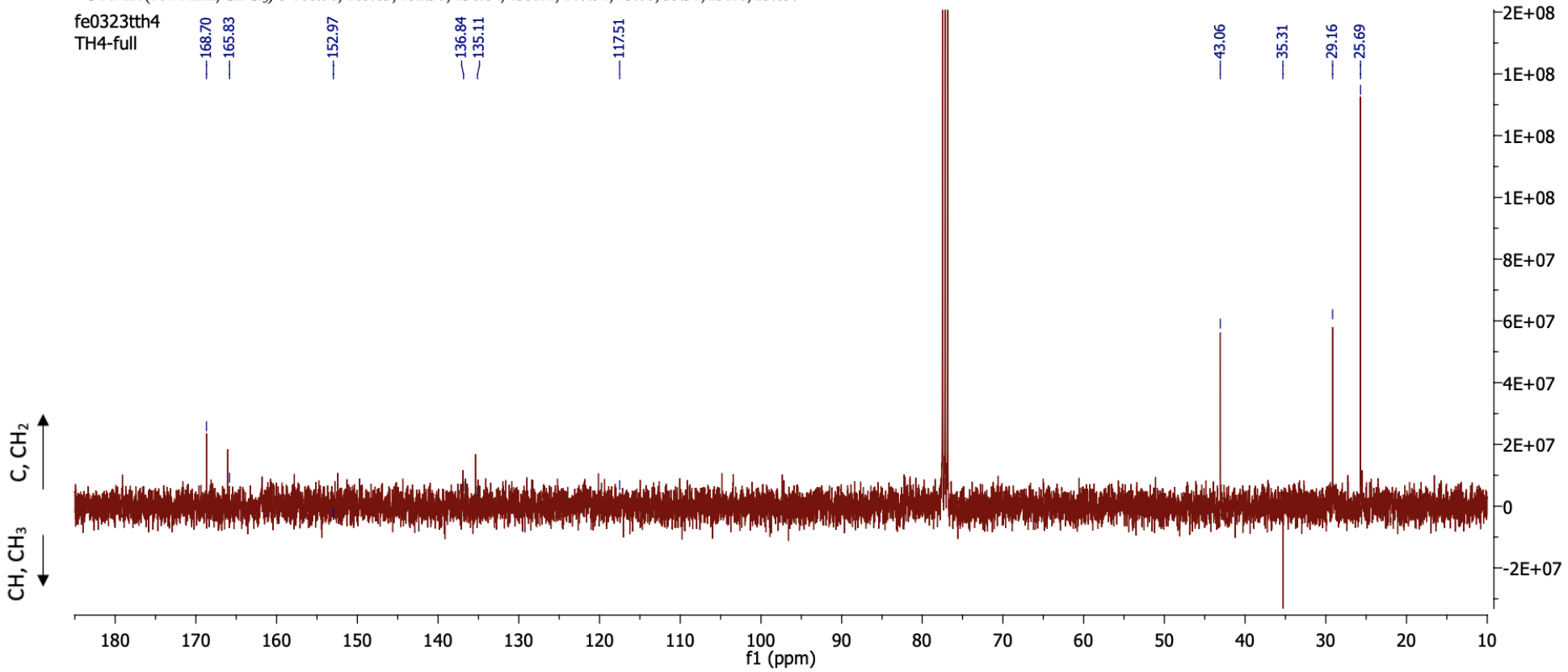

A.5 ^{1}H and ^{13}C JMOD NMR spectrum of diBrPD-8 in $CDCl_3$

Full spectrum

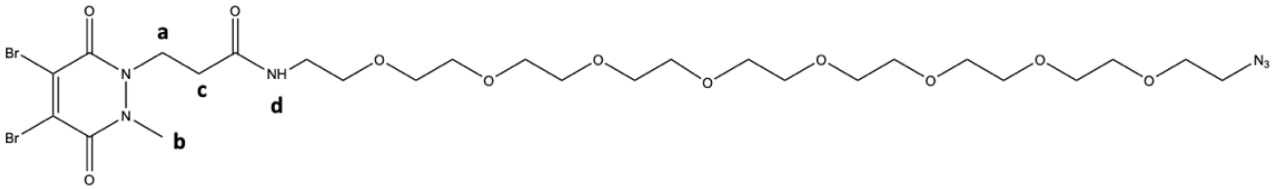

^{1}H NMR (400 MHz, $CDCl_3$) δ 6.76 (s, 1H), 4.42 (t, 2H), 3.71 (s, 2H), 3.68 – 3.57 (m, 31H), 3.51 (t, 2H), 3.40 (t, J = 5.3 Hz, 1H), 3.37 (t, 1H), 2.59 (t, J = 6.9 Hz, 2H).

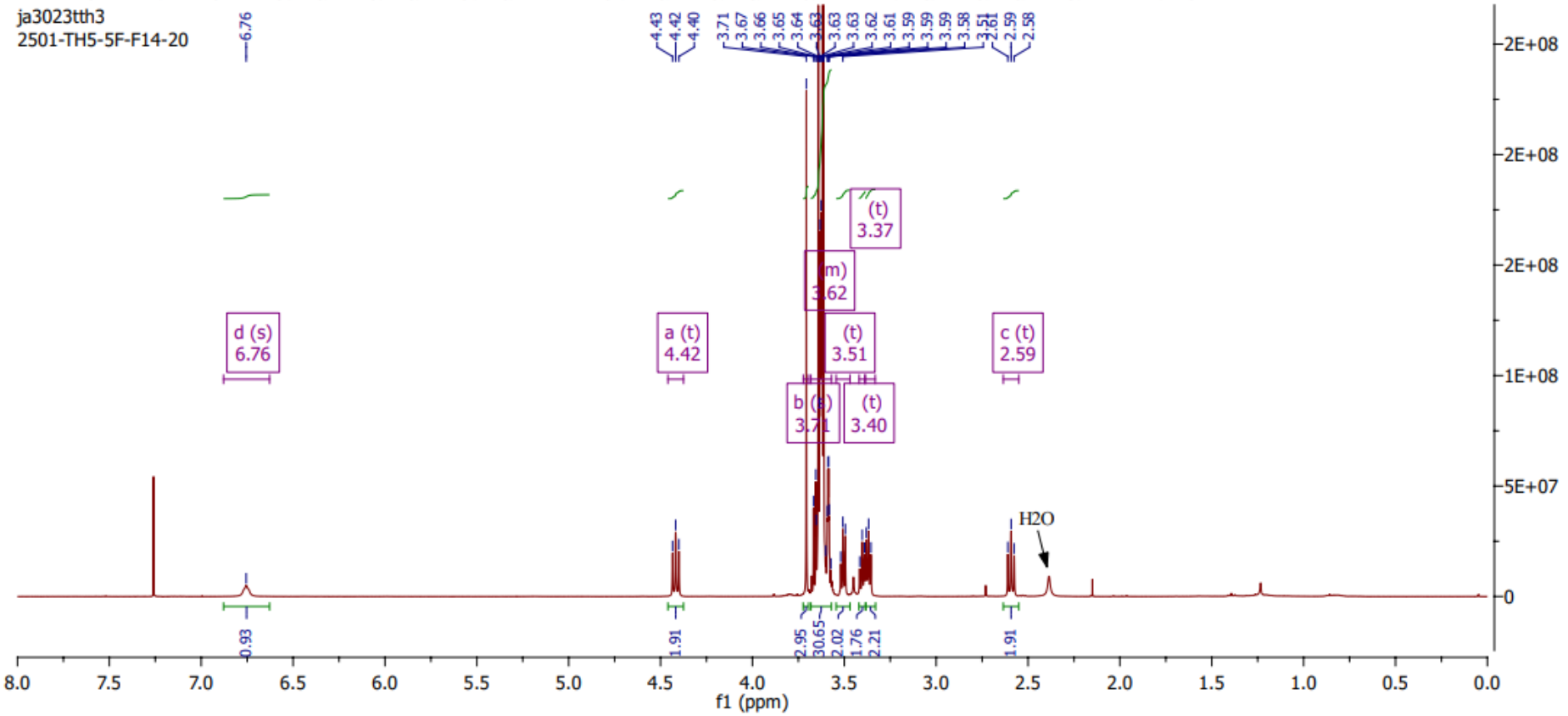

Zoomed region

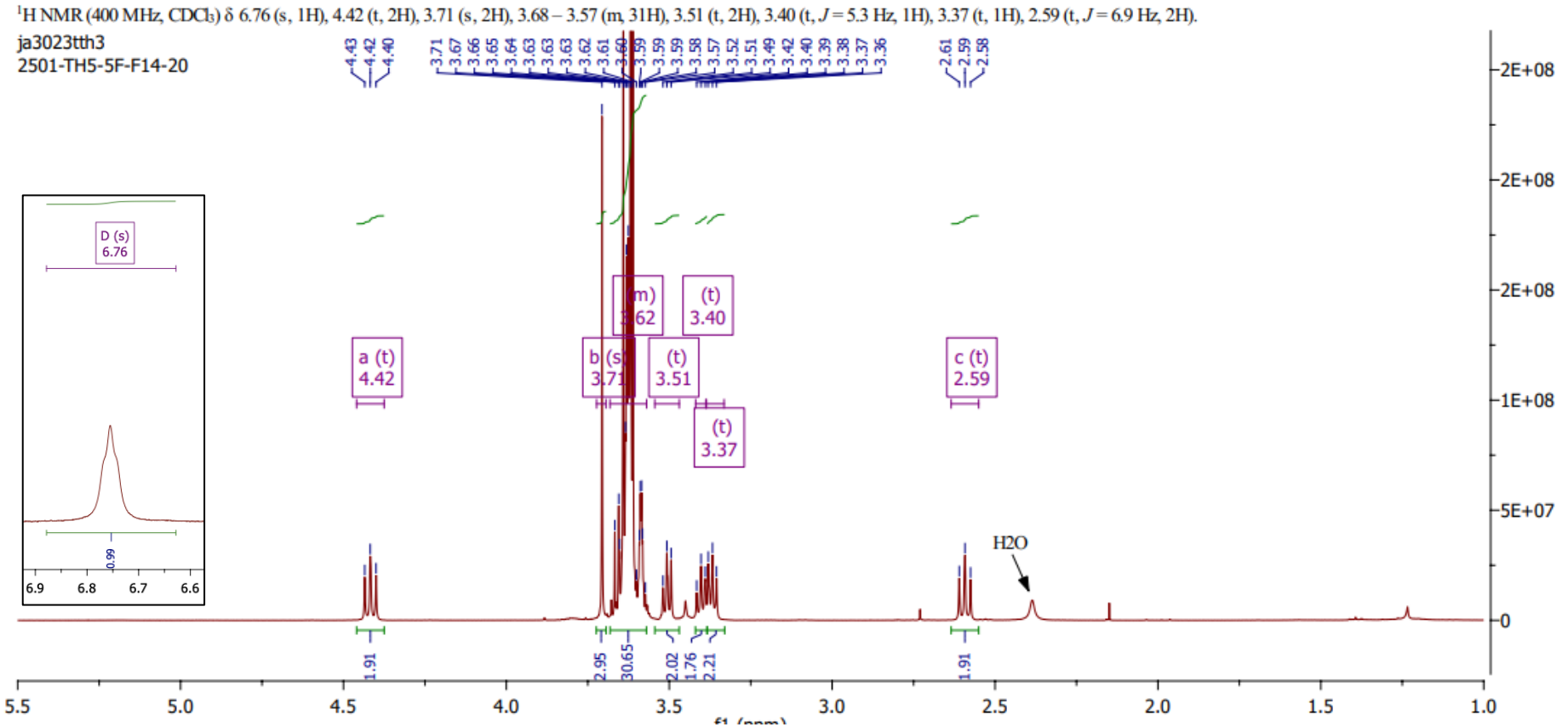

^{13}C NMR (101 MHz, $CDCl_3$) δ 169.23, 153.08, 152.89, 136.26, 135.50, 70.80, 70.76, 70.72, 70.67, 70.64, 70.61, 70.59, 70.57, 70.31, 70.12, 69.66, 50.79, 44.45, 39.53, 35.11, 33.92.

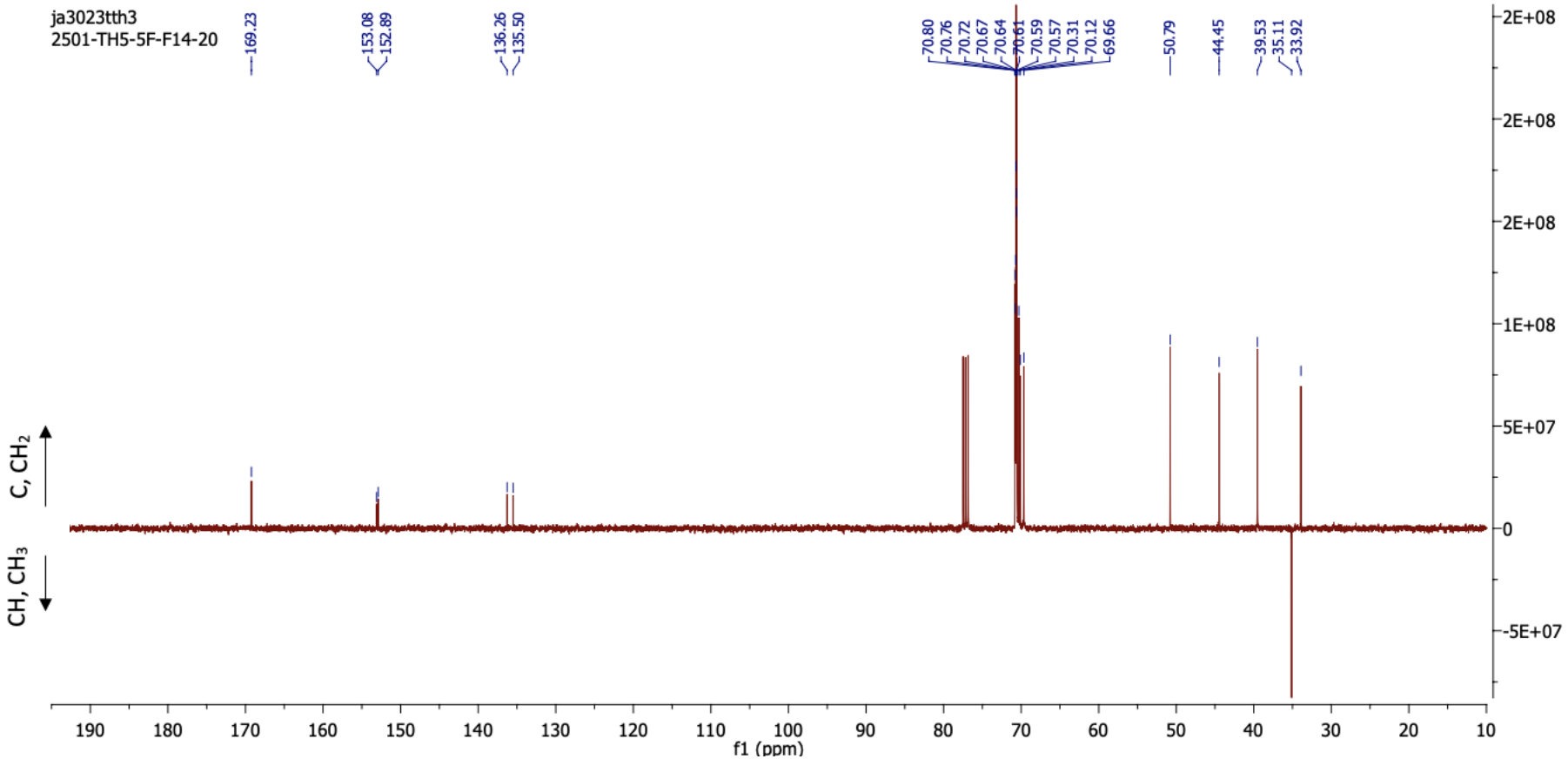

A.6 IR Spectrum of diBrPD-8

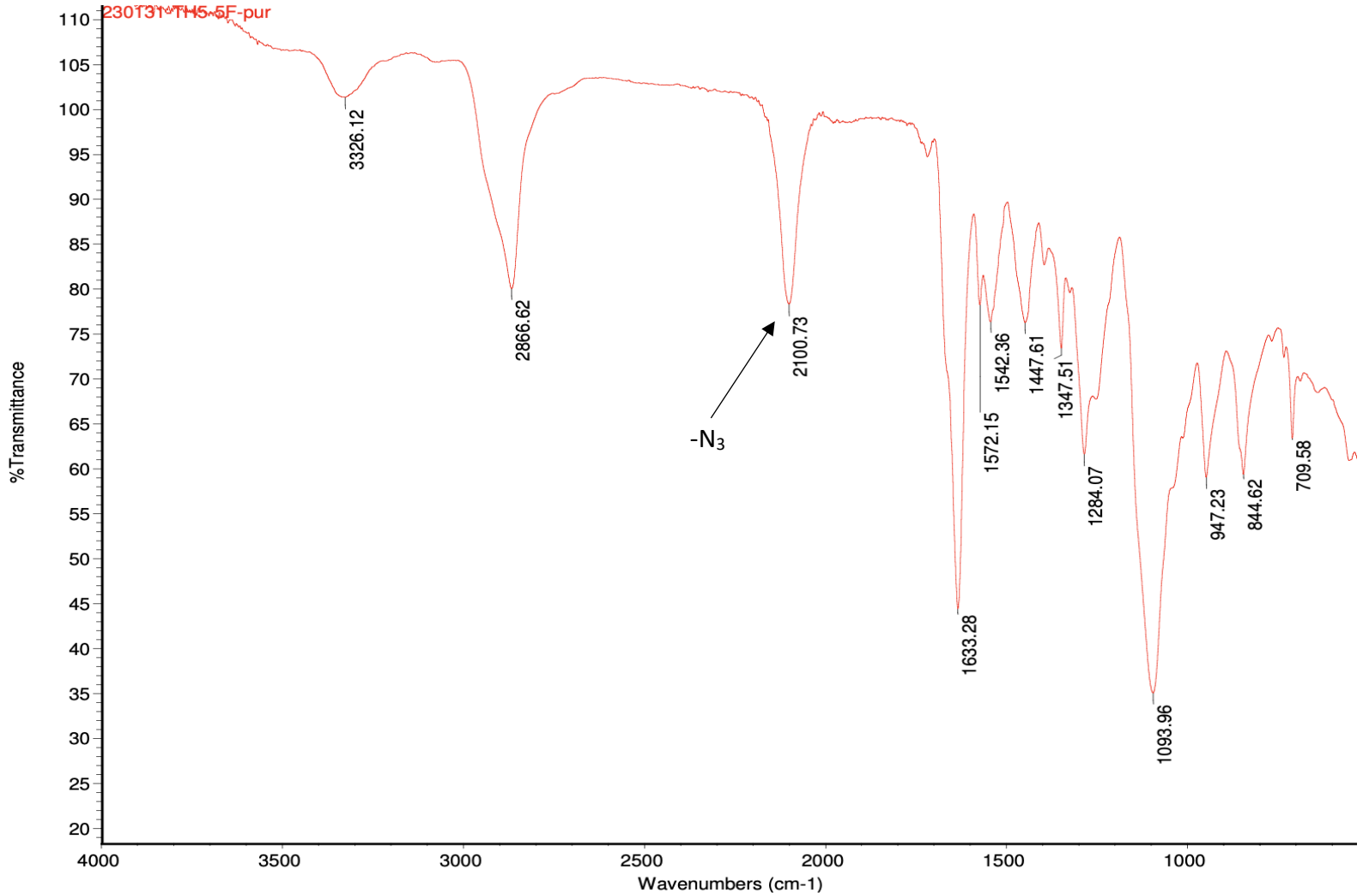

A.7 ^{1}H and ^{13}C JMOD NMR spectrum of diBrPD-23 in $CDCl_3$

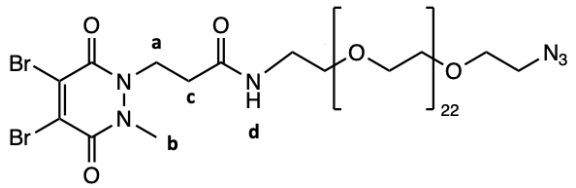

Full spectrum

^{1}H NMR (400 MHz, $CDCl_3$) δ 7.02 (s, 1H), 4.42 (t, 2H), 3.71 (s, 3H), 3.68 – 3.55 (m, 98H), 3.51 (t, 2H), 3.41 (t, J = 5.3 Hz, 2H), 3.38 (t, J = 6.7, 3.5 Hz, 2H), 2.60 (t, J = 6.9 Hz, 2H).

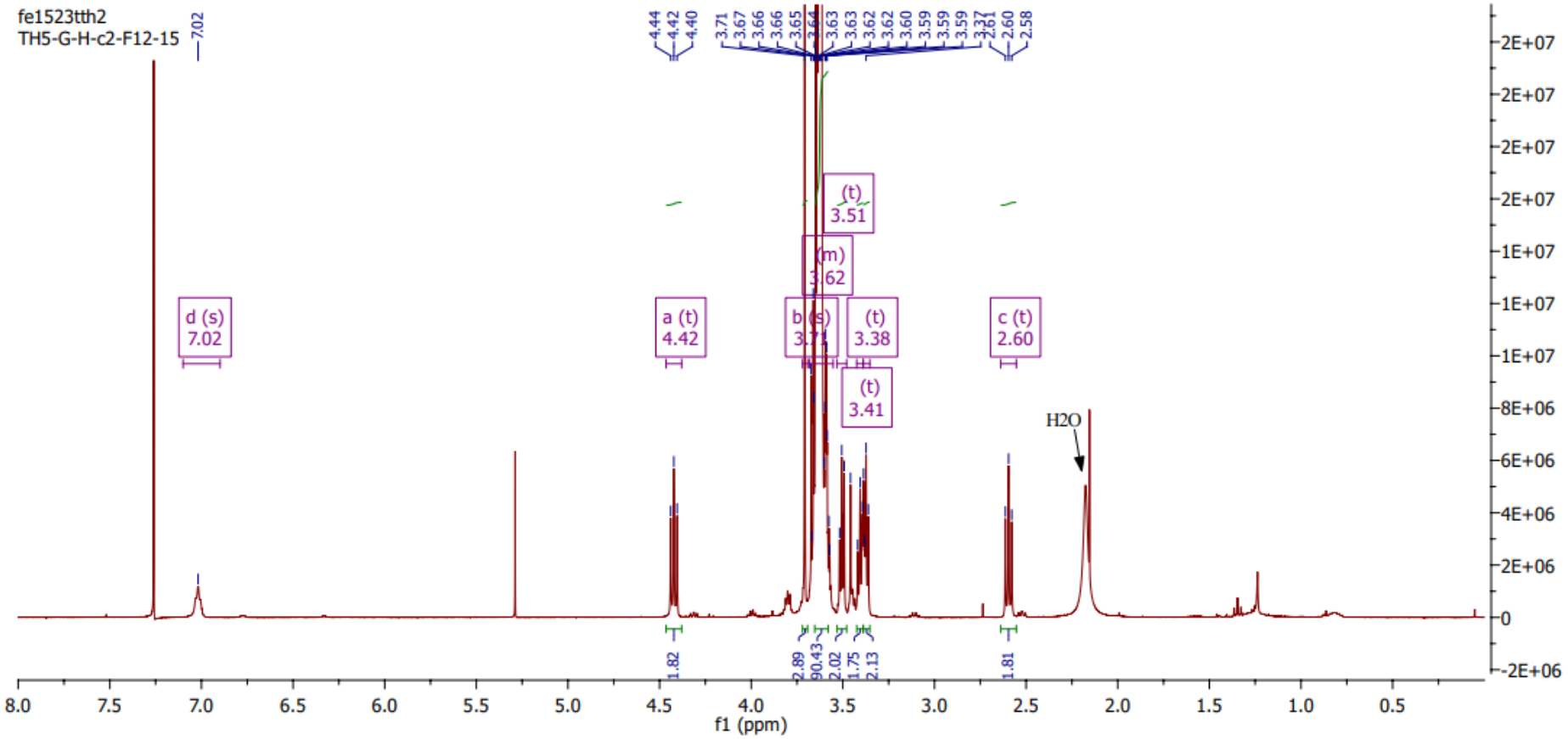

Zoomed region

^{1}H NMR (400 MHz, $CDCl_3$) δ 7.02 (s, 1H), 4.42 (t, 2H), 3.71 (s, 3H), 3.68 – 3.55 (m, 98H), 3.51 (t, 2H), 3.41 (t, J = 5.3 Hz, 2H), 3.38 (t, J = 6.7, 3.5 Hz, 2H), 2.60 (t, J = 6.9 Hz, 2H).

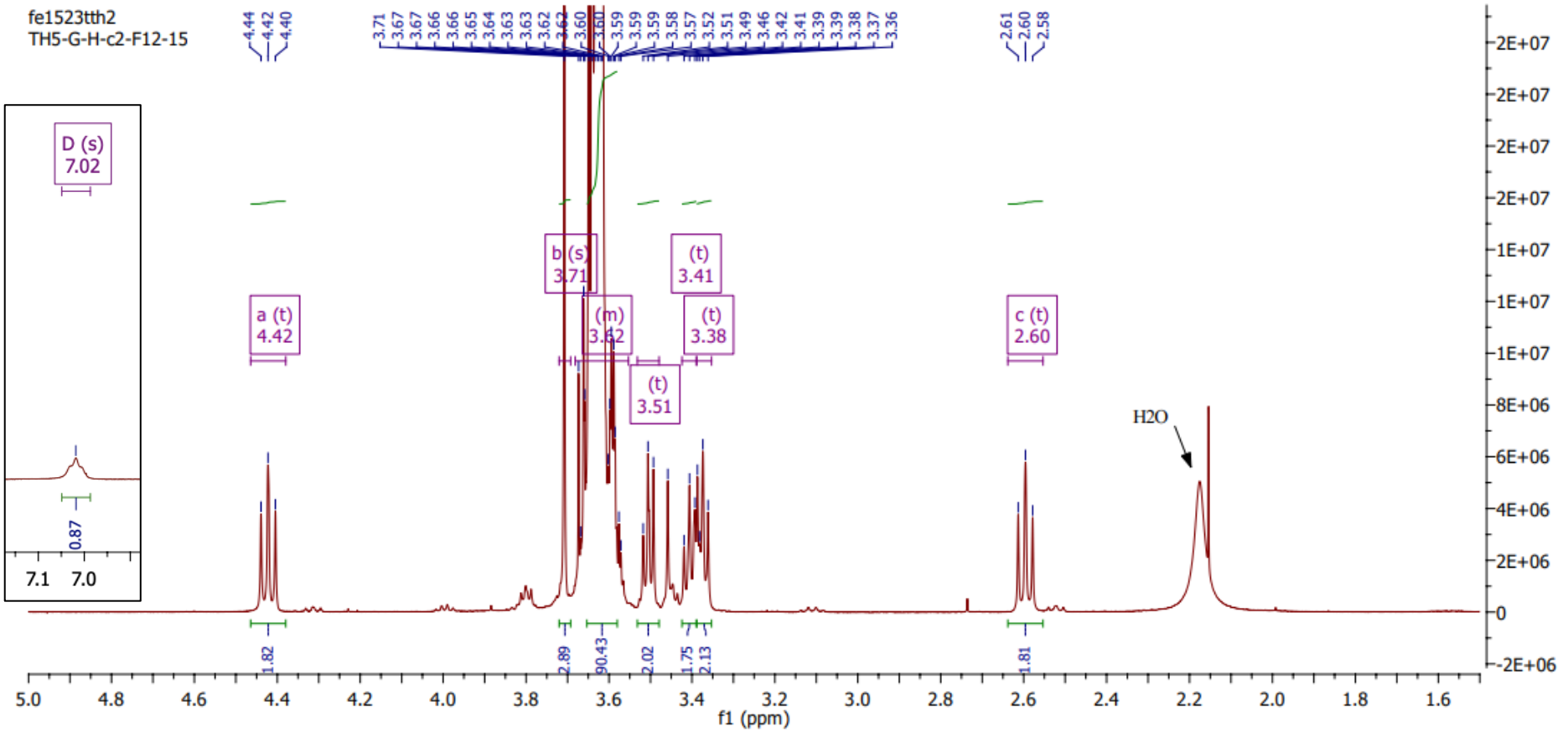

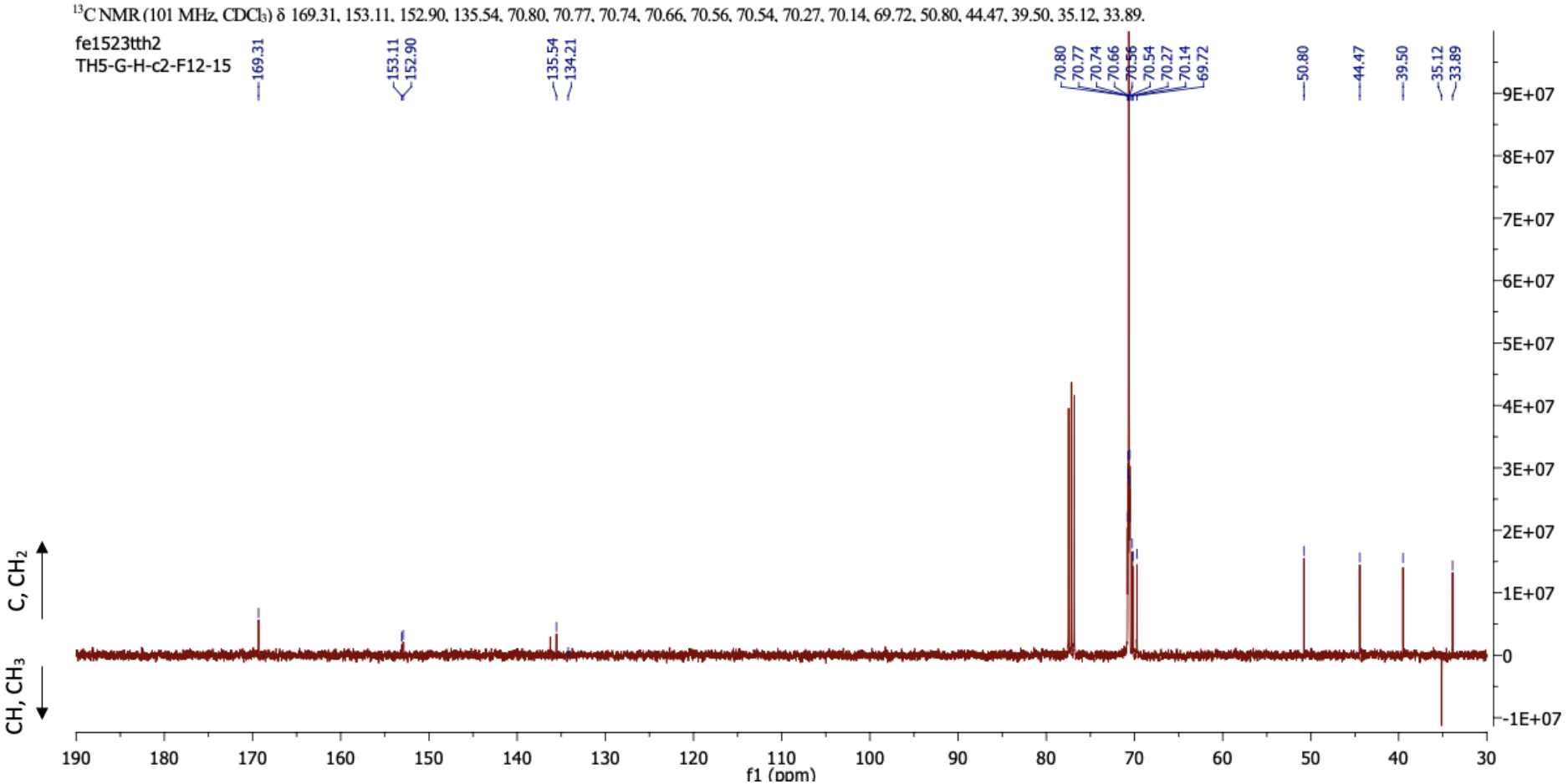
^{13}C NMR (101 MHz, $CDCl_3$) δ 169.31, 153.11, 152.90, 135.54, 70.80, 70.77, 70.74, 70.66, 70.56, 70.54, 70.27, 70.14, 69.72, 50.80, 44.47, 39.50, 35.12, 33.89.
fe1523tth2
TH5-G-H-c2-F12-15
169.31
153.11
152.90
135.54
134.21
70.80
70.77
70.74
70.66
70.56
70.54
70.27
70.14
69.72
50.80
44.47
39.50
35.12
33.89
C, CH2
CH, CH3
f1 (ppm)

A.8 IR Spectrum of diBrPD-23

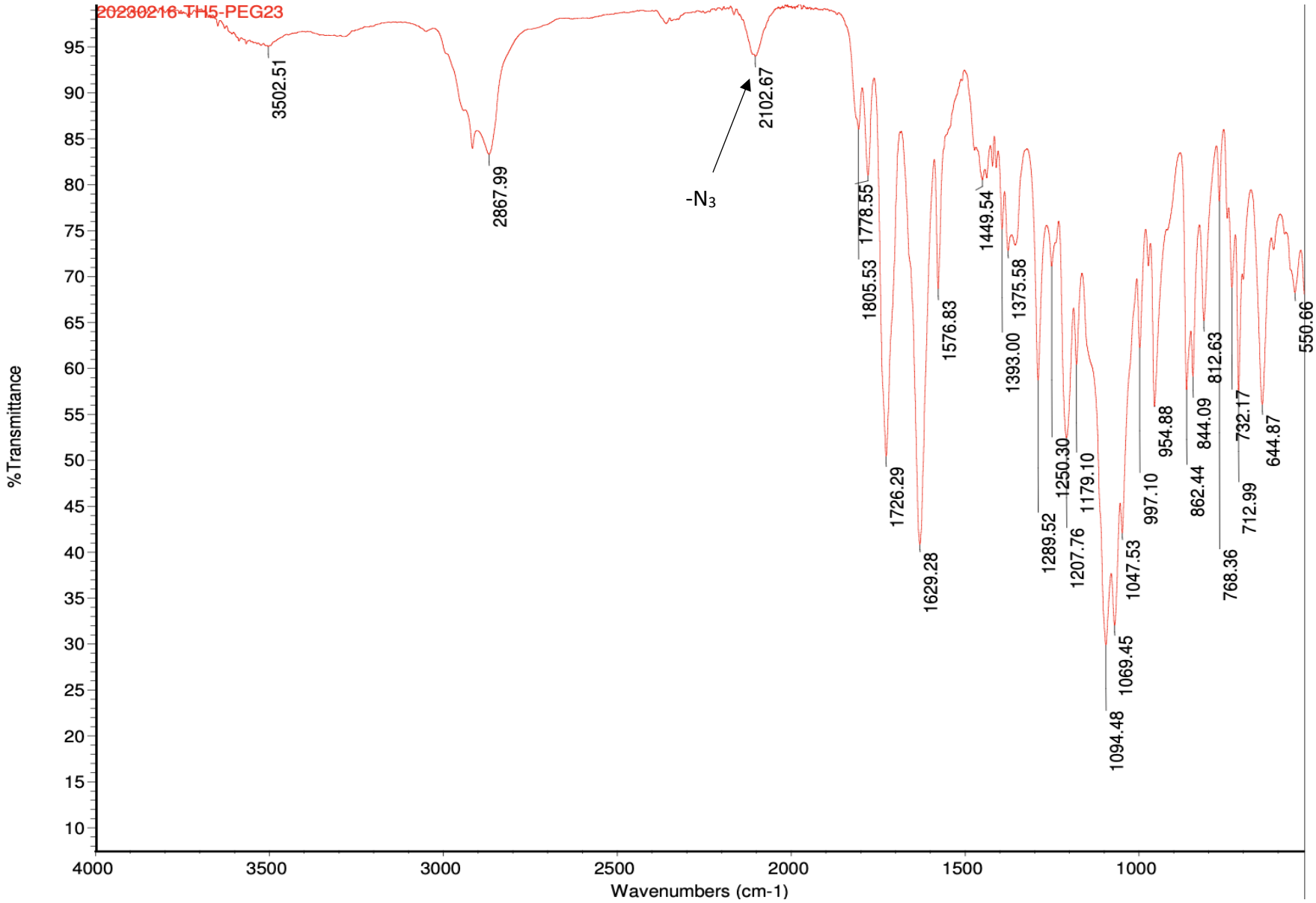

Appendix 9 LC-MS traces – rtx reference

A.9 UV-trace

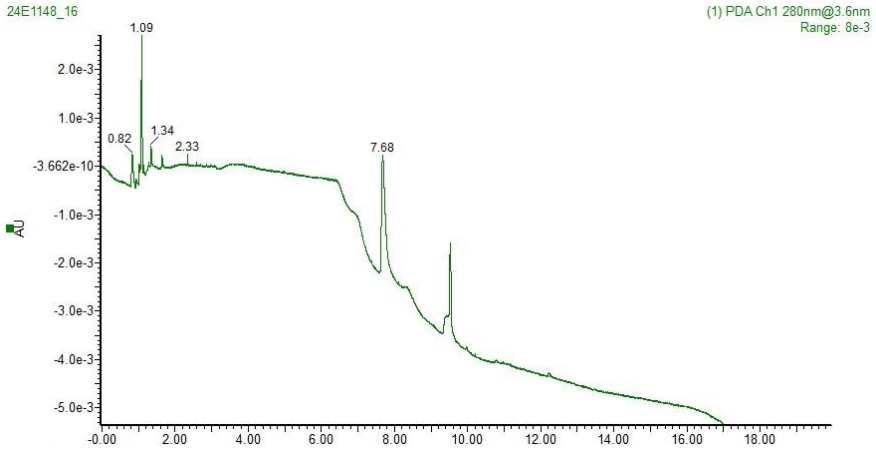

A.10 TIC

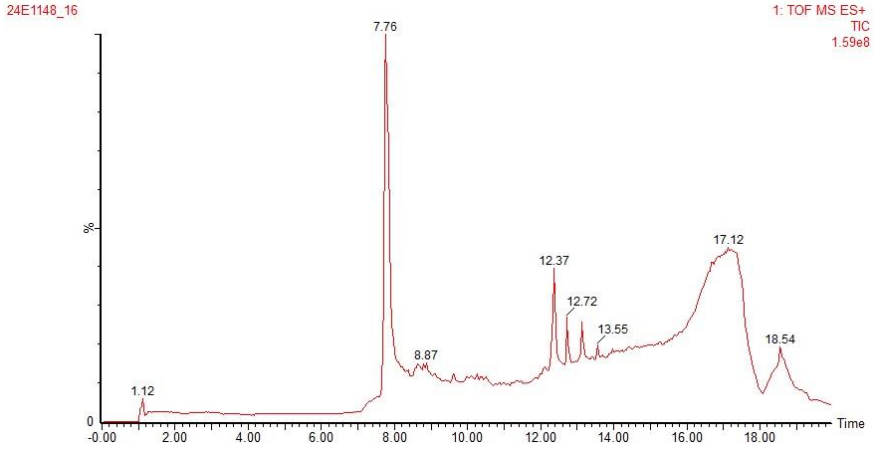

A.11 MS spectrum

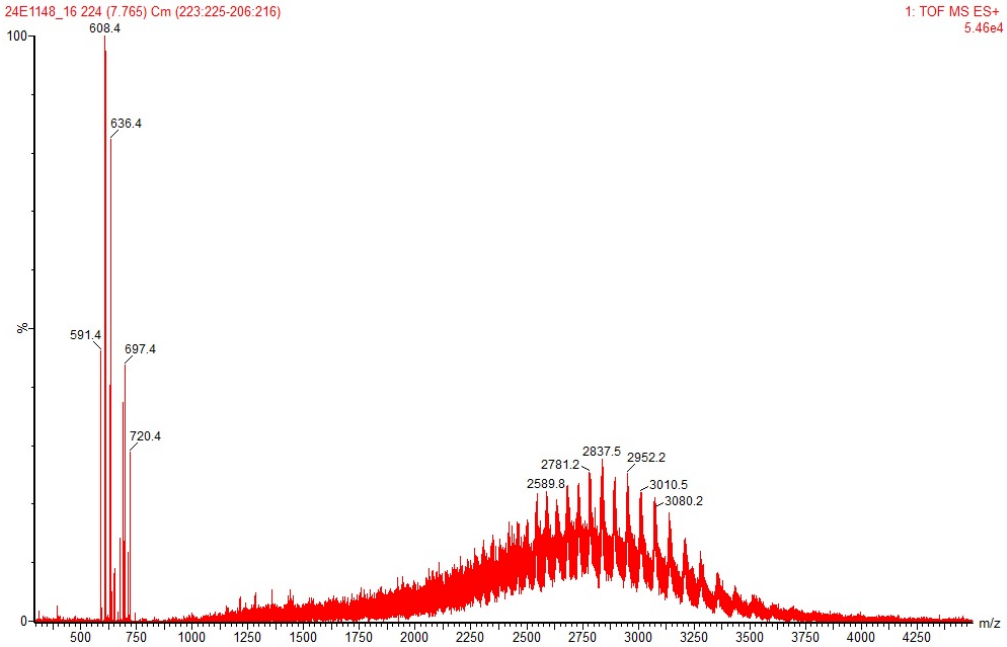

A.12 Deconvoluted spectrum

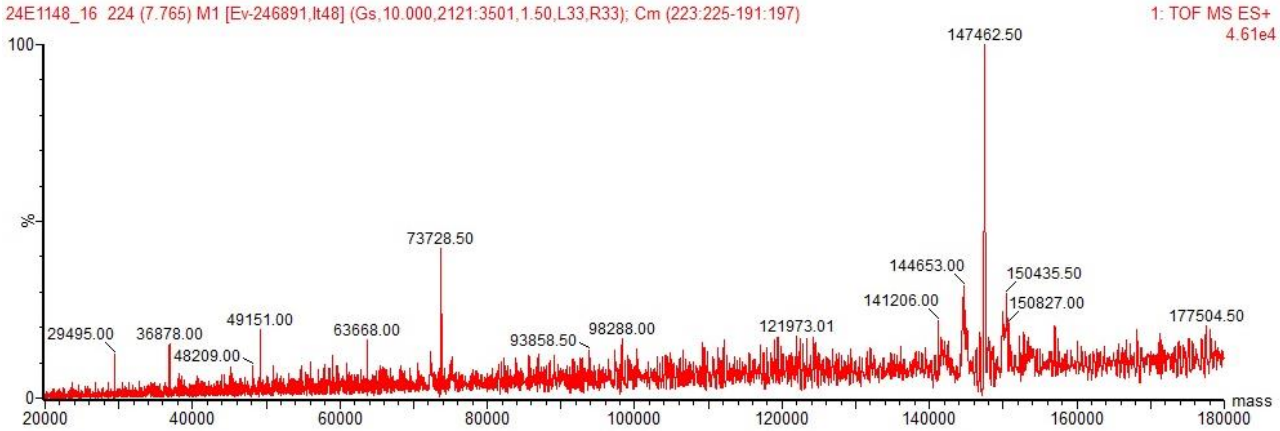

Appendix 10 LC-MS traces – rtx-diBrPD-8

A.13 UV-trace

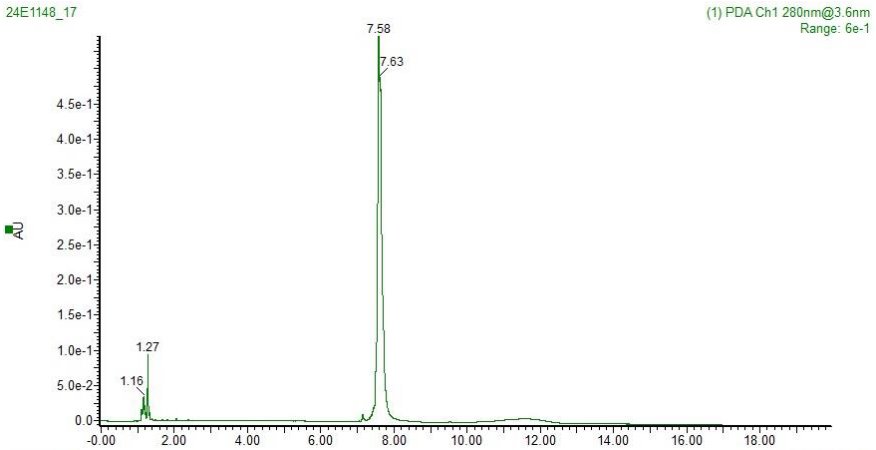

A.14 TIC

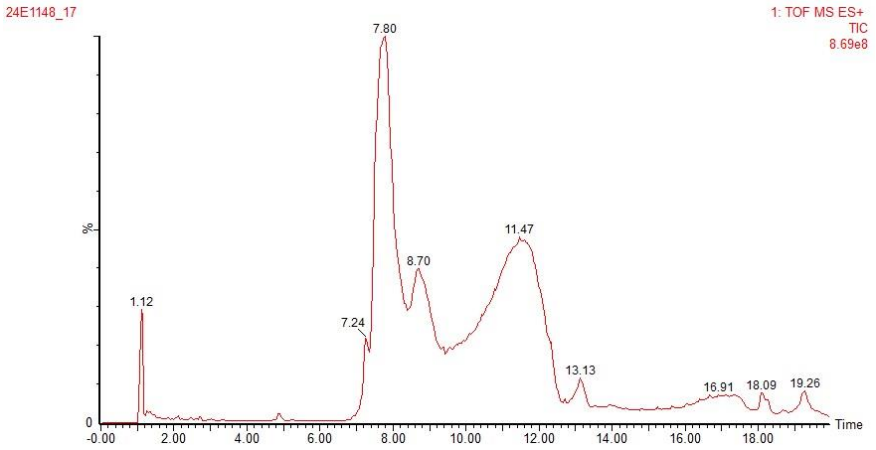

A.15 MS spectrum

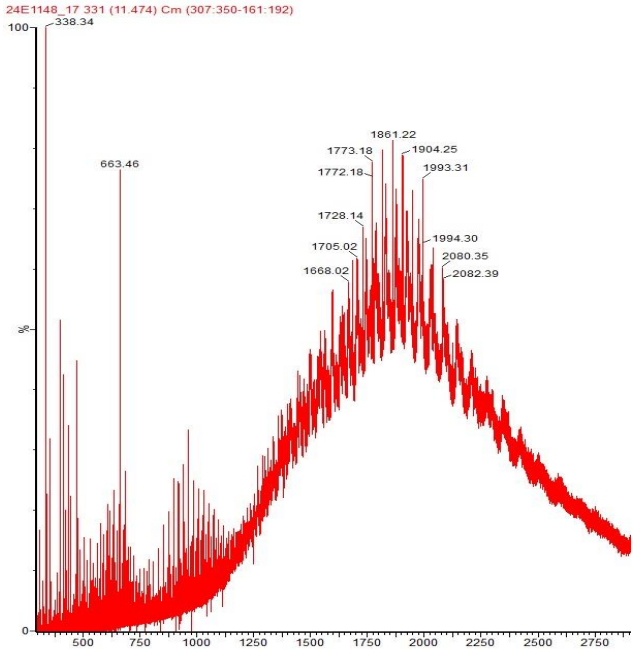

A.16 Deconvolution

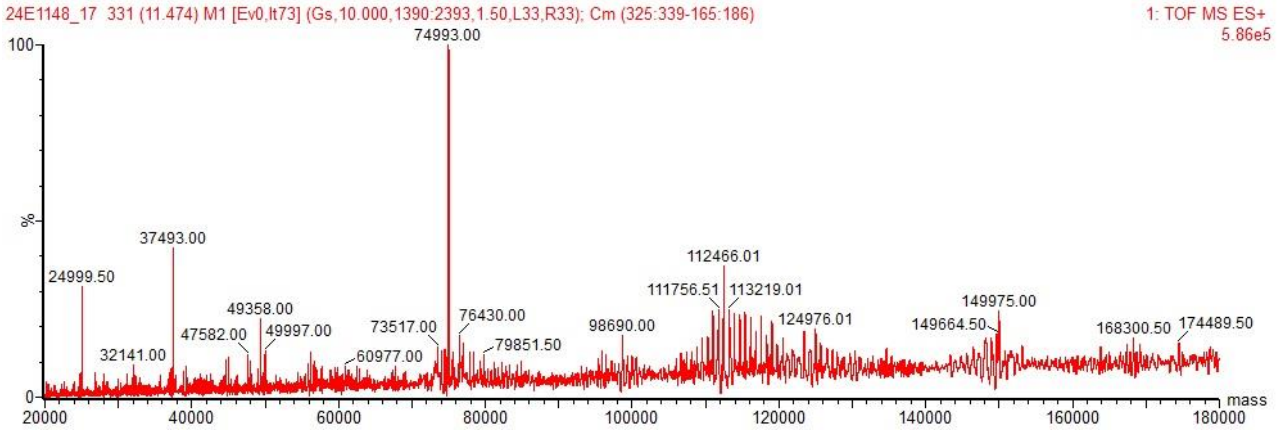

Appendix 11 TrypanBlue exclusion assay – single experiments on Ramos cells

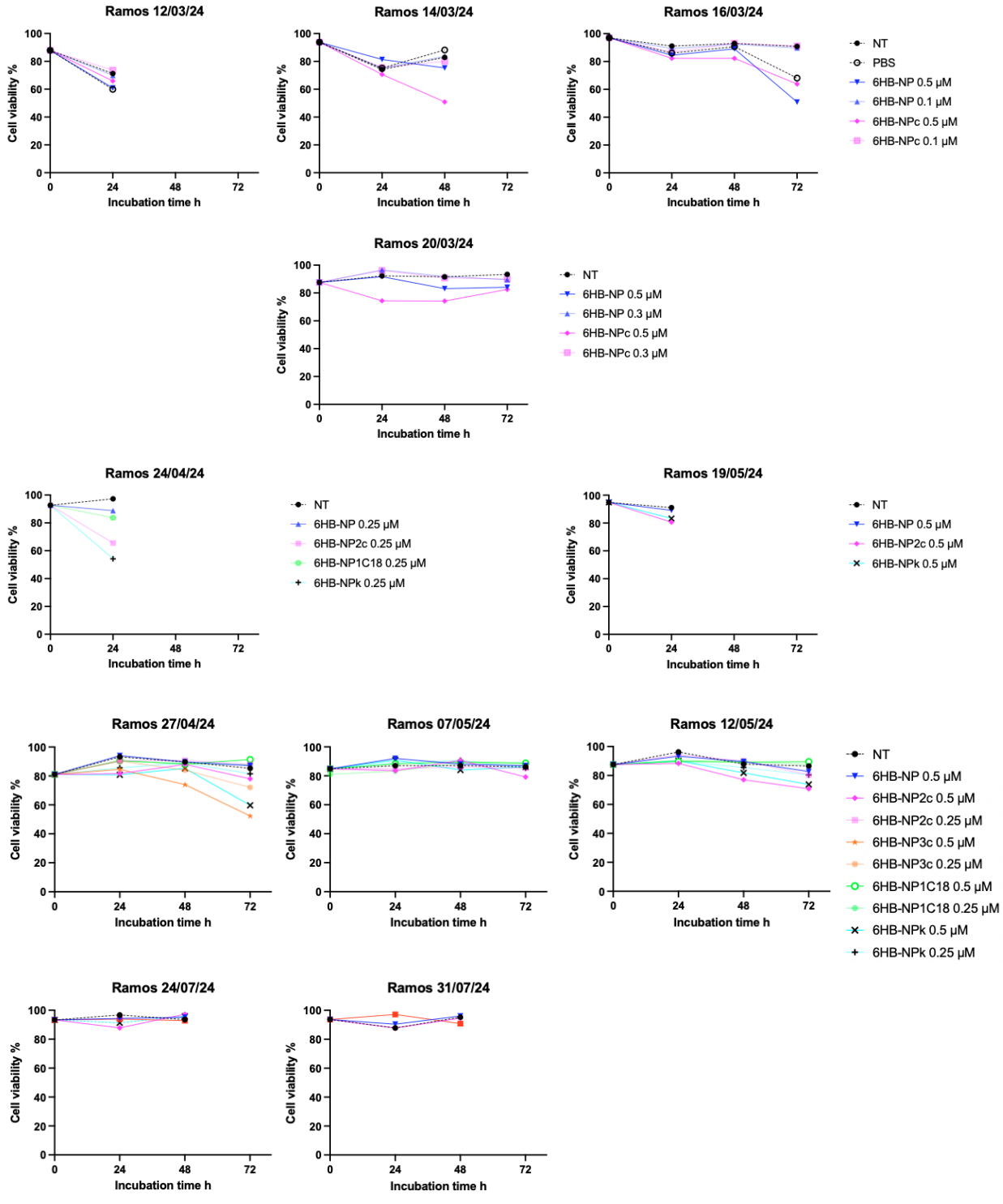

References

(1) International Agency for Research on Cancer World Health Organization, 2022. https://gco.iarc.who.int/today/en/dataviz/tables?mode=cancer&types=1&group_populations=1&multiple_populations=1 (accessed 2025 14/01/2025).

(2) Levine, M. H.; Haberman, A. M.; Sant'Angelo, D. B.; Hannum, L. G.; Cancro, M. P.; Janeway, C. A., Jr.; Shlomchik, M. J. A B-cell receptor-specific selection step governs immature to mature B cell differentiation. *Proc Natl Acad Sci U S A* **2000**, *97* (6), 2743-2748. DOI: 10.1073/pnas.050552997.

(3) Mikulic, M. *Global oncology spending 2013-2024*. Statista, 2024. https://www.statista.com/statistics/696208/oncology-costs-worldwide/ (accessed 2025 14/01/2025).

(4) Tfayli, A. H.; El-Halabi, L. N.; Khuri, F. R. Global disparities in cancer care: Bridging the gap in affordability and access to medications between high and low-income countries. *Cancer* **2025**, *131* (1), e35590. DOI: 10.1002/cncr.35590.

(5) Chen, S.; Cao, Z.; Prettner, K.; Kuhn, M.; Yang, J.; Jiao, L.; Wang, Z.; Li, W.; Geldsetzer, P.; Barnighausen, T.; et al. Estimates and Projections of the Global Economic Cost of 29 Cancers in 204 Countries and Territories From 2020 to 2050. *JAMA Oncol* **2023**, *9* (4), 465-472. DOI: 10.1001/jamaoncol.2022.7826.

(6) Krieghoff-Henning E, F. J., Penzkofer A, Weg-Remers S. Cancer - an overview. *Med Monatsschr Pharm.* **2017**, (Feb), 48-54.

(7) Dunn-Walters, D.; Thiede, C.; Alpen, B.; Spencer, J. Somatic hypermutation and B-cell lymphoma. *Philos Trans R Soc Lond B Biol Sci* **2001**, *356* (1405), 73-82. DOI: 10.1098/rstb.2000.0751.

(8) Fisher, S. G.; Fisher, R. I. The epidemiology of non-Hodgkin's lymphoma. *Oncogene* **2004**, *23* (38), 6524-6534. DOI: 10.1038/sj.onc.1207843.

(9) Perez-Vera, P.; Reyes-Leon, A.; Fuentes-Panana, E. M. Signaling proteins and transcription factors in normal and malignant early B cell development. *Bone Marrow Res* **2011**, *2011*, 502751. DOI: 10.1155/2011/502751.

(10) Kurosaki, T. B-lymphocyte biology. *Immunol Rev* **2010**, *237* (1), 5-9. DOI: 10.1111/j.1600-065X.2010.00946.x.

(11) Sehn, L. H.; Salles, G. Diffuse Large B-Cell Lymphoma. *N Engl J Med* **2021**, *384* (9), 842-858. DOI: 10.1056/NEJMra2027612.

(12) Kumar, R.; Parikh, R. R. Role of Radiotherapy in the Management of Elderly Patients With Lymphoma. *Semin Radiat Oncol* **2025**, *35* (1), 57-66. DOI: 10.1016/j.semradonc.2024.08.003.

(13) Li, L.; He, Z.; Zhou, Q.; Nie, B. The association between radiotherapy and the prognosis of follicular lymphoma patients with different characteristics in the rituximab era: a cohort study based on Surveillance, Epidemiology and End Results. *Ann Hematol* **2025**. DOI: 10.1007/s00277-025-06209-0.

(14) Mohan, G.; T P, A. H.; A J, J.; K M, S. D.; Narayanasamy, A.; Vellingiri, B. Recent advances in radiotherapy and its associated side effects in cancer—a review. *The Journal of Basic and Applied Zoology* **2019**, *80* (1). DOI: 10.1186/s41936-019-0083-5.

(15) Majeed, H.; Gupta, V. Adverse Effects of Radiation Therapy. In *StatPearls*, 2025.

(16) Hientz, K.; Mohr, A.; Bhakta-Guha, D.; Efferth, T. The role of p53 in cancer drug resistance and targeted chemotherapy. *Oncotarget* **2017**, *8* (5), 8921-8946. DOI: 10.18632/oncotarget.13475.

(17) Xu-Monette, Z. Y.; Medeiros, L. J.; Li, Y.; Orlowski, R. Z.; Andreeff, M.; Bueso-Ramos, C. E.; Greiner, T. C.; McDonnell, T. J.; Young, K. H. Dysfunction of the TP53 tumor suppressor gene in lymphoid malignancies. *Blood* **2012**, *119* (16), 3668-3683. DOI: 10.1182/blood-2011-11-366062.

(18) Bennett, R.; Thompson, E.; Tam, C. SOHO State of the Art Updates and Next Questions | Mechanisms of Resistance to BCL2 Inhibitor Therapy in Chronic Lymphocytic Leukemia and Potential Future Therapeutic Directions. *Clin Lymphoma Myeloma Leuk* **2022**, *22* (11), 795-804. DOI: 10.1016/j.clml.2022.07.013.

(19) Sehn, L. H.; Gascoyne, R. D. Diffuse large B-cell lymphoma: optimizing outcome in the context of clinical and biologic heterogeneity. *Blood* **2015**, *125* (1), 22-32. DOI: 10.1182/blood-2014-05-577189.

(20) [Internet], I. o. *The innate and adaptive immune systems*. Cologne, Germany: Institute for Quality and Efficiency in Health Care (IQWiG), 2006. https://www.ncbi.nlm.nih.gov/books/NBK279396/ (accessed 16/03/2022).

(21) AMBOSS. Überblick über das unspezifische und spezifische Immunsystem — Immunologie — AMBOSS Video. 05/03/2020. (accessed 15/03/2022).

(22) Malu, S.; Malshetty, V.; Francis, D.; Cortes, P. Role of non-homologous end joining in V(D)J recombination. *Immunol Res* **2012**, *54* (1-3), 233-246. DOI: 10.1007/s12026-012-8329-z.

(23) Schroeder, H. W., Jr.; Cavacini, L. Structure and function of immunoglobulins. *J Allergy Clin Immunol* **2010**, *125* (2 Suppl 2), S41-52. DOI: 10.1016/j.jaci.2009.09.046.

(24) Howard, M.; Farrar, J.; Hilfiker, M.; Johnson, B.; Takatsu, K.; Hamaoka, T.; Paul, W. E. Identification of a T cell-derived b cell growth factor distinct from interleukin 2. *J Exp Med* **1982**, *155* (3), 914-923. DOI: 10.1084/jem.155.3.914.

(25) Klein, U.; Dalla-Favera, R. Germinal centres: role in B-cell physiology and malignancy. *Nat Rev Immunol* **2008**, *8* (1), 22-33. DOI: 10.1038/nri2217.

(26) Janeway CA Jr, T. P., Walport M, et al. . *Immunobiology: The Immune System in Health and Disease*; Garland Science, 2001.

(27) Kuppers, R. Mechanisms of B-cell lymphoma pathogenesis. *Nat Rev Cancer* **2005**, *5* (4), 251-262. DOI: 10.1038/nrc1589.

(28) Miguez-Rey, E.; Choi, D.; Kim, S.; Yoon, S.; Sandulescu, O. Monoclonal antibody therapies in the management of SARS-CoV-2 infection. *Expert Opin Investig Drugs* **2022**, *31* (1), 41-58. DOI: 10.1080/13543784.2022.2030310.

(29) Sedeyn, K.; Saelens, X. New antibody-based prevention and treatment options for influenza. *Antiviral Res* **2019**, *170*, 104562. DOI: 10.1016/j.antiviral.2019.104562.

(30) Margolis, D. M.; Koup, R. A.; Ferrari, G. HIV antibodies for treatment of HIV infection. *Immunol Rev* **2017**, *275* (1), 313-323. DOI: 10.1111/imr.12506.

(31) White, N. J. Monoclonal Antibodies to Treat Diphtheria. *J Infect Dis* **2024**. DOI: 10.1093/infdis/jiae500 From NLM Publisher.

(32) Ghotloo, S.; Golsaz-Shirazi, F.; Amiri, M. M.; Jeddi-Tehrani, M.; Shokri, F. Neutralization of tetanus toxin by a novel chimeric monoclonal antibody. *Toxicon* **2021**, *201*, 27-36. DOI: 10.1016/j.toxicon.2021.08.011.

(33) Kohler, G.; Milstein, C. Continuous cultures of fused cells secreting antibody of predefined specificity. *Nature* **1975**, *256* (5517), 495-497. DOI: 10.1038/256495a0.

(34) Miller, R. A.; Maloney, D. G.; Warnke, R.; Levy, R. Treatment of B-cell lymphoma with monoclonal anti-idiotype antibody. *N Engl J Med* **1982**, *306* (9), 517-522. DOI: 10.1056/NEJM198203043060906.

(35) Milstein, C. The hybridoma revolution: an offshoot of basic research. *Bioessays* **1999**, *21* (11), 966-973. DOI: 10.1002/(SICI)1521-1878(199911)21:11<966::AID-BIES9>3.0.CO;2-Z.

(36) Chen, Z.; Kankala, R. K.; Yang, Z.; Li, W.; Xie, S.; Li, H.; Chen, A. Z.; Zou, L. Antibody-based drug delivery systems for cancer therapy: Mechanisms, challenges, and prospects. *Theranostics* **2022**, *12* (8), 3719-3746. DOI: 10.7150/thno.72594.

(37) Kubota, T.; Niwa, R.; Satoh, M.; Akinaga, S.; Shitara, K.; Hanai, N. Engineered therapeutic antibodies with improved effector functions. *Cancer Sci* **2009**, *100* (9), 1566-1572. DOI: 10.1111/j.1349-7006.2009.01222.x.

(38) Tsao, L. C.; Force, J.; Hartman, Z. C. Mechanisms of Therapeutic Antitumor Monoclonal Antibodies. *Cancer Res* **2021**, *81* (18), 4641-4651. DOI: 10.1158/0008-5472.CAN-21-1109.

(39) Rocco, D.; Della Gravara, L.; Battiloro, C.; Palazzolo, G.; Gridelli, C. Recently approved and emerging monoclonal antibody immune checkpoint inhibitors for the treatment of advanced non-small cell lung cancer. *Expert Opin Biol Ther* **2023**, *23* (3), 261-268. DOI: 10.1080/14712598.2023.2183116.

(40) Manso, T.; Kushwaha, A.; Abdollahi, N.; Duroux, P.; Giudicelli, V.; Kossida, S. Mechanisms of action of monoclonal antibodies in oncology integrated in IMGT/mAb-DB. *Front Immunol* **2023**, *14*, 1129323. DOI: 10.3389/fimmu.2023.1129323.

(41) Qin, D.; Zhang, Y.; Shu, P.; Lei, Y.; Li, X.; Wang, Y. Targeting tumor-infiltrating tregs for improved antitumor responses. *Front Immunol* **2024**, *15*, 1325946. DOI: 10.3389/fimmu.2024.1325946.

(42) Stashenko, P.; Nadler, L. M.; Hardy, R.; Schlossman, S. F. Characterization of a human B lymphocyte-specific antigen. *J Immunol* **1980**, *125* (4), 1678-1685.

(43) Pavlasova, G.; Mraz, M. The regulation and function of CD20: an "enigma" of B-cell biology and targeted therapy. *Haematologica* **2020**, *105* (6), 1494-1506. DOI: 10.3324/haematol.2019.243543.

(44) Salles, G.; Barrett, M.; Foa, R.; Maurer, J.; O'Brien, S.; Valente, N.; Wenger, M.; Maloney, D. G. Rituximab in B-Cell Hematologic Malignancies: A Review of 20 Years of Clinical Experience. *Adv Ther* **2017**, *34* (10), 2232-2273. DOI: 10.1007/s12325-017-0612-x.

(45) Lim, S. H.; Levy, R. Translational medicine in action: anti-CD20 therapy in lymphoma. *J Immunol* **2014**, *193* (4), 1519-1524. DOI: 10.4049/jimmunol.1490027.

(46) Lim, S. H.; Beers, S. A.; French, R. R.; Johnson, P. W.; Glennie, M. J.; Cragg, M. S. Anti-CD20 monoclonal antibodies: historical and future perspectives. *Haematologica* **2010**, *95* (1), 135-143. DOI: 10.3324/haematol.2008.001628.

(47) Goebeler, M. E.; Bargou, R. Blinatumomab: a CD19/CD3 bispecific T cell engager (BiTE) with unique anti-tumor efficacy. *Leuk Lymphoma* **2016**, *57* (5), 1021-1032. DOI: 10.3109/10428194.2016.1161185.

(48) Zhu, M.; Wu, B.; Brandl, C.; Johnson, J.; Wolf, A.; Chow, A.; Doshi, S. Blinatumomab, a Bispecific T-cell Engager (BiTE((R))) for CD-19 Targeted Cancer Immunotherapy: Clinical Pharmacology and Its Implications. *Clin Pharmacokinet* **2016**, *55* (10), 1271-1288. DOI: 10.1007/s40262-016-0405-4.

(49) Crick, F. Central dogma of molecular biology. *Nature* **1970**, *227* (5258), 561-563. DOI: 10.1038/227561a0.

(50) Brown, T., Brown, T. (Jnr). *Nucleic Acids Book*.

(51) Pray, L. A. Discovery of DNA Structure and Function: Watson and Crick. *Nature Education* **2008**, *1* (100).

(52) Kossel, A. *The Chemical Composition of the Cell Nucleus*. Elsevier Publishing Company, 1910. https://www.nobelprize.org/prizes/medicine/1910/kossel/lecture/ (accessed 2022 09/03/2022).

(53) Attar, N. Raymond Gosling: the man who crystallized genes. *Genome Biol* **2013**, *14* (4), 402. DOI: 10.1186/gb-2013-14-1-402.

(54) Watson, J. D.; Crick, F. H. C. Molecular Structure of Nucleic Acids. *Nature* **1953**, *171*, 737-738. DOI: 10.1038/171737a0.

(55) Wilkins, M. H.; Stokes, A. R.; Wilson, H. R. Molecular structure of deoxypentose nucleic acids. *Nature* **1953**, *171* (4356), 738-740. DOI: 10.1038/171738a0.

(56) Franklin, R. E.; Gosling, R. G. Molecular configuration in sodium thymonucleate. *Nature* **1953**, *171* (4356), 740-741. DOI: 10.1038/171740a0.

(57) Sinden, V. N. P. a. R. R. *Madame Curie Bioscience Database; DNA: Alternative Conformations and Biology*; Landes Bioscience, 2000-2013.

(58) Xiong, Y.; Sundaralingam, M. Crystal structure and conformation of a DNA-RNA hybrid duplex with a polypurine RNA strand: d(TTCTTBr5CTTC)-r(GAAGAAGAA). *Structure* **1998**, *6* (12), 1493-1501. DOI: 10.1016/s0969-2126(98)00148-8.

(59) Heinemann, U.; Roske, Y. Symmetry in Nucleic-Acid Double Helices. *Symmetry* **2020**, *12* (5). DOI: 10.3390/sym12050737.

(60) Zhang, C.; Maruggi, G.; Shan, H.; Li, J. Advances in mRNA Vaccines for Infectious Diseases. *Front Immunol* **2019**, *10*, 594. DOI: 10.3389/fimmu.2019.00594.

(61) Vinjamuri, B. P.; Pan, J.; Peng, P. A Review on Commercial Oligonucleotide Drug Products. *J Pharm Sci* **2024**, *113* (7), 1749-1768. DOI: 10.1016/j.xphs.2024.04.021.

(62) Hofman, C. R.; Corey, D. R. Targeting RNA with synthetic oligonucleotides: Clinical success invites new challenges. *Cell Chem Biol* **2024**, *31* (1), 125-138. DOI: 10.1016/j.chembiol.2023.09.005.

(63) Egli, M.; Manoharan, M. Chemistry, structure and function of approved oligonucleotide therapeutics. *Nucleic Acids Res* **2023**, *51* (6), 2529-2573. DOI: 10.1093/nar/gkad067.

(64) Li, Y.; Chen, S.; Rahimizadeh, K.; Zhang, Z.; Veedu, R. N. Inhibition of survivin by 2'-O-methyl phosphorothioate-modified steric-blocking antisense oligonucleotides. *RSC Adv* **2024**, *14* (19), 13336-13341. DOI: 10.1039/d4ra01925c.

(65) Hua, Y.; Vickers, T. A.; Baker, B. F.; Bennett, C. F.; Krainer, A. R. Enhancement of SMN2 exon 7 inclusion by antisense oligonucleotides targeting the exon. *PLoS Biol* **2007**, *5* (4), e73. DOI: 10.1371/journal.pbio.0050073.

(66) Finkel, R. S.; Mercuri, E.; Darras, B. T.; Connolly, A. M.; Kuntz, N. L.; Kirschner, J.; Chiriboga, C. A.; Saito, K.; Servais, L.; Tizzano, E.; et al. Nusinersen versus Sham Control in Infantile-Onset Spinal Muscular Atrophy. *N Engl J Med* **2017**, *377* (18), 1723-1732. DOI: 10.1056/NEJMoa1702752.

(67) Seeman, N. C. K., Neville R. Design of immobile nucleic acid junctions. *Biophysical Journal* **1983**, *44*, 201-209. DOI: 10.1016/S0006-3495(83)84292-1.

(68) Chen, J. H.; Seeman, N. C. Synthesis from DNA of a molecule with the connectivity of a cube. *Nature* **1991**, *350* (6319), 631-633. DOI: 10.1038/350631a0.

(69) Rothemund, P. W. Folding DNA to create nanoscale shapes and patterns. *Nature* **2006**, *440* (7082), 297-302. DOI: 10.1038/nature04586.

(70) Douglas, S. M.; Marblestone, A. H.; Teerapittayanon, S.; Vazquez, A.; Church, G. M.; Shih, W. M. Rapid prototyping of 3D DNA-origami shapes with caDNAno. *Nucleic Acids Res* **2009**, *37* (15), 5001-5006. DOI: 10.1093/nar/gkp436.

(71) Liu, W.; Duan, H.; Zhang, D.; Zhang, X.; Luo, Q.; Xie, T.; Yan, H.; Peng, L.; Hu, Y.; Liang, L.; et al. Concepts and Application of DNA Origami and DNA Self-Assembly: A Systematic Review. *Appl Bionics Biomech* **2021**, *2021*, 9112407. DOI: 10.1155/2021/9112407.

(72) Udomprasert, A.; Kangsamaksin, T. DNA origami applications in cancer therapy. *Cancer Sci* **2017**, *108* (8), 1535-1543. DOI: 10.1111/cas.13290.

(73) Langecker, M.; Arnaut, V.; Martin, T. G.; List, J.; Renner, S.; Mayer, M.; Dietz, H.; Simmel, F. C. Synthetic lipid membrane channels formed by designed DNA nanostructures. *Science* **2012**, *338* (6109), 932-936. DOI: 10.1126/science.1225624.

(74) Burns, J. R.; Stulz, E.; Howorka, S. Self-assembled DNA nanopores that span lipid bilayers. *Nano Lett* **2013**, *13* (6), 2351-2356. DOI: 10.1021/nl304147f.

(75) Burns, J. R.; Gopfrich, K.; Wood, J. W.; Thacker, V. V.; Stulz, E.; Keyser, U. F.; Howorka, S. Lipid-bilayer-spanning DNA nanopores with a bifunctional porphyrin anchor. *Angew Chem Int Ed Engl* **2013**, *52* (46), 12069-12072. DOI: 10.1002/anie.201305765.

(76) Burns, J. R.; Al-Juffali, N.; Janes, S. M.; Howorka, S. Membrane-spanning DNA nanopores with cytotoxic effect. *Angew Chem Int Ed Engl* **2014**, *53* (46), 12466-12470. DOI: 10.1002/anie.201405719.

(77) Kocabey, S.; Ekim Kocabey, A.; Schneiter, R.; Ruegg, C. Membrane-Interacting DNA Nanotubes Induce Cancer Cell Death. *Nanomaterials (Basel)* **2021**, *11* (8). DOI: 10.3390/nano11082003.

(78) Entwistle, L. L. Exploring the Cytotoxicity of DNA Nanopores for Treatment of Melanoma. University of Southampton, 2020.

(79) Li, Y.; Chen, X.; Lv, C.; Cheng, Y. Ethane groups modified DNA nanopores to prolong the dwell time on live cell membranes for transmembrane transport. *Front Chem* **2023**, *11*, 1148699. DOI: 10.3389/fchem.2023.1148699.

(80) Guo, X. L.; Yuan, D. D.; Song, T.; Li, X. M. DNA nanopore functionalized with aptamer and cell-penetrating peptide for tumor cell recognition. *Anal Bioanal Chem* **2017**, *409* (15), 3789-3797. DOI: 10.1007/s00216-017-0321-y.

(81) Fish, J. Investigating Clinical Cancer Therapeutics Conjugated with Spatially Biased DNA Nanopores. University of Southampton, 2020.

(82) M. D. Matteucci , M. H. C. Synthesis of deoxyoligonucleotides on a polymer support. *J. Am. Chem. Soc.* **1981**, *103*, 3185-3191. DOI: https://doi.org/10.1021/ja00401a041.

(83) S. L. Beaucage , M. H. C. Deoxynucleoside phosphoramidites - a new class of key intermediates for deoxypolynucleotide synthesis. *Tetrahedron Lett. 22* **1981**, 1859-1862.

(84) Riccardi, F.; Dal Bo, M.; Macor, P.; Toffoli, G. A comprehensive overview on antibody-drug conjugates: from the conceptualization to cancer therapy. *Front Pharmacol* **2023**, *14*, 1274088. DOI: 10.3389/fphar.2023.1274088.

(85) Dumontet, C.; Reichert, J. M.; Senter, P. D.; Lambert, J. M.; Beck, A. Antibody-drug conjugates come of age in oncology. *Nat Rev Drug Discov* **2023**, *22* (8), 641-661. DOI: 10.1038/s41573-023-00709-2.

(86) Gogia, P.; Ashraf, H.; Bhasin, S.; Xu, Y. Antibody-Drug Conjugates: A Review of Approved Drugs and Their Clinical Level of Evidence. *Cancers (Basel)* **2023**, *15* (15). DOI: 10.3390/cancers15153886.

(87) Dugal-Tessier, J.; Thirumalairajan, S.; Jain, N. Antibody-Oligonucleotide Conjugates: A Twist to Antibody-Drug Conjugates. *J Clin Med* **2021**, *10* (4). DOI: 10.3390/jcm10040838.

(88) Malecova, B.; Burke, R. S.; Cochran, M.; Hood, M. D.; Johns, R.; Kovach, P. R.; Doppalapudi, V. R.; Erdogan, G.; Arias, J. D.; Darimont, B.; et al. Targeted tissue delivery of RNA therapeutics using antibody-oligonucleotide conjugates (AOCs). *Nucleic Acids Res* **2023**, *51* (12), 5901-5910. DOI: 10.1093/nar/gkad415.

(89) Dovgan, I.; Ehkirch, A.; Lehot, V.; Kuhn, I.; Koniev, O.; Kolodych, S.; Hentz, A.; Ripoll, M.; Ursuegui, S.; Nothisen, M.; et al. On the use of DNA as a linker in antibody-drug conjugates: synthesis, stability and in vitro potency. *Sci Rep* **2020**, *10* (1), 7691. DOI: 10.1038/s41598-020-64518-y.

(90) Jiao, J.; Qian, Y.; Lv, Y.; Wei, W.; Long, Y.; Guo, X.; Buerliesi, A.; Ye, J.; Han, H.; Li, J.; et al. Overcoming limitations and advancing the therapeutic potential of antibody-oligonucleotide conjugates (AOCs): Current status and future perspectives. *Pharmacol Res* **2024**, *209*, 107469. DOI: 10.1016/j.phrs.2024.107469.

(91) Journeaux, T.; Bernardes, G. J. L. Homogeneous multi-payload antibody-drug conjugates. *Nat Chem* **2024**, *16* (6), 854-870. DOI: 10.1038/s41557-024-01507-y.

(92) Adhikari, P.; Zacharias, N.; Ohri, R.; Sadowsky, J. Site-Specific Conjugation to Cys-Engineered THIOMAB Antibodies. *Methods Mol Biol* **2020**, *2078*, 51-69. DOI: 10.1007/978-1-4939-9929-3_4.

(93) Malecova, B. *AOC 1020: An Antibody Oligonucleotide Conjugate (AOC) in Development for the Treatment of FSHD*. 2023. https://www.avidity biosciences.com/wp-content/uploads/2023/04/MDA-2023_AOC-1020-preclinical_v7.0_FINAL.pdf (accessed 2025 15.03.2025).

(94) Zavoiura, O.; Brunner, B.; Casteels, P.; Zimmermann, L.; Ozog, M.; Boutton, C.; Helms, M. W.; Wagenaar, T.; Adam, V.; Peterka, J.; et al. Nanobody-siRNA Conjugates for Targeted Delivery of siRNA to Cancer Cells. *Mol Pharm* **2021**, *18* (3), 1048-1060. DOI: 10.1021/acs.molpharmaceut.0c01001.

(95) Wang, X.; Xiao, X.; Feng, Y.; Li, J.; Zhang, Y. A photoresponsive antibody-siRNA conjugate for activatable immunogene therapy of cancer. *Chem Sci* **2022**, *13* (18), 5345-5352. DOI: 10.1039/d2sc01672a.

(96) Morgan, H. E.; Turnbull, W. B.; Webb, M. E. Challenges in the use of sortase and other peptide ligases for site-specific protein modification. *Chem Soc Rev* **2022**, *51* (10), 4121-4145. DOI: 10.1039/d0cs01148g.

(97) Bahou, C.; Richards, D. A.; Maruani, A.; Love, E. A.; Javaid, F.; Caddick, S.; Baker, J. R.; Chudasama, V. Highly homogeneous antibody modification through optimisation of the synthesis and conjugation of functionalised dibromopyridazinediones. *Org Biomol Chem* **2018**, *16* (8), 1359-1366. DOI: 10.1039/c7ob03138f.

(98) Rocha Tapia, A.; Abgottspon, F.; Nilvebrant, J.; Nygren, P. A.; Duclos Ivetich, S.; Bello Hernandez, A. J.; Thanasi, I. A.; Szijj, P. A.; Sekkat, G.; Cuenot, F. M.; et al. Site-directed conjugation of single-stranded DNA to affinity proteins: quantifying the importance of conjugation strategy. *Chem Sci* **2024**, *15* (23), 8982-8992. DOI: 10.1039/d4sc01838a.

(99) Livak, K. J.; Schmittgen, T. D. Analysis of relative gene expression data using real-time quantitative PCR and the 2(-Delta Delta C(T)) Method. *Methods* **2001**, *25* (4), 402-408. DOI: 10.1006/meth.2001.1262.

(100) Gopfrich, K.; Zettl, T.; Meijering, A. E.; Hernandez-Ainsa, S.; Kocabey, S.; Liedl, T.; Keyser, U. F. DNA-Tile Structures Induce Ionic Currents through Lipid Membranes. *Nano Lett* **2015**, *15* (5), 3134-3138. DOI: 10.1021/acs.nanolett.5b00189.

(101) Burns, J. R.; Howorka, S. Structural and Functional Stability of DNA Nanopores in Biological Media. *Nanomaterials (Basel)* **2019**, *9* (4). DOI: 10.3390/nano9040490.

(102) Zhang, J. DNA Nanopores. University of Southampton, 2021.

(103) Seifert, A.; Gopfrich, K.; Burns, J. R.; Fertig, N.; Keyser, U. F.; Howorka, S. Bilayer-spanning DNA nanopores with voltage-switching between open and closed state. *ACS Nano* **2015**, *9* (2), 1117-1126. DOI: 10.1021/nn5039433.

(104) Ohmann, A.; Gopfrich, K.; Joshi, H.; Thompson, R. F.; Sobota, D.; Ranson, N. A.; Aksimentiev, A.; Keyser, U. F. Controlling aggregation of cholesterol-modified DNA nanostructures. *Nucleic Acids Res* **2019**, *47* (21), 11441-11451. DOI: 10.1093/nar/gkz914.

(105) Albericio, F.; Carpino, L. A. Coupling reagents and activation. *Methods Enzymol* **1997**, *289*, 104-126. DOI: 10.1016/s0076-6879(97)89046-5.

(106) König, W., Geiger, R. Eine neue Methode zur Synthese von Peptiden: Aktivierung der Carboxylgruppe mit Dicyclohexylcarbodiimid unter Zusatz von 1-Hydroxy-benzotriazolen. *Chemische Berichte* **1970**, *103* (3), 788-798. DOI: https://doi.org/10.1002/cber.19701030319.

(107) Knorr, R.; Trzeciak, A.; Bannwarth, W.; Gillessen, D. New Coupling Reagents in Peptide Chemistry. *Tetrahedron Lett* **1989**, *30* (15), 1927-1930. DOI: Doi 10.1016/S0040-4039(00)99616-3.

(108) Henklein, P.; Beyermann, M.; Bienert, M.; Knorr, R. New Uronium Salts as Coupling Reagents in Peptide Chemistry. *Peptides 1990* **1991**, 67-68.

(109) Mizhiritskii, M.; Shpernat, Y. Trends in peptide chemistry. 1. New life of "old" coupling reagent. *Chim Oggi* **2002**, *20* (5), 41-44.

(110) Bunin, A. I., Lawrence G.; Manion, Douglas; Spiegel, David Adam; Welch, Matthew Ernest. CD16a Binding agents and uses thereof cross-reference to related applications. US 2019.

(111) Luu, T.; Gristwood, K.; Knight, J. C.; Jorg, M. Click Chemistry: Reaction Rates and Their Suitability for Biomedical Applications. *Bioconjug Chem* **2024**, *35* (6), 715-731. DOI: 10.1021/acs.bioconjchem.4c00084.

(112) Jiang, D.; Li, P.; Yuan, L. Bioanalysis of free antisense oligonucleotide payload from antibody-oligonucleotide conjugate by hybridization LC-MS/MS. *Bioanalysis* **2024**, *16* (15), 791-800. DOI: 10.1080/17576180.2024.2368339.

(113) Li, C.; Arakawa, T. Agarose native gel electrophoresis of proteins. *Int J Biol Macromol* **2019**, *140*, 668-671. DOI: 10.1016/j.ijbiomac.2019.08.066.

(114) Li, C.; Akuta, T.; Nakagawa, M.; Sato, T.; Shibata, T.; Maruyama, T.; Okumura, C. J.; Kurosawa, Y.; Arakawa, T. Agarose native gel electrophoresis for characterization of antibodies. *Int J Biol Macromol* **2020**, *151*, 885-890. DOI: 10.1016/j.ijbiomac.2020.02.185.

(115) Krishan, A. Rapid flow cytofluorometric analysis of mammalian cell cycle by propidium iodide staining. *J Cell Biol* **1975**, *66* (1), 188-193. DOI: 10.1083/jcb.66.1.188.

(116) Ji, X.; Wu, L.; Marion, T.; Luo, Y. Lipid metabolism in regulation of B cell development and autoimmunity. *Cytokine Growth Factor Rev* **2023**, *73*, 40-51. DOI: 10.1016/j.cytogfr.2023.06.008 From NLM Publisher.

(117) Jones, S. F.; Joshi, H.; Terry, S. J.; Burns, J. R.; Aksimentiev, A.; Eggert, U. S.; Howorka, S. Hydrophobic Interactions between DNA Duplexes and Synthetic and Biological Membranes. *J Am Chem Soc* **2021**, *143* (22), 8305-8313. DOI: 10.1021/jacs.0c13235.

(118) Sobota, D.; Joshi, H.; Ohmann, A.; Aksimentiev, A.; Keyser, U. F. Tailoring Interleaflet Lipid Transfer with a DNA-based Synthetic Enzyme. *Nano Lett* **2020**, *20* (6), 4306-4311. DOI: 10.1021/acs.nanolett.0c00990.

(119) Lacroix, A.; Vengut-Climent, E.; de Rochambeau, D.; Sleiman, H. F. Uptake and Fate of Fluorescently Labeled DNA Nanostructures in Cellular Environments: A Cautionary Tale. *ACS Cent Sci* **2019**, *5* (5), 882-891. DOI: 10.1021/acscentsci.9b00174.

(120) Lucas, A. T.; Price, L. S. L.; Schorzman, A. N.; Storrie, M.; Piscitelli, J. A.; Razo, J.; Zamboni, W. C. Factors Affecting the Pharmacology of Antibody-Drug Conjugates. *Antibodies (Basel)* **2018**, *7* (1). DOI: 10.3390/antib7010010.

(121) Samantasinghar, A.; Sunildutt, N. P.; Ahmed, F.; Soomro, A. M.; Salih, A. R. C.; Parihar, P.; Memon, F. H.; Kim, K. H.; Kang, I. S.; Choi, K. H. A comprehensive review of key factors affecting the efficacy of antibody drug conjugate. *Biomed Pharmacother* **2023**, *161*, 114408. DOI: 10.1016/j.biopha.2023.114408.

(122) Tang, H.; Liu, Y.; Yu, Z.; Sun, M.; Lin, L.; Liu, W.; Han, Q.; Wei, M.; Jin, Y. The Analysis of Key Factors Related to ADCs Structural Design. *Front Pharmacol* **2019**, *10*, 373. DOI: 10.3389/fphar.2019.00373.

(123) Johnson, P.; Glennie, M. The mechanisms of action of rituximab in the elimination of tumor cells. *Semin Oncol* **2003**, *30* (1 Suppl 2), 3-8. DOI: 10.1053/sonc.2003.50025.

(124) Bennett, I. D.; Burns, J. R.; Ryadnov, M. G.; Howorka, S.; Pyne, A. L. B. Lipidated DNA Nanostructures Target and Rupture Bacterial Membranes. *Small* **2024**, *20* (35), e2207585. DOI: 10.1002/smll.202207585.

(125) Taib, N.; Aime, A.; Moreau, L.; Camplo, M.; Houmadi, S.; Desbat, B.; Laguerre, M.; Grinstaff, M. W.; Bestel, I.; Barthelemy, P. Formation of supramolecular systems via directed Nucleoside-Lipid recognition. *J Colloid Interface Sci* **2012**, *377* (1), 122-130. DOI: 10.1016/j.jcis.2012.03.041.

(126) Luvino, D.; Khiati, S.; Oumzil, K.; Rocchi, P.; Camplo, M.; Barthelemy, P. Efficient delivery of therapeutic small nucleic acids to prostate cancer cells using ketal nucleoside lipid nanoparticles. *J Control Release* **2013**, *172* (3), 954-961. DOI: 10.1016/j.jconrel.2013.09.006.

(127) Ammala, C.; Drury, W. J., 3rd; Knerr, L.; Ahlstedt, I.; Stillemark-Billton, P.; Wennberg-Huldt, C.; Andersson, E. M.; Valeur, E.; Jansson-Lofmark, R.; Janzen, D.; et al. Targeted delivery of antisense oligonucleotides to pancreatic beta-cells. *Sci Adv* **2018**, *4* (10), eaat3386. DOI: 10.1126/sciadv.aat3386.

(128) Stulz, R.; Meuller, J.; Bazdarevic, D.; Wennberg Huldt, C.; Stromberg, R.; Andersson, S.; Dahlen, A. A Versatile and Convenient Synthesis of (34) S-Labeled Phosphorothioate Oligonucleotides. *Chembiochem* **2018**, *19* (19), 2114-2119. DOI: 10.1002/cbic.201800417.

(129) Kajino, R.; Sakamoto, S.; Ueno, Y. Synthesis, gene silencing activity, thermal stability, and serum stability of siRNA containing four (S)-5'-C-aminopropyl-2'-O-methylnucleosides (A, adenosine; U, uridine; G, guanosine; and C, cytidine). *RSC Adv* **2022**, *12* (18), 11454-11476. DOI: 10.1039/d2ra00705c.

(130) Jafari, M.; Xu, W.; Pan, R.; Sweeting, C. M.; Karunaratne, D. N.; Chen, P. Serum stability and physicochemical characterization of a novel amphipathic peptide C6M1 for siRNA delivery. *PLoS One* **2014**, *9* (5), e97797. DOI: 10.1371/journal.pone.0097797.

(131) Gick, G. G.; Arora, K.; Sequeira, J. M.; Nakayama, Y.; Lai, S. C.; Quadros, E. V. Cellular uptake of vitamin B(12): Role and fate of TCblR/CD320, the transcobalamin receptor. *Exp Cell Res* **2020**, *396* (1), 112256. DOI: 10.1016/j.yexcr.2020.112256.

(132) Mebrahtu, A.; Lauren, I.; Veerman, R.; Akpinar, G. G.; Lord, M.; Kostakis, A.; Astorga-Wells, J.; Dahllund, L.; Olsson, A.; Andersson, O.; et al. A bispecific CD40 agonistic antibody allowing for antibody-peptide conjugate formation to enable cancer-specific peptide delivery, resulting in improved T proliferation and anti-tumor immunity in mice. *Nat Commun* **2024**, *15* (1), 9542. DOI: 10.1038/s41467-024-53839-5.

(133) Eltahir, M.; Laurén, I.; Lord, M.; Chourlia, A.; Dahllund, L.; Olsson, A.; Saleh, A.; Ytterberg, A. J.; Lindqvist, A.; Andersson, O.; et al. An Adaptable Antibody-Based Platform for Flexible Synthetic Peptide Delivery Built on Agonistic CD40 Antibodies. *Advanced Therapeutics* **2022**, *5* (7). DOI: 10.1002/adtp.202200008.

(134) Swerdlow, S. H.; Campo, E.; Pileri, S. A.; Harris, N. L.; Stein, H.; Siebert, R.; Advani, R.; Ghielmini, M.; Salles, G. A.; Zelenetz, A. D.; et al. The 2016 revision of the World Health Organization classification of lymphoid neoplasms. *Blood* **2016**, *127* (20), 2375-2390. DOI: 10.1182/blood-2016-01-643569.